Matter Under Extreme Conditions:

Theoretical Studies in Two Energy Regimes

by

Abhijit Majumder

A thesis submitted
to the Faculty of Graduate Studies and Research
in partial fulfillment of the requirements
of the degree of

Doctor of Philosophy

Physics Department, McGill University, Montréal, Canada.

Your file Votre référence
ISBN: 0-612-85724-7
Our file Notre référence
ISBN: 0-612-85724-7

Abstract

We apply the methods of statistical mechanics and field theory at finite temperature to understand phenomena in intermediate and high energy heavy-ion collisions.

In the intermediate energy scenario we concentrate on the pervasive phenomena of multifragmentation. We introduce various extensions of the recently proposed Recursive Statistical Multifragmentation Model (RSM model). In particular, we devise a novel Monte-Carlo technique to improve the treatment of the excluded volume in the model. We consider extensions to account for Coulomb effects and inclusion of isospin degrees of freedom. We then devise a consistent decay formalism to account for the change in isotope ratios due to decay of particle unstable clusters produced in such systems. We demonstrate how, with the above mentioned extensions, populations of various intermediate mass fragments observed in experiments may be explained. We then focus on the possible observation of critical phenomena in experiments, and provide a criticism of the parametrization techniques currently used by practitioners in the field. We demonstrate how such techniques may lead to misleading interpretations and identifications of critical phenomena.

In high energy heavy-ion collisions, we focus on the ongoing search for the Quark-Gluon-Plasma (QGP). The QGP is formed for a very short time and hence its presence is inferred through indirect signatures. In this thesis, we concentrate on the electromagnetic signatures of such a plasma. We demonstrate how the explicit breaking of charge conjugation invariance by the QGP may lead to the appearance of processes hitherto considered absent due to symmetry considerations. These processes allow for gluons to fuse to form lepton pairs and turn out to be comparable, in certain regions of parameter space, to the tree level rate for lepton pair formation from quark anti-quark annihilation. We then investigate the issue of collinear and infrared divergences in two-loop dilepton production rates. This is done by calculating the imaginary part

of the retarded two-loop self-energy of a static vector boson in a plasma of quarks and gluons. We recombine the various cuts of the self-energy to generate physical processes. We demonstrate how cuts containing loops may be reinterpreted in terms of interference between $O(\alpha)$ tree diagrams and the Born term along with spectators from the medium. We apply our results to the rate of dilepton production in the limit of dilepton invariant mass $M >> T$. We find that all infrared and collinear singularities cancel in the final result obtained in this limit.

Résumé

Nous appliquons les méthodes du mécanique statistique et de la théorie des champs à température finie pour comprendre des phénomènes apparaissant lors de collisions d'ions lourds aux energies intermédiaires et élevées.

Dans le cas des energies intermédiaires, nous poursuivons l'étude des phénomènes de multifragmentation. Nous présentons plusieurs améliorations du modèle Récursif de Multifragmentation Statistique (modèle RMS), récemment proposé. En particulier, nous présentons une nouvelle technique Monte-Carlo permettant d'améliorer le traitement du volume exclu. Les développements étudiés tiennent compte à la fois des effets de Coulomb et de l'inclusion des degrés de liberté d'isospin. Nous proposons alors un formalisme cohérent de désintégration, expliquant le changement des rapports d'isotopes dûs à la désintégration des noyaux instables produits dans de telles collisions. Nous démontrons comment, avec les développements mentionnés ci-haut, les populations de divers fragments de masses intermédiaires observés dans les expériences peuvent être expliquées. Nous nous concentrons alors sur l'observation possible des phénomènes critiques dans les expériences, et fournissons une analyse des techniques de paramétrisation actuellement employées dans ce domaine. Nous démontrons comment de telles techniques peuvent mener à des interprétations trompeuses des phénomènes critiques.

Dans des collisions d'ions lourds aux énergies élevées, nous abordons la recherche du plasma de quarks et de gluons (PQG). La durée de vie du PQG est court et par conséquent sa présence est détectée grâce à des signatures indirectes. Dans cette thèse, nous étudions les signatures électromagnétiques d'un tel plasma. Nous démontrons comment la rupture explicite de l'invariance de la conjugaison de charge par le PQG peut mener à l'émergence de processus que l'on croyait jusqu'à présent absents. Ces processus permettent aux gluons de se fusionner et ainsi de former des

paires de leptons. Ces processus s'avérent comparables, dans certaines régions de l'espace des paramètres, au taux de formation à niveau d'arbre de paires de leptons provenant de l'annihilation d'un quark et d'un anti-quark. Nous étudions aussi la question des divergences collinéaires et infrarouges dans les taux de production de dileptons à deux boucles. Ceci s'exécute en calculant la partie imaginaire de l'énergie propre retardée à deux boucles d'un boson vectoriel statique dans un plasma de quarks et de gluons. Nous combinons les coupures de l'énergie propre pour produire des processus physiques. Nous démontrons comment les coupures contenant des boucles peuvent être réinterprétées en terme d'interférences entre les diagrammes d'arbres d'ordre α et le terme de Born, avec des spectateurs du milieu. Nous appliquons nos résultats au taux de production de dileptons dans la limite $M >> T$ de la masse invariante du dilepton. Le résultat final obtenu dans cette limite établit l'absence de singularités infrarouges et collinéaires.

Contents

List of Figures

List of Tables

Acknowledgement

It is a great pleasure to thank my supervisors: Prof. Subal Das Gupta and Prof. Charles Gale. I thank them not only for accepting me as their student but mostly for imparting in me the education that has helped me to progress towards the completion of this degree. Their suggestion of research topics, guidance during the difficult stages of a project, and the donation of enormous amounts of their time and knowledge in frequent discussions have been an invaluable aid for which I remain grateful.

Special thanks go out to Prof. C. S. Lam. Though I was never his student, I benefited enormously from his deep understanding of field theory through numerous long discussions. His generosity with his time, and patience with my often naive queries is gratefully acknowledged. Thanks also go out to Profs. C. P. Burgess, S. Jeon, G. Mahlon and G. D. Moore for invaluable discussions which led to an important part of my education here.

Graduate life can often become very difficult without the friendship and camaraderie of one's fellow graduate students. Special thanks go out to Y. Aghababaie for his help in innumerable issues both relating to this thesis and to life at McGill in general. I am also grateful to many other graduate students here for their help in various problems that I encountered and for the stimulating environment created by them here at McGill. I would also like to thank E. Filotas for providing the French translation of the abstract.

I thank my parents and my brother for their love, support and understanding throughout these five years. Last but by no means least I am grateful to my loving wife Nayana. Her ability and desire to take care of everything else as I focused solely on the thesis, along with her continuous support and encouragement leave me in her debt.

1

INTRODUCTION

The behaviour of ordinary matter subjected to extraordinary temperature and density remains an outstanding question in modern physics. By ordinary matter, we specifically mean strongly interacting matter composed of nuclei, or protons and neutrons, or mesons and baryons, or perhaps even quarks and gluons. Such an investigation, though interesting in its own right, would provide us with the theoretical tools to obtain a better understanding of a variety of phenomena occurring in such diverse scenarios as stellar interiors, neutron stars, the vicinity of black holes, and the early universe. Besides revealing novel, collective phenomena at each energy scale, it provides us with a deeper understanding of the complicated underlying theory of strong interactions. A comprehensive understanding of these topics is still greatly lacking. The fundamental science that describes these phenomena straddles both nuclear and particle physics and forms the background for the investigations reported in this thesis.

A detailed understanding of the physics of any phenomena would have to involve both the development of theories and models, and their detailed verification through a broad range of experiments. However, probing these phenomena experimentally is a complicated task. The natural occurrences of such behaviour pointed out in the previous paragraph are either too distant or provide too few and indirect probes of such physics. The sole laboratory tool at our disposal is that of heavy-ion collisions. Though such experiments, at present, may not span the entire variety of our queries, they provide information over a considerable range of parameters. The research

documented in the following pages will be concentrated primarily on the study of the kinds of hot and dense matter that is, or is expected to be, produced in heavy-ion collisions.

1.1 Heavy-Ion Collisions

Broadly speaking, heavy-ion collisions cover a wide range of different experiments: from high energy pions or protons incident on nuclei like Xe [1], to collisions of unequally sized nuclei *e.g.*, N on Ag [2], to collisions of very large nuclei *e.g.*, Au on Au [3]. The experiments also vary over a broad range in energies from tens of MeV in the c.m. frame at the NSCL[1], to hundreds of GeV at RHIC[2] (or even few TeV at the forthcoming LHC[3]). Each experiment provides data on the conditions prevailing in the very central or head on collisions to the peripheral or just grazing collisions. Thus, these experiments represent an indispensable tool as they allow the possibility, for the first time, to study matter at various temperatures and densities in a controlled laboratory environment. This allows one to make quantitative comparisons between theory and experiment over a wide range of conditions.

In spite of their broad range, there are certain unifying features of these experiments that allow us to classify them. Consider the collision of two heavy ions at a given impact parameter. The collision may be caricatured by the sketch in Fig. (1.1). Consider an imaginary line dividing the nuclei into two pieces A and A', and B and B'. During the collision, the parts A' and B' meet and form what is referred to as the participant zone. It is this zone that experiences the maximum compression and deposition of energy. We expect most of the particle production and the appearance of exotic phenomena to occur in this region. The pieces A and B are torn of from

[1]The National Superconducting Cyclotron Laboratory at Michigan State University, East Lansing, Michigan.

[2]The Relativistic Heavy-Ion Collider at Brookhaven National Laboratory, Upton, New York.

[3]The Large Hadron Collider at the European Centre for Nuclear Research (CERN), Geneva, Switzerland.

the participant region and fly down the beam line. They constitute the spectator regions. In heavy-ion collisions, often enough energy is deposited in the spectators that they undergo thermalization through compression and expansion, eventually often fragmenting into various clusters [4]. Ostensibly, the collisions where the participant region is much larger than the spectator region constitute the central events; the opposite case corresponds to the peripheral events.

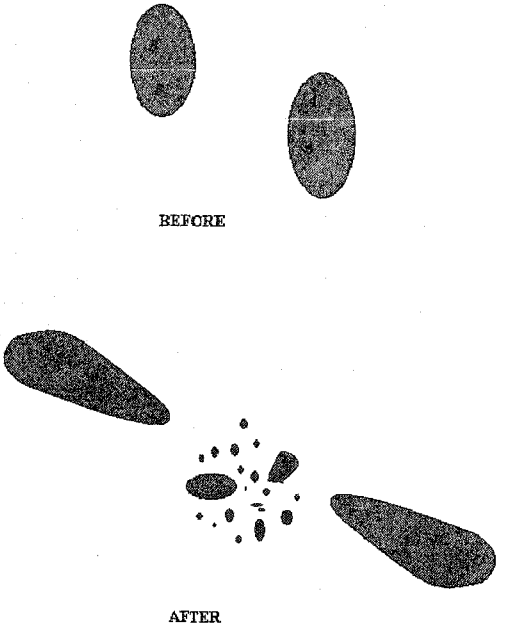

Figure 1.1: Generic picture of a heavy-ion collision

In a central event, a considerable fraction of the energy of the incoming beams is dissipated in the participant region through compression and/or multiple particle collisions. This leads to a thermalization of the constituents of the participant region. One may now attempt to describe the experimental data from this scenario with the help of models and theories based on the presence of an equilibrium temperature. In a peripheral event a lot of the matter and energy may simply 'flow' away from the central region with, or following, spectator escape; or it may get squeezed out of the

participant region without being thermally excited. The latter variety of flow may also occur in central collisions. In such cases, one needs to use models and theories based on transport considerations in conjunction with the thermal models. In this thesis we will explicitly concentrate on the thermalized region of the collision. All the calculations that will be presented will assume that in the region under consideration, matter has undergone multiple collisions or compression and expansion and has reached a certain amount of local thermal equilibrium. It should be noted that these constraints do not preclude the presence of quasi static or hydrodynamic expansion of the participant region.

Under the influence of the above mentioned assumptions, we have essentially confined our task within the area of equilibrium statistical mechanics. The general picture in most cases is the same: we consider a hot system undergoing thermal expansion. In the course of this expansion, the system cools and may, if the initial temperature is high enough, undergo a phase transition from one set of degrees of freedom to another. As the expansion continues the system eventually progresses to a dilute enough stage that interactions between the various constituents cease and each then begins to stream freely towards the detectors. This process is termed 'freeze out'. The time taken for this to occur, from the time when two nuclei impinge on each other, is called the freeze out time. Up to this point, interactions persist, and may continually change the composition of the hot expanding system as its temperature and density change with the expansion. Thus, we will essentially consider a system with a certain set of degrees of freedom in contact with an imaginary heat reservoir. At low energies, the main degrees of freedom will invariably be nuclei and nucleons. At intermediate energies, the degrees of freedom will be a cocktail of stable and unstable mesons and baryons. At very high energies the degrees of freedom may even be the elementary quarks and gluons that make up all hadrons.

1.2 Subject Area of the Thesis

No doubt, these collisions will produce a large number of objects (particles, nucleons and/or nuclei) after freeze out. These may be unstable and decay further as they stream towards the detectors. Thus the spectra of the outgoing objects, not only the total numbers but also their distributions constitute the experimental data. The theoretical task will be to explain the various facets of these spectra.

At the very outset, we may distribute the outgoing objects into two broad categories, depending on the physics used to describe their production: those produced by strong interaction, and those produced by weak or electro-magnetic interaction. In the best of cases (central collision, sufficient thermalization) most populations of the strongly interacting entities can usually be ascertained from a thermal model. These models become more complicated as we encounter greater particle production. At low energies the main objects that are detected are essentially nuclei and nucleons. These nucleons are essentially those that are brought in by the two colliding nuclei. There is no extra particle production. Any thermal model applied at this stage will essentially consider nucleons as its degrees of freedom and different partitions of a partition function will essentially consist in distributing these nucleons in a variety of clusters.

As one increases energy, one eventually achieves a temperature when the lightest strongly interacting particles (pions) will begin to appear. As the energy is raised, various other strongly interacting particles may be produced. As mentioned before: in the best of cases, one may ascertain these populations from a thermal model with the various masses of these elementary particles as inputs. At even higher energies, one may even obtain a thermalized plasma of deconfined quarks and gluons. Here, once again the populations of the quarks and gluons may be obtained from a partition function calculation. As the plasma expands and cools, the partons will eventually reconfine to a gas of hadrons. Thus we note that thermal models may become quite complicated as the energy is increased. In this thesis we will present a variety of

results from a thermal model, applied to the simpler case of multifragmentation in low energy heavy-ion collisions. It should be pointed out that not all populations of the produced particles/clusters nor their distributions can be explained by thermal modelling. Often, additional physics has to be invoked such as primordial effects, pre-equilibrium emission, flow effects etc. In many cases, the additional physics has yet to be understood.

In contrast to the strongly interacting particles, the spectra of weak and electromagnetically interacting particles is rather different. This is believed to be the case, due to their different production mechanism. The excited systems that are formed in the central participant region will live, typically, for a length of time of the order of the strong interaction time scale (10^{-24})s. In such a short time, electromagnetic and weak interactions fail to achieve equilibrium, *i.e.*, states that are formed by electromagnetic or weak interaction with the constituents in the medium will be formed in far fewer numbers. The cross section for the interaction of these particles with the constituents of the hot medium is set by the electromagnetic or weak interaction scale. This makes the cross section very low and hence the mean free path of these particles is much larger than the system size. Thus, states that are formed solely as a result of an electromagnetic or a weak interaction between the various strongly interacting constituents, will not only be produced in far fewer numbers but will in most cases escape the hot system. In this thesis we will also present results of calculations of the production rates of particles produced by electro-magnetic interactions (dileptons and real photons). These will pertain to the case of heavy-ion collisions at ultra-relativistic energies, where we expect the formation of a plasma of quarks and gluons. It will be demonstrated that due to their lack of rescattering in the medium, these spectra allow us to probe the very early stages of the collisions, a region often opaque to strongly interacting probes.

1.3 Structure and Originality of Thesis

In the following, the thesis will essentially be divided into two parts. In the first part we will present work on the phenomena of multifragmentation in low-energy heavy-ion collisions. In chapter 2, we will set up the thermal model that may be used to describe the production of nuclear clusters in these collisions. Various aspects of the model will be discussed such as excluded volume, Coulomb interactions; various inputs will be considered such as mass formulae, exact nuclear level schemes etc. In this work, I performed the first estimates of the effects of excluded volume and the Coulomb correction on the equation of state and the nature of the phase transition.

In chapter 3 we will describe in detail the estimation of the excluded volume in such models, this aspect has up to now been given little attention. We will present a novel Monte-Carlo technique to estimate this effect. Though a complete closed expression has not been devised, noticeable effects on the equation of state and the nuclear phase diagram have been demonstrated, making this an important effect. Here, I performed the entire Monte-Carlo calculation of the excluded volume effect and devised the parametrisation of the free volume. This work has been published in Physical Review C **59** 845 (1999).

As mentioned previously, the nuclear clusters produced in such reactions are particle unstable even at freeze out and may decay multiple times as they stream to the detectors. In chapter 4, we will describe how such a decay formalism may be set up. Using this we will estimate the populations of certain selected isotopes produced in such collisions and compare with experimental data. We demonstrate that such models coupled with a secondary decay formalism provide a very good fit to the data on isotope ratios obtained in experiments. Here I devised an entirely new decay formalism, based on the Weisskopf theory. Unlike previous formalisms, this method is completely compatible with the preceding canonical calculation. This work has been published in Physical Review C **61** 034603 (2000).

In chapter 5 we will turn our attention to the subject of critical phenomena ob-

served in such experiments. Using the predictions from this model, we will demonstrate how, by measuring a limited set of isotope yields, one may make an incorrect assessment of the order of the liquid gas phase transition observed in these experiments. We demonstrate this by parametrising the isotope yields from a multifragmentation model which displays an explicit first order phase transition. We show that if one were to concentrate on a small set of yields, as are measurable in experiments, it is possible to obtain a very good fit to the data with a formula which suggests that the disassembling system is nearing a second order phase transition. After reviewing Fisher's droplet model, I devised a parametrisation (based on the droplet model) to fit the yields from the multifragmentation model described above. I then devised, yet another formalism based on a general thermodynamic model with explicit first order phase transition. I then demonstrated how the two parametrisations (which are quite dissimilar) can be made to coincide exactly in the range of yields considered. Thus, proving that a limited fit of the yields with a scaling law may not be ascribed as evidence for critical behaviour. This work which also involved contributions from other collaborators has been published in Physical Review C **65** 034608 (2002).

In the second part of the thesis we will deal with the production of electromagnetically interacting particles (in particular photons and dileptons) from the hot plasma of quarks and gluons produced in ultra relativistic heavy-ion collisions. Most calculations of the number of dileptons and estimates of their observability rely on the rate of dilepton production at lowest order in the strong and electromagnetic coupling constant (Born Term). In this thesis we will demonstrate how in most cases this may not be the leading contribution to the rate of production of these particles. Higher order corrections may dominate. These corrections may arise from various medium dependent sources (high temperature, net plasma charge, remnant divergences). We will demonstrate if and where each of these contributions may become important. We will start with dilepton production at very low energy of the dilepton pair. In this region, high temperature effects may become important. Though most of this part does not constitute the author's own work, it will be presented here for completeness.

At intermediate energies, finite charge effects may become considerable due to the breaking of Furry's theorem by a charged medium. We will show that this may lead to a new channel of dilepton production via two gluon fusion, which may become comparable to the Born term in certain regions of the parameter space. To my knowledge, I am the first to predict such a possibility. I performed the first calculation of this effect and wrote all sections of the ensuing paper and related conference proceedings. This conjecture was first published in Physical Review D **63** 114008 (2001). Following that, it also appeared in the proceedings of the International Nuclear Physics Conference (INPC 2001) **nucl-th/0108011** , and in the proceedings of the Montreal-Rochester-Syracuse-Toronto meeting (MRST01) **nucl-th/0108169**. This process may also have important implications leading to the breaking of Yang's theorem in the medium. The calculation, incorporating this effect, has also been performed by me. These results will be submitted in the very near future to Physical Review D.

Finally at high invariant mass we will concentrate on the issue of infrared and collinear divergences arising in the various channels at next-to-leading order in the strong coupling constant. The topic as whether they cancel or not has led to some controversy in the field. If such divergences were not to cancel in the coherent sum of the contributions from the different channels then the next-to-leading order rates would dominate over the Born term. In Chapter 9, we will demonstrate how such contributions may be calculated both using the rigorous methods of the imaginary time formalism of finite temperature field theory and by the recently proposed elegant method of spectator interpretation. Spectators are particles in the medium which travel along with the reacting particles without taking part in the actual process. We demonstrate how the various cuts obtained from the imaginary time formalism may be recombined in terms of interference between order α tree diagrams and the Born term along with spectators from the medium. Finally we will show how various infrared and mass divergences which may have lead to the Born term being subdominant actually cancel when all the contributions to the rate at next-to-leading

order are summed. Here, I performed the entire calculation and demonstrated, for the first time, how the spectator interpretation may be explicitly deduced from the imaginary time formalism. This work has been published in Physical Review C **65** 055203 (2002).

2

MULTIFRAGMENTATION, THE SMM AND THE RSM MODEL.

2.1 *Introduction*

We begin this part of the thesis with a detailed study of heavy-ion collisions at intermediate energies. By 'intermediate energies' we specifically mean the phenomena occurring in the central participant region in heavy-ion collisions at beam energies from 10MeV to 50MeV [2, 5, 6] per particle. Similar scenarios may also be found in the spectator regions in heavy-ion collisions at energies up to 600 MeV per particle [4], where the spectator regions detach from the participant regions and experience excitation and fragmentation as they stream down the beam line. Such phenomena have also been noticed in the impinging of small hadrons (pions, protons, antiprotons) at energies from 10 to 300 GeV on large nuclear targets [1, 7]. In this, and the following three chapters, we concentrate on the physics of the production of nuclear clusters in such collisions.

In the collision of heavy ions or the impinging of a light high energy particle on a heavy target nucleus, it is believed that an excited compound nuclear system is formed. This will then de-excite. If the excitation energy is $\simeq$ 1 MeV/nucleon, then evaporation of the system by successive emissions of light particles [8, 9] or fission of the system are the main de-excitation mechanisms. In this regime, there is sufficient time between successive emissions for the system to relax to a new state of equilibrium. At excitation energies $\simeq$ 3 MeV/nucleon or higher, the time interval between emissions becomes comparable to the relaxation time. At excitation energies com-

parable to the binding energy $\simeq$ 8 MeV/nucleon, the very existence of a long lived compound nucleus is unlikely. At such energies it is believed that the compound system de-excites by an explosion like mechanism producing nuclear clusters of varying masses [10]. This process is called multifragmentation. It will form the central subject of our study in this and the next three chapters.

Very early on in the study of heavy-ion collisions, it was noted that the momentum spectra of the outgoing particles had a Boltzmann like distribution. This led to the conjecture that the source of these particles must have achieved some level of thermalization [1, 11]. This immediately led to two different approaches of understanding these phenomena: the study of infinite nuclear matter through a finite temperature many-body approach; and that of quantizing the spectra in terms of thermal models. This thesis will follow the latter approach, as it pertains much more to the experimental situation: allowing one to incorporate various facets of the system such as finite size, isospin, Coulomb interactions, shell effects of clusters etc.

Many-body approaches however do reveal important information. Various theoretical explorations of the thermodynamic behaviour of nuclear matter have been carried out [12, 13, 14]. Nuclear matter is an idealized infinite system filled with protons and neutrons, without coulomb interaction. One notices a consistent pattern. At zero temperature, nuclear matter is a fermi liquid. As the temperature is raised, one notices that hot nuclear matter displays an equation of state with a Van der Waals behaviour [12]. This is characteristic of a system which undergoes a liquid-gas-like phase transition. Considerable experimental evidence for such a transition has also been surmised from the power law fits to the fragment yields [15, 16], as well as from attempts to trace out the caloric curve [4, 17].

In heavy ion collisions one does not approach the infinite nuclear matter limit. Here, one considers the production of large clusters ($Z > 30$) as the production of large droplets of the nuclear liquid. In collisions at high energies one observes the disassembly of the whole colliding system into individual nucleons, and tightly bound small nuclei: this is considered as the gas phase. During multifragmentation

one will also observe the production of a large number of fragments which are in between these two extremes: with charge Z between 3 and 30. These are called the Intermediate Mass Fragments (IMFs). IMFs are considered to be small droplets of nuclear liquid and thus signify condensation and thus the passage of the system through the coexistence region. Hence, they constitute a very important experimental observable to study the nuclear liquid-gas phase transition. Most of the effort in this thesis will be directed towards understanding the spectrum of IMFs and the information that they convey.

Multifragmentation in heavy ion collisions is however a complex phenomenon. The amount of thermalization that has occurred in the system is uncertain; hence it is unclear as to whether the phenomena observed are thermal or dynamical in their origin. Besides the two major historical approaches cited previously, a variety of other approaches have been investigated: evaporative pictures [18], percolation models [19, 20], lattice gas models [21], and dynamical models based on Boltzmann simulations [22]. As mentioned before, we will consider the thermal model or alternatively the statistical approach [23, 24, 25, 26]. The model that we will develop is most similar to that of Ref. [26], where one considers sampling all configurations of non-interacting clusters and constructing a canonical partition function. This model is referred to as the Statistical Multifragmentation Model (SMFM or SMM). This model is throughly reviewed in Ref. [26]. To calculate the partition function, however, our model uses the recently developed recursion relation technique of Ref. [27]. By eliminating the need for computationally intensive Monte Carlo procedures and associated approximations, this technique allows a deeper insight into the thermodynamic principles which drive the statistics of fragmentation.

In the next section we introduce the *basic model* (This section is mostly based on Ref. [28]). Here we will treat the nuclear clusters as drops of nuclear liquid admitting a Bethe-Weizacker mass formula and the excitation spectrum of a Fermi liquid. We will outline the calculation strategy using the recursion relation technique. In section 2.3 we will present the results of the calculations from this model. In section 2.4 we

summarize and discuss various extensions that will be incorporated in the model in subsequent chapters. These will serve the purpose of making the model more realistic and allow for comparisons with data.

2.2 The R. S. M. model

Assume that the system which breaks up after two heavy ions hit each other can be described as a hot, equilibrated nuclear system characterised by a temperature T and a freeze-out volume V within which there are A nucleons. Assume also that the volume V is much larger than V_0, where $V_0 = A/\rho_0$ is the ground state volume of a nucleus of A nucleons. The A nucleons can appear as monomers or as composites of k nucleons. These composites do not interact with each other except through a Coulomb interaction to be introduced later. The canonical partition function for this system can be written as (see Ref. [29]),

$$Q_A = \sum_k \Pi_k \frac{\omega_k^{n_k}}{n_k!}, \tag{2.1}$$

where ω_k is the partition function of a single composite of size k, n_k is the number of such composites and the sum goes over all the partitions which satisfy $\sum n_k k = A$.

Note that we have not distinguished between neutrons and protons; this will be introduced later. All nuclear properties of the clusters are contained in their individual partition functions ω_k, given as

$$\omega_k = \frac{V_{\rm fr}}{\hbar^3}\left(\frac{kmT}{2\pi}\right)^{3/2} \times q_{k,\rm int}. \tag{2.2}$$

The first part is due to the kinetic motion of the centre of mass of the composite in the volume $V_{\rm fr}$ and the second part ($q_{k,\rm int}$) is due to the internal structure. In the above m is the mass of a single nucleon. We will have much more to say regarding the choice of $q_{k,\rm int}$ in subsequent chapters, as we make the model more realistic. For now we chose the simple form of

$$q_{k,\text{int}} = e^{-F_{k,\text{int}}/T}, \tag{2.3}$$

where $F_{k,\text{int}}$ is the internal free energy of the cluster of size k. The free energy can be decomposed in terms of the energy and entropy of the cluster as $F = E - TS$.

We will assume for the moment, that the clusters are drops of nuclear liquid with a Bethe-Weizacker mass formula and a Fermi excitation spectrum. Hence the internal energy of such a drop at a temperature T is

$$E_{k,\text{int}} = -W_0 k + \sigma(T)k^{2/3} + T^2 k/\epsilon_0. \tag{2.4}$$

Here W_0 is the volume energy per nucleon(=16 MeV), $\sigma(T)$ is the surface tension which is a function of the temperature T. The entropy is simply the entropy of a Fermi gas of k nucleons at a temperature T, (here we use the low temperature expansion) *i.e.*,

$$S = 2Tk/\epsilon_0. \tag{2.5}$$

Following reference [26] the value of ϵ_0 is taken to be 16 MeV. Lastly the temperature dependence of $\sigma(T)$ is taken from Ref. [26] as $\sigma(T) = \sigma(0)[(T_c^2 - T^2)/(T_c^2 + T^2)]^{5/4}$ with $\sigma(0) = 18$ MeV and $T_c = 18$ MeV. Any other dependence could be used including a dependence on the average density. Lastly the quantity V_{fr} is the free volume available for motion to each cluster; it is related to V as $V_{\text{fr}} = V - V_{\text{ex}}$, where V_{ex} is the volume excluded due to finite sizes of clusters. This quantity and its effect will be explored rigorously in the following chapter. For now V_{fr} is a variable of the calculation. We have also not included Coulomb energy or symmetry energy; these will be discussed later. For now, we attempt to evaluate the partition function with composites defined by simply these three characteristics (Eq. (2.4)).

A priori this appears to be a horrendously complicated problem; indeed, in previous calculations, the evaluation of the partition function involves complicated and

time consuming numerical algorithms [26]. It was noted in Ref. [27] that Q_A can be computed recursively via the formula,

$$Q_A = \frac{1}{A}\sum_k \omega_k Q_{A-k}. \tag{2.6}$$

Here ω_0 is 1. It is this formula and the generalisation of this to a more realistic case (see Chapter 4) that makes this model so readily soluble. Due to this recursion relation, we call this model the Recursive Statistical Multifragmentation Model (in short, the RSM model). All properties of the system are determined by the partition functions of independent clusters. The recursive formula, above, allows a great deal of freedom in the choice of partition functions for individual fragments, ω_k. Any function of temperature, density and k is allowed. One may even use actual energy levels. However, explicit dependence on the configuration of the remainder of the system is outside the scope of this treatment *i.e.*, we cannot include explicit interactions between various clusters. The model is thus valid for low densities. With this recursion relation, however, the partition function may be computed, readily, in a matter of minutes.

2.3 *The calculation.*

Having constructed the partition function for the model, we may now deduce a variety of properties of the system. We begin by evaluating the free energy F defined as

$$F_A = -T\log Q_A. \tag{2.7}$$

This is plotted as a function of temperature at constant density in Fig. (2.1) for three systems of size $A = 700, 1400, 2800$. Note the clean bend developing as the system size is increased. The location of the bend shifts towards higher temperature as the system size (or particle number A) is increased. We next evaluate the total multiplicity, which may be easily derived from Eq. (2.1) as,

$$m = \sum_a \langle n_a \rangle = \frac{1}{Q_A} \sum_a \sum \prod_k n_a \frac{\omega_k^{n_k}}{n_k!} = \sum_a \omega_a \frac{Q_{A-a}}{Q_A}. \tag{2.8}$$

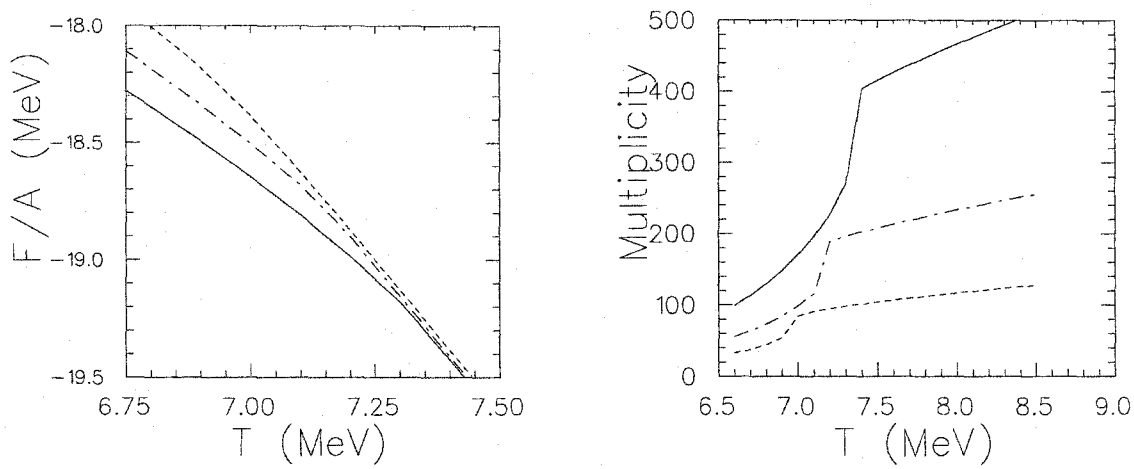

Figure 2.1: Free energy per nucleon and multiplicity as a function of temperature at constant density. This is plotted for three system sizes: $A = 700$, the dashed line; $A = 1400$, dot dashed line; $A = 2800$, solid line.

This is also plotted as a function of temperature at constant density in the second plot of Fig. (2.1). Note the developing discontinuity in the total multiplicity. As the particle number tends to infinity this will turn into a sharp discontinuity. The multiplicity can be re-expressed as a first derivative of the free energy with respect to a chemical potential and a discontinuity in the multiplicity indicates a discontinuity in the first derivative of the free energy *i.e.*, a first order phase transition. A similar pattern may also be noted in the behaviour of the energy per particle as a function of temperature (see Fig. (2.2)), where,

$$E/A = \frac{1}{A} \sum_k \left(E_{k,\text{int}} + \frac{3}{2} T \right) \langle n_k \rangle. \tag{2.9}$$

Note that the location of the discontinuity precisely matches the location of the bend of the free energy. We also plot the specific heat $C_v/A = \frac{1}{A} \frac{\partial E}{\partial T}$ as a function of temperature. As expected, we find a spike that grows with A. All these indicate the presence of a first order phase transition in the model. The transition occurs at

temperatures which rise with particle number: 6.95 MeV for 700 particles, 7.15 MeV for 1400 particles and 7.3 MeV for 2800 particles (see Fig. (2.2)).

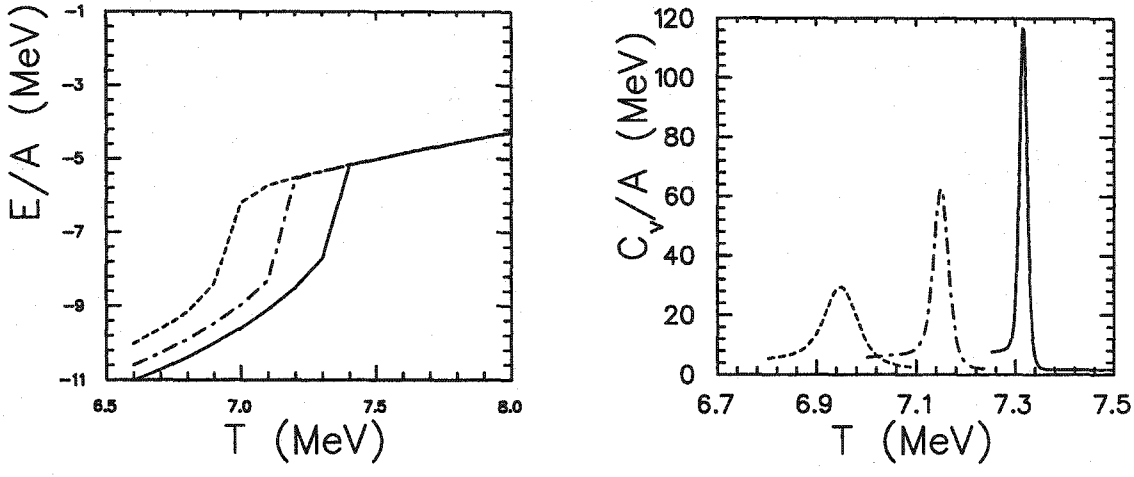

Figure 2.2: Energy per nucleon and C_v/A as a function of temperature at constant density. This is plotted for three system sizes: $A = 700$, the dashed line; $A = 1400$, dot dashed line; $A = 2800$, solid line.

Intrinsic thermodynamic quantities may be calculated in a straightforward manner. For instance the pressure and chemical potentials may be calculated through the relations,

$$\mu = -T\left(\ln \Omega_A - \ln \Omega_{A-1}\right) \qquad (2.10)$$
$$P = T\frac{\partial \ln(\Omega_A)}{\partial V}$$

Calculations of μ and P are displayed in Figure 2.3 as a function of density for a system of size $A = 200$. Both the pressure and chemical potential remain roughly constant throughout the region of phase coexistence. Of particular note is that the pressure actually falls in the coexistence region due to finite size effects.

We now make some comments about influences of various factors in Eq. (2.4). The bulk terms, $W_0 + T^2/\epsilon_0$, do not affect the free energy, thus they may be ignored when calculating fragmentation observables. Their influence with respect to intrinsic thermodynamic quantities is of a trivial character. The surface term $S(T)$ is completely responsible for determining all observables related to fragmentation and therefore all

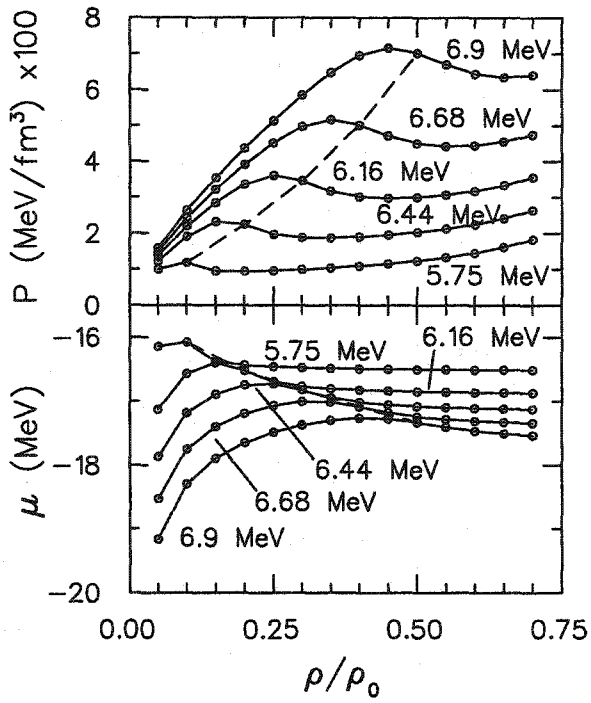

Figure 2.3: The $P-\rho$ diagram for A=200 at selected temperatures in the upper panel shows the flattening of the pressure throughout a range of densities, as expected in a first order phase transition. The dashed line shows where C_v is maximized as a function of temperature. The evolution of the chemical potential is displayed in the lower panel.

aspects of the phase transition. Aside from the system size A, fragmentation is determined by two dimensionless parameters. The first is the entropy associated with thermal motion, $(V/A)(mT/(2\pi\hbar^2))^{3/2}$ and the second is the surface term $S(T)/T$.

At a given temperature, the free energy $F = E - TS$ of A nucleons should be minimized. With the surface tension term, E is minimized if the whole system appears as one composite of A nucleons but the entropy term encourages break up into clusters. At low temperatures, the surface term dominates while at high temperatures entropy prevails and the system breaks into small clusters. The mass distribution may be calculated given the partition function, as,

$$\langle n_k \rangle = \frac{\omega_k Q_{A-a_k}}{Q_A}. \tag{2.11}$$

The mass distribution for a system of size $A = 700$ is displayed in the left panel of Fig. 2.4 for three temperatures, 6.5, 6.9 and 7.3 MeV which are centred about the

transition temperature of 6.9 MeV. The mass distribution changes dramatically in this small temperature range. Below the transition temperature we note the hump at large value of k. This indicates that, as speculated, the system exists mostly as a large drop (considered the liquid phase) and some small clusters. At temperatures above the transition temperature the system exists solely as small clusters (considered the gas phase). Note the broad distribution in the vicinity of the transition temperature. This may also be noted by noting the behaviour of the largest cluster. We plot this for three systems of size 200, 300 and 500 respectively in the right panel of Fig. (2.4). Note the sudden disappearance of a large cluster at the boiling temperature.

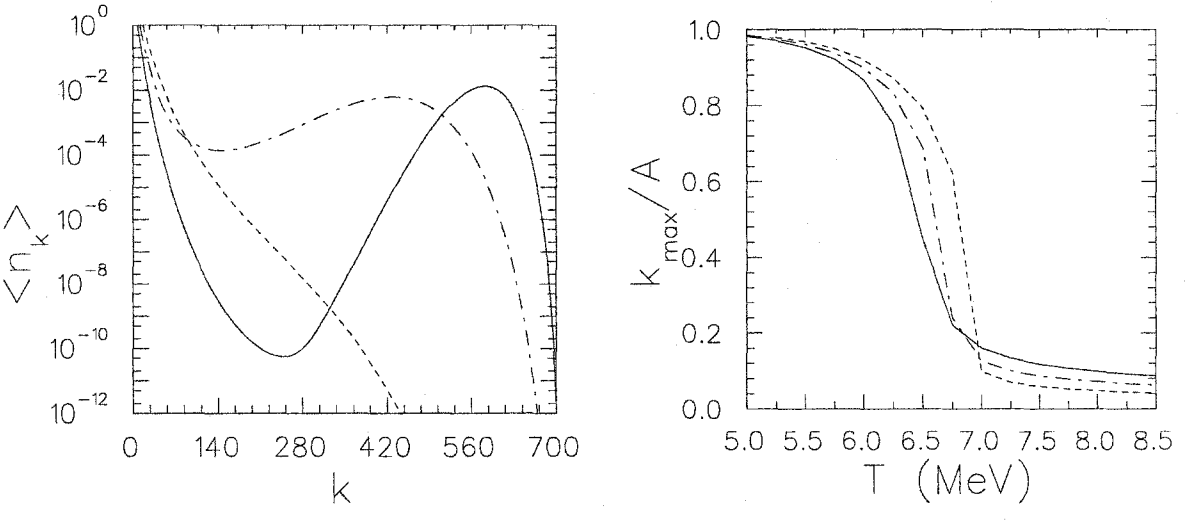

Figure 2.4: On the left, mass distributions $\langle n_k \rangle$ are displayed for three temperatures for $A = 700$. At 6.5 MeV (solid line), most nucleons reside in a single fragment, while at 7.3 MeV (dashed line), most nucleons are part of small fragments. At the critical temperature, 6.9 MeV (dot dashed line), the mass distribution is remarkably broad. On the right, we show the variation of the size of the largest cluster with increasing temperature for three systems of sizes 200 (solid line), 300 (dot dashed line) and 500 (dashed line) particles.

In the above, we have highlighted the various characteristics of a simplified version of the RSM model that we will use. Each of the facets has been demonstrated for systems with a variety of sizes and temperatures. In the next section we will describe a variety of extensions that may be introduced to make the model more realistic. These include a discussion on the excluded volume, Coulomb force, isospin degrees of freedom, inclusion of shell effects and secondary decay of fragments. The excluded

volume is a more complicated topic, and will be discussed in greater detail in the next chapter. As noted previously, one may evaluate the internal partition functions directly from experimental data on nuclear energy levels, instead of using a mass formula. Also, the above model describes the situation *at freezeout.* Considerable secondary decay takes place in the time from freezeout to detection. Incorporation of these last two topics will be discussed in greater detail in chapter 4.

2.4 Enhancements, extensions, etc.

The model that we have described in the preceding two sections is a rather rudimentary version of the RSM model that will be used to compare with experiment. It contains only the most minimal features of hot nuclei: a volume binding energy, a surface term and a fermi gas excitation. The reason for this is not merely simplicity of treatment but rather the exposure of the 'primal' characteristics of the model. In the following chapters we will invoke various extensions to the model. The reader will find that they will tend to smooth out many of the sharp features displayed in the previous section. Here we highlight some such extensions.

2.4.1 Excluded volume

The volume used to define the partition functions of individual fragments, ω_k given in Eq. (2.4), should reflect only that volume in which the fragments are free to move. It has been suggested [30], that one replace the full freeze out volume with $V \to V - A/\rho_0$ to incorporate the volume taken up by the nuclei. By inspecting Eq. (2.4) on can see that this affects the partition function by simply changing the density or volume used to plot observables. More realistically, the excluded volume could depend upon the multiplicity.

Incorporating a multiplicity dependence into the excluded volume will be the subject of the next chapter, and hence, we will not report any results here (see also Ref. [31]). It will, no doubt, require an explicit interaction between fragments. We will report on only the simplest of interactions: a hard core repulsion. Even this will turn

out to be a non-trivial correction, as it will add an m-dependence to the volume term to account for the difficulty of fitting fragments of various sizes into a tight volume. This might affect the model in a non-trivial fashion.

We like to remind the reader that the parameter b in the Van der Waals EOS: $(p+a/V^2)(V-b) = RT$ also has its roots in the excluded volume. But there b plays a crucial role. We could not for example set b=0 without creating an instability at high density. Furthermore, the phase transition disappears when a is set to zero. We will also point out, in the following chapter, the relationship between the excluded volume and the Mayer cluster expansion: a classic problem in statistical mechanics.

2.4.2 *Coulomb effects*

Nuclei are charged and hence the various clusters formed at freezeout will interact with one another through the Coulomb force. Far more importantly, each cluster itself will experience a Coulomb self-interaction due to the protons it contains. It has been understood that the Coulomb effects alter the phase structure of nuclear matter [32]. Although explicit Coulomb interactions are outside the scope of this treatment, they may be approximated by considering a Wigner-Seitz approximation for the Coulomb energy as has been used in Ref. [26]. The addition to the internal free energy given in Eq. (2.4) is

$$F_{\rm coul} = 0.70 \left(1 - \left(\frac{\rho}{\rho_0}\right)^{1/3}\right) \frac{k^{5/3}}{4} \text{ MeV}. \tag{2.12}$$

This form is obtained by first smearing the entire charge of the system over the freeze-out volume and considering its energy E_0^c. We then identify spherical cells in this volume that contain the charge of a particular fragment k. Now we consider the excess Coulomb energy obtained by shrinking this large dilute sphere of charge down to the size of the fragment being considered, ΔE_k^c. Summing over all k we add the excess contribution to E_0^c to obtain Eq. (2.12).

The effects of the Coulomb correction may be most clearly seen in the specific heat

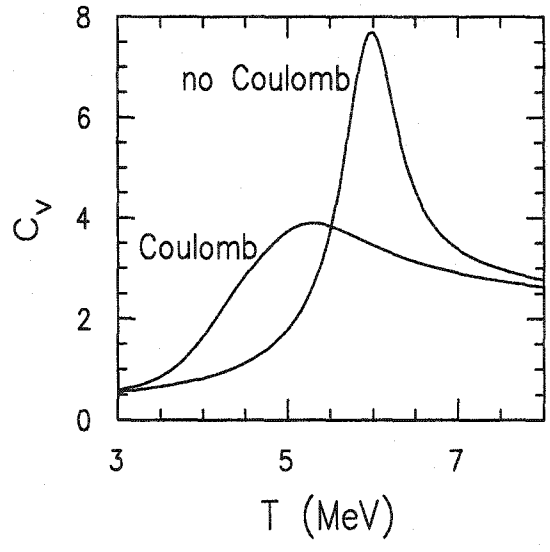

Figure 2.5: The peak in the specific heat of an $A = 100$ system is smeared by the inclusion of Coulomb effects. For large systems, Coulomb destroys the phase transition by making large drops energetically unfavourable.

near the boiling temperature. We display C_v, both with and without Coulomb terms for an $A = 100$ system in Fig. 2.5. Coulomb forces clearly reduce the temperature at which the transition occurs. They also reduce the height of the spike. This occurs as larger clusters formed at lower temperatures are now energetically less favourable. For sufficiently large systems, Coulomb destroys the transition as large drops become unstable to the Coulomb force.

2.4.3 Isospin

The presence of a Coulomb force implies the existence of protons. This in turn implies that we now allow for two kinds of particles: in other words we have introduced isospin. Thus, the partition function of the system will no longer be characterized by solely A but by Z, N. The system is assumed to break up into various nuclear clusters with i, j numbers of protons, neutrons respectively. The partition function is given as

$$Q_{Z,N} = \sum \Pi_{i,j} \frac{\omega_{i,j}^{n_{i,j}}}{n_{i,j}!} \tag{2.13}$$

Here $n_{i,j}$ is the number of composites with proton number i and neutron number j, and $\omega_{i,j}$ is the partition function of a single composite with proton, neutron numbers i, j respectively. There are two constraints: $\sum_{i,j} i n_{i,j} = Z$ and $\sum_{i,j} j n_{i,j} = N$. The recursion relation may be easily generalized to include isospin as

$$Qz, n = \frac{1}{z} \sum_{i,j} i \omega_{i,j} Q_{z-i,n-j}. \tag{2.14}$$

One may point out that inclusion of isospin also requires the introduction of a symmetry energy term in the energy of a cluster. This, along with the Coulomb energy and extension to isospin, will be incorporated into the model in chapter 4.

2.4.4 *Shell effects and secondary decay*

In the equation for the energy of a cluster of size k (Eq. (2.4)), we ascribed an energy based on the Bethe-Weizacker mass formula. No shell effects have been discussed. Such effects, though unimportant for large hot nuclei, are in fact important for small clusters lying in the valley of stability with well separated shell levels. Such effects may be naively incorporated into the internal partition function of each cluster q_k as

$$q_{i,j,int} = \sum_{k}^{E_{max}} (2J_k + 1) e^{(-E_k/T)} + q_{i,j,cont}. \tag{2.15}$$

Where E_{max} is the highest energy level that has been resolved for the given nucleus and is available from data tables; and $q_{i,j,cont}$ is the contribution from the continuum. Both these contributions will be consistently introduced in chapter 4 (or see Ref. [33]).

Up to now, our entire discussion has been focused on obtaining the various clusters at the instant of freezeout. At this point, all clusters contain large populations in

particle unstable states, these will decay multiple times by emitting a variety of particles. This will lead to a considerable change in the populations of various isotopes as they stream towards the detectors. Thus the freeze-out populations will have to be 'corrected' before comparison with experimental data. This correction will be introduced in a step by step manner in chapter 4 where we will finally compare the predictions of the RSM model with experiment.

2.5 Summary

After a brief introduction to the phenomena of multifragmentation in intermediate energy heavy-ion collisions, we delved into the development of a thermal model to explain the features of this phenomena. In this chapter we have simply described the basic building blocks of the model. Primary among these are the recursive techniques used to evaluate the partition function. These recursive techniques have several attractive features. They allow exact evaluations of the partition functions, even with the incorporation of various characteristics of nuclear composites and appear to endow the model with the standard features of a liquid-gas phase transitions. In the present form, this model (and may others in its genre) are restricted to low densities. For modelling nuclear disintegration this is not a serious problem, although for completeness it would be nice to be able to modify the model so that it can be extended to higher density.

In this chapter we studied the basic thermal properties of the model, and we emphasized the importance of the surface term and the entropy of thermal motion in determining these properties. We explicitly demonstrated (through a number of extensive and intensive variables) the existence of a first order phase transition in the model. We associated the sharp change in the variation of the energy density with temperature with that in the number of clusters. In addition, we have seen that including Coulomb effects lowers the temperature at which the fragmentation transition occurs and reduces the sharpness of the phase transition. We have also

presented a list of extensions to the model. These will be taken up sequentially in the upcoming chapters.

3

The Excluded Volume Correction

In the preceding chapter we presented a simple model of statistical multifragmentation. In this model, as in many others [26], it is assumed that the disassembly takes place in a volume larger than the normal nuclear volume (or alternatively at a lower density than normal nuclear density). Then the laws of equilibrium statistical mechanics were applied to calculate the populations of nucleons and clusters appearing in this volume. The volume makes an appearance in an overall multiplicative constant in the partition function, thus determining the phase space available to the clusters. Nuclei are not point objects but have a finite size, alternatively one may say that the internuclear force displays a hardcore repulsive component. Thus the clusters may not overlap. As a result, the 'free volume' within which particles may move is reduced. This reduced part is called the excluded volume. We discuss this facet of statistical models in this chapter.

3.1 Introduction

Imagine n non-interacting particles, enclosed in a volume V at a temperature T. The partition function (in classical statistical mechanics) may be generically written as,

$$Q = \frac{1}{h^{3n}} Q_{\text{kin.}} Q_{\text{conf.}}. \tag{3.1}$$

Where $Q_{\text{kin.}}$ is the kinetic part of the partition function: the portion generated by motion of the various constituents,

$$Q_{\text{kin.}} = \prod_i \int e^{-\beta p_i^2/2m} d^3p_i = \frac{2\pi m}{\beta}^{3n/2}. \tag{3.2}$$

The portion $Q_{\text{conf.}}$ is the configurational part of the partition function: generated by the interactions between various constituents at various locations. If there are no interactions and the particles are point particles, we have

$$Q_{\text{conf.}} = \int \prod_i d^3r_i = V^n. \tag{3.3}$$

There may be extra factors of $n!$ if the particles are indistinguishable. If we have a hard core interaction as suggested in the prelude *i.e.*,

$$U(|\vec{r}_i - \vec{r}_j|) = \infty \quad \text{for } |\vec{r}_i - \vec{r}_j| < (R_i + R_j)$$
$$U(|\vec{r}_i - \vec{r}_j|) = 0 \quad \text{for } |\vec{r}_i - \vec{r}_j| > (R_i + R_j),$$

then we would obtain

$$Q'_{\text{conf.}} = \int \prod_i d^3r_i \prod_{i<j} \theta\left(|\vec{r}_i - \vec{r}_j| - (R_i + R_j)\right). \tag{3.4}$$

Where $\theta(x)$ is the Heaviside step function. We will denote $Q'_{\text{conf.}}/Q_{\text{conf.}} = (V_{\text{fr}}/V)^n$, where V_{fr} is called the free volume. Thus $V_{\text{ex}} = V - V_{\text{fr}}$ is the excluded volume. We will study the ratio V_{fr}/V for typical cases as arise in statistical models of nuclear fragmentation. The radius R_i depends on the cluster in question. Here, we will take $R_i = r_0 A_i^{1/3}$, where A_i is the number of nucleons in the cluster, and $r_0 = 1.2fm$: a constant [26].

A variety of different cases may arise. At one extreme, we may have all the n particles as monomers (=nucleons, protons, and neutrons). The opposite limit is when all the particles form a single large cluster. In general there will be n_1 monomers, n_2 dimers, n_3 trimers and so on. The total number of particles will be constrained to $\sum_i i n_i = n$. In the following, dimers, trimers, etc. will be called composites or clusters. The density within each composite or monomer will be taken

to be a constant ρ_0: the ground state nuclear density of $0.16fm^{-3}$. The volume of any composite of k nucleons will thus be k/ρ_0. Here k can be one.

In our model, as in most models of statistical multifragmentation, one assumes that on collision of two heavy nuclei, the central participant region expands from its normal volume to a larger volume. In other words, its central density drops from ρ_0 to a smaller value ρ. It is at this expanded volume V or reduced density ρ that the various clusters are formed. Thus statistical mechanics has to be performed with this density as input. Previous models have assumed this density to be anywhere between $0.4\rho_0$ to $0.167\rho_0$ [21, 26, 34]. A naive guess would be that a cluster may not occupy the volume already occupied by another cluster. Thus the excluded volume for n clusters would be $V_{\rm ex} = n/\rho_0$. This estimate has been used previously by Hahn and Stocker, and others [30]. One could relax this to $V_{\rm ex} = c \times n/\rho_0$, where c is a constant. This leads to $\frac{\partial V_{\rm fr}}{\partial V} = 1$ and $\frac{\partial V_{\rm ex}}{\partial V} = 0$. In the following it will be demonstrated that this simple situation is not the case.

Finally, a study of the excluded volume is important as in nuclear physics problems $V_{\rm ex}$ is of the same order of magnitude as V. In high density multifragmentation, it may lead to a considerable reduction of the phase space available to various clusters, and thus change the out state. In many other problems in physics and chemistry this is a negligible factor. In our calculations of the partition function, as demonstrated in the preceding chapter, the input variable will be the free volume $V_{\rm fr}$. However the total volume V in which fragmentation occured, is also of importance. Typically Hanbury-Brown Twiss experiments can provide a measure of V. The total volume V is required when estimating the expectation values of the residual interactions between clusters. This refers mostly to the Coulomb force, but could also be a strong interaction if the clusters are close enough. In the remainder of this chapter we will study the relationshp between V and $V_{\rm fr}$. In Sect. 3.2, we will show how, given a V, a $V_{\rm fr}$ may be estimated by a numerical Monte-Carlo routine. In Sect. 3.3, we will explore the relation of V to $V_{\rm fr}$ in the simple case when only monomers are formed. This is related to the historical problem of Mayer cluster expansion and

experimentally relates to the case of multifragmentation at high energies. In Sect. 3.4, we will turn to the generic case of nuclear fragments of all sizes. In Sect. 3.5, we will summarize the results of our calculation and demonstrate how the general relationship deviates from the simple case of Hahn and Stocker.

3.2 Numerial procedure for evaluating $V_{\rm fr}/V$

We now approach the central theme of this work: estimating the ratio of $V_{\rm fr}/V$ in a disassembling system. For obvious reasons, we will assume throughout that the interaction between clusters is sperically symmetric. By extention, the thermalization volume V is also taken to be spherical. We thus have n particles which need to be put into a sphere of radius R. If there were no mutual hard core interactions to contend with, the n particles would be distributed uniformly within the sphere of radius R. This is achieved by the following simple numerical procedure. For each particle or cluster i, we call three random numbers between 0 and 1, denoted as α_i, β_i and γ_i. We then make the assignment $r_i = R(\alpha)^{1/3}$, $cos(\theta_i) = 1 - 2\beta_i$ and $\phi_i = 2\pi\gamma_i$. These quantities give us the Cartesian coordinates of the ith particle as $x_i = r_i \sin\theta_i \cos\phi_i$, $y_i = r_i \sin\theta_i \sin\phi_i$ and $z_i = r_i \cos\theta_i$. Each set of n such calls gives n different positions for the n clusters. Each such set is deemed 'successful' if there are no mutual hard core interactions.

Now, we introduce hard core repulsion among the clusters. If each cluster has a certain radius of this repulsion, not each set may be successful. The first may always be placed successfully at $\vec{r}_1$ as there is no other in its way. To place the second, we call the three random numbers $\alpha_2, \beta_2, \gamma_2$ which give us the position $\vec{r}_2$ of the second composite. This may only be placed if $(|\vec{r}_1 - \vec{r}_2|) > (R_1 + R_2)$, where R_1, R_2 are the hard core radii of composite 1 and 2 respectively. To successfully place the third particle, we again call three random numbers which generate the position $\vec{r}_3$. This may be placed successfully only if $(|\vec{r}_1 - \vec{r}_3|) > (R_1 + R_3)$ and $(|\vec{r}_3 - \vec{r}_2|) > (R_3 + R_2)$. In this way, we continue placing cluster after cluster. If we have managed to place all

n clusters successfully then we have one successful set. Failure at any stage of this buiding up process will constitute an unsuccessful set. Let the number of successful sets be denoted N_S; and the number of unsuccessful sets N_U. Then provided that both N_S and N_U are large, a good estimate of $V_{\rm fr}/V$ may be obtained by equating,

$$\left(\frac{V_{\rm fr}}{V}\right)^n = \frac{N_S}{N_S + N_U}. \tag{3.5}$$

Several comments are in order. First, the ratio $V_{\rm fr}/V$ is necessarily less than 1, therefore, for a very large n the computed quantity $(V_{\rm fr}/V)^n$ is very small and a very large number of attempts are needed to obtain good statistics. However, for typical cases of n in nuclear fragmentation this is perfectly feasible *i.e.*, can be computed within a reasonable time frame. Secondly, we have enforced the requirement that the centre of each cluster lies between 0 and R the radius of the spherical enclosure. This has also been followed by Koonin and Randrup [35]. We call this the first prescription. A possible alternate prescription (referred to as the second prescription) could be to allow the centre of the particle to lie between 0 and $R - R_i$. Although in the thermodynamic limit both prescriptions will give the same results, for finite number of particles they will not. The second prescription has the awkward feature that if the hard core radii of different composites are different (as will be the case for composites of different mass number), the $V_{\rm fr}$ factors will be different for different species. This is due to the hard core interaction with the wall of the spherical enclosure. As a result, even for a single compound nucleus there will be an excluded volume: the centre of the nucleus can only move upto $R - R_i$. However, our objective is only to find the excluded volume due to interaction between different clusters. Thus we do not use the second prescription and will not discuss it any further.

It should also be noted that in the above discussion, we do not worry about the motion of the centre of mass *i.e.*, at the end of the successful set we do not impose that the centre of mass of the composites coincide with the centre of the enclosure. Recall that, eventually, we will calculate a partition function in the canonical ensemble. The

movement of the centre of mass is in accord with the basic principle of the canonical ensemble *i.e.*, there exists a heat bath which can absorb both energy and momentum. For a large number of composites, the movement will obviously be very small. It will not be so for $n = 3$ or 4. The centre of mass motion correction is a separate issue, with or without the excluded volume correction. It is also obvious that the Monte-Carlo procedure described above may be easily modified to correct for this motion. We leave this for a future effort.

In the next section, we consider the case of n monomers whose centres lie within a sphere of radius R. There are several reasons to consider this first. This is the simplest. This is appropriate for high energies, where most of the nucleons appear as monomers and there are very few composites. More interesting is the relation of this problem to Mayer cluster expansion, which is a classic problem in statistical physics.

3.3 *Monomers of one kind: Low density expansion*

We want to derive the relationship between the total volume and the free volume in the case where only monomers are formed. This is related to the equation of state of such a system. The equation of state of such a system has already been obtained by Mayer and collaborators [36] in the form a series in density. The equation of state is written as

$$\frac{PV}{nT} = \sum_{l=1}^{\infty} a_l (\lambda^3 \rho)^{l-1}. \tag{3.6}$$

In the above, λ is the thermal wavelength, $a_1 = 1$ and the coefficients a_2, a_3, a_4 have been analytically obtained and a_5, a_6 were calculated numerically (the interested reader may see Ref. [36] for details). Putting in the values for the constants we get

$$\frac{PV}{nT} = 1 + 4\frac{\rho}{\rho_0} + 10\left(\frac{\rho}{\rho_0}\right)^2 + 18.365\left(\frac{\rho}{\rho_0}\right)^3 + 28.237\left(\frac{\rho}{\rho_0}\right)^4 + 39.526\left(\frac{\rho}{\rho_0}\right)^5 + \ldots \tag{3.7}$$

Here $\rho = n/V$ is the density of particles in the total volume; $\rho_0 = 3/4\pi r_0^3$ is the density within each composite. The power series expansion will obviously enjoy validity in

the region where $\rho << \rho_0$: hence this is called a low density expansion. We define $V_{\rm fr}$ in this situation by the equality

$$\frac{PV_{\rm fr}}{nT} = 1. \tag{3.8}$$

the ratio of the above two equations gives us the ratio $V_{\rm fr}/V$. We evaluate it for three different densities: $\rho/\rho_0 = 0.1, 0.2,$ and 0.3. This gives us the ratio of $V_{\rm fr}/V$ as 0.657, 0.416, and 0.255, respectively.

As we will soon demonstrate, this estimate is not rigourous. This is based on the assumption that $\frac{\partial V_{\rm fr}}{\partial V} = 1$. We have used the Mayer cluster expansion and the above assumption to obtain an expression of $V_{\rm fr}/V$, which, however, immediately shows that $\partial V_{\rm fr}/\partial V = 1+$ correction. Thus there is an inconsistency. The answers are however, resonably close to the answer we obtain from the direct calculation of $V_{\rm fr}/V$. This direct calculation exploits the numerical technique described in the previous section. The calculation is performed for a finite number of particles: calculating for very large numbers is very time consuming. However we note that the results seem to fall on a smooth curve (see the next section for the parametrization of these results). We extrapolate this curve to $n = \infty$ to obtain the thermodynamic limit of $V_{\rm fr}/V$. It turns out that this method of obtaining $V_{\rm fr}$, and using Eqs. (3.7,3.8) gives answers that are quite close to each other. They become identical if the *correction* alluded to above is also incorporated in an iterative fashion.

The results of the numerical calculation of $V_{\rm fr}/V$ are shown in Fig. (3.1). To obtain these, we pick a value of ρ/ρ_0 and n which then defines a value of V which is then used to find R. The numerical method of the previous section is then carried out to calculate $V_{\rm fr}/V$. Note that the results approach the Mayer formula as $n \to \infty$. Thus we find that this formula is appropriate at $n = \infty$. However, it provides a significantly different estimate for finite n relevant for multifragmentation studies. We are unable to write a closed expression for the curves of Fig. (3.1). However they can be parametrized quite accurately.

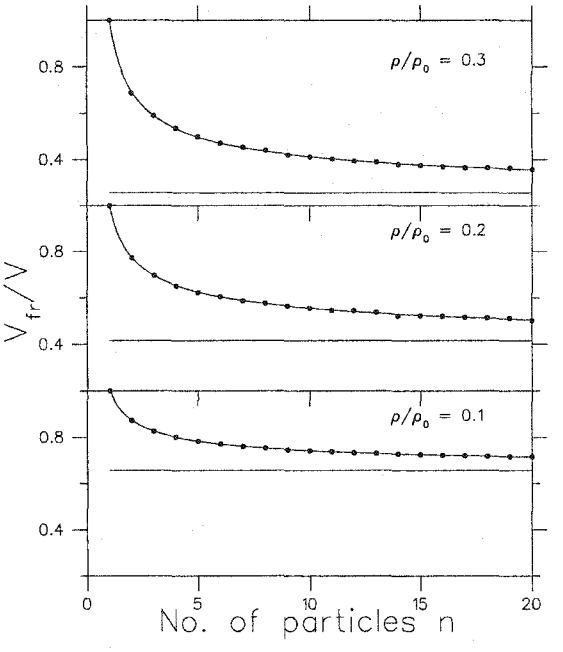

Figure 3.1: Monte Carlo results for $V_{\rm fr}/V$ for three different densitites for n monomers. Here $\rho = n/V$ and $\rho_0 = 1/(4\pi r_0^3/3))$. The straight line in each frame represents the value of the inverse of the *r.h.s* of Eq. (3.7) evaluated for the given value of ρ/ρ_0. The straight lines can be taken as an approximate answer in the limit $n \to \infty$. As in many of the rest of the graphs we show a fit of the Monte Carlo points by a parametrization given by the inverse of $1 + C_{2/3}(1 - n^{-2/3}) + C_{1/2}(1 - n^{-1/2}) + C_{1/3}(1 - n^{-1/3})$ (see text). These values are $C_{2/3} = 0.1122$, $C_{1/2} = 0.1237$, $C_{1/3} = 0.3266$ for $\rho/\rho_0 = 0.1$; $C_{2/3} = 2.6871$, $C_{1/2} = -6.6771$, $C_{1/3} = 6.0805$ for $\rho/\rho_0 = 0.2$; and lastly, $C_{2/3} = 3.0693$, $C_{1/2} = -10.7461$, $C_{1/3} = 11.8747$ for $\rho/\rho_0 = 0.3$.

An interesting feature is the behaviour of the excluded volume with density. Observing Fig. (3.1), we note that for a fixed n, the quantity $V/V_{\rm fr} = 1 + V_{\rm ex}/V_{\rm fr}$ increases as ρ/ρ_0 increases. However, $V_{\rm ex}$ decreases as ρ/ρ_0 increases (meaning that $V_{\rm fr}$ is decreasing at a faster rate). This sounds slightly counter intuitive. To understand this consider a very dilute system where the particles have been distributed at distant locations. If there are only two particles then the excluded volume is $8/\rho_0$ (as any one particle precludes the other from a sphere with a radius twice that of the individual partners: call this the exclusion sphere). For n particles the excluded volume is $4n/\rho_0$, where we have divided by 2 to eliminate double counting. This is the largest possible value of the excluded volume for n particles. As the density increases, many of the excluding spheres will be forced to occupy locations in the

vicinity of each other. The excluded zones of one particle may overlap with that of another. In this case the total volume excluded by both these particles will not be the sum of their exclusion spheres but a smaller volume. As the density rises the particles come closer together and the excluded volume decreases.

3.4 *Mixture of Many species: The case of nuclear multifragmentation*

We now turn the case of excluded volume in nuclear multifragmentation. Here we may have both nucleons and composites of different sizes appearing in the freeze-out volume. We denote the total number of objects (monomers and composites) as the multiplicity m. If n_k is the total number of composites of k nucleons, then $\sum n_k = m$ and $\sum k n_k = n$, where n is the total number of nucleons in the system. Specifying n and m however does not uniquely specify the system since for the same n and m we can have many partitions, e.g., for $n = 10$ and $m = 3$, partitions of 8, 1, 1; 7, 2, 1; 6, 2, 2 etc. are possible. To demonstrate the dependence of $V_{\rm fr}/V$ on each separate partion would become a very complicated task. Not only would we have to demonstrate multidimensional results (dependence on n, m and partition) but the number of partitions for large m will make this prohibitively difficult. We will thus present dependence of the ratio on n and m only, *i.e.*, we will chose a single partition. The choice of partition is not arbitrary, but is close to the average of the range of values obtained for each m from a thermodynamic calculation. Resonable variations in the choice of partitions were sometimes studied. This did not cause any major change in the parametrization used.

To obtain the excluded volume for a particular m we proceed in the following way. For a given n and temperature T we calculate $\langle n_k \rangle$ and obtain $\sum \langle n_k \rangle = m$. This is obtained by means of the thermodynamic calculation of chapter 2. To recall, one defines a cluster partition function ω_k for a cluster of k nucleons, drawing on the Bethe-Weizacker mass formula as,

$$\omega_k = \frac{V_f}{\hbar^3}\left(\frac{kmT}{2\pi}\right)^{3/2} \times e^{(W_0 k - \sigma(T)k^{2/3} + T^2 k/\epsilon_0)/T}. \tag{3.9}$$

Using this, a partition function for the entire disassembling system may be written down as (see chapter 2 for details),

$$Q_A = \sum_k \Pi_k \frac{\omega_k^{n_k}}{n_k!}. \tag{3.10}$$

The partition function is evaluated easily using the recursion relation

$$Q_A = \frac{1}{A}\sum_k \omega_k Q_{A-k}. \tag{3.11}$$

From here, one may easily derive the mean number of clusters of k nucleons as

$$\langle n_k \rangle = \frac{\omega_k Q_{A-a_k}}{Q_A}, \tag{3.12}$$

and as a result the total multiplicity m.

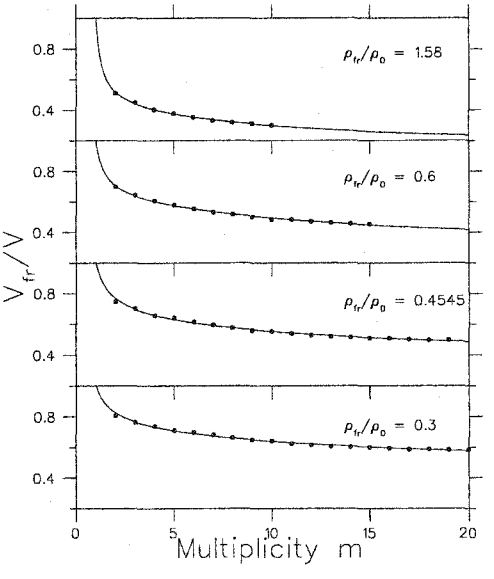

Figure 3.2: Monte Carlo results for $V_{\rm fr}/V$ where the total number of nucleons is $n = 100$ and multiplicity m varies as shown. The points are Monte-Carlo results and the smooth lines are fits using Eq. (3.13). The fits use $C_{2/3} = 8.812$, $C_{1/2} = -20.341$, $C_{1/3} = 14.111$ for $\rho_{\rm fr}/\rho_0 = 0.3$; $C_{2/3} = 13.037$, $C_{1/2} = -30.175$, $C_{1/3} = 20.927$ for $\rho_{\rm fr}/\rho_0 = 0.4545$; $C_{2/3} = 29.485$, $C_{1/2} = -66.753$, $C_{1/3} = 43.930$ for $\rho_{\rm fr}/\rho_0 = 0.6$; and lastly, $C_{2/3} = 70.452$, $C_{1/2} = -160.687$, $C_{1/3} = 106.298$ for $\rho_{\rm fr}/\rho_0 = 1.587$.

This m, will in general be non-integral as it is an average over many partitions. We fine tune the temperature until an integral value of m results. The values of $\langle n_k \rangle$, however, are still non-integral and fractional in most cases, as these are averages over many partitions. This is resolved in the following way: we start the sum over $\langle n_k \rangle$ from $k = 1$; everytime the sum crosses an integer we consider the presence of one particle. Thus if at $k = k_1$ we encounter the integer 1, *i.e.*, $\sum_1^{k_1} \langle n_k \rangle \simeq 1$, we consider this as an indication that a single cluster with number of nucleons between 1 and k_1 has appeared.

As we continue the sum, we may encounter the next integer at k_2, *i.e.*, $\sum_{k_1}^{k_2} \langle n_k \rangle \simeq 1$. We consider this as an indication that a cluster with number of nucleons between k_1 and k_2 has appeared. We continue in this way with the choice of the last composite controlled to ensure the conservation of nucleon number *i.e.*, $\sum_1^n k \langle n_k \rangle = n$. No doubt, this method of sampling the distribution is not unique, and the answer does depend on the choices made. Resonable variations were tried, and for large m, this variation turned out to have negligible effect.

In the preceding paragraphs, we have made the tacit assumption of a particular free volume $V_{\rm fr}$. We note, from chapter 2, that this is indeed an input of the thermodynamic calculation that provides us with the values of $\langle n_k \rangle$. Having chosen the clusters that are to appear, our task will now be to discern what the total volume V must have been to allow for such a value of $V_{\rm fr}$. The reader will recognize that we are following a reverse line of reasoning from that adopted in the case of monomers (Sect. 3.3). There we had chosen a total volume V first and then proceded to find what $V_{\rm fr}$ it implied. Here it is simpler to choose a $V_{\rm fr}$ first, perform a thermodynamic calculation obtaining the numbers and sizes of clusters, and then deduce the value of V that will produce this value of $V_{\rm fr}$. There is no direct method of computing this. The method will involve making a guess of the possible value of V. We then distribute the various clusters obtained in this volume and obtain the corresponding $V_{\rm fr}$. The Monte-Carlo sampling described previously is used in this estimation of $V_{\rm fr}$. Usually, the $V_{\rm fr}$ obtained as such will not coincide with the $V_{\rm fr}$ chosen as input to the

thermodynamic calculation. However, an iterative procedure may be readily devised by which we converge on the correct V which would generate the input $V_{\rm fr}$.

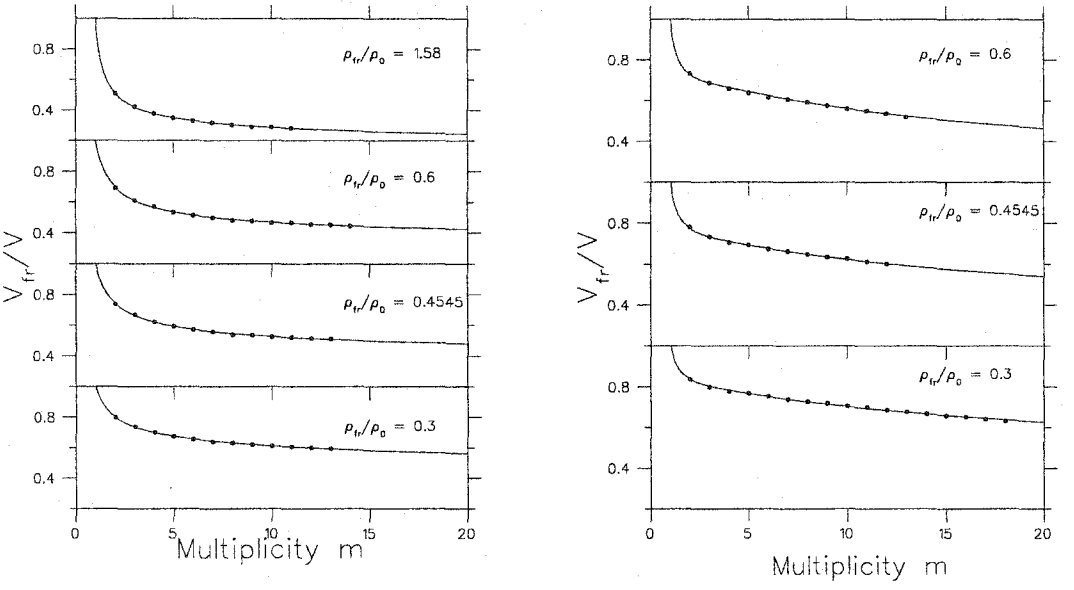

Figure 3.3: Left plot is same as Fig. (3.2), except this is for $n = 50$. The parameters for the fitted curves are $C_{2/3} = 6.404$, $C_{1/2} = -14.313$, $C_{1/3} = 10.069$ for $\rho_{\rm fr}/\rho_0 = 0.3$; $C_{2/3} = 3.456$, $C_{1/2} = -7.890$, $C_{1/3} = 6.687$ for $\rho_{\rm fr}/\rho_0 = 0.4545$; $C_{2/3} = 3.445$, $C_{1/2} = -7.953$, $C_{1/3} = 7.214$ for $\rho_{\rm fr}/\rho_0 = 0.6$; and lastly, $C_{2/3} = 25.951$, $C_{1/2} = -59.158$, $C_{1/3} = 42.110$ for $\rho_{\rm fr}/\rho_0 = 1.587$. Right plot is same as Fig. (3.2), except this is for $n = 200$. The parameters for the fitted curves are $C_{2/3} = 17.846$, $C_{1/2} = -39.845$, $C_{1/3} = 25.567$ for $\rho_{\rm fr}/\rho_0 = 0.3$; $C_{2/3} = 26.962$, $C_{1/2} = -59.860$, $C_{1/3} = 38.038$ for $\rho_{\rm fr}/\rho_0 = 0.4545$; and lastly $C_{2/3} = 63.693$, $C_{1/2} = -141.909$, $C_{1/3} = 89.299$ for $\rho_{\rm fr}/\rho_0 = 0.6$.

3.5 *Results of calculations*

Our results are essentially contained in Figs. (3.2,3.3,3.4). In Fig. (3.2), we show the variation of $V_{\rm fr}/V_0$ for $n = 100$ for different inputs of $\rho_{\rm fr}/\rho_0$ as multiplicity varies. Fig. (3.3) shows similar curves for the cases of $n = 50$ and 200, respectively. Qualitatively, they all show similar behaviour as is to be expected. For a given $\rho_{\rm fr}/\rho_0$, $V_{\rm fr}/V$ decreases as the multiplicity increases and appears to converge towards an asymptotic value for large m. For a fixed value of n and m the ratio of volumes decreases as the ratio $\rho_{\rm fr}/\rho_0$ increases, except for the case of $m = 1$ where $V_{\rm fr}/V$ is always 1. The ratio of volumes $V_{\rm fr}/V$ is thus a function of three quantities: $V_{\rm fr}/V = f(n, m, \rho_{\rm fr}/\rho_0)$. We

have been unable to find a simple functional dependence on the three parameters such that an accurate extrapolation outside of the actual region of investigation becomes dependable. However, we have managed to provide a simple parametrization for the dependence on m for a given density and n. This formula may be fitted almost exactly with all the three figures by simply varying three parameters, as demonstrated by the solid line in Figs. (3.2,3.3). We may express it as

$$\frac{V_{\rm fr}}{V} = \frac{1}{1 + C_{2/3}(1 - m^{-\frac{2}{3}}) + C_{1/2}(1 - m^{-\frac{1}{2}}) + C_{1/3}(1 - m^{-\frac{1}{3}})}. \tag{3.13}$$

The values of $C_{2/3}, C_{1/2}$, and $C_{1/3}$ are mentioned in the captions of each of the figures. As may be noted they are different for each density and total particle number. Finding a parametrization for the three constants in terms of the density and the total particle number would have achieved our stated goal of a universal closed expression for the ratio of the free volume to the total volume.

While it would have been satisfying to derive such a formula ($V_{\rm fr}/V = f(n, m, \rho_{\rm fr}/\rho_0)$) analytically, one soon realizes that this is a complicated task. In the Mayer formula (Eq. (3.7)) only the first three terms are simple. The rest are left as integrals with complicated limits, the evaluation of which requires numerical integration [36]. We would remind the reader that the case of the Mayer cluster expansion is in fact simpler than that of nuclear fragmentation. All the constituents are monomers. One calculates in the thermodynamic limit: as a result one has no surface to bother about; and one may employ various simplifying approximations. A sample excercise for calculating the free volume available to three unequal spheres whose centres are constrained to move within another sphere will convince the reader to try a phenomenological fit. The parametrization of Eq. (3.13) works very well in all the cases that we studied; however, we do concede that some other parametrization may work equally well.

We now turn to the plots of Fig. (3.4). Here we plot the full volume V as a function of $V_{\rm fr}$ or vice-versa. Both are measured in units of V_0, the normal volume of a nucleus of n nucleons ($n = 100$ in left plot, $n = 50$ in right plot). The choice of these

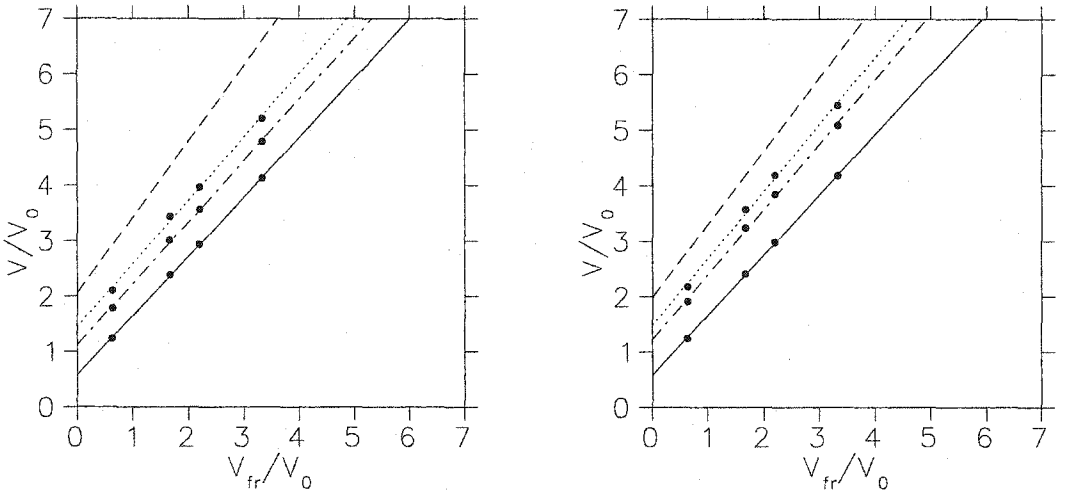

Figure 3.4: For $n = 100$ we plot V/V_0 against $V_{\rm fr}/V_0$ where V_0 is the normal nuclear volume for a given n. One might then hope that the plots would be almost independent of n (compare with right plot). For four values of $V_{\rm fr}/V_0$ we plot values of V/V_0 for selected values of $m = 2, 6$, and 10 and show that the calculated Monte-Carlo values fall nearly on a straight line. The solid line is through $m = 2$, the dash-dot line through $m = 6$, and the dotted line through $m = 10$. The top most line is our prediction for $m = 100$. That line is drawn from an extrapolation of the calculation done in Sec. 3.3. Since for $m = 100$ all particles are monomers the calclations of Sec. 3.3 apply. Notice that the lines are well represented by $V/V_0 = \alpha(m) \times V_{\rm fr}/V_0 + V_{\rm ex}(m)/V_0$, where the dependence of α on m is rather weak and also $\alpha \simeq 1$. The formula of Ref. [30] starts from (0,1) and has $\alpha = 1$. The right plot is the same as the left plot expect that it is for $n = 50$. Note the similarity with the left plot.

plotting units is obvious: the reader will notice that in these units the two plots are almost (although not exactly) identical. In the plots, four multiplicities are shown: $m = 2$, 6, 10, and 100, where the last one is obtained by extrapolating the formula of Sect. 3.3. As $m = 100$ is a case of all monomers, we essentially revert back to the case discussed in Sec. 3.3. The surpising point is that all four points (corresponding to four different free volumes) for each multiplicity lie almost perfectly on a straight line. Another important point to note is that if one performs a thermodynamic calculation where temperature may vary (and as a result multiplicity varies), then one cannot have a constant volume V and a constant free volume $V_{\rm fr}$. We may fix one, the other one is then temperature (or alternatively multiplicity) dependent. For the calculation of pressure at constant temperature and volume, the former has to be held constant. For a fixed V, it is clear that $V_{\rm fr}$ decreases as multiplicity increases, which is obvious

from the preceding discussion. In earlier versions of statistical multifragmentation models $V_{\rm fr}$ increased with multiplicity [26]. There, unlike in our case, the volume or free volume is not a free parameter, but is in fact temperature dependent. In such models, one cannot hold V constant and vary other quantities such as temperature.

From the curves we note that the approximation of Hahn and Stocker is accurate only for low multiplicities. For multiplicities greater than six is underestimates the the excluded volume $V_{\rm ex}$. Thus for a given $V_{\rm fr}$ it underestimates V. A better approximation will infact be to take

$$V = V(m) = \alpha(m)V_{\rm fr} + V_{\rm ex}(m), \tag{3.14}$$

where $\alpha(m)$ may be set to be 1 and $V_{\rm ex}$ may be read off the intercept with the y axis. This varies between 0.6 and 2 (in units of V_0). In the actual parametrization, the slope $\alpha(m)$ is slightly greater than one; the value increasing as m increases.

3.6 Summary and discussion

In this chapter we have performed a realistic calculation to estimate the magnitude of the excluded volume in nuclear fragmentation. This calculation was performed within the outline provided by the Recursive Statistical Multifragmentation Model (RSM model). In this model one calculates the partition function of a disassembling system at the instant of 'freeze out' *i.e.*, at the point at which clusters are far enough away that there is no residual attractive interaction between them. The only interaction allowed is that of a hard core repulsion. This hard core repulsion prevents the various clusters from enjoying the entire volume V in which fragmentation takes place; confining them instead to a small free volume $V_{\rm fr}$. A certain volume $V_{\rm ex} = V - V_{\rm fr}$ is thus excluded. This was a very general calculation in the sense that the radii of hard core interactions were allowed to vary accoding to the sizes of clusters. The disassembling systems considered were ascribed multiplicities that would be typically encountered in heavy-ion collision experiments.

Early formulations of the model naively estimated the excluded volume $V_{\rm ex}$ as simply the volume of the clusters themselves $V_{\rm ex_{min}} = V_0 = A/\rho_0$ (see chapter 2 or Ref. [28]). We explicitly demonstrate that this is not the case. The excluded volume $V_{\rm ex}$ can be much greater. The excluded volume tends to the estimate of $V_{\rm ex_{max}} = 4A/\rho_0$ in very dilute systems. In most cases of nuclear fragmentation the excluded volume lies between $V_{\rm ex_{min}}$ and $V_{\rm ex_{max}}$. The answer is multiplicity dependent.

In this calculation we introduced novel Monte-Carlo sampling techniques with which the excluded volume may be calculated in the RSM model. These techniques had to be used in tandem with the numerical, recursive, calculations of the RSM model to estimate this effect. The plots demonstrate how the excluded volume in typical multifragmentation settings varies with multiplicity (m), density ($\rho_{\rm fr}/\rho_0$), and total particle number of the system (n). We could not devise an analytic expression for the dependence of $V_{\rm fr}/V$ on these parameters. However, we demonstrate that for a given n and $\rho_{\rm fr}/\rho_0$, the ratio of volumes $V_{\rm fr}/V$ is a universal function of m and involves merely three dimensionless constants which depend on n and $\rho_{\rm fr}/\rho_0$.

4

Secondary Decay

Our investigation of multifragmentation with the RSM model has led us to continually develop various additional features of the model; so as to ultimately explain experimental data. We outlined various extensions in chapter 2 after presenting a rather simplified base model. In the preceding chapter, we concentrated solely on only one such extension: excluded volume. In this chapter we will incorporate all remaining features highlighted in chapter 2. After the completion of all extensions we will achieve the first of our stated goals: comparison with experimental data.

4.1 Introduction

We begin by clearly stating the basic aim of this chapter (and one of the aims of the thesis in general): to attempt to calculate the populations of various isotopes of Boron, Carbon and Nitrogen that were measured in a number of experiments at the NSCL-MSU facility [5, 37]. The reason for concentrating on these isotopes is manifold. Experimentally such nuclei are large enough that they cannot constitute pre-equilibrium emission, which is mostly in small tightly bound clusters or nucleons: we are thus definitely observing clusters from the central thermalized region. Populations of higher mass isotopes are rather small and have considerable errors. In the interest of simplicity we make approximations that tend to somewhat blur out discrete shell effects; such approximations are not completely justified for smaller isotopes of Lithium and Beryllium, where exact shell effects may be important.

The calculation proceeds in two stages. In the first part we will incorporate all

but one of the features to be included: isospin effects, Coulomb interaction, symmetry energy, discrete levels and continuum populations. The populations of isotopes calculated at this stage will be called the primary populations and will represent the populations of isotopes at the instant of freeze-out. The calculations in the first part are exact although numerical. These populations are both in particle stable and unstable states. In the second stage the particle unstable states are allowed to decay. Here we introduce the final extension of the RSM model: secondary decay. This is done in a Weisskopf formalism. Exact calculations are very long and some approximations had to be introduced. These approximations will be discussed. After the decays, the populations are compared with experiments.

This calculation serves as an application of the RSM model where an exact calculation can be done with recursive techniques. This, therefore, could serve as a benchmark of how far one can trust the predictions of the model. Here we are essentially referring to the primary populations. In the next chapter these populations will be subjected to a different study as to the order of the phase transition occurring in such experiments. In reality these populations will be subjected to significant secondary decay, changing their spectrum considerably. A two step model such as this, provides us with both the populations at freeze-out and those after secondary decay. A good fit with experimental data will not only promote the RSM model as an accurate model, but also boost confidence in its primary populations, allowing us to make definitive statements regarding the liquid-gas phase transition at freeze out.

The sections are organised as follows. Sect. 4.2 gives a description of the various extensions to RSM model. After presenting, in Sect. 4.3, in words and simple formulae, the overview of the secondary decay calculation, we present in Sect. 4.4 the formalism that we use to model secondary decay. In Sect. 4.5 we present some calculational details, Sect. 4.6 presents the results of the calculation. A summary and discussions are presented in Sect. 4.7. A short appendix of the more complicated formulae are presented in Sect. 4.8.

4.2 The two component RSM model.

We begin by presenting the details of the extensions to the RSM model . The one component base model was described in chapter 2 and in Ref. [28].

We have assumed that the system which breaks up after two heavy ions hit each other can be described as a hot, equilibrated nuclear system characterised by a temperature T and a freeze-out volume V within which there are A nucleons ($A = Z+N$). Here we introduce the distinction between protons and neutrons. Thus, the partition function of the system will no longer be characterized by solely A but by Z, N. The system is assumed to break up into various nuclear clusters with i, j numbers of protons, neutrons respectively. We assume that there is minimal interaction between clusters. Thus, the partition function is given as

$$Q_{Z,N} = \sum \Pi_{i,j} \frac{\omega_{i,j}^{n_{i,j}}}{n_{i,j}!}. \tag{4.1}$$

Here $n_{i,j}$ is the number of composites with proton number i and neutron number j, and $\omega_{i,j}$ is the partition function of a single composite with proton, neutron numbers i, j respectively. There are two constraints: $\sum_{i,j} i n_{i,j} = Z$ and $\sum_{i,j} j n_{i,j} = N$. These constraints would appear to make the computation of $Q_{Z,N}$ prohibitively difficult, but yet another recursion relation can be devised which allows for the numerical computation of $Q_{Z,N}$. Three equivalent recursion relations exist, any one of which could be used. For example, one such relation is

$$Qz, n = \frac{1}{z} \sum_{i,j} i \omega_{i,j} Q_{z-i,n-j}. \tag{4.2}$$

All nuclear properties are contained in $\omega_{i,j}$. It is, as before, given by

$$\omega_{i,j} = \frac{V_{\rm fr}}{\hbar^3} (\frac{mT}{2\pi})^{3/2} (i+j)^{3/2} \times q_{i,j,int} \tag{4.3}$$

Here $V_{\rm fr}$ is the free volume within which the particles move; $V_{\rm fr}$ is related to V through $V_{\rm fr} \simeq V - V_{\rm ex}$ where $V_{\rm ex}$ is the excluded volume due to finite sizes of composites. This

quantity and its relation to the density, multiplicity and total particle number have been rigorously explored in the previous chapter. Here we take $V_{\rm fr}$ to be a variable of the calculation, it is set to be equal to fV_0 where V_0 is the normal volume for $(Z+N)$ nucleons, f is then varied to obtain the best fit with experimental data. From $V_{\rm fr}$With a knowledge of the multiplicity, we can calculate the total volume V and hence the freeze out density. This has to be low enough so that the approximation of ignoring interactions between composites is viable. This becomes a consistency check for our calculation.

The quantity $q_{i,j,int}$ is the internal partition function of the composite. In the previous chapters we ascribed a rather simple form to $q_{i,j,int}$, based on a simplified mass formula with only a volume and surface term and a Fermi-gas excitation. In general, however, for a nuclei which has both discrete energy levels and a continuum, $q_{i,j,int}$ can be expressed as

$$q_{i,j,int} = \sum_{k}^{E_{max}} (2J_k + 1)e^{(-E_k/T)} + q_{i,j,cont}. \tag{4.4}$$

Where the summation on the right hand side is the contribution from the discrete spectrum(The cut-off E_{max} is simply the highest energy level that has been resolved for the given nucleus and is available from data tables); and $q_{i,j,cont}$ is the contribution from the continuum. Without loss of generality we can write

$$q_{A,int} = \int \rho_A(E)e^{-\beta E}dE, \tag{4.5}$$

where we have used the abbreviation $A = i + j$, to stand for both i and j; $\rho_A(E)$ is usually partly discrete and partly continuous.

We will need both $q_{A,int}$ and $\rho_A(E)$. Volumes of work are available on $\rho_A(E)$. This is dealt with in detail in appendix 2B of [38]. The saddle-point approximation for the density of states assuming a Fermi-gas model is (see e.g. 2B-14 in [38])

$$\rho_A(E) = \rho_A^0(E) \times \exp(lnz_{gr} - \alpha_0 A + \beta_0 E). \tag{4.6}$$

For explanations of how α_0 and β_0 are to be chosen see Ref. [38] . In the Fermi-gas model the quantity which is exponentiated is simply the total entropy $S = As$. Thus the density of states is given by a familiar expression $\rho_A(E) = \rho_A^0(E)\exp(S)$ where $\rho_A^0(E)$ is the pre-factor. Approximate values of $\rho_A^0(E)$ are known provided one does not have to concern with very low values of E (which we do need). At temperatures we will be concerned with, $\exp(S)$ in the Fermi-gas model is given quite accurately by $\exp[\pi(\frac{AE}{\epsilon_F})^{1/2}]$.

In the bulk of this chapter we adopt this prescription. For up to ^{20}F we write the density of state as $\rho_A(E) = \rho_A^0 \times \exp(S)$, where the low temperature Fermi-gas expression for S, as written above, is used. The energy independent value of the pre-factor is fixed from experimentally known levels:

$$\sum_{k=0}^{E_{max}} (2J_K + 1)e^{-E_k/T} = \rho_A^0 \int_0^{E_{max}} e^{(S(E)-\beta E)} dE. \tag{4.7}$$

While objections can be raised against this procedure, it achieves three objectives which we wanted to have: (a) we did not want to lose the information of the experimentally measured discrete excited states ; (b) we did want to take into account the contribution from the continuum and (c) with this procedure calculations are fairly simple. Although, we will not report on all other formulae for density of states that we also used, our final results for the isotope populations are quite stable within reasonable variations that were tried. We estimate the continuum contribution as a similar integral from E_{max} to infinity *i.e.*,

$$q_{i,j,cont} = \int_{E_{max}}^{\infty} \rho_A^0 \rho_A(E) e^{-\beta E} dE. \tag{4.8}$$

This process is continued up to ^{20}F wherein we can read off energy levels from data tables. For elements above ^{20}F, a parametrised version had to be used. No doubt,

any such parametrization will be based on a mass formula. Unlike the case of the preceding chapters, this parametrization will include isospin dependence, Coulomb interaction and symmetry energy. This is given as

$$q_{i,j,int} = \exp\left[\left(W_0(i+j) - \sigma(i+j)^{2/3} - \kappa\frac{i^2}{(i+j)^{1/3}} - s\frac{(j-i)^2}{j+i} + T^2(i+j)/e\right)/T\right], \tag{4.9}$$

where $W_0 = 15.8MeV$, $\sigma = 18.0MeV$, $\kappa = 0.72MeV$, $s = 23.5MeV$ and $e = 16.0MeV$. The first four terms in the right hand side of Eq. (4.9) arise from a parametrised version of the binding energy of the ground state. The last term arises from an approximation to the Fermi-Gas formula for level density. This was also used in [26]. For protons and neutrons q is 1.

The average number of particles of a composite is given by

$$\langle n_{i,j}\rangle = \omega_{i,j}\frac{Q_{Z-i,N-j}}{Q_{Z,N}}. \tag{4.10}$$

However, this population is partly over particle stable states and partly over particle unstable states which will decay into other nuclei before reaching the detectors. This last feature of the model will be introduced in the remaining sections.

4.3 *Secondary decay.*

In keeping with the way experimental data are presented, we will compute ratios of yields of different isotopes of Boron, Carbon, and Nitrogen. To lowest order one can consider the $\langle n_{i,j}\rangle$ obtained from equation (4.10) above, remove the particle unstable fractions, and compare them directly with experiment. This is shown in the figures as the dotted line with a filled triangle plotting symbol. These populations contain only particle stable states.

Next we consider decay of the particle unstable states. We restrict the secondary decay to be due to emission of six species: neutron, proton, deuteron, ^{3}He, triton, and

alpha particles. Any given nucleus (i,j) from a particle unstable state can in principle go to at most six other nuclei. As the populations are canonically distributed among the various energy levels, we can calculate the fraction that are in particle stable or unstable states. If the fraction of nuclei (i,j) at the first stage in unstable states is $f^0_{i,j}$, then the stable population of (i,j) after these have decayed is given by $(1-f^0_{i,j})\langle n_{i,j}\rangle$. Now of the ones that decayed a fraction $\frac{\Gamma_{a,b}}{\Gamma_T}$ decayed by the channel (a,b) (where $\Gamma_{a,b}$ is the decay rate by channel (a,b) and Γ_T is the total decay rate), thus the new population of nuclei $(i-a,j-b)$ is given simply as $(1-f^0_{i-a,j-b})\langle n_{i-a,j-b}\rangle+\frac{\Gamma_{a,b}}{\Gamma_T}f^0_{i,j}\langle n_{i,j}\rangle$. Of the newly decayed population again a fraction $f^1_{i-a,j-b}$ will be unstable and will decay further. We subtract these and quote only the stable population of the isotope $(i-a,j-b)$. Thus in our simple formalism, the number of nuclei (i,j) left in particle stable states at the stage we call 'up to single decay' is given by

$$\langle n_{i,j}\rangle^1 = (1-f^0_{i,j})\langle n_{i,j}\rangle + \sum_{a,b}(1-f^1_{i,j})\frac{\Gamma_{a,b}}{\Gamma_T}f^0_{i+a,j+b}\langle n_{i+a,j+b}\rangle, \tag{4.11}$$

where $f^1_{i,j}$ is the fraction of the once decayed nuclei in unstable states. We will indicate how to calculate $f^1_{i,j}$ in the next section. The quantity $\Gamma_{a,b}$ is the width for emission of (a,b) from $(i+a,j+b)$ and Γ_T is the total width.

We can then take these revised populations $\langle n_{i,j}\rangle^1$ and again compute the ratios. We label these 'up to single decay'. These are reported in the plots as the small dashed line with the diamond plotting symbol. Note: this is just the stable fraction of the population after one stage of decay, the actual population is possibly greater and contains unstable states. These would subsequently decay and raise the stable populations of the different isotopes.

After the first decay there may still be some fraction in particle unstable states. These can decay, thereby, changing the population of (i,j) to $\langle n_{i,j}\rangle^2$. If we take the ratios now we get what we call 'up to double decay', this is denoted by the dot–dashed line and the square plotting symbol. Again at this stage the $\langle n_{i,j}\rangle^2$ represent only the sum of the stable fractions of the populations obtained from the initial distribution, single decays and double decays.

It is clear the procedure can be continued. The fraction remaining in particle unstable states will continue to decrease. We found no significant difference between the 'up to triple decay' and the 'up to quadruple decay' calculation. Thus we do not continue beyond. Once again it should be noted that all the plotted populations, $\langle n_{i,j}\rangle$, $\langle n_{i,j}\rangle^1$, $\langle n_{i,j}\rangle^2$, $\langle n_{i,j}\rangle^3$ etc., quote only the stable fractions at freezeout, after single, double, and triple decay respectively.

The formalism for the decay calculation is given in the next section, there the quantities $f_{i,j}$, $\Gamma_{a,b}$ will be calculated in somewhat greater detail. The reader who is only interested in the final results could skip to Sects. 4.6 and 4.7.

4.4 *The decay formalism.*

As the heated clusters stream out from the hot source, many of them will be in particle unstable states, these will decay by particle emission, for example, by emitting a neutron, proton, α particle etc. They will then leave a residue nucleus which may be particle stable or unstable; if it is unstable then it will decay further into another isotope and this process will continue till the residue is produced in a particle stable state.

The primary calculation assumes that thermal equilibrium is achieved at freezeout; if this is true then the number of composites with i protons and j neutrons with an energy in the interval E and $E + dE$ is given by the canonical factor

$$dn_A(E) = C_{i,j}\rho_A(E)e^{-\beta E}dE. \tag{4.12}$$

Where, we have abbreviated A to mean (i, j), and $\rho_A(E)$, from Sect. 4.2, is given as $\rho_A(E) = \rho_A^0 \exp(S)$. The multiplicative constant ρ_A^0 will, henceforth, be absorbed into the overall normalization constant $C_{i,j}$. Thus from now on the density function is given simply as

$$\rho_A(E) = \exp\left[\pi\left(\frac{(i+j)E}{\epsilon_F}\right)^{1/2}\right]. \tag{4.13}$$

$C_{i,j}$ is a normalization constant such that

$$\int_0^\infty C_{i,j}\rho_A(E)e^{-\beta E}dE = \langle n_{(i,j)}\rangle. \tag{4.14}$$

Now of the various levels in a particular nucleus, some will be at a very low energy and as a result will be stable to any form of particle decay. Those that lie above an energy

$$E_{x,y} = (M_{x,y} + M_{i-x,j-y} - M_{i,j}) + V_{x,y}, \tag{4.15}$$

will in general be unstable to decay via emission of a particle (x, y) (i.e., a particle with neutron number y and proton number x) , where $M_{x,y}$ is the mass of the particle, $M_{i,j}$ is the mass of the decaying nucleus (i, j), $M_{i-x,j-y}$ is the mass of the residue left over after decay and $V_{x,y}$ is the coulomb barrier for that particle. Note that (x, y) could represent a variety of particles; in this chapter we will consider 'six' such particles, as mentioned in the introduction.

As is evident from Eq. (4.15), different particle decays have different energy thresholds. Consider an isotope (i, j), as an example let us take ^{12}C $(i = 6, j = 6)$. As we start from the ground state level and move upwards, we will encounter different thresholds. The lowest will be the ^4He decay threshold at an energy $L_1 = E_{2,2}$ (in ^{12}C it is at $9.6MeV$ approximately) , the next higher threshold is for proton decay at $L_2 = E_{1,0}$ (in ^{12}C it is at $18.14MeV$ approximately), and so on; we will get different thresholds one after the other(note: the order of different thresholds is different for different isotopes).

All nuclei of type (i, j) which are formed between the ground state and the lowest threshold L_1, will remain as isotopes (i, j), this number is given by

$$n_{i,j}(0 \leftrightarrow L_1) = \int_0^{L_1} C_{i,j}\rho(E)e^{-\beta E}dE. \tag{4.16}$$

Those that are formed between L_1 and the next threshold L_2, will all completely decay by ^4He emission, and these nuclei will then appear as nuclei of type $(i-2, j-2)$ and

must be added on to the population of isotope $(i-2, j-2)$.

Then, those nuclei of type (i, j) which are formed between L_2 and the next threshold L_3, will decay both by ^4He emission and by proton emission. In the next zone there will be three kinds of decay, and so on. We now ask, how many of the initial nuclei formed in a particular zone will decay by each of the channels that are available, and how many of the residues formed will be stable or unstable?

To answer the above questions: we start by writing down the number of particles of type (x, y) with energy between $(\varepsilon, \varepsilon + d\varepsilon)$ that are emitted, in a time interval between t and $t + dt$, by nuclei of type (i, j), lying between an energy $(E, E + dE)$, leaving behind a residue nucleus $(i - x, j - y)$ (we may alternatively refer to (x, y), (i, j), and $(i - x, j - y)$ by simply their mass numbers a, A and B where $a = x + y$, $A = i + j$ and $B = i - x + j - y$)

$$d^3N_a = W(E, \varepsilon)d\varepsilon dt dN(E, t). \tag{4.17}$$

Where $dN(E, t)$ is the number of nuclei of type (i, j) initially formed at an energy $(E, E + dE)$ which are still left undecayed after a time t, given by

$$dN(E, t) = C_{i,j}e^{-\Gamma_T(E)t}\rho_A(E)e^{-\beta E}dE. \tag{4.18}$$

The quantity $W(E, \varepsilon)d\varepsilon$ is the Weisskopf decay probability per unit time [8] given by the expression

$$W(E, \varepsilon)d\varepsilon = g_a\gamma_a\varepsilon\sigma_{[a+B\to A]}\frac{\rho_B(E - B_a - \varepsilon)}{\rho_A(E)}. \tag{4.19}$$

In Eq. (4.18), $\Gamma_T(E)$ is the the total decay probability per unit time from an energy level E of the isotope A. In Eq. (4.19), g_a is the spin degeneracy factor of the emitted particle, γ_a is a constant of a particular decay [8, 9], given by

$$\gamma_a = \frac{m_p}{\pi^2\hbar^3} \times \frac{a(A - a)}{A}, \tag{4.20}$$

where m_p is the mass of a nucleon. In Eq. (4.19), $B_a = M_{i-x,j-y} + M_{x,y} - M_{i,j}$, is the separation energy of the decay; $\sigma_{[a+B\to A]}$ is the cross-section for the reverse reaction to occur, (i.e. $a + B \to A$). It is given semiclassically for uncharged particles as

$$\sigma_{[a+B\to A]} = \pi R_a^2, \tag{4.21}$$

and for charged particles as

$$\sigma_{[a+B\to A]} = \pi R_a^2 \frac{\varepsilon - V}{\varepsilon}\theta(\varepsilon - V). \tag{4.22}$$

Where R_a is the radius associated with the geometrical cross-section of the formation of A from B and a. Following the prescription of Friedmann and Lynch [9], R_a is given by

$$R_a = \begin{cases} [(A-a)^{1/3} + (a)^{1/3}]r_0 & \text{, for } a \geq 2 \\ r_0(A-1)^{1/3} & \text{, for } a = 1 \end{cases}$$

where $r_0 = 1.2fm$

The quantity V in Eq. (4.22), is the Coulomb barrier for the formation of A from B and a. Again following [9], this is written in the touching sphere approximation as

$$V_a = \begin{cases} \frac{x(i-x)e^2}{((A-a)^{1/3}+(a)^{1/3})r_c} & \text{, for } a \geq 2, \\ \frac{(i-1)e^2}{r_c(A)^{1/3}} & \text{, for protons,} \end{cases}$$

where $r_c = 1.44fm$

Also in Eq. (4.19), $\rho_A(E)$, $\rho_B(E - B_a - \varepsilon)$ are the respective density of states of the two nuclei. They have the same form as in Eq. (4.13).

We note that d^3N_a in Eq. (4.17) is also equal to the number of nuclei that were initially formed as nuclei of type A at an energy between E and $E + dE$, and then decayed into nuclei B with an excitation energy of $E - B_a - \varepsilon$. To get the total number of states that decayed from a level E by emission of a particle of any allowed energy, we integrate over ε from its minimum value V_a to its maximum value $E - B_a$, and obtain

$$d^2N = \Gamma_a(E) C_{i,j} e^{-\Gamma_T(E)t} \rho_A(E) e^{-\beta E} dE dt, \tag{4.23}$$

where,

$$\Gamma_a(E) = \int_{V_a}^{E-B_a} W(E,\varepsilon) d\varepsilon. \tag{4.24}$$

On integration this gives

$$\begin{aligned}\Gamma_a(E) = \frac{2\gamma_a\prime}{\rho_A(E)} \Bigg[(E - B_a - V_a) \left(\frac{e^{C\mathcal{B}}}{C}(\mathcal{B} - 1/C) - \frac{e^{C\mathcal{A}}}{C}(\mathcal{A} - 1/C) \right) \\ - \frac{e^{C\mathcal{B}}}{C} \left(\mathcal{B}^3 - \frac{3\mathcal{B}^2}{C} + \frac{6\mathcal{B}}{C^2} - \frac{6}{C^3} \right) \\ + \frac{e^{C\mathcal{A}}}{C} \left(\mathcal{A}^3 - \frac{3\mathcal{A}^2}{C} + \frac{6\mathcal{A}}{C^2} - \frac{6}{C^3} \right) \Bigg].\end{aligned} \tag{4.25}$$

The derivation of the above equation is given in the appendix, where, $C = \pi(\frac{i+j-x-y}{\epsilon_F})^{1/2}$, $\mathcal{B} = \sqrt{E - B_a - V_a}$, $\mathcal{A} = 0$. In the above equation g_a (Eq. (4.19)), and some of the factors of σ (Eq. (4.22)) have been absorbed into γ_a', thus,

$$\gamma_a\prime = \gamma_a g_a \pi R_a^2. \tag{4.26}$$

We may now integrate out the time to get

$$dN_a = \frac{\Gamma_a(E)}{\Gamma_T(E)} C_{i,j} \rho_A(E) e^{-\beta E} dE. \tag{4.27}$$

To get the total number of states that have decayed from nuclei of type A by channel a we must integrate over E from L_1 to ∞,

$$N_a = \int_{L_1}^{\infty} \frac{\Gamma_a(E)}{\Gamma_T(E)} C_{i,j} \rho_A(E) e^{-\beta E} dE. \tag{4.28}$$

This integration is quite involved for as we crossover from one zone of decay (L_1, L_2) to another zone (L_2, L_3), $\Gamma_T(E)$ changes discontinuously as a new channel of decay becomes accessible to the nuclei. Thus we break up the integration into 6 zones,

corresponding to the 6 real decay zones, and integrate within each zone independently. Note that the last zone extends from L_6 to $L_7 = \infty$, and is thus considerably larger than the other zones. However, at the low temperatures that will be encountered, this zone will be sparsely populated. Thus the following approximation is valid. Within each zone, with an energy from L_k to L_{k+1}, the integral can be replaced by a mean value expression,

$$N_a(L_k, L_{k+1}) = \frac{{}_{L_k}\langle \Gamma_a \rangle_{L_{k+1}}}{{}_{L_k}\langle \Gamma_T \rangle_{L_{k+1}}} \Delta n_{i,j}(L_k, L_{k+1}). \tag{4.29}$$

Where $N_a(L_k, L_{k+1})$ is the mean number of nuclei of type (i, j) (or A) that were initially formed at an energy between L_k and L_{k+1}, and decayed by the (x, y) (or a) channel. In the above equation,

$${}_{L_k}\langle \Gamma_a \rangle_{L_{k+1}} = \int_{L_k}^{L_{k+1}} \Gamma_a(E) C_{i,j} \rho_A(E) e^{-\beta E} dE. \tag{4.30}$$

Of course, the left hand side is zero if channel a is not open in the region L_k to L_{k+1}. The mean decay rate over all channels is

$${}_{L_k}\langle \Gamma_T \rangle_{L_{k+1}} = \int_{L_k}^{L_{k+1}} \Gamma_T(E) C_{i,j} \rho_A(E) e^{-\beta E} dE, \tag{4.31}$$

and

$$\Delta n_{i,j}(L_k, L_{k+1}) = \int_{L_k}^{L_{k+1}} C_{i,j} \rho_A(E) e^{-\beta E} dE. \tag{4.32}$$

Thus by summing up all the contributions from the six different zones, we get the total number of nuclei that have decayed from isotope A by the a channel as,

$$N_a = \sum_{k=1}^{6} N_a(L_k, L_{k+1}). \tag{4.33}$$

To find out how many of these have decayed to stable isotopes, we must first calculate from Eq. (4.17) the stable decay rate $\Gamma_a^s(E)$. Two cases emerge in this calculation. If $E - B_a - V_a \geq E_{A-a}^s$, $\Gamma_a^s(E)$ is obtained by integrating over ε, from

$(E - B_a - E^s_{A-a})$ to its maximum value $(E - B_a)$, where E^s_{A-a} is the stable level or the lowest threshold L_1 of the residue nucleus B above which B is unstable. The expression for $\Gamma^s_a(E)$ is obtained from that of $\Gamma_a(E)$ in Eq. (4.25) by replacing $\mathcal{B} = \sqrt{E^s_{A-a}}$. If $E - B_a - V_a < E^s_{A-a}$, then $\Gamma^s_a(E) = \Gamma_a(E)$. Then, following a similar procedure as above for Γ_a, we get the total number of nuclei A (or (i,j)) lying in an energy range between (L_k, L_{k+1}), that decay by the a channel to a stable state as,

$$N^s_a(L_k, L_{k+1}) = \frac{L_k\langle\Gamma^s_a\rangle_{L_{k+1}}}{L_k\langle\Gamma_T\rangle_{L_{k+1}}}\Delta n_{i,j}(L_k, L_{k+1}). \tag{4.34}$$

The unstable decay rate from a particular level or zone is the probability of a decay per unit time from A to an unstable level or levels of B from which further decay can take place. It is easy to see that they are given simply as the difference of the total decay rate and the stable decay rate *i.e.*,

$$\Gamma^u_a = \Gamma_a - \Gamma^s_a. \tag{4.35}$$

The derivations and expressions for the full decay rates are given in the appendix.

After a decay has taken place ($A \rightarrow B + a$), we ask what is the population distribution of the residue as a function of its energy ($x = E - B_a - \varepsilon$). This can, in principle, be calculated from Eq. (4.17) by integrating over E and ε, such that $(x = E - B_a - \varepsilon)$, the energy of the residue, is a constant. First we make a change of variables from (E, ε) to (E, x) and then integrate over E only. We get

$$dN_a(x) = \left(\int_{B_a+V_a+x}^{\infty} dE\gamma'_a \frac{E - B_a - V_a - x}{\Gamma_T(E)}\rho_B(x)C_{i,j}e^{-\beta E}\right)dx. \tag{4.36}$$

This integration is quite involved. We assume that the residue population is canonically distributed, but with a new temperature $1/\beta'$ *i.e.*,

$$dN_a(x) = \mathcal{D}_{i,j\rightarrow k,l}\rho_B(x)e^{-\beta' x}. \tag{4.37}$$

There are two unknowns in this formula, the new temperature $1/\beta'$ and the overall normalization constant $\mathcal{D}_{i,j\rightarrow k,l}$. To find these two constants we will impose that the

total population of this interim stage (*i.e.*, $N_{i,j\to k,l}$), and the mean energy of the distribution $\langle x\rangle$, be reproduced by this new temperature.

We can obtain formal expressions for the total population of the residue B as contributed by the decay of A, as well as its mean energy $\langle x\rangle$, from Eq. (4.37) as

$$\begin{aligned} N_a(\beta', \mathcal{D}, C) &= \int_0^\infty dN_a(x) \\ &= \frac{\mathcal{D}_{i,j\to k,l}}{\beta'}\left[1 + C\sqrt{\frac{\pi}{4\beta'}}e^{C^2/4\beta'}\left(1 - erf\left(\frac{C}{2\sqrt{\beta'}}\right)\right)\right], \end{aligned} \tag{4.38}$$

and,

$$\begin{aligned} \langle x(\beta', C)\rangle &= \frac{1}{N_a(\beta', \mathcal{D}, C)}\int_0^\infty x dN_a(x) \\ &= \mathcal{D}_{i,j\to k,l}\left[\frac{1}{\beta'^2} + \frac{3\sqrt{\pi}C}{\beta'^{5/2}}\left\{1 + erf\left(\frac{C}{2\sqrt{\beta'}}\right)\right\}e^{C^2/4\beta'}\right. \\ &\quad \left. + \frac{C^2}{4\beta'^3} + \frac{C^3\sqrt{\pi}}{8\beta'^{7/2}}\left\{1 + erf\left(\frac{C}{2\sqrt{\beta'}}\right)\right\}e^{C^2/4\beta'}\right]. \end{aligned} \tag{4.39}$$

Where the formal expression for $N_a(\beta', \mathcal{D}, C)$ is used in Eq. (4.39). The numerical value of N_a is taken from Eq. (4.33). The numerical value of $\langle x\rangle$ is found by explicit use of Eq. (4.36). From these two equations we obtain the two constants $\mathcal{D}_{i,j\to k,l}$ and β'.

The numerical value of $\langle x\rangle$ is derived from Eq. (4.36) as follows.

$$\langle x\rangle = \frac{1}{N_a}\int_0^\infty dx x\left(\int_{B_a+V_a+x}^{E_{max}} dE\gamma_a'\frac{E - B_a - V_a - x}{\Gamma_T(E)}\rho_B(x)C_{i,j}e^{-\beta E}\right). \tag{4.40}$$

In the above equation, the numerical value of N_a is taken from Eq. (4.33). We may now change the order of integration to get

$$\langle x\rangle = \frac{1}{N_a}\int_{B_a+V_a}^\infty dE\int_0^{E-B_a-V_a} dx x\gamma_a'\frac{E - B_a - V_a - x}{\Gamma_T(E)}\rho_B(x)C_{i,j}e^{-\beta E}. \tag{4.41}$$

The x integration is now done simply to obtain

$$\langle x\rangle = \frac{1}{N_a}\int_{B_a+V_a}^{\infty} dE\gamma'_a \frac{I(E)}{\Gamma_T(E)} C_{i,j}\rho_A(E)e^{-\beta E}, \tag{4.42}$$

where $I(E)$ is given by

$$\begin{aligned} I(E) = \frac{1}{\rho_A(E)}\Bigg[&\frac{4(E-B_a-V_a)^2 e^{C\sqrt{E-B_a-V_a}}}{C^2} - \frac{28(E-B_a-V_a)^{3/2}e^{C\sqrt{E-B_a-V_a}}}{C^3} \\ &+ \frac{108(E-B_a-V_a)e^{C\sqrt{E-B_a-V_a}}}{C^4} - \frac{240(E-B_a-V_a)^{1/2}e^{C\sqrt{E-B_a-V_a}}}{C^5} \\ &+ \frac{240e^{C\sqrt{E-B_a-V_a}}}{C^6} + \frac{12(E-B_a-V_a)}{C^4} - \frac{240}{C^6}\Bigg]. \end{aligned} \tag{4.43}$$

In the ensuing integration over E, we, once again, replace the integral with its mean value expression.

$$\langle x\rangle = \frac{1}{N_a}\int_{B_a+V_a}^{\infty} dE\gamma'_a \frac{{}_{B_a+V_a}\langle I(E)\rangle_\infty}{{}_{B_a+V_a}\langle \Gamma_T(E)\rangle_\infty} C_{i,j}\rho_A(E)e^{-\beta E}, \tag{4.44}$$

where,

$${}_{B_a+V_a}\langle \Gamma_T(E)\rangle_\infty = \sum_{E_k>B_a+V_a} L_k \langle \Gamma_T(E)\rangle_{L_{k+1}}, \tag{4.45}$$

and

$$\begin{aligned} {}_{B_a+V_a}\langle I(E)\rangle_\infty &= \int_{B_a+V_a}^{\infty} dE I(E) C_{i,j}\rho_A(E)e^{-\beta E} \\ &= C_{i,j}e^{-\beta G_a}\Bigg[\frac{1}{\beta^4} + \frac{3C\sqrt{\pi}}{4\beta^{9/2}}\left\{1+erf\left(\frac{C}{2\sqrt{\beta}}\right)\right\}e^{C^2/4\beta} \\ &\quad + \frac{C^2}{4\beta^5} + \frac{C^3\sqrt{\pi}}{8\beta^{11/2}}\left\{1+erf\left(\frac{C}{2\sqrt{\beta}}\right)\right\}e^{C^2/4\beta}\Bigg]. \end{aligned} \tag{4.46}$$

Thus the formal expressions for $N_a(\beta', \mathcal{D}, C)$ (Eq. (4.38)), and $\langle x(\beta', C)\rangle$ (Eq. (4.39)), are compared to the actual values obtained for N_a (Eq. (4.33)), and $\langle x\rangle$ (Eq. (4.44)), and the two unknowns of Eq. (4.37) are evaluated. We can now proceed with further decays following the same procedure as before with decay occurring from a canonically distributed population at a temperature $1/\beta'$.

We can thus model an n−step decay process by assuming that at each intermediate stage the population is canonically distributed with a new temperature and overall normalization constant. The decay rates to the next stage are calculated with the new temperature. Following this, the fraction of the population that decays through a particular channel, and the mean energy of the resultant residue nucleus, are calculated. These are then used to secure the temperature and normalization constant of the next stage of decay. This process will continue till the fraction of decay to particle unstable states becomes negligible.

4.5 *The calculation.*

From the primary calculation, we obtain that $\langle n_{i,j} \rangle$ nuclei of type (i,j) (or A) are formed from the initial multifragmentation. The population $\langle n_{i,j} \rangle$ is distributed canonically among the various energy levels as demonstrated by Eq. (4.12). If a particular nucleus is at a sufficiently excited state then it will emit a particle (x,y) (or a) and leave a residue $(i-x=k, j-y=l)$ (or B), which may again decay by emitting a particle (u,v) (or b) leaving a nucleus $(k-u=m, l-v=n)$ (or D), and so on until it finally reaches a nucleus (p,q) (or Z) in a stable state. We ask the question that if $\langle n_{i,j} \rangle$ nuclei of type A were initially formed, then how many of these will finally end up as stable nuclei of type A, B, D ... Z. The contribution of $\langle n_{i,j} \rangle$ to the final stable population of A is given simply by Eq. (4.16) as

$$n_A^f = \int_0^{L_1} C_{i,j} \rho_A(E) e^{-\beta E} dE = \Delta n_{i,j}(0, L_1). \tag{4.47}$$

The number of nuclei initially formed as (i,j) which decay to $(i-x, j-y) = (k,l)$ is given as

$$n_{A \to B} = \sum_{k=1}^{6} \frac{L_k \langle \Gamma_a \rangle_{L_{k+1}}}{L_k \langle \Gamma_T \rangle_{L_{k+1}}} \Delta n_{i,j}(L_k, L_{k+1}). \tag{4.48}$$

The mean energy of the newly formed residue nucleus is given by

$$\langle x \rangle = \frac{1}{n_{A\to B}} \gamma'_a \frac{{}_{B_a+V_a}\langle I(E)\rangle_\infty}{{}_{B_a+V_a}\langle \Gamma_T(E)\rangle_\infty} \Delta n_{i,j}(B_a + V_a, \infty). \tag{4.49}$$

We assume that this population is canonically distributed from an excitation energy of $E_0 = 0$ to ∞ with a new temperature $1/\beta'$ (Eq. 4.37). Extraction of the new temperature $1/\beta'$ and the overall normalization constant $\mathcal{D}_{i,j\to k,l}$ is done as detailed in Sect. 4.4. In most cases, where this procedure was implemented, we obtained a new temperature $1/\beta'$ which was lower than the initial temperature $1/\beta$; however, in about 3% of the cases $1/\beta'$ turned out to be higher than $1/\beta$; this occurs when the residue of the decay process is far from the valley of stability. We can then calculate the number of nuclei that initially started out as A's and finally ended up as 'stable' B's as

$$n^f_{A\to B} = \int_0^{L_1} \mathcal{D}_{i,j\to k,l} \rho_B(x) e^{-\beta' x} dx. \tag{4.50}$$

Note that in the above equation $\rho_B(x)$ and L_1 are the density of states and lowest decay threshold for the nucleus of type $(i - x = k, j - y = l)$. This number can also be calculated directly by using the stable decay rates (Eq. (4.34)), as

$$n^f_{A\to B} = \sum_{k=1}^{6} \frac{L_k \langle \Gamma^s_a \rangle_{L_{k+1}}}{L_k \langle \Gamma_T \rangle_{L_{k+1}}} \Delta n_{i,j}(L_k, L_{k+1}). \tag{4.51}$$

The second equation is more correct as it does not depend on the assumption that the residue is canonically distributed. A comparison of the $n^f_{A\to B}$ obtained from the above two equations gives an estimate of the error involved in the assumption of a canonically distributed residue population. Now we ask, what is the number of nuclei of the B's just formed which will decay by emitting a particle b to a nucleus of type D; this is calculated simply as

$$n_{A\to B\to D} = \sum_{k=1}^{L_6} \frac{L_k \langle \Gamma_b \rangle_{L_{k+1}}}{L_k \langle \Gamma_T \rangle_{L_{k+1}}} \Delta n_{A\to B}(L_k, L_{k+1}). \tag{4.52}$$

The decay rates in the above equation are calculated with the temperature $1/\beta'$. We then calculate the mean energy $\langle y \rangle$ of the new distribution as

$$\langle y \rangle = \frac{1}{n_{A\to B\to D}} \gamma_b' \frac{_{B_b+V_b}\langle I(x)\rangle_\infty}{_{B_b+V_b}\langle \Gamma_T(x)\rangle_\infty} \Delta n_{A\to B}(B_b + V_b, \infty). \tag{4.53}$$

Using these, we continue the process on, by again calculating the temperature and norm of a canonical distribution, which when summed from excitation energy 0 to ∞ is equal to $n_{A\to B\to D}$, and whose mean energy is equal to $\langle y \rangle$. We can then proceed to find how many of these will be in stable states, how many will decay on further etc. We continue this process till the contribution from this decay chain, $A \to B \to D \to ...$, will give numbers of nuclei negligible compared to the already present number in stable states.

The above mentioned method is easy to understand. However, in this work we invoke a slightly different procedure. Instead of starting from a nucleus A and calculating its contributions to all nuclei lying below it, we ask for all the contributions to this nucleus A from nuclei lying above it in the periodic table. This is done in a step-wise manner. First, we calculate the primary populations $\langle n_{i,j} \rangle$ from Eq. (4.10). We then subtract off the unstable part of the population and add on contributions from nuclei which can decay to A by emitting only one particle. Then, we add on the contributions from two particle decays, three particle decays, and so on. In each of the contributions from two and more decays, one has to calculate population distributions of the interim isotopes, *i.e.*, elements which are encountered midway through a decay sequence. Following the discussion from the end of Sect. 4.4, we take these interim populations to be distributed with a canonical probability, with a temperature and normalization constant that reproduces the interim population and the mean energy of the interim isotope. Thus we approach the final stable population of the isotope A in an order by order fashion. This is quite useful as it allows us to terminate the process when higher order contributions bring about negligible change in the stable population of A. After calculating the final populations for A, we ignore all the interim populations that were calculated in the process and start with another isotope afresh.

4.6 Comparison with experiment

Our objective is to calculate the yields of the Boron,Carbon and Nitrogen isotopes measured in the $S + Ag$ Heavy-Ion collision at an energy of $22.3AMeV$ [5]. In Figs. (4.1) to (4.5) the data are shown as empty squares. The method of calculation is simple, first we calculate the primary populations of the isotopes using Eq. (4.10). We then remove the unstable fraction of the population, and quote only the stable part. This is denoted by the dotted line and triangle plotting symbol. We then incorporate secondary decay by adding on all the populations of nuclei that can reach a stable level of the isotopes by emitting only one of the six particles considered. We call these the 'up to single decay' populations and denote them by the small dashed line and diamond plotting symbol. We then add on all those unstable nuclei which can reach a stable level of the given isotopes by sequentially emitting any two particles of the six considered. We call these the 'up to double decay' populations and denote them by the dot−dashed line and square plotting symbol. We then add on all those that can reach the isotopes by three particle emissions, called the 'up to triple decay' population and denoted by the large dashed line and star plotting symbol. And finally we add on the 'up to quadruple decay' population denoted by the solid line and circle plotting symbol. As there is negligible difference between 'up to triple decay' and 'up to quadruple decay' we stop after 'quadruple decay'.

To fit with experimental data, we have four parameters to tune, the obvious ones being the initial temperature β or T, the free volume V_f of the primary calculation, the ratio A/Z (as one does not know how much loss due to pre−equilibrium emission has taken place) and an overall multiplicative constant $\mathcal{H}$ (as we do not know how many nuclei collided in the experiment). The plots are noted to be most sensitive to β and A/Z. Thus in fitting the data we first set particular values of β and A/Z, and calculate the multiplicities at all stages of decay (V_f is varied to get the best possible fit at this temperature and A/Z) . We then multiply all the multiplicities by an appropriate $\mathcal{H}$ and take the logarithm. These are then plotted and compared

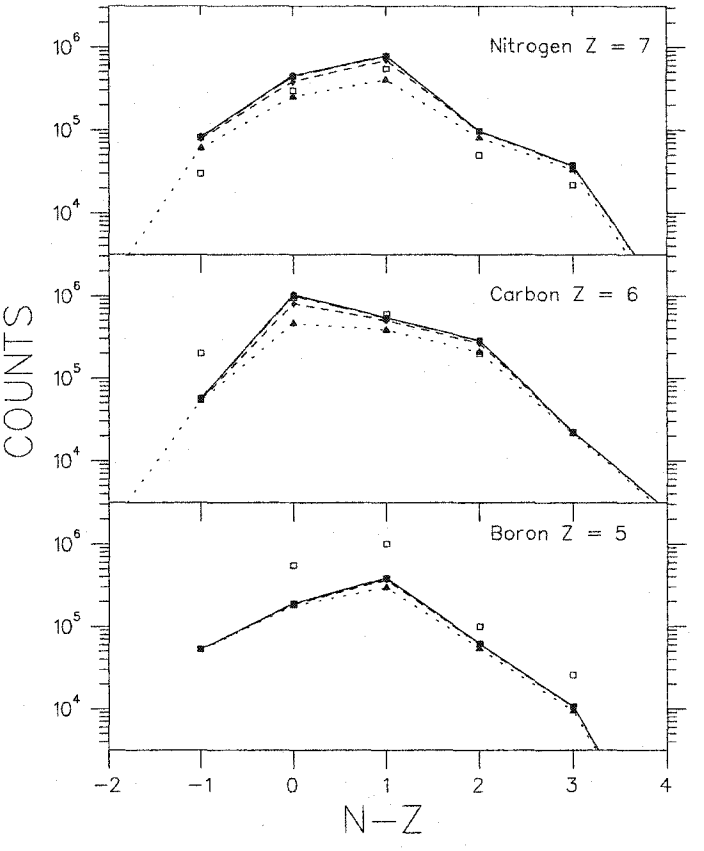

Figure 4.1: Log(counts) vs. Neutron number (N) − Proton Number (Z) for the three cases of Boron,Carbon and Nitrogen. The experimental data are from [1] S+Ag at $22.3AMeV$. The fits show varying stages of decay for a total $Z_T = 50$, $A_T = 110$, $T = 3.0MeV$, $V_{fr}/V_0 = 3.0$ and $\log \mathcal{H} = 6.73$. The empty squares are the experimental data. The dotted line with the triangle plotting symbol is the primary calculation. The small dashed line with diamond plotting symbol is the 'up to single decay' calculation. The dot-dashed line with square plotting symbol is the 'up to double decay' calculation. The dashed line with star plotting symbol is the 'up to triple decay' calculation. The solid line with circle plotting symbol is the 'up to quadruple decay' calculation.

with $\log(counts)$ obtained from the experiment. We then vary β, A/Z and repeat the above procedure till a good fit is obtained. We present fits for three different temperatures, and different A/Z for each temperature. V_f and $\mathcal{H}$ are set to obtain the best fit possible for a given β and A/Z.

We note that the $S + Ag$ system is one with $A = 139$ and $Z = 63$ thus $A/Z = 2.2$. The authors of [5] state that some pre-equilibrium emission may have taken place. As

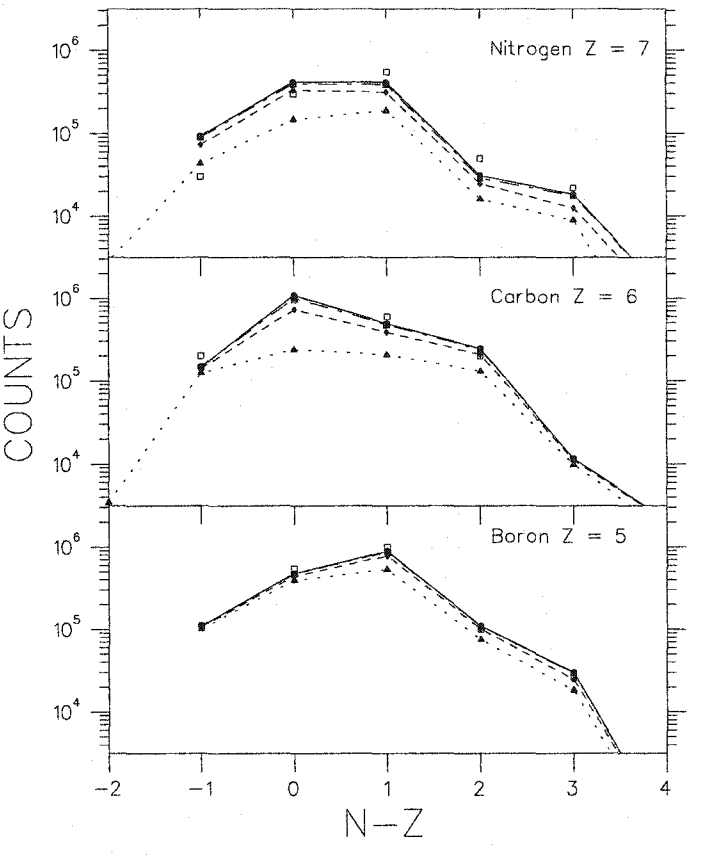

Figure 4.2: Same as fig.1 but with $Z_T = 50$, $A_T = 110$, $T = 5.0MeV$, $V_{fr}/V_0 = 5.5$ and $log\mathcal{H} = 6.34$. The best fit with the data has been obtained with these parameters

we do not know what proportion of neutrons and protons are lost in such a process, we start the calculation with the same A/Z as the $S + Ag$ system. We start with a $Z = 50$ and $A/Z = 2.2$ *i.e.*, $A = 110$. We start the calculation with a low temperature of $3MeV$ in Fig. (4.1) (V_f and $\mathcal{H}$ are varied to get the best fit). We note that overall there is a slight excess of the heavier Nitrogen isotopes as compared to data and a deficit of the lighter Boron isotopes, this implies that the temperature is too low and enough of the light isotopes are not being formed. We proceed by raising the temperature to $5MeV$, maintaining the same A/Z. By now varying V_f and $\mathcal{H}$ we find an excellent fit with the data (Fig. (4.2)).

One may ask at this point, if there is more than one set of parameters which fits the data well. To answer this question we increase, first, the temperature to $7MeV$,

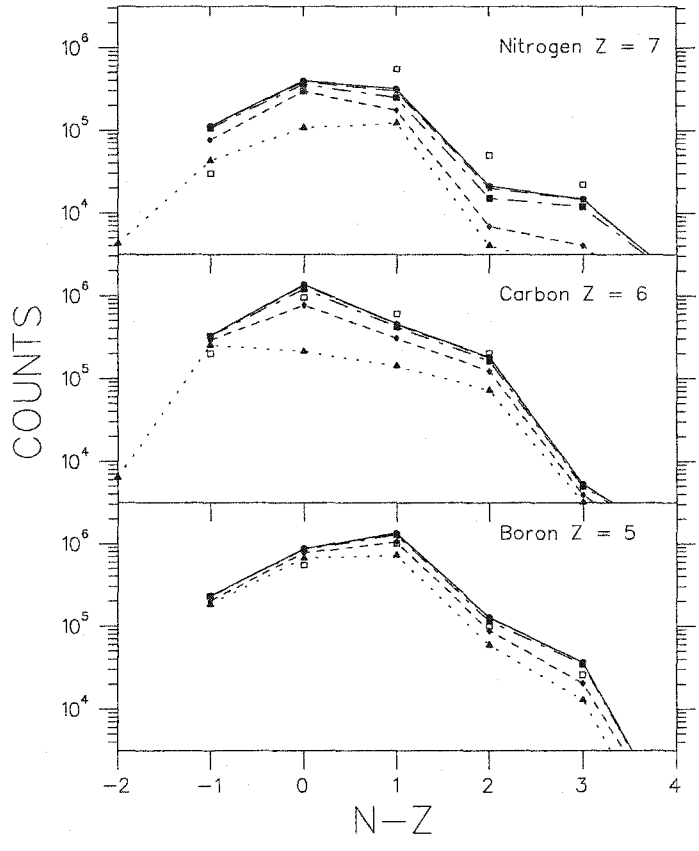

Figure 4.3: Same as fig.1 but with $Z_T = 50$, $A_T = 110$, $T = 7.0MeV$, $V_{fr}/V_0 = 3.0$ and $log\mathcal{H} = 6.73$.

maintain the same A/Z and redo the calculation. We get a very bad fit (Fig. (4.3)). There is an overall deficit in the Nitrogen population and within a particular Z a deficit in the neutron rich isotopes. We try to remedy this situation by increasing the A/Z ratio. The best fit at this temperature is obtained at an $A/Z = 2.3$ (Fig. (4.4)), but we still obtain an overall deficit in the Nitrogen population; the Carbon fit is not as good as in Fig. (4.2).

On inspection of the fits (Figs. (4.1) to (4.4)), we note that the best fit is obtained at Fig. (4.2). In this fit $T = 5.0MeV$, $A/Z = 2.2$, $V_{fr}/V_0 = 5.5$, and $\log(\mathcal{H}) = 6.34$. In this figure we note that, for the Boron populations we get an excellent agreement with the data. In this case there seems to be little change after single decay. For the Carbon isotopes the agreement is good. For Nitrogen, we have a good fit except for

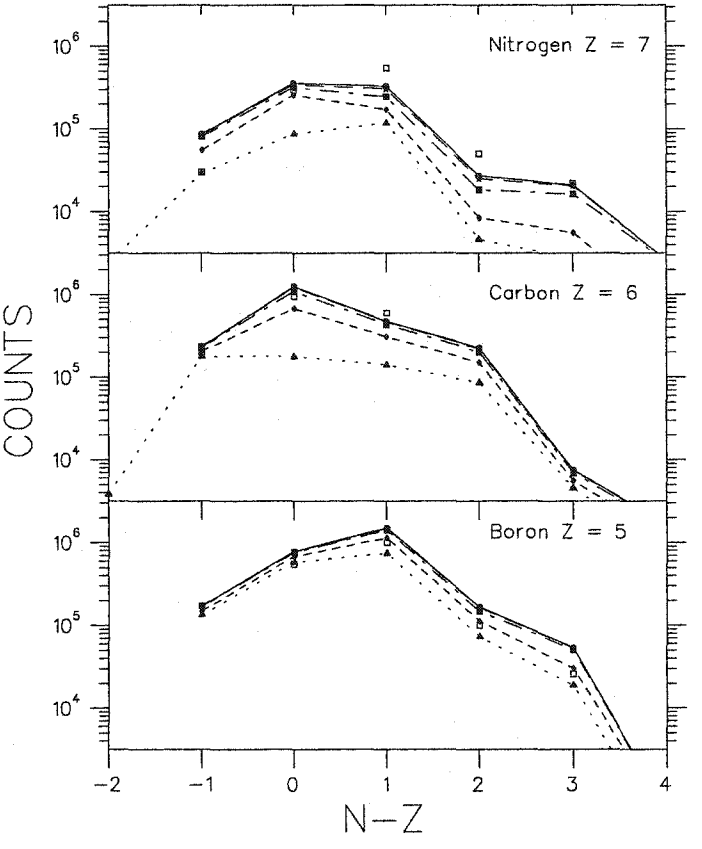

Figure 4.4: Same as fig.1 but with $Z_T = 50$, $A_T = 115$, $T = 7.0MeV$, $V_{fr}/V_0 = 3.0$ and $log\mathcal{H} = 6.73$.

the case of ^{13}N.

Another property of the fits noticed is that they do not seem to depend on A and Z independently but rather on the ratio A/Z. As a demonstration of this, we plot in Fig. (4.5) a fit for $A = 140$ and $Z = 63$ (i.e., $A/Z = 2.22$). We note that we are able to obtain a fit very similar to Fig. (4.2), with the same temperature and V_{fr}/V_0 as in Fig. (4.2), but with a slightly lower $\mathcal{H}$. This is very much expected, as in this case each source has a larger number of nucleons than before.

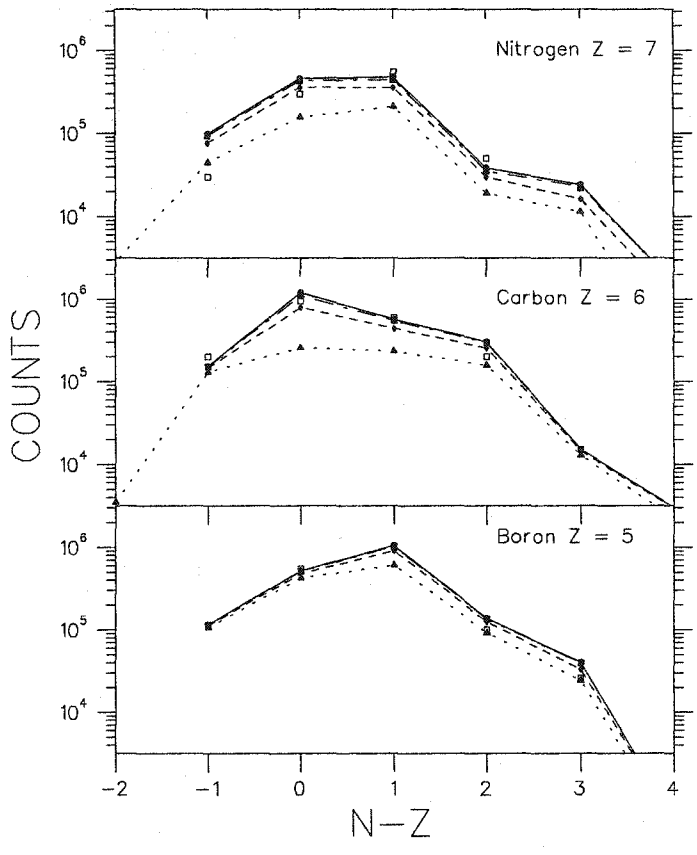

Figure 4.5: Same as fig.2 but with $Z_T = 63$, $A_T = 140$, $T = 5.0MeV$, $V_{fr}/V_0 = 5.5$ and $log\mathcal{H} = 6.30$.

4.7 *Summary and discussions*

In this chapter, we have presented a variety of extensions to the RSM model and in particular introduced a complicated secondary decay formalism. We performed calculations to fit the populations of various isotopes measured in [5]. We obtain very good fits (Fig. (4.2)) with experiment for the Boron and Carbon isotopes. In the Nitrogen isotopes, we obtain a good fit except for the case of ^{13}N. No particular reason could be found for this, but let us go over several approximations (introduced to keep the calculation at a reasonably simple level) which may have contributed.

Actual energy levels from data tables were used only up to $A = 20$ (Eq. (4.4)) for the primary populations. For higher masses, the empirical mass formula (Eq. (4.9))

was used. The secondary decay is very approximate; instead of calculating decay level to level, we have blurred out such details by using a smoothed level density. In doing this we have also ignored the effects of angular momentum degeneracy in the levels. There is also the problem of the discrete level cutoff, and the ensuing approximation of the continuum by a simple Fermi-gas like formula.

For the capture cross-section (Eq. (4.22)), we have used a simple semiclassical formula, assuming that all nuclei are spherically symmetric which is definitely not true. A more precise calculation involving level to level decay would use a more accurate expression for the cross-sections e.g., the Hauser–Feshbach formalism [39, 40].

Still another problem lies in the assumption made in calculating the effects of higher order decay, that the interim populations can be taken to be canonically distributed. This is true only in first order decay, thus making the higher order contributions subject to some error.

There is also an experimental problem according to the authors of [5], the angular distributions were forward peaked, indicating significant emission prior to attainment of thermodynamic equilibrium. Such an emission could affect the populations of the various isotopes.

No doubt, incorporating changes to correct the above mentioned problems will improve the accuracy of the calculation. However, such changes may make the expressions analytically intractable and one would have to resort to numerical means. This may slow down the calculation considerably. The calculations presented in this chapter take minimal computer time. In spite of the shortcomings of the calculation presented above, this still remains a good test of the RSM model, and shows that such a model can definitely be used to explain certain experimental data quite accurately. In the next and final chapter in this topic we use the RSM model to understand the nature of the liquid-gas phase transition occurring at freeze-out in such collisions. The accuracy of our statements there will be directly dependent on the accuracy of our fits to the experimental data here.

4.8 Appendix.

(i) Derivation of equation 4.25.

The full decay rate from a particular energy level E of a nucleus A (or (i,j)) which is decaying by emitting a particle a (or (x,y)), is given as Eq. (4.24),

$$\Gamma_a = \int_{V_a}^{E-B_a} W(E,\varepsilon)d\varepsilon. \tag{4.54}$$

Where $W(E,\varepsilon)$ is the Weisskopf decay probability per unit time given by Eq. (4.19). On writing down the full expression for W we get

$$\Gamma_a = \int_{V_a}^{E-B_a} \frac{\gamma_a'}{\rho_A(E)}(\varepsilon - V_a)\exp\left[\frac{\pi}{\sqrt{\epsilon_F}}\left\{\sqrt{(i+j-x-y)(E-B_a-\varepsilon)}\right\}\right]d\varepsilon. \tag{4.55}$$

Now we substitute $z = (\sqrt{E-B_a-\varepsilon})$ and integrate over z and let $C = \left(\frac{\pi}{\sqrt{\epsilon_F}}\sqrt{i+j-x-y}\right)$, then

$$\Gamma_a(E) = \int_0^{\sqrt{E-B_a-V_a}} \frac{\gamma_a'}{\rho_A(E)} 2z(E-B_a-V_a-z^2)\exp(Cz)dz, \tag{4.56}$$

on carrying out this simple integration we get,

$$\begin{aligned}\Gamma_a(E) = \frac{2\gamma_a\prime}{\rho_A(E)}\Bigg[&(E-B_a-V_a)\left(\frac{e^{C\mathcal{B}}}{C}(\mathcal{B}-1/C) - \frac{e^{C\mathcal{A}}}{C}(\mathcal{A}-1/C)\right)\\ &-\frac{e^{C\mathcal{B}}}{C}\left(\mathcal{B}^3 - \frac{3\mathcal{B}^2}{C} + \frac{6\mathcal{B}}{C^2} - \frac{6}{C^3}\right)\\ &+\frac{e^{C\mathcal{A}}}{C}\left(\mathcal{A}^3 - \frac{3\mathcal{A}^2}{C} + \frac{6\mathcal{A}}{C^2} - \frac{6}{C^3}\right)\Bigg],\end{aligned} \tag{4.57}$$

with $\mathcal{B} = \sqrt{E-B_a-V_a}$, $\mathcal{A} = 0$. The stable decay rate, i.e., the decay rate from an energy level E of the nucleus A to any of the allowed stable levels of B is given simply from the above expression by replacing the upper limit to $\mathcal{B} = \sqrt{E_B^s}$ where E_B^s is the stable threshold of the residue nucleus B . However in the event that $E - B_a - V_a \leq E_B^s$ then the above mentioned replacement should not be made. In this case the total decay rate is the same as the stable decay rate.

(ii) Derivation of the generic expression for $_{L_k}\langle\Gamma_a\rangle_{L_{k+1}}$

From Eq. (4.30) we obtain the definition of $_{L_k}\langle\Gamma_a\rangle_{L_{k+1}}$ as

$$_{L_k}\langle\Gamma_a\rangle_{L_{k+1}} = \int_{L_k}^{L_{k+1}} \Gamma_a(E) C_{i,j} \rho(E) e^{-\beta E} dE, \tag{4.58}$$

now taking the expression of $\Gamma_a(E)$ from Eq. (4.57) and substituting $z = \mathcal{B} = (\sqrt{E - B_a - V_a})$ we get

$$\begin{aligned} _{L_k}\langle\Gamma_a\rangle_{L_{k+1}} = \int_{\sqrt{L_k - B_a - V_a}}^{\sqrt{L_{k+1} - B_a - V_a}} 4\gamma_a' C_{i,j} \Bigg[\left\{ \frac{2z^3}{C^2} - \frac{6z^2}{C^3} + \frac{6z}{C^4} \right\} e^{Cz} \\ + \frac{z^3}{C^2} - \frac{6z}{C^4} \Bigg] e^{-\beta(z^2 + B_a + V_a)} dz. \end{aligned} \tag{4.59}$$

Now we may separate the integration into three parts

$$_{L_k}\langle\Gamma_a\rangle_{L_{k+1}} = I^1_{L_k,L_{k+1}} + I^2_{L_k,L_{k+1}} + I^3_{L_k,L_{k+1}}, \tag{4.60}$$

where,

$$I^1_{L_k,L_{k+1}} = \int_{\sqrt{L_k - B_a - V_a}}^{\sqrt{L_{k+1} - B_a - V_a}} -C_{i,j} 24\gamma_a' \frac{z}{C^4} e^{-\beta(z^2 + B_a + V_a)} dz, \tag{4.61}$$

$$I^{k+1}_{L_k,L_2} = \int_{\sqrt{L_k - B_a - V_a}}^{\sqrt{L_{k+1} - B_a - V_a}} C_{i,j} 4\gamma_a' \frac{z^3}{C^4} e^{-\beta(z^2 + B_a + V_a)} dz, \tag{4.62}$$

$$I^3_{L_k,L_{k+1}} = \int_{\sqrt{L_k - B_a - V_a}}^{\sqrt{L_{k+1} - B_a - V_a}} 2\gamma_a' C_{i,j} \left\{ \frac{4z^3}{C^2} - \frac{12z^2}{C^3} + \frac{12z}{C^4} \right\} e^{Cz - \beta(z^2 + B_a + V_a)} dz. \tag{4.63}$$

The three integrals can be done simply to give

$$I^1_{L_k,L_{k+1}} = \frac{-12\gamma_a' C_{i,j}}{C^4 \beta} \left[e^{-\beta L_k} - e^{-\beta L_{k+1}} \right], \tag{4.64}$$

$$I^2_{L_k,L_{k+1}} = \frac{2\gamma_a' C_{i,j}}{C^2 \beta} \left[L_k e^{-\beta L_k} - L_{k+1} e^{-\beta L_{k+1}} + \{1/\beta - B_a - V_a\} \left(e^{-\beta L_k} - e^{-\beta L_{k+1}} \right) \right], \tag{4.65}$$

$$I^3_{L_k,L_{k+1}} = \frac{4\gamma'_a C_{i,j}}{C^2\beta} e^{-\beta(B_a+V_a)} e^{\frac{C^2}{4\beta^2}} \Bigg[M_k^2 e^{-\beta M_k^2} - M_{k+1}^2 e^{-\beta M_{k+1}^2} + e^{-\beta M_k^2} - e^{-\beta M_{k+1}^2} + \left(\frac{3C^2}{2\beta} - \frac{3}{C}\right)\left\{M_k e^{-\beta M_k^2} - M_{k+1} e^{-\beta M_{k+1}^2}\right\} + \left(\frac{3C^2}{4\beta^2} - \frac{3}{\beta} + \frac{3}{C^2}\right)\left\{e^{-\beta M_k^2} - e^{-\beta M_{k+1}^2}\right\} + \frac{C^3\sqrt{\pi}}{8\beta^2}\left\{erf(\sqrt{\beta}M_{k+1}) - erf(\sqrt{\beta}M_k)\right\}\Bigg]. \quad (4.66)$$

Where $M_k = \sqrt{L_k - B_a - V_a} - C/(2\beta)$ and $M_{k+1} = \sqrt{L_{k+1} - B_a - V_a} - C/(2\beta)$ and C is the same as in Eq. (4.57).

The calculation of the stable decay rate is a bit more involved in the limits of integration and three cases emerge. If $L_k - B_a - V_a < E_B^s$, and $L_{k+1} - B_a - V_a \leq E_B^s$, then

$$_{L_k}\langle \Gamma_a^s \rangle_{L_{k+1}} = _{L_k}\langle \Gamma_a \rangle_{L_{k+1}}. \quad (4.67)$$

If $L_k - B_a - V_a < E_B^s$, but $L_{k+1} - B_a - V_a > E_B^s$, then the calculation of $_{L_k}\langle \Gamma_a^s \rangle_{L_{k+1}}$ has to be done in two parts

$$_{L_k}\langle \Gamma_a^s \rangle_{L_{k+1}} = I_1^s + I_2^s, \quad (4.68)$$

where

$$I_1^s = \int_{L_k}^{E_B^s+B_a+V_a} \Gamma_a(E) C_{i,j} \rho(E) e^{-\beta E} dE. \quad (4.69)$$

The expression for this is the same as Eq. (4.59) with the appropriate change of limits:

$$I_2^s = \int_{E_B^s+B_a+V_a}^{L_{k+1}} \Gamma_a^s(E) C_{i,j} \rho(E) e^{-\beta E} dE; \quad (4.70)$$

if however, $L_k - B_a - V_a \geq E_B^s$, and $L_{k+1} - B_a - V_a > E_B^s$, then

$$ {}_{L_k}\langle \Gamma_a^s \rangle_{L_{k+1}} = \int_{L_k}^{L_{k+1}} \Gamma_a^s(E) C_{i,j} \rho(E) e^{-\beta E} dE. \tag{4.71}$$

5

Critical Phenomena

In this final chapter on intermediate energy heavy-ion collisions, we concentrate exclusively on the liquid-gas phase transition occurring in such collisions. In the preceding chapters we analysed the phenomenon of multifragmentation in the RSM model. We invoked various extensions to this model to allow for a successful comparison with experiment. Now we return to the base model to further study the phase transition encountered in this model.

5.1 Introduction

Up to this point, we have developed a sophisticated thermal model (the RSM model) that allows us to successfully explain experimental data on yields of isotopes. We would like to make it clear that to explain the experimental data, in general, we require the presence of a surface tension term in the mass formula used (see chapter 2). Two choices for this term were used with results very close to each other: $\sigma = 18$ MeV, independent of temperature; $\sigma(T) = \sigma(0)[(T_c^2 - T^2)/(T_c^2 + T^2)]^{5/4}$ with $\sigma(0) = 18$ MeV and $T_c = 18$ MeV. The temperature T_c is the temperature at which the surface tension vanishes. This is in fact the critical temperature of the RSM model: at the critical point there exists no distinction between a liquid and a gas and thus no surface exists. The reader may feel that we have not adequately explored this region. This is because to reach the critical point one requires a very high density as well; at which the approximation of no interaction between clusters (and as a result the RSM model) breaks down. All experimental data that we encountered (or have been

fitted by other practitioners) may be explained by temperatures $\sim 3-7$ MeV. Note that T_c is much larger than this. Choosing a much lower T_c within the range of $3-7$ MeV, will not allow us to fit the data, even qualitatively. These characteristics are also shared by the older SM model [26].

In a sense, we may argue that the agreement of the RSM model predictions with the data, imposes that the input parameters (including T_c) have been well estimated. Thus, in the region of interest and its vicinity, the data imply that a first order phase transition is the *status quo*. First order phase transitions usually terminate in a second order point. From all accounts, in intermediate energy heavy-ion collisions where multifragmentation is seen, this point seems far beyond the realm of the densities and temperatures deduced. This presence of a clear first order phase transition is also borne out by the measurements of the caloric curve in Refs. [4, 17]. However, in a recent experiment [16], a more direct method of obtaining T_c was attempted. There the yields of various isotopes with mass numbers approximately lying between 10 and 40 were studied. It was noted that the yield of a cluster of k nucleons tended to display a scaling law, parametrized as

$$\langle n_k \rangle = q_0 k^{-\tau} \exp\left(\frac{k\Delta\mu}{T} - \frac{c_0 \varepsilon k^{\sigma}}{T}\right), \tag{5.1}$$

where, q_0 is a normalization constant; τ is the topological Fisher exponent; $\Delta\mu$ is the difference of chemical potentials between liquid and gas phase; and $c_0\varepsilon k^{\sigma}$ is the surface tension. The quantity $\varepsilon = (T_c - T)/T_c$ is called the control parameter, where T_c is the critical temperature. This parametrization is somewhat similar to the formula for droplet distribution in the Fisher theory of condensation [41]. Multifragmentation studies based on Fisher's theory have been attempted before [13]. The authors of Ref. [16], subject the above parametrization to a best fit to the data and deduce the various free parameters. They obtain a $T_c = 6.7 \pm 0.2$ MeV, which is much lower than the value used in the SMM and the RSM model. In fact it is within the range of temperatures observable in nuclear collisions, indicating that critical phenomena

may in fact be observable in these experiments. The above two results (ours and those of Ref. [16]) seem to be in contradiction with each other.

Our method of resolution will be as follows. We will retrace the steps of Ref. [16] but subject their analysis not to experimental data but rather to the primary populations obtained from the RSM model. We begin by first assuming an even more general scaling formula than that of Eq. (5.1). The following parametrisation, often used to fit nuclear multifragmentation data, gives an elegant expression for yields of composites:

$$\langle n_k \rangle = k^{-\tau} f(k^{\sigma}(T - T_c)). \tag{5.2}$$

Here a is the mass number of the composite, T_c is the critical temperature, τ is the topological Fisher exponent [41] and the expansion is valid in the neighbourhood of T_c and for "large" k. Variants of the equation are also used. Note that Eq. (5.1) is a subset of the scaling form of Eq. (5.2).

How well does Eq. (5.2) work for models such as the RSM model or the SMM? Just by itself, this is a relevant question in view of the fact that there already exist many applications of such models to fit actual data (see chapter 4 and Refs. [26, 33, 42]). We take a simplified version of the RSM model, similar to the base model presented in chapter 2. The story that unfolds is quite interesting. For simplicity, we consider an RSM model of one kind of particle in the next section, in particular we concentrate on the grand canonical approach. This is then analysed for parametrisation. The method of analysis is explained in Sect. 5.3. Results are presented in Sect. 5.4. After this, we try a fit with a droplet model in Sect. 5.5. A comparison between different models is presented in Sect. 5.6. Our conclusions are summarised in Sect. 5.7.

5.2 *The RSM model: grand canonical approximation*

The reader may refer to chapter 2 or Refs. [28, 43] for details of the RSM model. Summarised here is a grand canonical formulation of the model. We first consider just one kind of particles as the thermodynamic properties for this model were studied in

detail in chapter 2 and Refs. [28, 44, 45, 46]. We can have monomers or composites of k nucleons. The composites have ground state energy $-Wk + \sigma(T)k^{2/3}$. The first term is the volume energy with W=16 MeV. The second term is the surface tension term. As mentioned before, the surface tension term is taken to be temperature dependent as in the SMM [26]: $\sigma(T) = \sigma_0[(T_c^2 - T^2)/(T_c^2 + T^2)]^{5/4}$ with σ_0 =18 MeV and T_c = 18 MeV. The internal partition function of a composite of $k > 1$ nucleons is:

$$z_k = \exp[(Wk - \sigma(T)k^{2/3} + T^2k/\epsilon_0)/T], \tag{5.3}$$

where we have, once again used the standard Fermi-gas model for excited states. For $k = 1$ we take z_1=1.

The canonical partition function $Q_A(T)$ of A nucleons is then given by

$$Q_A = \sum \prod_{k\geq 1} \frac{\omega_k^{n_k}}{n_k!}, \tag{5.4}$$

where ω_k is the partition function of one composite of k nucleons:

$$\omega_k = \frac{V_f}{h^3}(2\pi mT)^{3/2}k^{3/2} \times z_k, \tag{5.5}$$

and the sum rule must be obeyed:$A = \sum kn_k$. As noted before in chapter 2 and Ref. [28], the partition function Q_A for A nucleons can be easily generated on the computer by utilising a recursion relation. Starting with $Q_0 = 1$ one can build all higher ones using

$$Q_p = \frac{1}{p}\sum_{k=1}^{p} k\omega_k Q_{p-k}. \tag{5.6}$$

The expression for the yield of composites is, of course, of primary interest. This is given by

$$\langle n_k \rangle = \omega_k \frac{Q_{A-k}}{Q_A}. \tag{5.7}$$

As mentioned in the introduction, several things are known for this model. The critical temperature for the model is the temperature at which the surface tension

vanishes [44] and hence it is at $T = T_c = 18$MeV. The critical volume is at $V = V_0$. At temperatures below 18 Mev there is a first order phase transition (see chapter 2 and Refs. [28, 44]). The temperature of the phase transition depends upon the density. This temperature signals the disappearance of a large cluster and a sudden spike like behaviour of the specific heat: as a result it was called the boiling temperature in Ref. [28]. In the temperature range we are concerned with in this paper, there is only a first order phase transition. The phase transition temperature is characterised by a spike in specific heat. In finite systems we will take boiling temperature to be the temperature at which the specific heat maximises.

We will try to fit the yields of Eq. (5.7) by the generic formula (Eq. (5.2)). The exact expressions (Eqs.(5.4) to (5.7)) give no clue of a simple parametrisation. Provided V is reasonably bigger than V_0 (see however Ref. [44]) and A is also large we can use the grand canonical formalism to obtain some insight on simple parametrisation. Here there is no longer any constraint on the total number of particles in the sum, Thus we obtain the grand canonical partition function as

$$\mathcal{Q} = \sum_{n_1=0}^{\infty}\sum_{n_2=0}^{\infty}\cdots\sum_{n_\infty=0}^{\infty}\prod_{k\geq 1}\frac{(e^{\beta\mu k}\omega_k)^{n_k}}{n_k!}. \tag{5.8}$$

In this ensemble, the mean number of clusters of size a is given as

$$\begin{aligned}\langle n_a\rangle &= \frac{1}{\mathcal{Q}}\times\sum_{n_1=0}^{\infty}\sum_{n_2=0}^{\infty}\cdots\sum_{n_\infty=0}^{\infty} n_a\prod_{k\geq 1}\frac{(e^{\beta\mu k}\omega_k)^{n_k}}{n_k!}\\ &= e^{\beta\mu a}\omega_a\frac{1}{\mathcal{Q}}\times\sum_{n_1=0}^{\infty}\sum_{n_2=0}^{\infty}\cdots\sum_{n_\infty=0}^{\infty}\prod_{k\geq 1}\frac{(e^{\beta\mu k}\omega_k)^{n_k}}{n_k!} = e^{\beta\mu a}\omega_a.\end{aligned} \tag{5.9}$$

Substituting the expression for ω_k we get the well-known answer of :

$$\langle n_k\rangle = \frac{V_f}{h^3}(2\pi mT)^{3/2}k^{3/2}\exp[(\mu(T)+W+T^2/\epsilon_0)k/T-\sigma(T)k^{2/3}/T]. \tag{5.10}$$

There is no exact correspondence between Eq. (5.10) and Eq. (5.2). Thus we may at best hope to get an approximate fit. How we do it is detailed in the next section.

5.3 *The fitting procedure*

The scaling function of Eq. (5.2) has been used previously to fit experimental data. The reader will convince himself that the presence of the unspecified function f allows for more than one methodology of obtaining a fit. Here we follow the very elegant methods given in [47]. For later use in the text, we will give adequate details.

The quality of fit is given by the smallness of χ^2. If the calculated quantity Y is a function of two parameters $Y = Y(a_i, b_i)$ and we are trying to fit it to a function $g(a_i, b_i, \alpha, \beta, \gamma...)$ then $\chi^2 = \sum_i (Y(a_i, b_i) - g(a_i, b_i, \alpha, \beta, \gamma....))^2 / \sum_j Y(a_j, b_j)^2$. Variations of this criterion are also possible. Eq. (5.2) requires us to find "best" values for τ, σ and T_c. This is done in several steps.

(1) At each temperature (set in the RSM model) we try to fit the yield with the expression $\langle n_a \rangle = a^{-\tau} C$, where C is a constant. From this we obtain the best τ and C. This form is obtained from Eq. (5.2) at $T = T_c$, hence one can argue that if Eq. (5.2) were exact for yields calculated by Eq. (5.7), we would get null χ^2 and the correct τ at $T = T_c$. This would determine both T_c and τ. Of course, null χ^2 is not found since an "exact" fit is not given by Eq. (5.2) However we can draw a best "τ" *vs.* T curve for a pure power law. This τ as a function of T will have a minimum which we label τ_{min}. Since at T_c, the fit is strictly a power law, one can accept that temperature as T_c where the χ^2 of the fit is minimum. However, we will determine T_c using the method described in step 3.

(2) Let $z = a^{\sigma}(T - T_c)$; $f(z)$ has a maximum at some value of $z = \tilde{z}$: $f_{max} = f(\tilde{z})$. For each mass number a the yield $\langle n_a \rangle$ as a function of temperature has a maximum at some value of temperature, $T_{max}(a)$. At this temperature $\langle n_a \rangle (max) = a^{-\tau} f_{max}$ where f_{max} is a constant independent of a. This relationship allows us to choose "best" values for τ and f_{max}.

(3) The value of τ found from step (2) is higher than τ_{min} found at step (1). This means that if we look for T appropriate for τ, two values of T are available from the graph at step (1). The lower value is to be chosen as the value of T_c. The scaling

property (see steps (4) and (5)) is badly violated for the other choice.

(4) Now that we know T_c and $T_{max}(a)$, the temperature at which the yield of composite a is maximised, we find, by least squares fit the "best" value of σ from the condition $a^\sigma(T_{max}(a) - T_c) = const.$ for all a.

(5) The scaling law can now be tested by plotting $\langle n_a \rangle a^\tau$ *vs.* $a^\sigma(T - T_c)$. Plots for all a's should fall on the same graph.

In following steps (1) to (5) the range of a is to be chosen judiciously. It can not be very small (since Eq.(5.2) applies to "large" a's). But a should also be truncated on the high side significantly smaller than the size of the dissociating system. This is so, as in Fisher's theory the scaling refers to the small droplets of the condensed liquid; a cluster of the size of the dissociating system represents the liquid state itself.

5.4 *Scaling results for the RSM model*

We present our results in Figs. (5.1) to (5.3). The sizes of the systems are taken to be $A = 174$ and $A = 240$. The upper panels of the figures use the freeze-out volume $V = 3V_0$ and the lower panels use $V = 4V_0$. Both are shown here for completeness. It will suffice here to discuss only the cases with $V = 3V_0$.

Fig. (5.1) shows τ *vs.* T drawn according to step (1) of Sect. 5.3. The dotted line is the value of τ deduced from step (2). This cuts the curve of step (1) at two temperatures (step (3)). The lower value of the temperature is taken as T_c. In the same Fig. we also plot C_v/A as a function of T. The peak of this curve corresponds to the first order phase transition, called "boiling" temperature in [28]. It is remarkable that the T_c of Eq.(5.2) is very close to "boiling temperature" in this particular example. In Fig. (5.1) we have also plotted the value of χ^2 as a function T (step 1).

In Fig. (5.2) we plot $\ln\langle n_a \rangle$ *vs.* $\ln a$. Two graphs are shown for each disintegrating systems. The graph with higher values of $\langle n_a \rangle$ (shown as diamonds) follows from step (2) of Sect. 5.3. These are the maximum values of $\langle n_a \rangle$ for each a obtained at

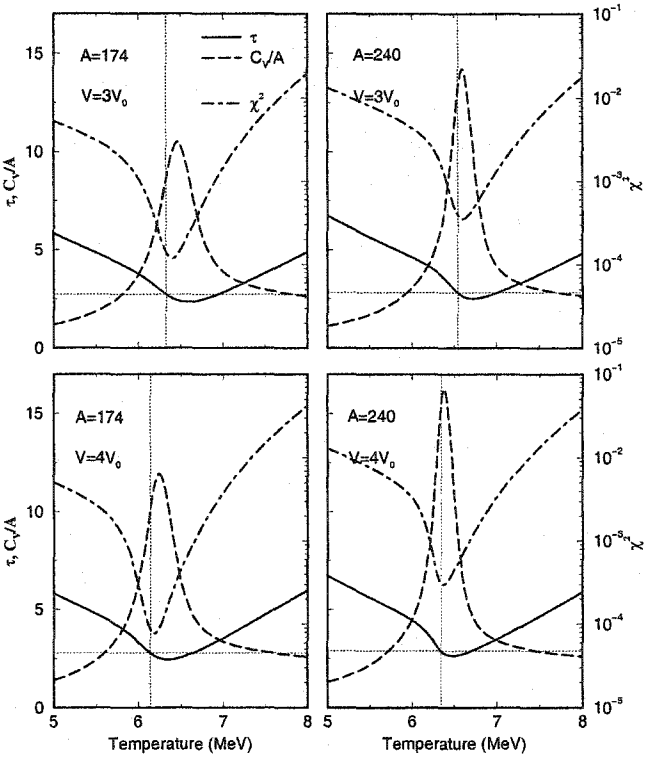

Figure 5.1: τ, C_v/A (left-hand scale) and χ^2 (right-hand scale) plotted against temperature in the model of one kind of particles. The different panels are for different choices of A and V.

corresponding temperatures $T_{max}(a)$. The lower values of $\langle n_a \rangle$ (shown as stars) are all at the same temperature, namely at T_c which, for example, is 6.32 MeV for A=174 and is 6.54 MeV for A=240. This is how τ would be estimated from experiments [48]. The crucial testing of the scaling law is shown in Fig. (5.3). where we plot $\langle n_a \rangle a^\tau$ *vs.* $a^\sigma(T - T_c)$. For the range of a chosen (10 to 40) the results nearly fall on the same graph. Since one does not know *a priori* how much error is due to finite particle number of the disintegrating system, one might be tempted to to conclude that the fit to Eq. (5.2) is adequate. The parameters τ, σ from best fits are 2.72, 1.06 respectively for A=174 and 2.78, 1.23 respectively for A=240. The deduced T_c are 6.32 MeV and 6.54 MeV which are very different from the critical temperature of 18 MeV for the model but compare remarkably well with the temperatures where the specific heats peak and which correspond to first order phase transition temperatures

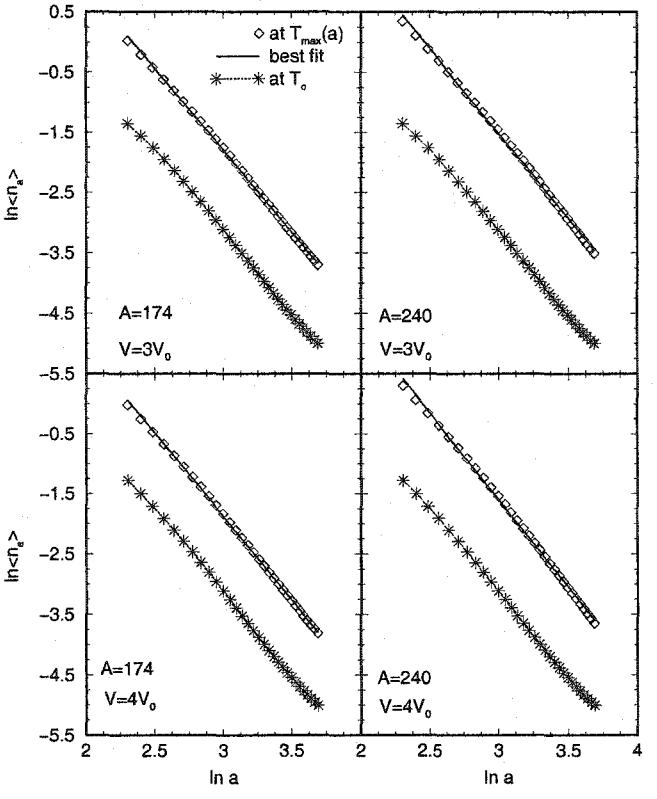

Figure 5.2: $ln\langle n_a\rangle$ vs. lna. The solid line is the best fit to $ln\langle n_a\rangle$ at each $T_{max}(a)$ presented by diamonds. The dotted line joining stars represents the distribution at T_c.The different panels are for different choices of A and V.

at the given densities.

Here we want to comment that, as seen from Fig. (5.1), χ^2 has a minimum at a temperature very close to T_c. So one may conclude that the methods of determining T_c using step 1 or 3 yield almost the same result.

These then are the two salient features: (1) Numerical fits of Eq. (5.2) are surprisingly close and (2) interpreting T_c as the critical temperature is wrong although the deduced T_c does correspond to a phase transition temperature.

5.5 *Fit to a Droplet Model*

We will now try to fit the predicted yields given by the model of Sect. 5.2 (one kind of particles) with a well-known droplet model[41]. An early application of the model,

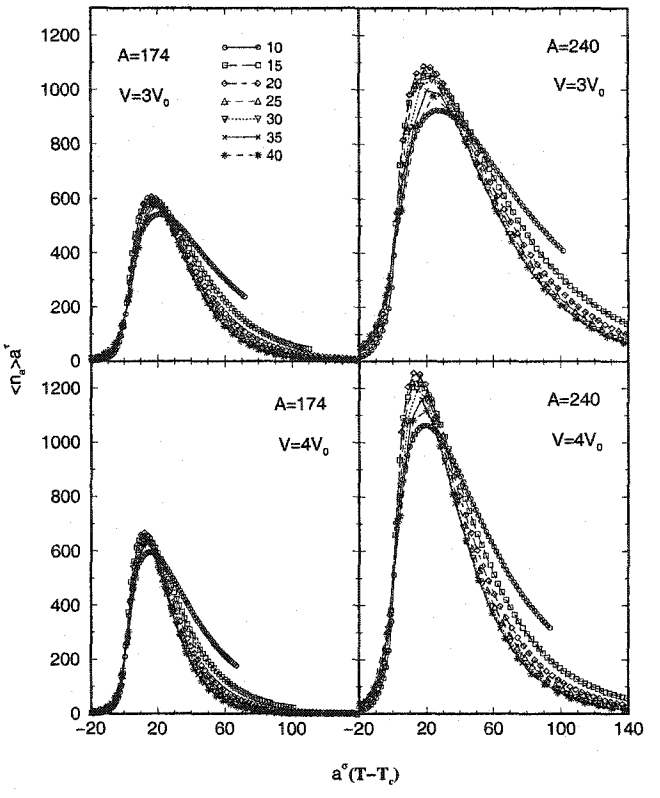

Figure 5.3: The scaling behaviour in the mass range ($10 \leq a \leq 40$)

to heavy-ion collisions, can be found in [13]. The model has been revived recently [49].

In Fisher's model, the condensation of a real gas into large drops(clusters) of liquid is modelled. This shares various similar features with multifragmentation models. For instance, the potential energy of large clusters consists entirely of a bulk term and a term associated with the loss of binding energy at the surface. There is no Fermi energy term, as the molecules inside the cluster are assumed to be Boltzmann distributed. The entropy of large clusters is, however, more complicated. As clusters become large, the dominant effect may be ascribed, once again, to a bulk term, and the remainder to a surface term. It was pointed out that liquid clusters may not be restricted to spherical shapes, as is the case in most multifragmentation models. This prohibits the use of one form of surface area to parametrize the surface contribution.

In reference [41] it is argued that, at low temperatures, the most important configurations will be compact and globular. Their surface areas $\bar{s}$ are not much greater than the minimum possible, and are assumed to admit the asymptotic condition that,

$$\begin{aligned} \bar{s}(k,\beta)/k &\to 0 \qquad \text{as} \qquad k \to \infty \qquad \text{and} \\ \bar{s}(k,\beta)/\log k &\to \infty \qquad \text{as} \qquad k \to \infty. \end{aligned} \tag{5.11}$$

Where, k is the number of molecules occupying the cluster. If, for finite clusters, one introduces this surface area to calculate various surface contributions, one must introduce a correction term which varies as $\tau \log k$. The sign and magnitude of τ is estimated from various other considerations involving other models.

One may thus, very generally, obtain the mean number of clusters of size k as

$$\langle n_k \rangle = Ck^{-\tau} \exp((\mu_g - \mu_l)k/T + c_2 k^{2/3}/T). \tag{5.12}$$

Here both μ_g and μ_l are functions of T. At coexistence and also at the critical temperature, they become equal to one another. Also c_2 is a function of temperature and at T_c the coefficient c_2 goes to zero. Since above T_c there is no distinction between the liquid and the gas phase, one can not speak of droplets. Thus the theory only applies to $T < T_c$. As such the formulation is more limited than the model of Eq. (5.2) which applies to both sides of T_c. The following fit was tried. We set $\tau = 2$. let $\alpha = (\mu_g - \mu_l)/T$, $\gamma = c_2/T$. We fit the calculated $\langle n_k \rangle$ to $Ck^{-2} \exp(\alpha k + \gamma k^{2/3})$ at different temperatures where α, γ values at each temperature are varied for best fit. The values of α, γ as a function of temperature is shown in Fig. (5.4) where we also show rather remarkable fit with the values of $\langle n_k \rangle$ obtained from the model of Sect. 5.2. The values of α and γ both go to zero near temperature $T = 6.5$ MeV suggesting that the critical temperature is 6.5 MeV.

In a sense, we have now explained the contradictory results of Ref. [16]. Not only have we devised a parametrization based on Fisher's droplet model, but also written down a very general scaling parametrization (Sect. 5.3). Both these formulae seem to offer excellent fits to the data. In both fits the parameter $T_c \simeq 6 - 6.5$ MeV. Does

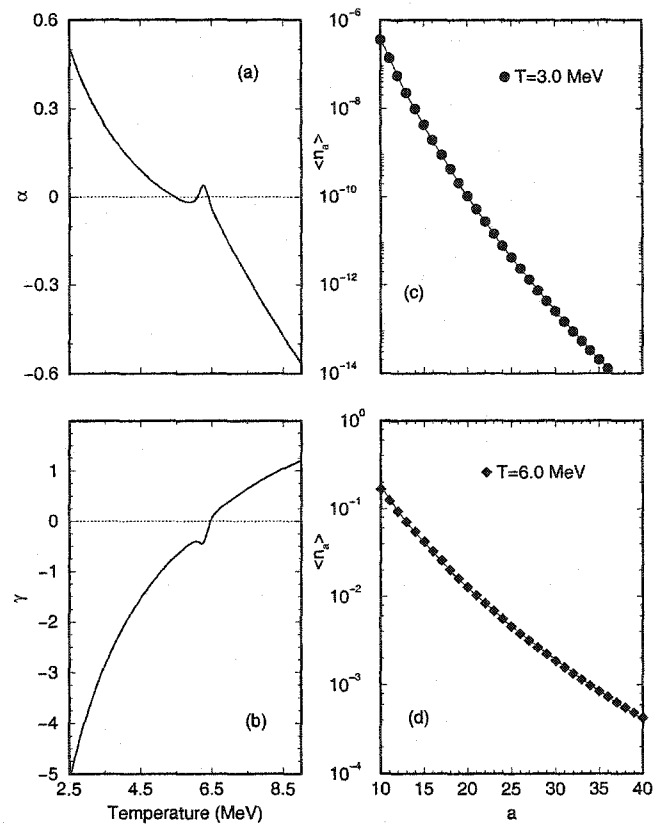

Figure 5.4: The parameters of the droplet model α and γ as a function of temperature for a system with $A = 240$ and $V = 4V_0$. The right panels show the fit of the droplet model to the yields obtained in the model of one kind of particles described in Sect. 5.2. On the graph one can not distinguish between fitted points and the actual points from canonical calculations.

this immediately imply that we are in the vicinity of a critical point? We do not think this is the case, as the yields emanate from a model undergoing a first order phase transition with a boiling temperature of $6 - 6.5$ MeV (depending on system size). The yields change dramatically at the boiling temperature (see Fig. (5.5)), this is the probable cause for this temperature dominating the value of one of the parameters of the fit. We are left to explain why the fit is so precise. The reader will note that never is the entire set of yields being fit: in all cases the range from $A = 10 - 40$ is being fit (see right panel of Fig. (5.5)). This is also the case in Ref. [16]. We claim that this is a range of yields for system of size ~ 200 where a scaling formula of the type of Eq. (5.2) or Eq. (5.12) fits the yields from a model with a first

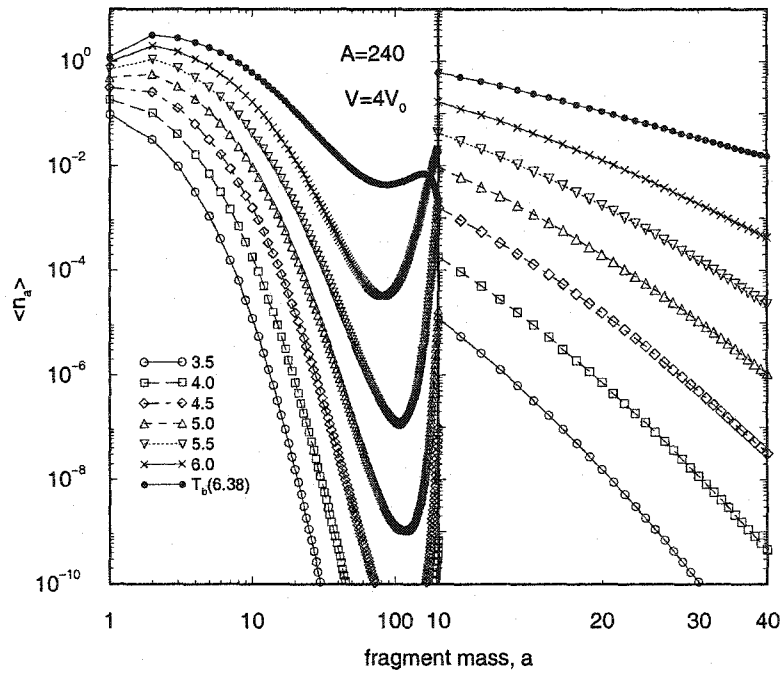

Figure 5.5: $\langle n_a \rangle$ vs. a on a logarithmic plot. The right panel expands the region $10 \leq a \leq 40$.

order phase transition. This assertion will be proved in the following section.

5.6 *Relationship between different models*

In the previous Sects. (5.2 through 5.5), we were concerned with fitting the output from the canonical model with two different parametrizations. Both of these can be regarded as having origins in critical phenomena. In this section, we attempt to obtain a better understanding as to why the droplet model fits the data points so well in the region of interest. Our method will consist of making approximations to the canonical model of Sect. 5.2 (or chapter 2). The parametrizations obtained will be motivated with ideas from standard thermodynamics, which in our view leads to a better understanding of these and other related phenomena. The essential point will be that parametrizations based on a first order phase transition and those based on a second order phase transition may coincide precisely in a small range of yields. Parametrizations based on a second order transition provide a value for a critical

temperature T_c; those based on a first order transition provide a value for a boiling temperature T_b. As is already evident, from the fits already performed in this chapter, coincidence of the two parametrizations leads to the equivalence of these two temperatures.

We begin by studying the grand canonical approximation to the RSM model as done in Sect. 5.2. As in the previous section, this will be concentrated in the region below the boiling temperature. A different parametrization of the output from the exact canonical calculation is obtained. Though this parametrization has not been as throughly investigated as that of the previous section, it will serve to provide a qualitative understanding of the behaviour of the yields below the boiling temperature.

The yields (Fig.(5.5), Fig.(5.7)) are, no doubt, obtained from the exact expressions Eq. (5.7). For the present analysis they can be adequately approximated by Eq. (5.10). The parametrization offered by Eq. (5.10) is of the form

$$\langle n_k \rangle = \tilde{C} k^{3/2} \exp(\tilde{\alpha} k + \tilde{\gamma} k^{2/3}). \tag{5.13}$$

The above is different from the parametrization of the droplet model where $\tau = 2$. Though the expressions look similar, the fit parameters $\tilde{C}, \tilde{\alpha}, \tilde{\gamma}$ will assume values different from those of C, α, γ. The interpretation of $\tilde{\alpha}$ is also quite precise in this approximation.

When using Eq.(5.10) to estimate the result of a canonical calculation, the free parameter is the chemical potential μ. It is usually determined by imposing that the model correctly reproduce the total number of particles composing the system(*i.e.*, $\sum_k \langle n_k \rangle k = A$). This is a complicated problem in general. A clue may be obtained by observing the behaviour of μ as obtained from the canonically calculated Helmholtz free energy $F = -T \log Q_A$. A plot of μ obtained thus, is plotted in Fig. (8.3) (data points).

The behaviour of this μ may be estimated by the following simple argument. Far below the boiling temperature the system exists mostly as one large cluster and a

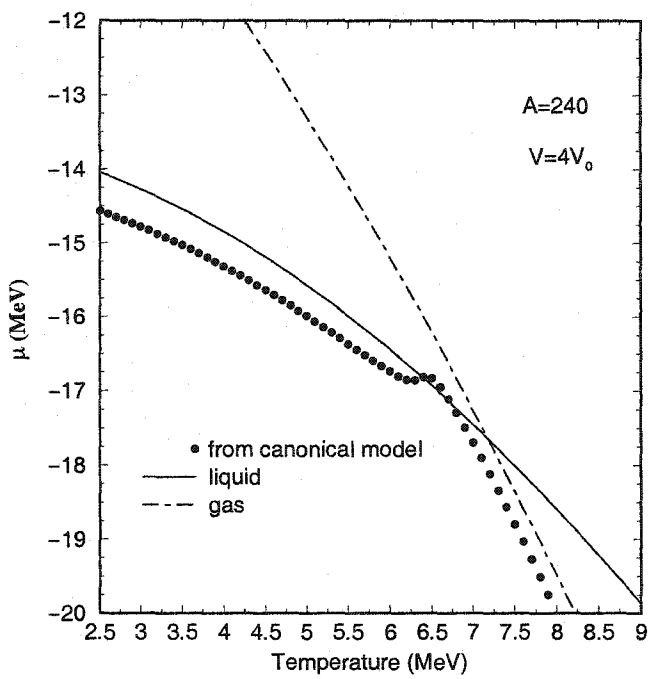

Figure 5.6: μ vs. T for a system with $A = 240$ and $V = 4V_0$. Data points represent results from a canonical calculation (see Sect. 5.2). Solid line represents μ for addition to the largest cluster, dot-dashed line is μ for addition to a small cluster (see Sect. 5.6 for details).

few small ones (see Fig. (5.5)). The large cluster is considered as the liquid state. Far above the boiling temperature the system exists mostly as many small clusters: this is considered as the gas phase. The chemical potential of either system may be estimated by keeping the system in contact with a heat reservoir, adding one particle to the system, and noting the change in free energy, *i.e.*, $\mu = \left[\Delta F\right]_{V,T} = F(T, V, A+1) - F(T, V, A)$. On entering the system, the new particle, may *a priori* attach itself to any of the existing clusters, or simply thermalize as a monomer in the system. It will attach itself to the cluster that minimises the free energy at that temperature and density. There may be more than one unique choice. The resulting change in energy and entropy of the system may be decomposed as the sum of two parts: a kinetic part$(\Delta E_{kin}, \Delta S_{kin})$, to do with the cluster's motion in the environment; and an internal part$(\Delta E_{in}, \Delta S_{in})$, to do with the internal motion of the particles constituting the cluster. If the volume is large, one may assume that the

clusters form an almost ideal gas. In this case the average kinetic energy of a cluster of size k is $(3/2)T$. It does not depend on k and thus $\Delta E_{kin} = 0$. The change in internal energy ΔE_{in} may be estimated simply as,

$$\Delta E_{in} = -W + \frac{T^2}{\epsilon_0} + \sigma(T)\left[(k+1)^{2/3} - k^{2/3}\right]. \tag{5.14}$$

The change in internal entropy is given simply as $\Delta S_{in} = 2T/\epsilon_0$. The kinetic entropy of an ideal gas of n_k clusters is given as (see Ref. [50]),

$$S_{kin} = n_k\left[\frac{3}{2}\log T + \log V + \frac{3}{2}\log\frac{2\pi m}{h^2} + \frac{3}{2}\log k + \frac{3}{2}\right] - \log n_k!. \tag{5.15}$$

In most cases in nuclear fragmentation, n_k lies between 0 and 1 (see Fig. (5.5)). Thus we may ignore the $n_k!$ term. Thus we get the total change in entropy for the addition of one particle to a cluster of size k as,

$$\Delta S = 2T/\epsilon_0 + \frac{3}{2}\log\left(1 + 1/k\right). \tag{5.16}$$

As a result, the total change in free energy and hence μ, is given as

$$\mu = \Delta F = -W - \frac{T^2}{\epsilon_0} + \sigma(T)\left[(k+1)^{2/3} - k^{2/3}\right] - \frac{3}{2}T\log\left(1 + 1/k\right). \tag{5.17}$$

We note that μ becomes progressively more negative with rising k. Thus the added particle prefers to attach to large clusters. In a fragmenting system under the boiling temperature, such a large fragment exists, of about half the size of the system (see chapter 2 or Ref. [28]). The new particle thus preferentially attaches to this cluster. To illustrate this point more quantitatively, we calculate this μ for a system with $A = 240$ and a $V = 4V_0$. We assume the largest cluster is of size $A/2$. No doubt, this size falls gradually with rising temperature [28], with the fall becoming rapid near the boiling temperature. In Fig. (8.3) we plot the value of this μ (solid line) assuming

that the largest cluster remains of the same size throughout the temperature range. Above the boiling point the system exists mostly as small clusters, here we assume that the added particle attaches itself to a cluster of size $k = 2$. This μ is plotted as the dot-dashed line in Fig. (8.3).

We are interested in obtaining an approximate expression for $\langle n_k \rangle$ underneath the boiling temperature. Using the expression for μ as derived in Eq. (5.17), we obtain the expression for $\langle n_k \rangle$ as

$$\langle n_k \rangle = e^{\beta\mu k}\omega_k = V(\frac{2\pi mT}{h^2})^{3/2}k^{3/2} \times \exp\Big[\Big\{\sigma(T)\Big((k_{max}+1)^{2/3} - k_{max}^{2/3}\Big) - \frac{3}{2}T\log(1+1/k_{max})\Big\}k/T - \sigma(T)k^{2/3}/T\Big]. \tag{5.18}$$

For most systems, in general, the behaviour of k_{max} with T and V is difficult to estimate. However, we note that the above equation is precisely of the form of Eq. (5.13). On fitting the data points obtained from Eq. (5.7) we obtain the fit parameters as $\tilde{C} = 2.73, \tilde{\alpha} = 0.36, \tilde{\gamma} = -3.11$ (note that, as in the droplet model, only range of k between 10 to 40, is fitted). A plot of the fit to the values of n_k obtained from a system with $A = 240$, $T = 5$MeV and $V = 4V_0$ is shown in Fig. (5.7). Here the entire region from $k = 2$ to 240 is plotted. Note that both fits coincide extremely well in the region of $k = 10$ to 40. This proves our assertion at the end of the last section: parametrizations based on a first order transition and those on a second order transitions can be made to coincide in a limited region of yields.

5.7 *Summary and discussions*

This investigation started out with the attempt to understand the discrepancy introduced by the experimental fits of Ref. [16]. These fits by a scaling formula, seemed to indicate that the system was in the vicinity of a second order phase transition. This was in contradiction to the findings in this thesis, where we had fitted the data with a model with an explicit first order phase transition.

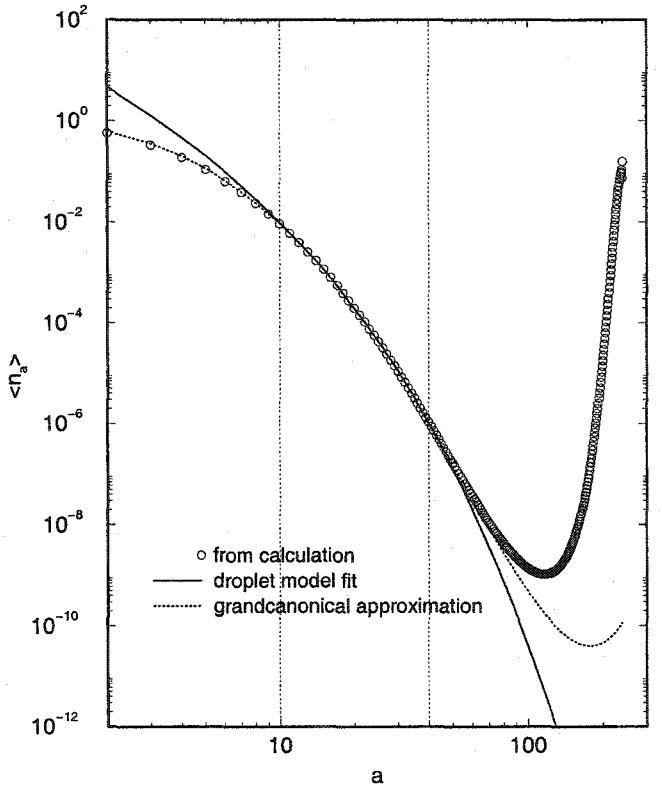

Figure 5.7: Fits to $\langle n_a \rangle$ vs. a from two different models: open circles are from an exact canonical calculation; the solid line represents the fit by a droplet model; the dotted line represents the fit from the grand canonical approximation

To resolve this strife we posed the the following question: suppose "experimental data" are given by the predictions of a theoretical model which, we know, does not conform to Eq. (5.2) exactly. Could we still describe the "data" approximately with the formula? If the answer is positive then the significances of the parameters τ, σ and T_c is to be determined. We began by trying to fit the primary populations of the RSM model with Eq. (5.2) and obtained a very good fit if we restricted our attention only to the yields lying between 10 and 40. The parameter T_c assumed a value very close to the boiling temperature of the system. Subsequently we tried a fit with the droplet model and again found a very adequate fit with $T_c \simeq 6 - 6.5$ MeV *i.e.*, close to the boiling temperature.

Thus, we find that the scaling law is still approximately obeyed, if we restrict

ourselves to a limited set of yields. While we can not attach much significance to the extracted values of τ or σ (they are different from those given by the percolation or Ising model, but not terribly so), T_c seems to be a genuinely physical parameter, namely, it reflects the first order phase transition temperature. We then devised yet another parametrization, this time based on an explicit first order phase transition. Once again we obtained a very good fit with the yields from the RSM model. The two fits coincided almost exactly in the region of yields between 10 and 40. We have not been able to find a physical explanation for such a coincidence. As we are merely dealing with two different fitting formulae no physical reason may exist. This may solely be a mathematical statement regarding the fitting equations ((5.2), (5.12 and (5.13))).

We believe that the story does not end here, many different fits can be obtained because by necessity the mass number of the composites is limited on the lower as well as on the higher side. We have no control over that since the dissociating systems are extremely finite. This apparently makes even deciding on the order of phase transition very difficult. If two different models (with different orders of phase transition) explain the data, the model with a first order transition is by definition the more general case, as a first order transition will eventually in some domain converge to a second order point. If one depends on theories to decide on what order of phase transition to expect, one is driven towards expecting a first order phase transition [51]. To date, all the models which used a Hamiltonian [47, 52, 26, 28, 33] suggest a first order phase transition [10]. No model based on a second order phase transition explains the data with the accuracy demonstrated in chapter 4. We thus state, once again, that the RSM model provides a very good explanation of the phenomenon of multifragmentation in intermediate energy heavy-ion collisions.

6

The Quark Gluon Plasma and its Dilepton Spectrum

6.1 Introduction

In this chapter we turn to the second theme of this thesis *i.e.*, the production of electromagnetically interacting particles *i.e.*, real photons and lepton pairs (e^+e^-, $\mu^+\mu^-$), in heavy-ion collisions. As the title suggests, we will not discuss photon production, choosing to concentrate only on dilepton production. This is mainly due to the larger parameter space of the dilepton spectra as compared to the photon spectra (dileptons are qualified by both the energy and momenta of the virtual photon, whereas for real photons, these are identical). One may also point towards the larger and more accurate data available to dileptons as compared to real photons. In this part of the thesis, we will shift focus from intermediate to very high energy. The energies will be high enough that a quark-gluon-plasma may be formed in the central region. The existence of such a state has long been speculated [54]. Various experimental signatures have been put forward to detect its fleeting existence in such collisions: *e.g.*, J/ψ suppression [55], strangeness enhancement [56], and of course, the electromagnetic spectra of photons and dileptons [57]. In the rest of this thesis, we will invoke various refinements to the calculation of dilepton spectra.

At lower energies, we presented a picture of heavy-ion collisions which involved compression and expansion of the central region leading to an explosive fragmentation of the entire system. There, the nucleons constituted the sole degrees of freedom, and particle number was strictly conserved. This, along with a small enough number of

participants, led us to cast the system in the canonical ensemble. At very high energies the physical picture is rather different. At such high energies, the degrees of freedom, that are invoked are those of the individual nucleons, along with various mesons and baryons; and, depending on the collision, may also be the quarks and gluons that make up the nucleons. Also, such collisions may lead to energy densities high enough that the partons (quarks and gluons) which had hitherto been bound inside nucleons may become de-confined over a much larger region $\sim$ 10 fm. This state is called the Quark Gluon Plasma (QGP) or simply the partonic plasma.

If the energy in the central region is not that high, or the system has cooled and expanded from the partonic stage, one would still find a large number of mesons and baryons prevalent in the system, forming a hot hadronic plasma. Eventually, interactions will freeze out and these particles will stream out and may undergo secondary decay. The large number of particles is mainly due to the fact that the energy densities are high enough to allow for new particles to be produced, which were not brought in by the colliding nuclei. The large number of particles, along with the lack of conservation of particle number, allow us to use the grand canonical ensemble in these calculations. As mentioned in the introduction, the numbers of many of these particles may be obtained from thermal models based on such ensembles [58]. In passing, we also point out that deviations form the predictions of such models have been observed [59, 60].

Our focus, in the following chapters will not be on these thermal models and their predictions for hadronic observables. We will henceforth concentrate on the spectra of particles that interact very weakly with the rest of partonic or hadronic plasma. The main candidates in this category are the particles produced by electomagnetic interaction between the hadrons in the system. These are the photons and lepton pairs produced and emitted by the system. As photons and dileptons are produced by electromagnetic interaction, they are produced far less copiously than hadrons and partons. Also, the small coupling constant leads to mean free paths much larger than the system size; as a result, once produced they suffer almost no further rescattering

and emerge almost unchanged from the hot interiors of the system. As will be pointed out subsequently, this turns out to be a great advantage, as these turn out to be good probes of local densities and temperatures. This property is being rigorously exploited in heavy-ion collisions.

It may be possible, in heavy-ion collisions to produce sufficient energy densities in the central region, so that the quarks and gluons may become deconfined. Since its inception, the main drive in ultra-relativistic heavy-ion collisions has been the production of this exotic state of matter. This form of matter last prevailed in the early universe a few microseconds after the big bang. If formed in a collision, the partonic plasma will exist for a very short time($\simeq 10 - 15$ fm/c): as the plasma expands and cools, it will undoubtedly undergo a change from a partonic to a hadronic plasma of mesons and baryons [61]. Thus the possible formation of this plasma has to be inferred from the spectrum of particles arriving at the detectors. Photons and dileptons naturally become privileged probes of such an investigation as they suffer minimal rescattering. They, thus convey information from the very interiors, and earliest stages of the hot plasma created in these collisions. They are, however, emitted throughout the entire history of the collision. Hence, they will contain information, not merely of the partonic state, but also of the hadronic plasma formed after the partonic plasma has cooled and undergone a phase transition. The spectrum of dileptons and photons may thus serve as an important signal for the formation of a quark gluon plasma. A careful study would reveal information regarding the temperatures, charge and baryon densities, equation of state and the evolution of such facets with time in a QGP. The main background is the spectrum of dileptons and photons emitted by the later formed hadronic plasma and by the spectrum of dileptons emitted by primordial Drell-Yan processes. The spectra from the three sectors may be disentangled from each other only by a careful study of each of these processes. In the following pages, we undertake such a study on the dilepton spectrum emanating from the partonic sector.

6.2 An order-by-order approach.

In our preceding study involving intermediate energy heavy-ion collisions, we assumed that the constituents in the participant region had thermalized and this allowed us to investigate the system using statistical mechanics in the canonical ensemble. The inputs were nuclei, treated as non-relativistic objects with finite size and an internal quantum mechanical excitation spectrum. In this case, we shall again assume that the system is at least in thermal equilibrium and has achieved this condition early on in the history of the collision. The large number of constituents involved will allow us to use the grand canonical ensemble. The degrees of freedom will, however, not be classical particles. The quarks, gluons, photons, leptons, and even the composite hadrons will be treated appropriately as particle excitations of the respective relativistic quantum fields. Our calculations will thus involve the full machinery of quantum field theory at finite temperature (in particular that of thermal QCD). There are various formalisms of this theory used by practitioners in this field; we will describe our formalism in the next section. In this section we will attempt to accurately formulate the problem to be explored.

6.2.1 A Space-time picture.

Let us sketch the history of a high energy heavy-ion collision (see Fig. (6.1)). At these ultrarelativistic energies ($\simeq$ 200 AGeV in c. m. frame), the incoming nuclei have been Lorentz-contracted to almost pancake like structures. The largest fraction of the baryon charge is being carried by the valence quarks. These also constitute the large momentum excitations in the incoming nuclei. The sea quarks and the gluons, which don't carry any net baryon number, have large populations in the low momentum sector. Asymptotic freedom in strong interactions [62, 63] dictates that the strong coupling constant will decrease for interactions involving large momentum transfer. This implies that, to a first approximation, processes involving a large momentum transfer are essentially forbidden and those involving a small momentum transfer are pervasive. On impact, the valence quarks suffer only small angle scattering; as

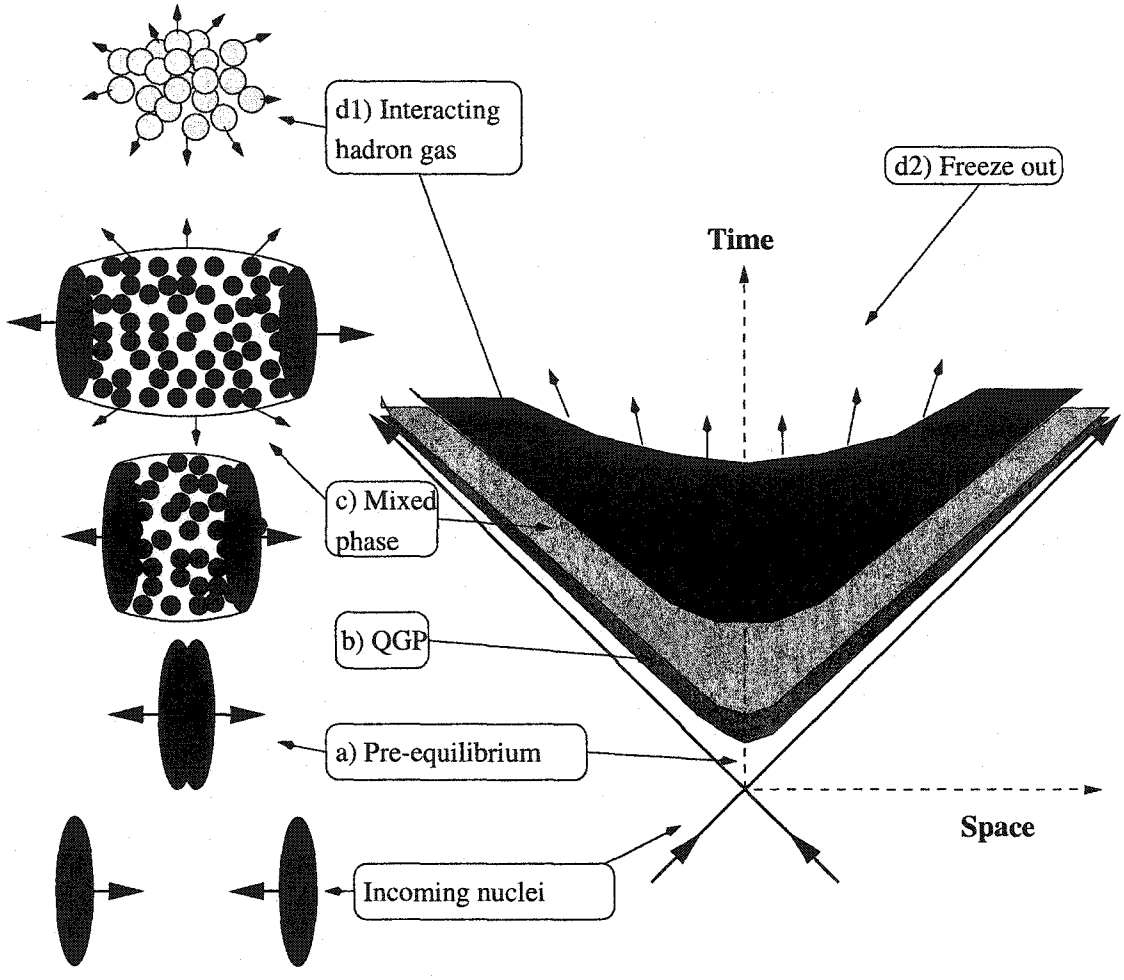

Figure 6.1: Space time picture of a high energy heavy-ion collision

large angle scattering would involve a large momentum transfer. The baryon charge carrying valence quarks and the sea partons with very high momentum hence pass through the central region with little or no deflection. The soft sea quarks and gluons can however undergo large angle scattering with small or medium momentum transfer. These are thus stopped and will constitute the components of the hot central interaction region.

These will then scatter multiple times with each other; and after a brief period of non-equilibrium, produce a hot plasma in thermal equilibrium. As this happens, the central region will continually keep expanding and cooling and finally begin to undergo a phase transition. There will most probably be a period in which the plasma is in a mixed phase of partonic and hadronic components. This state will

eventually undergo full conversion to an interacting hadron gas. This will continue to expand and cool. Finally the plasma will have expanded to a density where interactions between the various hadrons will cease and we achieve what is termed 'freeze out'. The hadrons will now continue to stream freely towards the detectors while undergoing possible secondary decay into more stable hadrons. The space time picture of the above scenario is represented in Fig.(6.1).

Dileptons will be emitted from all time sectors of the above scenario. At the earliest point of contact there will be lepton pairs produced via the Drell-Yan process between a quark in one nucleus and an antiquark in the other. There will presumably be dileptons emitted from the pre-equilibrium region, through a mixture of jet and plasma interactions. These will precede the dileptons emanating from the partonic plasma, the mixed phase and the hadron gas phase; dileptons from these three sources are referred to as thermal dileptons.

We will assume that after a small time τ_0 the plasma has attained, local thermal equilibrium, *i.e.*, it is possible to fragment the plasma into space time cells of arbitrarily small size; each of which may be ascribed a temperature. In the event that chemical equilibrium is established, a chemical potential may also be ascribed. At this point, dilepton emission from Drell-Yan or jet plasma interaction has more or less ceased to occur and thermal dilepton production begins to dominate. Under this assumption, the total number of dileptons per unit invariant mass M may be summed up by the formula [64],

$$\frac{dN_{e^+e^-}}{dM} = \int_{\tau_0}^{t_f} dt \int_{x_-(t)}^{x_+(t)} \int_{z_-(t)}^{z_+(t)} \int_{y_-(t)}^{y_+(t)} d^3x \int d^3q \frac{M}{q^0} \frac{d^4R_{e^+e^-}}{d^4q}(q^0, \vec{q}, T(t,\vec{x}), \mu(t,\vec{x}). \tag{6.1}$$

where, $\frac{d^4R_{e^+e^-}}{d^4q}$ is the number of lepton pairs produced per unit space time, per unit four momentum, from the unit cell at $(\vec{x}, t)$ in a plasma in local equilibrium. Ostensibly, this depends on the four momentum of the virtual photon $(q^0, \vec{q})$, the temperature (T), and the relevant chemical potential (μ). The temperature and

relevant chemical potential are, in general, local properties for an expanding plasma and vary from point to point in the plasma as indicated. Finally, the rates from each space time cell have to be integrated over the entire space time evolution of the plasma; where, the spatial limits of the expanding plasma are represented by the variables $x_-(t), x_+(t)$, $y_-(t), y_+(t)$, $z_-(t), z_+(t)$.

6.2.2 *The dilepton production rate.*

To theoretically obtain the rate of Eq. (6.1), one assumes that one can represent the space-time evolution of the plasma size, temperatures, and chemical potentials by means of some dynamical model. Various such models exist: hydrodynamical model [65], fireball model [64], parton cascade [66], UrQMD [1] model [67]. Each has its own set of assumptions and calculational techniques. Each provides a set of space-time and momentum distribution functions for the components of the plasma. The one used most often is the hydrodynamical model, or its simpler manifestation the thermal fireball model. In these models, the plasma is respectively in local or global thermal equilibrium; *i.e.*, the constituents of the plasma have thermal momentum distribution functions. Each of these also has an inbuilt assumption for the time during which the plasma is in the partonic phase, the mixed phase, or the hadron gas phase. The source of dileptons at a given space-time point will vary depending on the current phase in which the plasma finds itself at that space-time point.

Without venturing into the applicability of the above models, we instead focus our attention on the actual inputs to this calculation *i.e.*, the actual processes used to calculate the rates in each of the three phases of the plasma. In the remaining thesis we will not return to the question of which space-time model to use, or is applicable in a given situation. We will ignore this question for the most part; choosing instead to focus attention on the calculation of the differential dilepton production rate $\frac{d^4R_{e^+e^-}}{d^4q}$. Much work has gone into devising more accurate and detailed space-time models of the plasma, not as much has been done in exploring what set of processes of dilepton

[1] Ultra-relativistic Quantum Molecular Dynamics

production are to be used in computing the rates. In the remaining chapters, we shall explore precisely this question in the partonic sector.

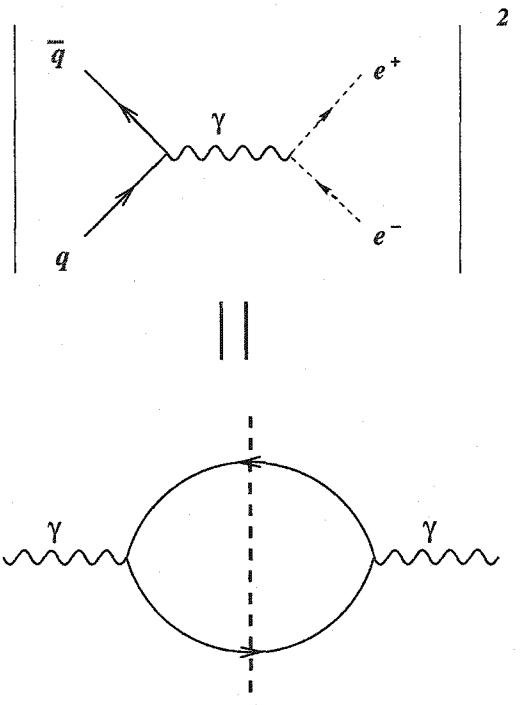

Figure 6.2: The Born term in dilepton production

In various calculations of the total dilepton signal [64, 65, 68], the process used as input for the partonic sector has always been the leading order (LO) term *i.e.*, the Born term (see upper diagram of Fig.(6.2)). This represents a thermal quark annihilating with an antiquark producing a time-like virtual photon which will eventually materialize as a lepton pair. The justification for this is the assumption that the formation of a quark gluon plasma would imply that the strong coupling constant must be small enough to subdue the contributions from higher order diagrams compared to the leading order term. There is some recent theoretical evidence for such an assumption [69]. It is this assumption which will be subjected to closer scrutiny in the following chapters. We will explore a variety of medium dependent effects which may lead to higher order terms being comparable to, or even dominant over the Born

term in certain regions of parameter space.

To aid our study, we divide up the parameter space of dilepton production into three regions. The low energy region: where the energy of the lepton pair is much smaller than the plasma temperature $E << T$. The intermediate energy region where energy is of the order of temperature $E \sim T$. The high energy region, where the energy of the dilepton pair is much higher than the temperature $E >> T$. The remaining chapters are organised as follows: in chapter 7 we concentrate on dileptons with low four momentum, *i.e.*, the soft sector: we point out how high temperature effects may lead to higher order terms being more dominant over the Born term. In chapter 8 we focus on intermediate energies, here we demonstrate how a net charge may lead to various symmetries being broken by the medium. This leads to the onset of entirely new processes which may become comparable to the Born term at low mass. Finally in chapter 9, we turn to high energy and high invariant mass dileptons. In this region the effects discussed in the preceding chapters become negligible. At such high energies, the quarks masses become negligibly small compared to the other scales in the problem, and this may lead to the onset of collinear and infrared divergences. We demonstrate explicitly that at next to leading order all infrared and collinear singularities cancel (at high mass) and the Born term is by far the leading thermal contribution.

6.3 *Methodology and formalism*

Before concluding this chapter, we discuss our methodology and point out the salient features of our notation. We intend to calculate the differential production rate of dilepton pairs *i.e.*, the quantity $\frac{d^4R_{e^+e^-}}{d^4q}$ in Eq. (6.1). Here we present a simple derivation of the basic formula that will be used repeatedly in the remaining thesis. This formula will connect the rate to the various many-body processes which lead to heavy virtual photon production. Most of this section is based on Refs. [70, 71].

6.3.1 *Dilepton rate → spectral density.*

Under the assumption of local thermal equilibrium, we focus our attention on a given space-time cell in the plasma of four volume Ω. Imagine that we have lepton pairs (of momenta p_1, p_2) being emitted from this four volume when it is in a given state $|i\rangle$, leading to the state $|e^+e^-f\rangle$. After emission they are free to leave the source. The inclusive differential probability for the emission of lepton pairs into dimensionless cells of phase space is

$$\sum_f \left|\langle e^+e^-f|\mathcal{M}|i\rangle\right|^2 \frac{d^3p_1}{(2\pi)^3 2E_1}\frac{d^3p_2}{(2\pi)^3 2E_2}. \tag{6.2}$$

As always, $\hbar$ is set to 1. Integrating over the total phase space, will give us the number of dileptons emitted from this initial state. As the plasma cell is thermalized, we average over all possible initial states with a thermal weight to get the number of dileptons emitted into a differential volume in momentum space as

$$N = \sum_i \frac{e^{-\beta E_i}}{Z} \sum_f \left|\langle e^+e^-f|\mathcal{M}|i\rangle\right|^2 \frac{d^3p_1}{(2\pi)^3 2E_1}\frac{d^3p_2}{(2\pi)^3 2E_2}. \tag{6.3}$$

Where, Z is the grand canonical partition function, and β is the inverse temperature. We do not explicitly mention a chemical potential μ, the tacit assumption being that it be included in the presence of a finite baryon density.

It should also be pointed out that $|i\rangle$ and $|f\rangle$ are, in general, eigenstates of the full interaction Hamiltonian (strong and electromagnetic). The matrix operator $\mathcal{M}$ is merely that part of the interacting electromagnetic Hamiltonian which connects the photon to the lepton current. This allows for the transformation from the state $|i\rangle$ to the state $|fe^+e^-\rangle$. As will be imposed, later in this derivation, any photons created by the electromagnetic interaction will escape the plasma. This is achieved by always treating the electromagnetic interaction to first order in the coupling (*i.e.*, only one power of α_{EM} in the amplitude), and exploring the effect of the strong interaction 'order by order'. Thus, we are essentially focusing on the production of a pair of leptons from a single photon emanating from a solitary electromagnetic interaction

between the strongly interacting constituents of $|i\rangle$. This is justified as the time scale and mean free paths calculated on the basis of pure e.m. interaction do not warrant multiple scattering in a QGP.

We may thus write down the matrix element of the operator $\mathcal{M}$ for the production of two leptons of four momenta $\mathbf{p_1} = (E_1, \vec{p}_1)$ and $\mathbf{p_2} = (E_2, \vec{p}_2)$ from a single heavy photon of four momentum $\mathbf{p} = (E, \vec{p})$ as

$$\langle e^+e^- f|\mathcal{M}|i\rangle = e\bar{u}_1\gamma_\mu v_2 \int d^4x e^{i(\mathbf{p_1}+\mathbf{p_2})\cdot\mathbf{x}}\langle f|A^\mu(x)|i\rangle, \tag{6.4}$$

where $A^\mu(x)$ is the field in the Heisenberg picture. Substituting Eq. (6.4) into Eq. (6.3) gives the total number of dileptons as

$$N = e^2 L_{\mu\nu}M^{\mu\nu}\frac{d^3p_1}{(2\pi)^3E_1}\frac{d^3p_2}{(2\pi)^3E_2}. \tag{6.5}$$

where the lepton tensor has been averaged over all spins to yield

$$L_{\mu\nu} = \frac{1}{4}\sum_{spins}\bar{u_1}\gamma_\mu v_2\bar{v_2}\gamma_\nu u_1 = \mathbf{p_1}_\mu\mathbf{p_2}_\nu + \mathbf{p_2}_\mu\mathbf{p_1}_\nu - (\mathbf{p_1}\cdot\mathbf{p_2} + m^2)g_{\mu\nu}. \tag{6.6}$$

while, the photon tensor is

$$M^{\mu\nu} = \sum_f\sum_i\int d^4x d^4y e^{i(\mathbf{p_1}+\mathbf{p_2})\cdot(\mathbf{x}-\mathbf{y})}\langle f|A^\mu(x)|i\rangle \times \langle i|A^\nu(y)|f\rangle\frac{e^{-\beta E_i}}{Z}. \tag{6.7}$$

Replacing $E_i \to E_f + E$, we may perform the sum over the initial states $|i\rangle$ by completeness. We assume that the entire process is translationally invariant inside the space-time cell of the plasma; thus the matrix element only depends on the difference of the two space time points $\mathbf{x}, \mathbf{y}$. We thus invoke the standard variable transformation: $x' = x - y$ and $x'' = (x + y)/2$. We then integrate over x'' to obtain the four volume Ω of the space-time cell. Then we replace $x' \to x$ to obtain

$$M^{\mu\nu} = \Omega\int d^4x e^{i(\mathbf{p_1}+\mathbf{p_2})\cdot\mathbf{x}}e^{-\beta E}\sum_f\langle f|A^\mu(x)A^\nu(0)|f\rangle\frac{e^{-\beta E_f}}{Z}. \tag{6.8}$$

In quantum statistical mechanics the quantity $\int d^4x e^{i\mathbf{p}\cdot\mathbf{x}} \sum_f \langle f|A^\mu(x)A^\nu(0)|f\rangle \frac{e^{-\beta E_f}}{Z}$ is referred to as $D^{>\mu\nu}(p^0,\vec{p})$ (see Refs. [72, 73]). This quantity may be expressed in terms of the photon spectral density $\rho^{\mu\nu}$ as

$$D^{>\mu\nu}(p^0,\vec{p}) = (1+n(p^0))\rho^{\mu\nu}(p^0,\vec{p}), \tag{6.9}$$

where $n(p^0) = 1/(e^{\beta p^0}-1)$ is the photon distribution function. This relation will be justified in the following paragraph. Thus, we get the photon tensor as

$$\begin{aligned} M^{\mu\nu} &= \Omega \int d^4x e^{i(\mathbf{p_1}+\mathbf{p_2})\cdot\mathbf{x}} e^{-\beta E} \int \frac{d^4p}{(2\pi)^4} e^{-i\mathbf{p}\mathbf{x}} (1+n(p^0))\rho(p^0,\vec{p}) \\ &= \Omega \int d^4p \delta^4(\mathbf{p_1}+\mathbf{p_2}-\mathbf{p}) e^{-\beta E}(1+n(p^0))\rho^{\mu\nu}(p^0,\vec{p}) \end{aligned} \tag{6.10}$$

We now have an expression for the dilepton production rate in terms of the spectral density. The last part of this derivation will attempt to relate the spectral density in terms of the imaginary part of the retarded photon self-energy.

6.3.2 *Spectral density → imaginary part of self-energy*

To begin, we review some of the propagators in quantum statistical mechanics (we already used one of them in the preceding subsection),

$$D^{>\mu\nu}(p^0,\vec{p}) = \int d^4x e^{i\mathbf{p}\mathbf{x}} \sum_f \langle f|A^\mu(x)A^\nu(0)|f\rangle \frac{e^{-\beta E_f}}{Z}, \tag{6.11}$$

$$D^{<\mu\nu}(p^0,\vec{p}) = \int d^4x e^{i\mathbf{p}\mathbf{x}} \sum_f \langle f|A^\mu(0)A^\nu(x)|f\rangle \frac{e^{-\beta E_f}}{Z}, \tag{6.12}$$

$$D^{ret\mu\nu}(p^0,\vec{p}) = \int d^4x e^{i\mathbf{p}\mathbf{x}} \theta(x^0) \sum_f \langle f|[A^\mu(x),A^\nu(0)]|f\rangle \frac{e^{-\beta E_f}}{Z}. \tag{6.13}$$

The last propagator is the retarded photon propagator. The two propagators $D^{>\mu\nu}$, $D^{<\mu\nu}$, admit an algebraic relation between them due to the KMS condition(see Refs. [72, 73]), i.e.,

$$D^{<\mu\nu}(p^0,\vec{p}) = e^{-\beta p^0} D^{>\mu\nu}(p^0,\vec{p}). \tag{6.14}$$

The spectral density may be defined using these two propagators as $\rho = D^{>\mu\nu} - D^{<\mu\nu}$. Using this definition and the above relation we can easily verify Eq. (6.9). Drawing from the expression of the theta function in the usual complex representation, *i.e.*,

$$\theta(x^0) = \lim_{\epsilon\to 0} i \int_{-\infty}^{\infty} \frac{d\omega}{(2\pi)} \frac{e^{-i\omega x^0}}{\omega + i\epsilon},$$

we may express the retarded propagator in Eq. (6.13) in terms of the spectral density as

$$D^{ret\mu\nu}(p^0,\vec{p}) = \lim_{\epsilon\to 0} i \int_{-\infty}^{\infty} \frac{d\omega}{2\pi} \frac{\rho^{\mu\nu}(\omega,\vec{p})}{p^0 - \omega + i\epsilon} \tag{6.15}$$

Noting that the spectral density is always real, we separate the real and imaginary parts of the denominator in terms of the principal value and the imaginary part, hence obtaining

$$\rho^{\mu\nu}(p^0,\vec{p}) = \mathrm{Disc}\left[D^{ret\mu\nu}(p^0,\vec{p})\right]. \tag{6.16}$$

Expanding the propagator in terms of the Schwinger-Dyson equation, we obtain the following expressions:

$$\begin{aligned} D^{\mu\nu}(p^0,\vec{p}) &= D_0^{\mu\nu}(p^0,\vec{p}) + D_0^{\mu\alpha}(p^0,\vec{p}) i\Pi_{\alpha\beta}(p^0,\vec{p}) D^{\beta\nu}(p^0,\vec{p}) \\ &= D_0^{\mu\nu}(p^0,\vec{p}) + D_0^{\mu\alpha}(p^0,\vec{p}) iP_{\alpha\beta}(p^0,\vec{p}) D_0^{\beta\nu}(p^0,\vec{p}), \end{aligned} \tag{6.17}$$

where $i\Pi^{\mu\nu}$ is the proper retarded self-energy and $iP^{\mu\nu}$ is the improper retarded self-energy (we have dropped the superscript *ret* in the expressions). At lowest order in the electromagnetic coupling constant, these two quantities are the same. If we always insist on calculating to lowest order in the electromagnetic coupling constant,

we note that, the propagators for massive photons are free propagators and have no discontinuities. Thus the only discontinuity may arise in the self-energies P or Π. This also achieves our previously stated goal of insisting that any heavy photons, created by electromagnetic interaction in the plasma, materialize as dileptons and escape. In Ref. [70] the photons were allowed to interact multiple times in the plasma preceding escape; leading to the occurrence of effective propagators. Thus, to lowest order in the electromagnetic coupling constant

$$\mathrm{Disc}[D^{\mu\nu}(p^0,\vec{p})] = D_0^{\mu\alpha}\mathrm{Disc}[iP_{\alpha\beta}(p^0,\vec{p})]D_0^{\beta\nu} = D_0^{\mu\alpha}\mathrm{Disc}[i\Pi_{\alpha\beta}(p^0,\vec{p})]D_0^{\beta\nu}.$$

Substituting the above equations back into Eq. (6.10) gives

$$M^{\mu\nu} = \Omega\int d^4p\delta^4(\mathbf{p_1}+\mathbf{p_2}-\mathbf{p})e^{-\beta E}(1+n(p^0))D_0^{\mu\alpha}\mathrm{Disc}[i\Pi_{\alpha\beta}(p^0,\vec{p})]D_0^{\beta\nu}. \quad (6.18)$$

In the above equation $p^0 = E$ is the energy of the photon; using this we may carry out the integral over $\mathbf{p}$ using the delta function. The propagators are essentially (as $\mathbf{p}$ is offshell we no longer retain the $i\epsilon$ in the denominator),

$$D_0^{\mu\nu}(\mathbf{p}) = \frac{-i\left(g^{\mu\nu}-\frac{\mathbf{p}^\mu\mathbf{p}^\nu}{\mathbf{p}^2}\right)}{\mathbf{p}^2}.$$

Utilizing the Ward identity satisfied by the self-energy (i.e., $\mathbf{p}^\mu\Pi_{\mu\nu} = 0$), we may reduce the numerators of the propagators to simply the factors of the metric. Substituting these results into Eq. (6.5) for the total number of dileptons emitted by the space time cell, we obtain

$$N = \Omega e^2 L_{\mu\nu}\frac{-\mathrm{Disc}[i\Pi^{\mu\nu}]}{(\mathbf{p}^2)^2}\frac{1}{e^{\beta E}-1}\frac{d^3p_1}{(2\pi)^3E_1}\frac{d^3p_2}{(2\pi)^3E_2}. \quad (6.19)$$

To obtain the number of lepton pairs emitted per unit four volume we divide by the four volume of the space-time cell Ω. Assuming, once more, translational invariance of the rate we may write $\frac{N}{\Omega} = \frac{d^4N}{dx^4} = dR$. Substituting the expression for the spin averaged lepton tensor (Eq. (6.6)), we obtain the differential rate of production of

lepton pairs with four-momenta lying in a small segment of momentum space around $\mathbf{p_1}$ and $\mathbf{p_2}$ as [71],

$$E_1 E_2 \frac{dR}{d^3p_1 d^3p_2} = \frac{e^2}{(2\pi)^6}\left[\mathbf{p_1}_\mu \mathbf{p_2}_\nu + \mathbf{p_2}_\mu \mathbf{p_1}_\nu - (\mathbf{p_1}\cdot\mathbf{p_2} + m^2) g_{\mu\nu}\right] \frac{-\mathrm{Disc}[i\Pi^{\mu\nu}]}{(\mathbf{p}^2)^2} \frac{1}{e^{\beta E}-1}. \tag{6.20}$$

The above is the general result and it depends on the directions of $\mathbf{p_1}$ and $\mathbf{p_2}$. We are however interested only in the total photon momentum $\mathbf{p}$. Thus we integrate over the directions with the obvious delta function, and set the mass of the leptons to zero, we obtain,

$$\int \frac{d^3p_1}{E_1}\int \frac{d^3p_2}{E_2}\delta^4(\mathbf{p_1}+\mathbf{p_2}-\mathbf{p})\left[\mathbf{p_1}_\mu \mathbf{p_2}_\nu + \mathbf{p_2}_\mu \mathbf{p_1}_\nu - (\mathbf{p_1}\cdot\mathbf{p_2}) g_{\mu\nu}\right] = \frac{2\pi}{3}(p_\mu p_\nu - \mathbf{p}^2 g_{\mu\nu}) \tag{6.21}$$

Thus the rate of dilepton production per unit four momentum of the pair is

$$\frac{dR}{d^4p} = \frac{e^2}{3(2\pi)^5}\left[\frac{p_\mu p_\nu}{\mathbf{p}^2} - g^{\mu\nu}\right] \frac{-\mathrm{Disc}[i\Pi^{\mu\nu}]}{(\mathbf{p}^2)} \frac{1}{e^{\beta E}-1} \tag{6.22}$$

6.4 Notation

In the previous section, we have related the production rate of dileptons to the imaginary part of the retarded in-medium photon self-energy. The in-medium self-energy encodes the entire gamut of strong interaction, medium effects which may lead to the production of a massive virtual photon from the plasma. This then constitutes the essential quantity of interest. In the remaining chapters, we will endeavour to calculate this quantity in a variety of many-body scenarios, to various orders in the strong coupling constant. To calculate the retarded photon self-energy in a thermal environment we use the standard method of the imaginary time formalism[73, 74]. This essentially consists of replacing the continuous energies of all particles in the self-energy Feynman diagrams by discrete imaginary frequencies called Matsubara

frequencies. The Feynman rules that characterize our calculations are however somewhat different from the standard literature (it however displays considerable similarity with the notation of Ref.[72]).

Our notation is categorized by the explicit presence of an apparent Minkowski time $x^0 = -i\tau$ and a momentum $q^0 = i(2n+1)\pi T + \mu$. Our metric is $(1,-1,-1,-1)$. For the case of zero chemical potential our bosonic propagators have the same appearance as at zero temperature, *i.e.*(for the massless case),

$$i\Delta(q) = \frac{i}{(q^0)^2 - |q|^2}. \tag{6.23}$$

The Feynman rules are also the same as at zero temperature, with the understanding that we replace the zeroth component of the momentum by Eq. (8.7) for a fermion and by an even frequency in the case of a boson. For the zero temperature Feynman rules, we utilize those of Ref. [75]. One may, in the case of zero chemical potential, relate this to the familiar case of reference [76] by noting that

$$\Delta(q) = \frac{1}{(q^0)^2 - |q|^2} = \frac{-1}{(\omega_n)^2 + |q|^2} = -\Delta_E(\omega_n, q), \tag{6.24}$$

where $\Delta_E(\omega_n, q)$ is the familiar Euclidean propagator presented in the literature ([76, 74]). One may immediately surmise the form of the non-covariant propagator $\Delta(|\vec{q}|, x^0)$, the Fourier transform of which is the covariant propagator.

$$\begin{aligned}\Delta(q, q^0) &= -\int_0^\beta d\tau e^{-i\omega_n \tau} \Delta_E(|\vec{q}|, \tau) \\ &= -i\int_0^{-i\beta} dx^0 e^{iq^0 x^0} \Delta_E(|\vec{q}|, \tau) \\ &= -i\int_0^{-i\beta} dx^0 e^{iq^0 x^0} \Delta(|\vec{q}|, x^0).\end{aligned} \tag{6.25}$$

In the presence of a finite chemical potential our full fermionic propagators become

$$S(q, q^0) = (\gamma^\mu q_\mu)(-i)\int_0^{-i\beta} dx^0 e^{i(q^0-\mu)x^0} \Delta_\mu(|\vec{q}|, x^0), \tag{6.26}$$

where,

$$\Delta_\mu(|\vec{q}|, x^0) = \frac{1}{2E_q} \sum_s f_s(E_q - s\mu) e^{-isx^0(E_q - s\mu)}. \tag{6.27}$$

In the above two equations $q^0 = i(2n+1)\pi T + \mu$. In each self-energy calculation all frequencies except that of the photon are summed. Finally the discrete imaginary 'energy' of the photon is analytically continued onto the real axis and its imaginary part or discontinuity across the real axis is computed. The details of this procedure will be borne out in the subsequent chapters.

7

Low Mass Dileptons and Hard Thermal Loops

7.1 Introduction

In this chapter, we commence our exploration of higher order effects on the dilepton spectrum. We begin by focusing on the soft sector, *i.e.*, the region where the energy E and momentum p of the virtual photon are both much smaller than the temperature T of the medium. No doubt this will lead to a dilepton invariant mass $M = \sqrt{E^2 - p^2}$ also much smaller than the temperature. We would however distinguish this case from that where E and p are both large but almost equal, where once again M is very small. Hence, in this situation, the quark, anti-quark pair annihilating to form the virtual photon will also be soft compared to T. The motion of soft particles in a hot plasma is greatly modified by the effect of particles with momenta of the order of the temperature. This will lead to the soft modes achieving various dispersion relations. The influence of these dispersion relations on the production of timelike virtual photons will form the topic of discussion in this chapter. The calculations discussed as well as the results quoted or cited in this chapter, do not constitute the author's own work. This chapter has been included in the thesis merely to achieve completeness in the general topic presented. Thus no effort will be made towards discussing technical details; rather the stress will be on motivations, basic physics ideas used, and on the nature of the results. The interested reader may refer to the articles cited for further details.

In a typical quark gluon plasma produced in heavy-ion collisions, the temperature

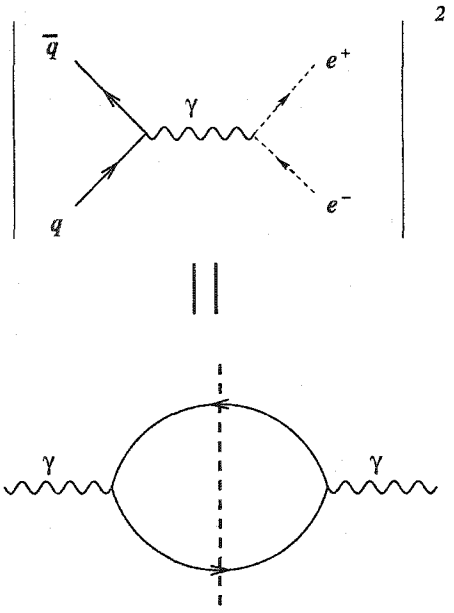

Figure 7.1: The Born term and corresponding imaginary part of the photon self-energy.

in the central region is expected to reach no more than several hundred MeV [66, 77]. The processes we are interested in have energies much smaller than T *i.e.*, imagine a very soft quark annihilating a very soft antiquark and producing a soft virtual photon as shown in Fig. (7.1). The presence of a much higher temperature is only belied by the distribution functions that control the numbers of such soft partons in the system. As we will be considering higher order corrections to this process, the calculations will involve the explicit presence of hard particles (momenta of the order of T). The combination of large phase space factors for such particles coupled with the Boltzmann distribution will lead to the dominant prevalence of hard particles. Thus the maximum influence in loop calculations (that sum over all kinds of particles) will be from these hard components. The scale that drives the strong coupling constant will thus be the temperature. At such temperatures the strong coupling, fine structure constant is expected to be $\alpha \simeq 0.3$. The coupling constant is $g \simeq 2$. At coupling constants of this size, perturbation theory may not be strictly valid.

The guiding principle of perturbation expansions in field theories is that the cou-

pling constant be small enough to subdue large dynamic contributions from higher order processes. If such is not the case and one still insists on expanding in the coupling constant, one may obtain nonsensical results. Such an occurrence was first witnessed in a series of calculations of the gluon self-energy and the resulting damping rate in the medium [78, 79, 80, 81] (see also [82] and references therein). By all accounts, the damping rate is a physical quantity and thus deserves the mantle of being gauge invariant. The gluon one loop self-energies do not provide this distinction and the result even seems to change sign in different gauges. Such a result was seen as a failure of the perturbation expansion. The resolution was sought in a resummation of higher order diagrams and a different perturbation expansion. This problem was partially solved by Braaten and Pisarski using a method coined by them as hard thermal loops (HTL) [82]. This method was also discovered independently by Frenkel and Taylor [83]. In the rest of this chapter we will follow the analysis of Braaten and Pisarski expounded by them in a series of papers [76, 82, 84, 85, 86].

7.2 *Hard Thermal Loops*

In the method of Hard thermal loops one imagines a plasma where the temperature has been set to an extremely large value $T \to \infty$. In such a situation the coupling constant must necessarily become very small $g \to 0$. The temperature is taken to be high enough that a clear separation of scales emerges: a hard scale of the order of the temperature T, a soft scale of the order gT. It may be easily demonstrated that tree diagrams with all their external momenta soft receive contributions from higher order corrections that are of the same order of magnitude as the tree diagram. The simplest example is the boson propagator. The bare propagator with a soft momentum $\mathbf{p} \sim gT$ flowing through it produces a contribution of order $\frac{1}{g^2T^2}$. The first higher order correction is obtained in the form of a loop as shown in the upper diagram of Fig. (7.2). At very high temperature the dominant contribution in the loop integral occurs from momenta of the order of the temperature. This allows

us to neglect all other factors of external momenta in the loop that occur in an additive combination with the thermal loop momenta. This simplifies the calculation immensely and produces a contribution from the loop of order $L = T^2$. The Feynman rule for the propagator, with a loop or self-energy insertion is

$$\Delta = \frac{1}{p^2} g L g \frac{1}{p^2} \sim \frac{1}{p^2} \frac{g^2 T^2}{p^2}.$$

Thus if $p \sim gT$. The one-loop corrected propagator is of the same order of magnitude as the bare propagator. To obtain all the contributions at this order of magnitude, one must sum over infinitely many such loop insertions to obtain the effective propagator,

$$\Delta_{eff} = \frac{1}{p^2 - \Sigma_T}.$$

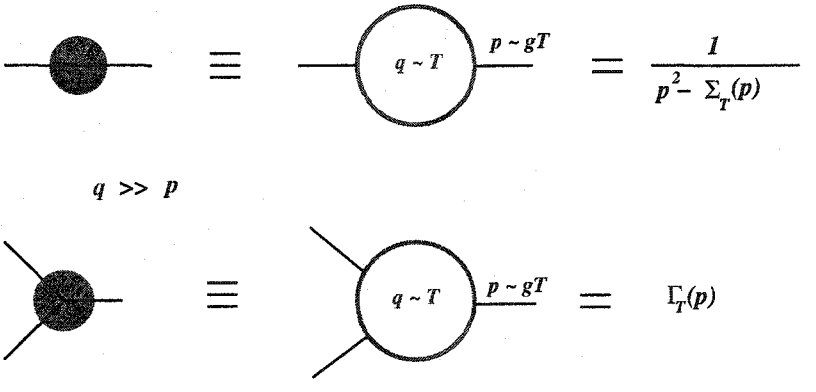

Figure 7.2: Hard thermal loop resummation for boson propagator and vertex.

The situation for the vertex is more or less the same: in addition to the bare vertex, one adds on the one loop correction, where the momenta in the loop are very large compared to the external momenta. In this approximation, one may easily demonstrate that on expanding the result of the loop in a series in gT, there exist terms of the order of the tree diagram for external momenta soft. These hard loops are

the only terms retained in the effective vertex of Fig. (7.2). It should be pointed out that all possible vertices do not contain HTLs, e.g., while the three gluon vertex has an HTL the two-gluon-one-photon vertex even at finite density does not [98]. With these resummed propagators and vertices one may demonstrate the gauge invariance of the gluon damping rate [82, 85]. Thus, in this limit we have managed to compile the correct effective theory of soft modes propagating in a hot non-abelian plasma.

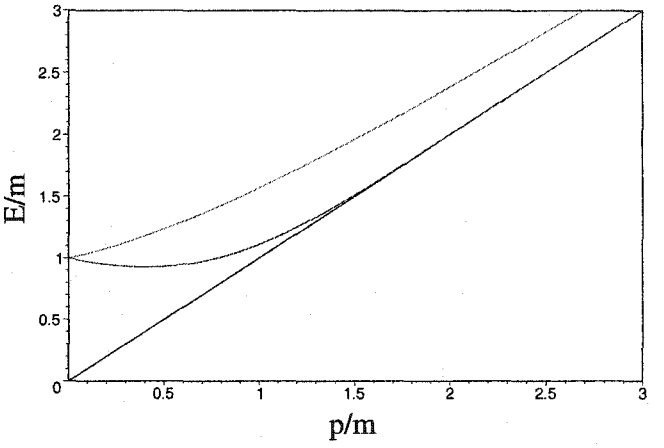

Figure 7.3: Quark dispersion relations from Hard thermal loops: m is the thermal mass. These despersion relations are obtained as poles of the thermal effective propagators (see Fig. 7.2). The upper branch represents the propagation of ordinary quarks with a thermal mass. The lower branch represents a collective mode with no analog at zero temperature. The straight line is the light cone.

7.3 *HTL dilepton production.*

In the previous sections we mostly highlighted the motivations and sketched a hand waving derivation of the effective theory of soft modes in a hot plasma. This involved resumming an infinite class of hard loops to obtain effective propagators and vertices. The effective propagators for soft quarks and gluons, do not merely endow these particles with a thermal mass, but present them will a non-trivial dispersion relation (see Fig. (7.3)). These soft modes will have an important influence on the dilepton spectrum.

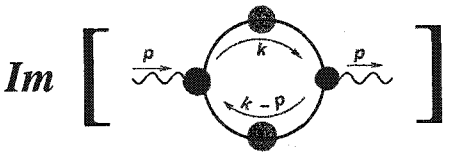

Figure 7.4: One loop HTL resummed dilepton production

The lowest order process, in the effective theory that leads to the production of a dilepton is the diagram of Fig. (7.4). Here the photon self-energy at one loop is modified: bare propagators are replaced by effective propagators, bare vertices by effective vertices. This diagram will contain all contributions at leading order to the process of soft dilepton production. Evaluated in Ref. [86], this leads to a rich structure in the spectrum (Fig. (7.5)). This is evaluated for the case of exact back-to-back lepton pairs, *i.e.*, lepton pairs produced with their three momenta equal and opposite. The peaks in the spectrum occur as the dispersion relation of the quark depends on its helicity and one of these helicities admits a minimum at non-zero three momentum. Annihilation of two soft quarks with this momentum, or the decay of a quark from the more energetic mode to a quark with this helicity and momentum lead to the two peak in the figure. However, this rich structure is completely masked by the effects of scattering of the soft modes by hard medium particles. Dileptons from such processes are far more numerous and are represented by the solid curve, at the top of the figure. The dashed curve represents the contribution from the Born term at these temperatures and energies (for further details on the exact nature of these processes see Ref. [86]).

The next to leading order calculation has also been performed in the effective theory [87], using diagrams such as those of Fig. (7.6). The total rate from these processes is of the same order of magnitude as the leading order rates. Thus we note that at lower energies, Born term dilepton production is completely dominated by

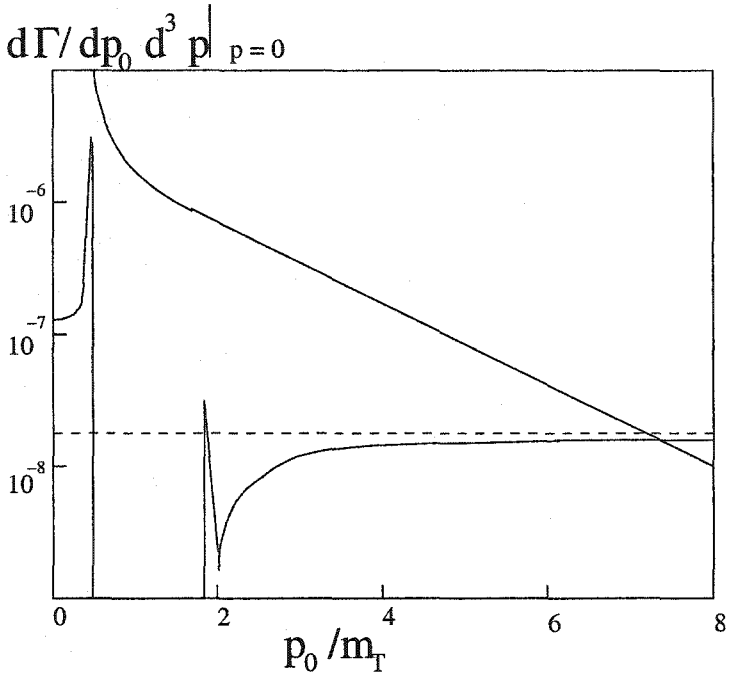

Figure 7.5: Differential dilepton production rate from one loop HTL effective theory (adapted from Ref. [86]). Dashed line is the rate from the Born term. Solid lines are rates from the HTL effective theory. See text for details.

the effects of the one loop effective theory.

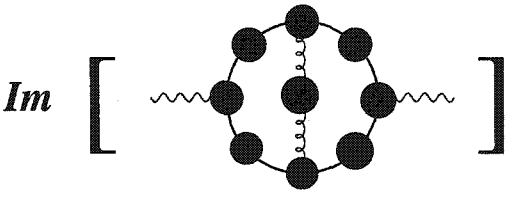

Figure 7.6: Two loop HTL resummed dilepton production.

7.4 Summary and discussions

In this chapter, we have presented a rather terse description of the complicated field of high temperature plasmas. We argued heuristically as to the need for resummation in the contribution from soft modes. We presented a method by which an infinite class of diagrams may be resummed in to the propagators and vertices of a given

theory. Thus one needs to use these resummed expressions to calculate the effect of any phenomena that involves the presence of soft modes.

We later focused on dilepton production from soft modes in a hot medium and enumerated some of the diagrams that have to be evaluated to estimate the order by order contribution to the dilepton spectrum. We noted that these rates from the resummed calculation dominate over the Born term or tree level rate. The resummed rates are nothing but a class of higher order effects which in this range of parameters has become comparable, or in this case much larger than the bare rate. In the previous chapter we asked the question: is the bare rate always dominant over higher order contributions? This is clearly not the case in the scenario discussed in this chapter.

The region of applicability of the results of this chapter is in plasmas where the temperature is extremely high, so that the strong coupling constant is very small. Such a condition may be achieved only past a temperature of many TeV. The temperatures expected to be achieved in heavy-ion collisions is not more that 1GeV. Applying these high temperature results to such low temperature plasmas represents an open question. Traces of such large rates in the actual dilepton spectrum in heavy-ion collisions is under much current investigation.

8

Intermediate Energy Dileptons and Symmetry Breaking

8.1 Introduction

In the previous chapter we concentrated exclusively on the soft sector of dilepton production. There both energy and momentum of the dileptons were much smaller than the temperature. We now proceed to the intermediate energy region, here both the energy and the momenta of the virtual photon (E, p) are of the order of the temperature T. From the results of the previous chapter we may discern the following information: even if high temperature (or Hard Thermal Loop) effects are important at low energies, their effect is completely subdued at energies of the order of the temperatures. Hence, one may argue that at these energies the Born term is the most dominant thermal dilepton source. Indeed, early calculations of the dilepton radiation in the deconfined sector were concerned exclusively with this process $q\bar{q} \to e^+e^-$ [57, 68]. These calculations are carried out assuming that the plasma is in complete thermal and chemical equilibrium and there is *no net local baryon density.*

It has been suggested that there could be a large gluon excess in the early plasma [88]: that the plasma would achieve thermal equilibrium early and chemical equilibrium between quarks, antiquarks and gluons would be realised much later, if at all. A recent calculation has estimated the effects of chemical non-equilibrium and of a large gluon excess on dilepton spectra [89]. There, a fugacity was introduced to account for chemical non-equilibrium. The function of this fugacity is essentially to

change the gluon and quark numbers from their equilibrium values. Possible sources of dileptons, such as $q + \bar{q}$ annihilation, $q + g$ Compton scattering, and $g + g$ fusion had been investigated and at chemical and thermal equilibrium the spectrum was found to be dominated by $q\bar{q} \to e^+e^-$, followed by $qg \to qge^+e^-$ which is an order of magnitude lower, followed by $gg \to q\bar{q}e^+e^-$ which is lower than the first process by 3 orders of magnitude [89].

It has been experimentally noticed that there exists a net baryon excess in the central collision region of a heavy-ion collision [90]. The effect of a net baryon density was also explored in a limited series of works (see Refs. [91, 92]) but these mostly concentrated on employing the standard channels of dilepton production (Born term, HTL corrected propagators and vertices), with a chemical potential added to the quark distribution functions. In this chapter, we propose that, when there is an asymmetry in the populations of quarks and antiquarks (i.e., a finite baryon chemical potential) a new set of diagrams actually arise. Using these we calculate a new contribution to the 3-loop photon self-energy. The various cuts of this self-energy contain higher loop contributions to the usual processes of $q\bar{q} \to e^+e^-$, $qg \to qe^+e^-$, $qq \to qqe^+e^-$, but also an entirely new process: $gg \to e^+e^-$. We calculate the contribution of this new channel to the differential production rate of dileptons. It is finally shown that in certain regions of phase space this may be comparable or even outshine the differential rate from the standard tree level $q\bar{q} \to e^+e^-$.

Imagine a scenario where the plasma is not just heated vacuum, but actually displays an asymmetry between quarks and antiquarks. This asymmetry would eventually manifest itself as an asymmetry between the baryon antibaryon populations in the final state: this has been noted experimentally at RHIC[1] [90]. In theory calculations, this asymmetry may be achieved by the introduction of a quark chemical potential μ_q. It may be argued that any baryon number asymmetry prevalent in the QGP must have been introduced by valence quarks, which, having encountered a hard scattering, failed to exit the central region. We thus provide a μ for the up and

[1]The Relativistic Heavy Ion Collider, at Brookhaven Natl. Lab., Upton, New York.

the down quark. The strange quarks are brought in by the sea or produced thermally in the medium in equal proportion with anti-strange quarks. Hence, they are assigned a $\mu = 0$. In most heavy-ion collisions, the nuclei of choice are rather large and display isospin asymmetry, hence there is an asymmetry in the populations of neutrons and protons being brought into the central region. If the stranded valence quarks in the plasma arrive with equal probability from either nucleon, one would require a higher μ for down quarks. As a first approximation, we ignore this effect, and, in the remaining, accept $\mu_u = \mu_d$. We also assume that the chemical potential for gluons is zero. We have thus assumed full thermal and chemical equilibrium, choosing to postpone the question of an early gluon excess for later study.

The rest of the chapter is organised as follows: Sect. 8.2 discusses a class of diagrams which are non-existent at zero temperature, and also at finite temperature and zero density. These become finite at finite density. Sect. 8.3 focuses on a specific channel which will become a source of dileptons. This is then evaluated using different regulators: results of a pilot calculation are presented. In Sect. 8.4, yet another symmetry of this channel is pointed out and discussed. Full symmetry breaking calculations are presented in Sect. 8.5. In Sect. 8.6 we derive a new contribution to the photon self-energy at three loops and discuss its various cuts. Finally, in Sect. 8.7 we calculate the production rate of low mass, intermediate energy dileptons. A summary is presented in Sect. 8.8.

8.2 New diagrams from broken charge conjugation invariance

At zero temperature, and at finite temperature and zero charge density, diagrams in QED that contain a fermion loop with an odd number of photon vertices (*e.g.*, Fig. 8.1) are cancelled by an equal and opposite contribution coming from the same diagram with fermion lines running in the opposite direction, this is the basic content

of Furry's theorem ([93, 94]). This statement can also be generalized to QCD for processes with two gluons and an odd number of photon vertices.

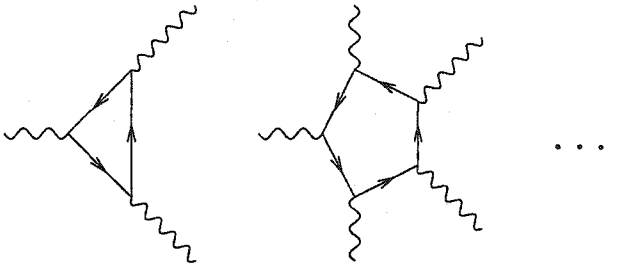

Figure 8.1: Diagrams that are zero by Furry's theorem and extensions thereof at finite temperature. These become non-zero at finite charge density.

A physical perspective is obtained by noting that all these diagrams are are encountered in the perturbative evaluation of Green's functions with an odd number of gauge field operators. At zero (finite) temperature, in the well defined case of QED we observe quantities like $\langle 0|A_{\mu 1}A_{\mu 2}...A_{\mu 2n+1}|0\rangle$ $(Tr[\rho(\mu,\beta)A_{\mu 1}A_{\mu 2}...A_{\mu 2n+1}])$ under the action of the charge conjugation operator C. In QED we know that $CA_\mu C^{-1} = -A_\mu$. In the case of the vacuum $|0\rangle$, we note that $C|0\rangle = |0\rangle$, as the vacuum is uncharged. As a result

$$\begin{aligned}\langle 0|A_{\mu_1}A_{\mu_2}...A_{\mu_{2n+1}}|0\rangle &= \langle 0|C^{-1}CA_{\mu_1}C^{-1}CA_{\mu_2}...A_{\mu_{2n+1}}C^{-1}C|0\rangle \\ &= \langle 0|A_{\mu_1}A_{\mu_2}...A_{\mu_{2n+1}}|0\rangle(-1)^{2n+1} \\ &= -\langle 0|A_{\mu_1}A_{\mu_2}...A_{\mu_{2n+1}}|0\rangle = 0. \end{aligned} \tag{8.1}$$

At a temperature T, the corresponding quantity to consider is

$$\sum_n \langle n|A_{\mu_1}A_{\mu_2}...A_{\mu_{2n+1}}|n\rangle e^{-\beta(E_n-\mu Q_n)},$$

where $\beta = 1/T$ and μ is a chemical potential. Here, however, $C|n\rangle = e^{i\phi}|-n\rangle$, where $|-n\rangle$ is a state in the ensemble with the same number of antiparticles as there are particles in $|n\rangle$ and vice-versa. If $\mu = 0$ i.e., the ensemble average displays zero density then inserting the operator $C^{-1}C$ as before, we get

$$\langle n|A_{\mu_1}A_{\mu_2}...A_{\mu_{2n+1}}|n\rangle e^{-\beta E_n} = -\langle -n|A_{\mu_1}A_{\mu_2}...A_{\mu_{2n+1}}|-n\rangle e^{-\beta E_n}. \qquad (8.2)$$

The sum over all states will contain the mirror term $\langle -n|A_{\mu_1}A_{\mu_2}...A_{\mu_{2n+1}}|-n\rangle e^{-\beta E_n}$, with the same thermal weight

$$\Rightarrow \sum_n \langle n|A_{\mu_1}A_{\mu_2}...A_{\mu_{2n+1}}|n\rangle e^{-\beta E_n} = 0, \qquad (8.3)$$

and Furry's theorem still holds. However, if $\mu \neq 0$ ($\Rightarrow$ unequal number of particles and antiparticles) then

$$\langle n|A_{\mu_1}A_{\mu_2}...A_{\mu_{2n+1}}|n\rangle e^{-\beta(E_n-\mu Q_n)} = -\langle -n|A_{\mu_1}A_{\mu_2}...A_{\mu_{2n+1}}|-n\rangle e^{-\beta(E_n-\mu Q_n)} \qquad (8.4)$$

the mirror term this time is $\langle -n|A_{\mu_1}A_{\mu_2}...A_{\mu_{2n+1}}|-n\rangle e^{-\beta(E_n+\mu Q_n)}$, with a different thermal weight, thus

$$\sum_n \langle n|A_{\mu_1}A_{\mu_2}...A_{\mu_{2n+1}}|n\rangle e^{-\beta(E_n-\mu Q_n)} \neq 0, \qquad (8.5)$$

and Furry's theorem will now break down.

As an illustration consider the diagrams of Fig. (8.2) for the case of two gluons and a photon attached to a massless quark loop (the analysis is the same even for QED i.e., for three photons connected to an electron loop). In order to obtain the full matrix element of a process containing the above as a sub-diagram one must coherently sum contributions from both diagrams which have fermion number running in opposite directions. The amplitude for $T^{\mu\rho\nu}(= \mathcal{T}^{\mu\rho\nu} + \mathcal{T}^{\nu\rho\mu})$ are :

$$\mathcal{T}^{\mu\rho\nu} = \frac{-1}{\beta}\sum_{n=-\infty}^{\infty}\int_{-\infty}^{\infty} eg^2 tr[t^a t^b]\frac{d^3q}{(2\pi)^3} Tr[\gamma^\mu\gamma^\beta\gamma^\rho\gamma^\delta\gamma^\nu\gamma^\alpha]$$
$$\frac{(q+p-k)_\alpha q_\beta (q+p)_\delta}{(q+p-k)^2 q^2 (q+p)^2},$$

and

$$\mathcal{T}^{\nu\rho\mu} = \frac{1}{\beta}\sum_{n=-\infty}^{\infty}\int_{-\infty}^{\infty} eg^2 tr[t^a t^b]\frac{d^3q}{(2\pi)^3}Tr[\gamma^\nu\gamma^\delta\gamma^\rho\gamma^\beta\gamma^\mu\gamma^\alpha] \frac{(q+k-p)_\alpha q_\beta (q-p)_\delta}{(q+k-p)^2 q^2 (q-p)^2} \tag{8.6}$$

At finite temperature (T) and density (chemical potential μ), we have the zeroth component of the fermion momenta given by,

$$q_0 = i(2n+1)\pi T + \mu \qquad \forall\, n \in I. \tag{8.7}$$

We assume that μ is the same for both flavours of quarks. Note that the extension of Furry's theorem to finite temperature does not hold at finite density: as, if we set $n \to -n-1$, we note that $q_0 \not\to -q_0$ and as a result

$$T^{\mu\rho\nu}(\mu, T) \neq -T^{\nu\rho\mu}(\mu, T). \tag{8.8}$$

Of course, If we now let the chemical potential go to zero ($\mu \to 0$) we note that for the transformation $n \to -n-1$, we obtain $q_0 \to -q_0$ and thus $T^{\mu\rho\nu}(0,T) \to -T^{\nu\rho\mu}(0,T)$. The analysis for fermion loops with larger number of vertices is essentially the same. Thus we may argue that many such processes may arise in a medium with finite density, and will lead to additional contributions to the dilepton or photon spectrum. The appearance of processes that can be related to symmetry-breaking in a medium has been noted before [95]. In the remaining, we will concentrate on one such diagram or process and explore its characteristics in greater detail.

8.3 *The two-gluon-photon vertex: an exploratory calculation*

In the previous section we have argued that a whole new set of processes may arise in the presence of a finite baryon density. Let us now focus our attention on the

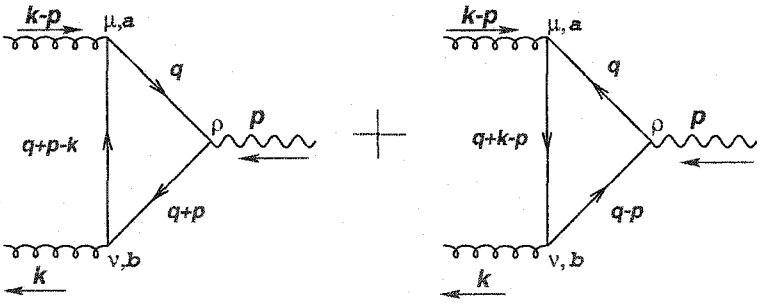

Figure 8.2: The two gluon photon effective vertex as the sum of two diagrams with quark number running in opposite directions.

diagrams of Fig. (8.2). Such a process does not exist at zero temperature or even at finite temperature and zero density. At finite density this may lead to a new source of dilepton or photon production. In this section we discuss this diagram in more detail.

8.3.1 General considerations.

Many points are in order: there is more than one kind of density that may manifest itself in the plasma. There is the net baryon density which requires that there be a difference in the populations of quarks and anti-quarks of a given flavour. There is the net charge density which simply requires that there be more of one kind (either positive or negative) of charge carrier in the medium. Note that it is possible to have a net baryon density and yet no charge density and visa-versa as table (8.1) indicates. We had deliberately avoided this discussion in the previous section to focus attention on the mechanism of symmetry breaking. As mentioned in the introduction, we will assume that there is a net baryon density, which manifests itself solely in the up and down flavours of the quarks. As the up quark has a charge of $+\frac{2}{3}$ and the down quark $-\frac{1}{3}$; equal densities of both will lead to a plasma with a net electric charge density. As will become clear during the calculations, the production of a virtual photon, from the process of Fig. (8.2), depends directly on the electric charge density. The baryon density merely serves the purpose of generating such a charge density. Hence this

signal is not present in a plasma with $\mu_u = \mu_d = \mu_s$, where the net charge is zero.

No. of u's	No. of $\bar{u}$'s	No. of d's	No. of $\bar{d}$'s	No. of s's	No. of $\bar{s}$'s	Baryon density	Charge density
n	n	n	n	n	n	0	0
n	n	0	0	0	0	0	0
n	m	0	0	0	0	(n-m)/3	2(n - m)/3
0	0	n	m	0	0	(n-m)/3	(m-n)/3
n	m	n	m	0	0	2(n-m)/3	(n-m)/3
n	m	n	m	n	m	(n-m)	0
n	m	m	n	0	0	0	(n - m)

Table 8.1: Different scenarios of plasmas with different baryon and charge densities.

In the previous section we had treated the diagram (diagrams) almost solely in QED. In this calculation we will only make the most trivial extension to QCD. It is to be noted that while the photon is an eigenstate of the charge conjugation operator C the gluon is not [96]. There are eight gluons, each carrying a colour charge in the adjoint representation of $SU(3)$. The sole role played by colour in this calculation will be to furnish the factor of $\mathrm{Tr}[t^a t^b]$ in the Feynman rules. The remaining rule and subsequent calculation are identical to the case in QED. The reason for considering this sort of diagram over others is obvious: this is the lowest order effect in the series, loops with more particles attached will invariably be suppressed by coupling constants and phase space requirements for may different momenta to sum up to zero. Also, diagrams with more than two gluons are non-zero in the vacuum itself and finite density effects may then be a mere excess on top of an already non-zero contribution.

We will consider cases with almost all values of the three momentum $\vec{p}$ of the photon from zero (maximum timelike) up to almost the energy E of the photon (almost lightlike). We will consider cases where the quarks will be both massive and massless. The gluons will, in all cases, be considered as massless. However, before

undertaking a complete analysis of the entire parameter space, we feel it wise to make a swift estimate of the order of magnitude of the dilepton contribution from this process.

8.3.2 *A first estimate.*

To calculate the contribution made by the diagram of Fig. (8.2) to the dilepton spectrum emanating from a quark gluon plasma we calculate the imaginary part of the photon self-energy containing the above diagram as an effective vertex. As we will be presenting the complete calculation in the upcoming sections we will not present calculational details here. The Matsubara sum in this calculation was, however, performed by an entirely different method to that being presented later. Instead of the standard technique of contour integration [74], we use the non-covariant method of Pisarski [76] (see Ref. [97, 98] for complete details).

To simplify the estimate even further, we calculate in the limit of photon three momentum $\vec{p} = 0$. The imaginary part of the considered self energy contains various cuts. We concentrate solely on the cut that represents the process of gluon-gluon to e^+e^-. The differential production rate for pairs of massless leptons with total energy E and and total momentum $\vec{p} = 0$ is given in terms of the discontinuity in the photon self-energy as (see chapter 6, or Refs. [70, 71]),

$$\frac{dR}{dEd^3p}(\vec{p}=0) = \frac{e^2}{3(2\pi)^5}\left[\frac{p_\mu p_\nu}{\mathbf{p}^2} - g_{\mu\nu}\right]\frac{-\mathrm{Disc}[i\Pi^{\mu\nu}]}{(\mathbf{p}^2)}\frac{1}{e^{\beta E}-1} \tag{8.9}$$

The rate of production of a hard lepton pair with total momentum $\vec{p} = 0$ at one-loop order in the photon self-energy (*i.e.*, the Born term) is given, for the three flavours as

$$\frac{dW}{dEd^3p}(\vec{p}=0) = \frac{5\alpha^2}{6\pi^4}\tilde{n}(E/2-\mu)\tilde{n}(E/2+\mu) + \frac{\alpha^2}{6\pi^4}\tilde{n}(E/2)\tilde{n}(E/2), \tag{8.10}$$

where we have, a five parts in six contribution coming from the up and down quark sector; and a one part in six contribution from the strange sector.

As mentioned before, the net baryon imbalance is caused by the valence quarks brought in by the incoming baryon rich nuclei. The baryon imbalance is thus manifested solely in the up and down quark sector: hence the chemical potential influences only the distribution function of the up and down quarks. The strange and anti-strange quarks are produced in equal numbers in the plasma; resulting in a strangeness chemical potential of zero. The initial temperatures of the plasma formed at RHIC and LHC have been predicted to lie in the range from 300-800 MeV [64, 77]. For this exploratory calculation we use a conservative estimate of $T = 400$ MeV. To evaluate the effect of a finite chemical potential we perform the calculation with two extreme values of chemical potential $\mu = 0.1T$ (1st plot in Fig. 8.3) and $\mu = 0.5T$(2nd plot Fig. 8.3) [66]. The calculation, is performed for three massless flavours of quarks. In this case the strong coupling constant is (see Ref. [99])

$$\alpha_s(T) = \frac{6\pi}{27ln(T/50MeV)}. \tag{8.11}$$

The differential rate for the production of dileptons with an invariant mass from 0.5 to 2.5 GeV is presented. In the plots, the dashed line is the rate from tree level $q\bar{q}$ (Eq. (8.10)); the solid line is that from the process $gg \to e^+e^-$. We note that in both cases the gluon-gluon process dominates at low energy and dies out at higher energy leaving the $q\bar{q}$ process dominant at higher energy.

8.3.3 *A critical review*

There are various caveats to the above calculation. Various sections of the calculation, most notably the quark momentum integrations over each pole configuration were performed numerically. As the theory considered here is massless, we encounter various collinear divergences. These were regulated in the numerical integration by cutting out the offending piece of phase space. This is similar in spirit to the invariant regulator used in [99, 100, 101]. The regulating cutoffs have dimensions of energy and avoid any propagator from acquiring a null denominator. The results from each pole configuration were calculated independently; with only those containing divergences,

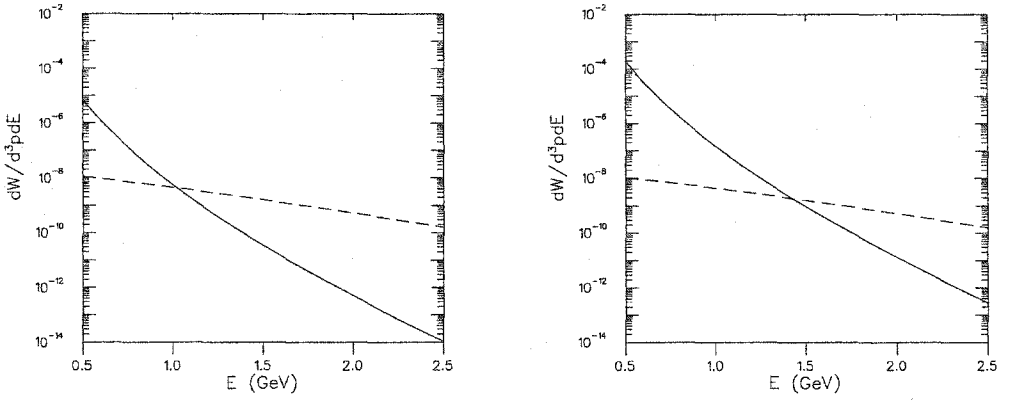

Figure 8.3: The differential production rate of back to back dileptons from two processes. Invariant mass runs from 0.5 GeV to 2.5 GeV. The dashed line represents the contribution from the process $q\bar{q} \rightarrow e^+e^-$. The solid line corresponds to the process $gg \rightarrow e^+e^-$. Temperature is 400 MeV. Quark chemical potential is 0.1T. The second figure is the same as the first but with $\mu = 0.5T$

regulated as above. Then the contributions are summed to obtain a regulator dependent result. The calculation is then repeated with ever smaller regulators (*i.e.*, smaller pieces of divergent phase space cut out). After a reduction of several orders of the magnitude the results seem to stabilize to a particular value. Beyond this point numerical noise ensues: the regulators cannot be made smaller. The results quoted in the figures above are thus regulator-dependent.

No doubt, the results are encouraging and definitely warrant further study. In the above calculation, we greatly simplified our task by considering the virtual photon to be produced at rest and the quarks in the loop to be massless. This inevitably led to various divergences, which were regulated numerically by simply removing that piece of phase space. We now make the simplest extension: performing the calculation with massive quarks. All collinear divergences vanish and we are dealing with strictly finite quantities. The analytic effort may now be extended further (details in the following sections). We still insist that the virtual photon be produced at rest. In this limit we obtain the surprising new result of a vanishing contribution. The contributions from different pole configurations all cancel exactly to yield zero.

Arguably, we are witnessing a situation where the calculation of a particular pro-

cess by two different regulators seems to be inconsistent (one should point out here that the pilot calculation was mostly numerical, thereby requiring constraints on the regulators). Such an occurrence is not without precedent: the calculation of the one loop self-energy of the photon in QED gives different results depending upon the regulators used. The resolution, in that case, was the observation that there existed a symmetry in the process that was being respected by one regulator, but not by another. We note that such a symmetry may exist in this case as well. It is well know that Lorentz invariance is broken by a heat bath. In the process we have considered: that of a virtual photon produced at rest, we note that only boost invariance is broken, rotational invariance is still manifest. A through examination of the constraints imposed on this process by rotational invariance will be carried out in the subsequent section.

8.4 Rotational invariance and Yang's theorem.

The vacuum analogue of the two-gluon-photon process does not exist due to Furry's theorem. If it did, it would represent an instance of two identical massless vectors fusing to form a massive spin one object; or alternatively a massive spin one object decaying into two massless vectors. There exist other such processes not protected by Furry's theorem, e.g., $\rho \to \gamma\gamma$. Such a process though not blocked by Furry's theorem is still vanishing in the vacuum. We effectively have a situation where there are two massless spin one particles in the in state and a spin one particle in the out state, or vice versa. In such circumstances another symmetry principle is invoked. This symmetry principle, due to C. N. Yang [102], is based on the parity and rotational symmetries of the in and out states and will, henceforth, be referred to as Yang's theorem.

8.4.1 Yang's theorem in vacuum

The basic statement of Yang's theorem, as far as it relates to this calculation, is that it is impossible for a spin one particle in vacuum to decay into two massless

vector particles. This statement is obviously also true for the reverse process of two massless vectors fusing to produce a spin one object and as a result a fermion and an antifermion combination in the triplet state. This may be understood through the following simple observation. Imagine that we boost to the frame where the two incoming vectors (in this case gluons) are exactly back-to-back with their three momenta equal and opposite. The outgoing vector (the virtual photon in this case) is produced at rest and eventually disintegrates into a lepton pair. We will now apply various symmetry operators (parity, rotation, etc.) on both the incoming and outgoing states. Note that, as we are only interested in strong and electromagnetic interaction, parity is a good quantum number. If both incoming and outgoing states are found to be eigenstates of the symmetry operator then they must be eigenstates with exactly the same eigenvalues, else this transition is not allowed.

We begin the discussion with the parity operator $\mathcal{P}$. We align the z axis along the direction of one of the incoming gluons. The outgoing or final state is parity odd, as we know that our final state is the photon, or a state composed of a lepton and anti-lepton in the ${}^3S$ state. The gluons, on-shell in this calculation, are each parity odd. We may still construct a parity odd in state via the following method: we label the possible instates as

$$|R+;R-\rangle, \quad |L+;L-\rangle, \quad |L+;R-\rangle, \quad |R+;L-\rangle.$$

Where, the $|R+;R-\rangle$ is the state where both gluons are right handed. The $|L+;R-\rangle$ state indicates that the gluon moving in the positive z direction is left-handed while that moving in the negative z direction is right handed (we have used the notation that the $+$ sign indicates the gluon moving in the positive z direction). The parity operation interchanges the momenta of the two gluons but leaves the direction of their spins intact. Hence the state $|R+R-\rangle - |L+L-\rangle$ is odd under parity operation. This implies that only this combination of incoming gluons is allowed by parity to fuse to form the virtual photon and hence the lepton pair.

We next turn to the rotation operator, $\mathcal{R}$. The in state is the state of two gluons;

the out state may be considered to be either the temporary virtual photon, or the finally produced pair of lepton anti-lepton. One may chose either for this analysis; we decide on the photon as it is simpler. For the in state we use the only state that is allowed by parity i.e., $|R+R-\rangle - |L+L-\rangle$. This state may be reexpressed as the action of creation and annihilation operators on the vacuum state as,

$$|R+R-\rangle - |L+L-\rangle = \left[a^\dagger_{R+}a^\dagger_{R-} - a^\dagger_{L+}a^\dagger_{L-}\right]|0\rangle. \tag{8.12}$$

Where $|0\rangle$ is the vacuum state. The creation operator $a^\dagger_{R+}$ creates a right handed gluon travelling in the positive z direction. The remaining creation operators have obvious meanings. The outstate is the photon at rest and thus has the rotation properties of the spherical harmonics $Y_{1,m}(\theta,\phi)$. As the in state has both gluons either right handed or left handed, the z component of the net angular momentum is zero. Hence $m = 0$ in the outstate of the photon.

We will rotate the in-state and the out-state by angle π about the z axis and then about the x axis. The outstate of the photon, mimicking the rotation properties of $Y_{1,0}(\theta,\phi)$, is an eigenstate of either rotation with eigenvalues $+1$ and -1 respectively. Focusing on the in state, we note that rotation by an angle ϕ about the axis $\hat{n}$ is achieved by the action of the appropriate operator $U(R^n_\phi)$ on the state in question,

$$\begin{aligned} U(R^z_\phi)|R+;R+\rangle &= U(R^z_\phi)a^\dagger_{R+}a^\dagger_{R+}|0\rangle \\ &= U(R^z_\phi)a^\dagger_{R+}U^{-1}(R^z_\phi)U(R^z_\phi)a^\dagger_{R+}U^{-1}(R^z_\phi)U(R^z_\phi)|0\rangle. \end{aligned} \tag{8.13}$$

Recalling the action of the rotation operators on creation operators (see Ref. [94]), *i.e.*,

$$U(R^z_\phi)a^\dagger_{R+}U^{-1}(R^z_\phi) = \sum_h \mathcal{D}(R^z_\phi)_{Rh}a^\dagger_{h,\hat{p}}. \tag{8.14}$$

Where $\mathcal{D}(R^z_\phi)_{Rh} = \langle R|e^{iJ_z\phi}|h\rangle$ is the rotation matrix for the rotation of the state (in this case vector). The index h runs over all the possible z components of the spin

of the particle. The vector $\hat{p}$ represents the new direction of motion of the particle after rotation. The action of any unitary operator, such as a rotation, on the vacuum will result in the vacuum again. Setting $\phi = \pi$ we obtain the simple relation for the action of the rotation operator on the gluon creation operator,

$$\begin{aligned} U(R^z_\pi)a^\dagger_{R+}U^{-1}(R^z_\pi) &= e^{i\pi}a^\dagger_{R+} \\ U(R^z_\pi)a^\dagger_{R-}U^{-1}(R^z_\pi) &= e^{-i\pi}a^\dagger_{R-} \end{aligned} \tag{8.15}$$

Using the above it is not difficult to demonstrate that the in state of two gluons is an eigenstate of R^z_ϕ with eigenvalue +1. Thus, there is no restriction to this transition, on the basis of this symmetry.

We now concentrate on rotation by π about the x axis. The outstate is an eigenstate of this operation with eigenvalue -1. Using Eq. (8.14) we note that,

$$\begin{aligned} U(R^x_\pi)a^\dagger_{R+}U^{-1}(R^x_\pi) &= a^\dagger_{R-} \\ U(R^x_\pi)a^\dagger_{R-}U^{-1}(R^x_\pi) &= a^\dagger_{R+} \\ U(R^x_\pi)a^\dagger_{L+}U^{-1}(R^x_\pi) &= a^\dagger_{L-} \\ U(R^x_\pi)a^\dagger_{L-}U^{-1}(R^x_\pi) &= a^\dagger_{L+} \end{aligned} \tag{8.16}$$

One may, thus, demonstrate that the two gluon in state is an eigenstate of the above rotation with eigenvalue +1,

$$\begin{aligned} U(R^x_\pi)\left(|R+;R-\rangle - |L+;L-\rangle\right) &= \Big[U(R^x_\pi)a^\dagger_{R+}U^{-1}(R^x_\pi)U(R^x_\pi)a^\dagger_{R-}U^{-1}(R^z_\phi) \\ &\quad - U(R^x_\pi)a^\dagger_{L+}U^{-1}(R^z_\phi)U(R^x_\pi)a^\dagger_{L-}U^{-1}(R^z_\phi)\Big]\,U(R^x_\pi)|0\rangle \\ &= \left[a^\dagger_{R-}a^\dagger_{R+} - a^\dagger_{L-}a^\dagger_{L+}\right]|0\rangle \\ &= |R-;R+\rangle - |L-;L+\rangle. \end{aligned} \tag{8.17}$$

Thus the in state rotates back to itself. This implies that this transition is not

allowed by any interaction. Thus, we demonstrate Yang's theorem in the vacuum: this transition is not allowed

8.4.2 *Yang's theorem in media*

The above argument for no transition has been formulated for two massless vectors fusing to a spin one final state in the vacuum. We now intend to extend this to a transition in the medium. One may argue at this point that the correct method of analysing this situation would be to start from a particular many body state; invoke the matrix element of the transition (this would give us the requisite creation and annihilation operators) and end up in a particular final many body state, *i.e.*,

$$\mathcal{M} = \langle n_1^f, n_2^f ... n_\infty^f | \left(\int d^4x H_I(x) \right)^n | n_1^i, n_2^i ... n_\infty^i \rangle \tag{8.18}$$

This has to be followed by squaring the matrix element and weighting it by the Boltzmann factor $e^{-\beta E_i}$, where E_i is the total energy of the in state, β is the inverse temperature. Then this quantity must be summed over all initial and final states to obtain the total transition probability per unit phase space for this process as

$$\mathcal{P} = \sum_f \sum_i e^{-\beta E_i} \left| \langle n_1^f, n_2^f ... n_\infty^f | \left(\int d^4x H_I(x) \right)^n | n_1^i, n_2^i ... n_\infty^i \rangle \right|^2 \tag{8.19}$$

The above method though comprehensive, does not allow a simple amplitude analysis as the case for the vacuum. Such an analysis may be constructed by drawing on the spectator analysis of loop diagrams. This method is explained in detail in the subsequent chapter.

The following analysis with spectators may appear to be rather heuristic at times. The reader not interested in such a discussion may consider the fact that the introduction of the medium formally involves the introduction of a new four vector $\mathbf{n}$ into the problem. If we were to consider the case of dileptons produced back-to-back in the rest frame of the medium, the results from the vacuum should still hold as in this case the only new ingredient is a new four vector of the bath ($\mathbf{n} = (1, 0, 0, 0)$). This

four vector is obviously rotationally invariant and cannot in any way introduce rotational non-invariance via dot or cross products with any three vector in the problem. However, if the two gluons are not exactly back-to-back or equivalently the medium has a net three momentum, then rotational invariance is explicitly broken. Even if we were to boost to the frame where the gluons are exactly back-to-back, we would find the medium streaming across the reaction. The above argument for the validity of the theorem for static dileptons will now be demonstrated via the spectator interpretation.

The spectator interpretation of loop diagrams, allows one to reexpress the results of Feynman diagrams with loops in terms of tree diagrams where one of the legs of the loops have been opened up to indicate a particle coming in along with the in state and an identical particle leaving with the out state (see Sect. 9.7). For this example, the effect of the medium on the transition (to next-to-lowest order) may be understood as a change in the in-state to include an incoming quark from a particular quantum state σ. Where, the index σ will be used to indicate all the characteristics of the quark in question such as the momenta, spin or helicity, colour etc. The outstate will also be suitably modified to include a quark emanating from the transition and re-entering the medium in the same quantum state σ vacated by the incoming extra quark. That this method indeed represents the process will be borne out by the actual calculation presented in the next section. In the discussion that follows, we will keep referring to the original state of two incoming gluons as the in-state, and the outgoing dilepton as the outstate. The extra particles from the medium that enter the reaction from the medium or exit the reaction and go back into the medium will be referred to as 'medium particles'. The full effect of the medium will only be incorporated on summation of the transition rates obtained by including all such states σ weighting the entire process (incoming particles $\rightarrow$ reaction $\rightarrow$ outgoing particles) by appropriate thermal factors for the incoming and out going medium particles. No doubt, there must also appear thermal factors for the incoming gluons: but, as for the entire discussion, we will constrain the two gluons to have the same

momenta, the distribution functions will play no role, and hence have been ignored.

The new total in-states and out-states will now be given by state vectors that look like,

$$\sum_{\sigma} \left(|R+;R-\rangle|\sigma\rangle - |L+;L-\rangle|\sigma\rangle \rightarrow |\gamma^*\rangle|\sigma\rangle \right) (1 - 2\tilde{n}(E_\sigma)).$$

In the above equation, we have taken the incoming and outgoing particle from the medium to be a fermion, as is appropriate in this case. Each state may once again be obtained by the action of the corresponding creation operators on the vacuum state. The new additional factors $\tilde{n}(E_\sigma)$ are the appropriate distribution functions, used in the expressions to indicate particles leaving and entering the medium. The factor of $1 - 2\tilde{n}(E_\sigma)$ may be broken up into two parts as $[1 - \tilde{n}(E_\sigma)] - [\tilde{n}(E_\sigma)]$. The first factor represents the distribution function for the case where emission of the medium-particle into the medium has occurred before its absorption by the process from the medium. The second process represents the reverse possibility. In contrast to the states of two gluons and a photon which have been designated as the in and out states, these particles from the medium are treated rather differently. Unlike the in and out states, the contributions from these medium states are added coherently, *i.e.*, one does not square the amplitude and then sum over spins and momenta but rather the procedure is carried out in reverse. The sum $\sum_\sigma$, represents integration over all momenta, sum over spins and colours etc.

Our method of extending Yang's symmetry will involve identifying certain subsets of the entire sum to be performed, which will turn out to be eigenstates of the rotation and parity operations to be carried out once more on these states. The argument will essentially be the following: if we can decompose the entire in and out state into certain subsets, with each subset being an eigenstate of the symmetry operator with the same eigenvalue, then the entire in and out states will also be eigenstates with the same eigenvalues. Then, as for the vacuum process, we will compare the eigenvalues for the in state and outstate.

To illustrate, we focus on a subset of four terms in the full sum in which one of the

incoming medium-fermions has a three momentum $\vec{q}$. To keep the discussion simple we pick $\vec{q}$ to be in the yz plane (the discussion may be easily generalized to include $\vec{q}$ in an arbitrary direction). The four processes under consideration are:

$$\begin{aligned}
&\Big[\left(|R+;R-\rangle - |L+;L-\rangle\right)|\vec{q};\uparrow\rangle \to |\gamma^*\rangle|\vec{q};\uparrow\rangle\Big](1-2\tilde{n}(E_{\vec{q},\uparrow})) \\
&+\Big[\left(|R+;R-\rangle - |L+;L-\rangle\right)|\mathcal{R}_\pi^z\vec{q};\uparrow\rangle \to |\gamma^*\rangle|\mathcal{R}_\pi^z\vec{q};\uparrow\rangle\Big](1-2\tilde{n}(E_{\mathcal{R}_\pi^z\vec{q},\uparrow})) \\
&+\Big[\left(|R+;R-\rangle - |L+;L-\rangle\right)|\mathcal{R}_\pi^x\vec{q};\downarrow\rangle \to |\gamma^*\rangle|\mathcal{R}_\pi^x\vec{q};\downarrow\rangle\Big](1-2\tilde{n}(E_{\mathcal{R}_\pi^x\vec{q},\downarrow})) \\
&+\Big[\left(|R+;R-\rangle - |L+;L-\rangle\right)|\mathcal{R}_\pi^z\mathcal{R}_\pi^x\vec{q};\downarrow\rangle \to |\gamma^*\rangle|\mathcal{R}_\pi^z\mathcal{R}_\pi^x\vec{q};\downarrow\rangle\Big](1-2\tilde{n}(E_{\mathcal{R}_\pi^z\mathcal{R}_\pi^x\vec{q},\downarrow})).
\end{aligned} \tag{8.20}$$

Where, $\mathcal{R}_\pi^z\vec{q}$ represents the three momentum $\vec{q}$ rotated by an angle π about the z axis, $\mathcal{R}_\pi^x\vec{q}$ represents $\vec{q}$ rotated about by an angle π about the x axis. The arrows $\uparrow,\downarrow$ represent the z component of the spin of the medium-fermion. As we are in the centre of mass of the thermal bath we have

$$E_{\vec{q},\uparrow} = E_{\mathcal{R}_\pi^z\vec{q},\uparrow} = E_{\mathcal{R}_\pi^x\vec{q},\downarrow} = E_{\mathcal{R}_\pi^z\mathcal{R}_\pi^x\vec{q},\downarrow}. \tag{8.21}$$

Thus we may completely factor out the distribution functions. Without loss of generality we may combine all four in states and out states to give,

$$\begin{aligned}
&\left(|R+;R-\rangle - |L+;L-\rangle\right)\Big[\ |\vec{q};\uparrow\rangle + |\mathcal{R}_\pi^z\vec{q};\uparrow\rangle + |\mathcal{R}_\pi^x\vec{q};\downarrow\rangle + |\mathcal{R}_\pi^z\mathcal{R}_\pi^x\vec{q};\downarrow\rangle\ \Big] \\
&\to |\gamma^*\rangle\Big[\ |\vec{q};\uparrow\rangle + |\mathcal{R}_\pi^z\vec{q};\uparrow\rangle + |\mathcal{R}_\pi^x\vec{q};\downarrow\rangle + |\mathcal{R}_\pi^z\mathcal{R}_\pi^x\vec{q};\downarrow\rangle\ \Big]
\end{aligned} \tag{8.22}$$

Now, it is simple to demonstrate using the methods of rotation of creation operators outlined in the vacuum case, that both the in and out states are eigenstates of $\mathcal{R}_\pi^x$. Concentrating on the rotation of the in state we obtain

$$\begin{aligned}
&U(R_\pi^x)\left(|R+;R-\rangle - |L+;L-\rangle\right)\Big[\ |\vec{q};\uparrow\rangle + |\mathcal{R}_\pi^z\vec{q};\uparrow\rangle + |\mathcal{R}_\pi^x\vec{q};\downarrow\rangle + |\mathcal{R}_\pi^z\mathcal{R}_\pi^x\vec{q};\downarrow\rangle\ \Big] \\
&= U(R_\pi^x)\left(a^\dagger_{R;+}a^\dagger_{R;-} - a^\dagger_{L;+}a^\dagger_{L;-}\right)U^{-1}(R_\pi^x)
\end{aligned}$$

$$\left[\ U(R^x_\pi)a^\dagger_{\vec{q};\uparrow}U^{-1}(R^x_\pi)U(R^x_\pi)a^\dagger_{\mathcal{R}^z_\pi\vec{q};\uparrow}U^{-1}(R^x_\pi)U(R^x_\pi)a^\dagger_{\mathcal{R}^x_\pi\vec{q};\downarrow}U^{-1}(R^x_\pi)U(R^x_\pi)a^\dagger_{\mathcal{R}^z_\pi\mathcal{R}^x_\pi\vec{q};\downarrow}U^{-1}(R^x_\pi)\ \right]$$
$$= -i\left(|R+;R-\rangle - |L+;L-\rangle\right)\left[\ |\mathcal{R}^x_\pi\vec{q};\downarrow\rangle + |\mathcal{R}^x_\pi\mathcal{R}^z_\pi\vec{q};\downarrow\rangle + |\vec{q};\uparrow\rangle + |\mathcal{R}^z_\pi\vec{q};\uparrow\rangle\ \right] \tag{8.23}$$

Note that the medium-fermions just mix into each other, but the over all state remains the same. Following the above method one can show that the outstate is also an eigenstate of $\mathcal{R}^x_\pi$ but with an eigenvalue of i. Thus, we can decompose the entire sum over spins and integration over the three momenta of the medium-fermions into sets of states as indicated, each will result in an in state and an out state between which no transition is allowed. For the rotation $\mathcal{R}^z_\pi$ we note that the eigenstates are in fact a subset of two states: in this case, the sum of the first two states of Eq. (8.20) are eigenstates of $\mathcal{R}^z_\pi$; as is the sum of the third and fourth state.

This would imply that such a transition, as implied by the Feynman diagrams of Fig. (8.2), can not occur. There is however a caveat to the above discussion. Note that in the vacuum case we expressly boosted to the frame where the two gluons would be exactly back-to-back with their three momenta equal and opposite. Then, rotational symmetry was invoked to demonstrate the impossibility of this transition. In the case of the processes occurring in medium, we tacitly began the analysis with the two gluon once again exactly back-to-back in the rest frame of the bath. It is perhaps no surprise that our results from the vacuum still hold as in this case the only new ingredient is a new four vector of the bath $(1,0,0,0)$. This four vector is obviously rotationally invariant and cannot in any way introduce rotational non-invariance via dot or cross products with any three vector in the problem. However, if the two gluons are not exactly back-to-back or equivalently the medium has a net three momentum, then rotational invariance is explicitly broken. Even if we were to boost to the frame where the gluons are exactly back-to-back, we would find the medium streaming across the reaction. This would make the distribution functions of the two gluons different (even though in this frame they have the same energy), Eq. (8.21) would no longer hold. As a result it will not be possible to construct eigenstates of the rotation operators $\mathcal{R}^z_\pi$ and $\mathcal{R}^z_\pi$ as done previously. As the in and out states

will no longer be eigenstates of $\mathcal{R}^z_\pi$ and $\mathcal{R}^z_\pi$ with different eigenvalues, transitions will, now, be allowed between them.

In the above discussion, we have demonstrated how the medium may, once again, break another symmetry of the vacuum; in this case rotational symmetry. This allows the transition of Fig. (8.2) to take place in the medium. This process is strictly forbidden, in the vacuum, by two different symmetries (charge conjugation and rotation). It is forbidden in the exact back to back case by rotational symmetry in a C broken medium. We thus resolve the inconsistency at the end of the previous section. The results derived using the numerical regulator, which leads to the plots is incorrect. The effect is zero for $\vec{p} = 0$. To obtain a non-zero contribution, rotational symmetry has to be broken by a net $\vec{p}$. The magnitude of the signal from such a symmetry breaking effect may only be deduced via detailed calculation. In the next section we shall outline just such a calculation.

8.5 *The two-gluon-photon vertex at $\mu \neq 0$ and $\vec{p} \neq 0$*

We begin by first writing down the Feynman rules for the two-gluon-photon vertex. We use a slightly different momentum routing from that illustrated in Fig. (8.2). The two vertices for the general case of massive quarks is:

$$\mathcal{T}^{\mu\nu\rho} = \frac{-1}{\beta}\int \frac{d^3q}{(2\pi)^3}\sum_n \mathrm{Tr}\Big[\; ie\delta_{ki}\gamma^\mu \frac{i(\not{\mathbf{q}}+m)}{\mathbf{q}^2-m^2} igt^b_{ij}\gamma^\nu \times \frac{i(\not{\mathbf{q}}-\not{\mathbf{k}}+m)}{(\mathbf{q}-\mathbf{k})^2-m^2} igt^c_{jk}\gamma^\rho \frac{i(\not{\mathbf{q}}-\not{\mathbf{p}}+m)}{(\mathbf{q}-\mathbf{p})^2-m^2}\;\Big] \tag{8.24}$$

$$\mathcal{T}^{\mu\rho\nu} = \frac{-1}{\beta}\int \frac{d^3q}{(2\pi)^3}\sum_n \mathrm{Tr}\Big[\; ie\delta_{ik}\gamma^\mu \frac{i(\not{\mathbf{q}}+\not{\mathbf{p}}+m)}{(\mathbf{q}+\mathbf{p})^2-m^2} igt^c_{kj}\gamma^\rho \times \frac{i(\not{\mathbf{q}}+\not{\mathbf{k}}+m)}{(\mathbf{q}+\mathbf{k})^2-m^2} igt^b_{ji}\gamma^\nu \frac{i(\not{\mathbf{q}}+m)}{\mathbf{q}^2-m^2}\;\Big] \tag{8.25}$$

Where the trace is implied over both colour and spin indices. Though not explicitly elucidated above the zeroth components of each four momentum is a discrete even or

odd frequency, i.e.,

$$q^0 = i(2n+1)\pi T + \mu, \qquad p^0 = i2m\pi T, \qquad k^0 = i2j\pi T.$$

where n, m, j are integers, μ is the quark chemical potential. The overall minus sign is due to the fermion loop. The sum over n runs over all integers from $-\infty$ to $+\infty$. This sum may be performed by two distinct methods: the method of contour integration [74], the method of non-covariant propagators [73]. Each method is more advantageous in certain cases. We will evaluate the above and other expressions by both these methods. Presently, we use the method of contour integration to evaluate Eq. (8.24).

We separate the momentum dependent and mass dependent parts of the numerators of Eqs. (8.24,8.25) i.e.,

$$\begin{aligned}\mathcal{T}^{\mu\nu\rho} = \mathfrak{B}^{\mu\alpha\nu\beta\rho\gamma}\mathfrak{T}_{1\alpha\beta\gamma} + \mathcal{A}_1^{\mu\nu\rho} = \frac{eg^2\delta^{bc}}{2\beta}\int\frac{d^3q}{(2\pi)^3}\sum_n \mathrm{Tr} \\ \left[\frac{\mathfrak{B}^{\mu\alpha\nu\beta\rho\gamma}q_\alpha(q-k)_\beta(q-p)_\gamma}{(\mathbf{q}^2-m^2)((\mathbf{q}-\mathbf{k})^2-m^2)((\mathbf{q}-\mathbf{p})^2-m^2)}\right. \\ \left. + m^2\frac{\mathfrak{A}^{\mu\alpha\nu\rho}q_\alpha + \mathfrak{A}^{\mu\nu\beta\rho}(q-k)_\beta + \mathfrak{A}^{\mu\nu\rho\gamma}(q-p)_\gamma}{(\mathbf{q}^2-m^2)((\mathbf{q}-\mathbf{k})^2-m^2)((\mathbf{q}-\mathbf{p})^2-m^2)}\right]\end{aligned} \tag{8.26}$$

$$\begin{aligned}\mathcal{T}^{\mu\rho\nu} = \mathfrak{B}^{\mu\alpha\rho\beta\nu\gamma}\mathfrak{T}_{2\alpha\beta\gamma} + \mathcal{A}_2^{\mu\nu\rho} = \frac{eg^2\delta^{bc}}{2\beta}\int\frac{d^3q}{(2\pi)^3}\sum_n \mathrm{Tr} \\ \left[\frac{\mathfrak{B}^{\mu\alpha\rho\beta\nu\gamma}(q+p)_\alpha(q+k)_\beta(q)_\gamma}{(\mathbf{q}^2-m^2)((\mathbf{q}+\mathbf{k})^2-m^2)((\mathbf{q}+\mathbf{p})^2-m^2)}\right. \\ \left. + m^2\frac{\mathfrak{A}^{\mu\alpha\rho\nu}(q+p)_\alpha + \mathfrak{A}^{\mu\rho\beta\nu}(q+k)_\beta + \mathfrak{A}^{\mu\rho\nu\gamma}q_\gamma}{(\mathbf{q}^2-m^2)((\mathbf{q}+\mathbf{k})^2-m^2)((\mathbf{q}+\mathbf{p})^2-m^2)}\right]\end{aligned} \tag{8.27}$$

Where $\mathfrak{A}^{\mu\nu\rho\gamma}$ represents the trace of four γ matrices and $\mathfrak{B}^{\mu\alpha\nu\beta\rho\gamma}$ represents the trace of six γ matrices. Employing the methods of residue calculus, the sum over n may be formally rewritten as a contour integration over the infinite set of contours C_1 (See Fig. (8.4))i.e.,

$$T\sum_n f(q^0 = i(2n+1)\pi T + \mu) = \frac{T}{2\pi i}\oint_{C_1} dq^0 f(q^0)\frac{1}{2}\beta \tanh\left(\frac{1}{2}\beta(q^0-\mu)\right) \qquad (8.28)$$

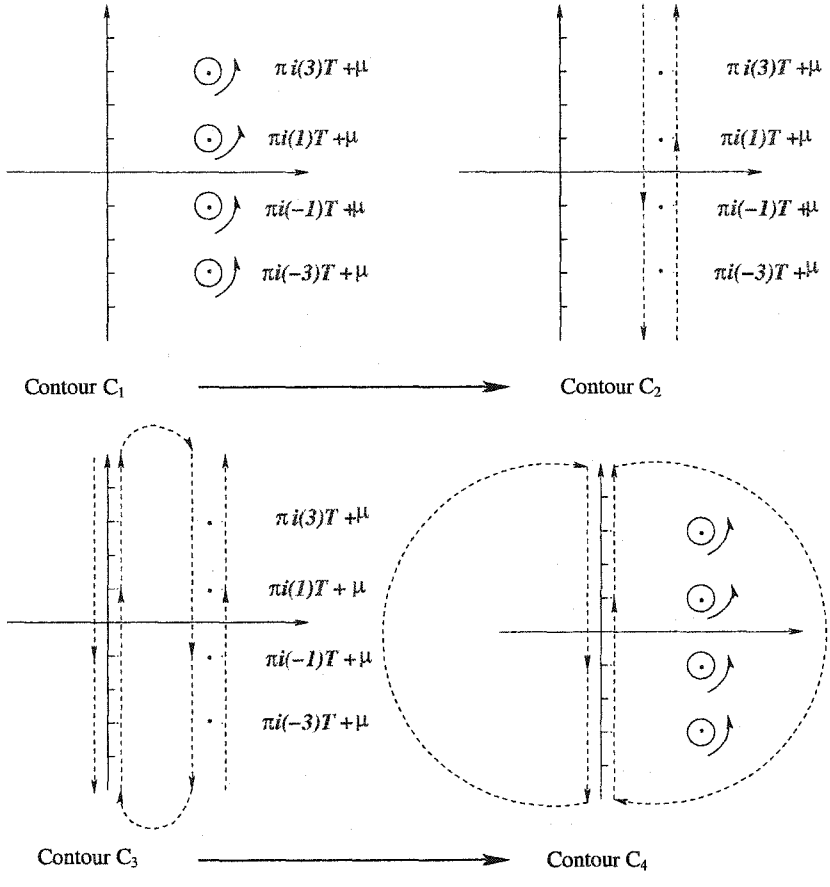

Figure 8.4: The contours used to evaluate the Matsubara sum with a finite chemical potential. See text for details.

The contours C_1 may indeed be deformed to those of C_2 (see Fig. (8.4)). These are a set of two linear contours meeting at $\pm i\infty$, one from $q^0 = -i\infty + \mu + \epsilon \rightarrow q^0 = i\infty + \mu + \epsilon$, and another from $i\infty + \mu - \epsilon \rightarrow -i\infty + \mu - \epsilon$. Here, and henceforth in all discussions of contours, residues and analytic continuations, ϵ will represent a

vanishingly small quantity. We can now proceed by the method of [74] and separate a vacuum part, thermal part and a pure density contribution. Instead, we introduce another set of contours along the y axis from $q^0 = -i\infty + \epsilon \to q^0 = i\infty + \epsilon$ and from $i\infty - \epsilon \to -i\infty - \epsilon$. Admittedly, as $\epsilon \to 0$ this contour will produce a vanishing contribution. The integrand in Eq. (8.24) has six powers of q^0 in the denominator and only three in the numerator. Hence it vanishes faster than a linear term as $q^0 \to \infty$. This quantity thus obeys Jordan's Lemma and we may connect the two integration contours around 0 and μ by line segments at $\pm i\infty$. These line segments shown as curved lines in the third contour of Fig. (8.4) will have zero contribution to the entire integral. The total contour thus obtained is referred to as C_3. We now split the integrand into two, one piece for all the contours on the positive of the x axis denoted as C_3^a, one piece for the sole contour on the negative side of the x axis denoted as C_3^b, i.e.,

$$\frac{T}{2\pi i}\oint_{C_1} dq^0 f(q^0)\frac{1}{2}\beta\tanh\left(\frac{1}{2}\beta(q^0-\mu)\right) = \frac{1}{2\pi i}\int_{i\infty-\epsilon_{C_3^b}}^{-i\infty-\epsilon} dq^0 f(q^0)\left(-\frac{1}{2}+\frac{1}{e^{\beta(\mu-q^0)}+1}\right)$$
$$+\frac{1}{2\pi i}\left(\int_{-i\infty+\epsilon}^{i\infty+\epsilon}+\int_{i\infty+\mu-\epsilon}^{-i\infty+\mu-\epsilon}+\int_{-i\infty+\mu+\epsilon}^{i\infty+\mu+\epsilon}\right)_{C_3^a} dq^0 f(q^0)\left(\frac{1}{2}-\frac{1}{e^{\beta(q^0-\mu)}+1}\right). \tag{8.29}$$

We now separate the terms into a vacuum piece and a matter piece, note the similarity between this and the zero density separation. In this procedure, we differ from the standard method [74] in not extracting an explicit finite density piece. The main reason for the extra contour deformation is to obtain the final answer in a form from whence the special situation of zero density will be obvious. In this spirit, we now reverse the direction of integration in C_3^b and note that the vacuum piece has no poles at $i(2n+1)\pi T + \mu$. Thus the contours in the vacuum term may be allowed to overlap by setting $\epsilon = 0$. We obtain

$$\frac{T}{2\pi i}\oint_{C_1} dq^0 f(q^0)\frac{1}{2}\beta\tanh\left(\frac{1}{2}\beta(q^0-\mu)\right) = \frac{1}{2\pi i}\int_{-i\infty}^{i\infty} dq^0 f(q^0)$$
$$+\frac{1}{2\pi i}\int_{-i\infty-\epsilon}^{i\infty-\epsilon} dq^0 f(q^0)\frac{-1}{e^{\beta(-q^0+\mu)}+1}$$

$$+\left(\int_{-i\infty+\epsilon}^{i\infty+\epsilon}+\int_{i\infty+\mu-\epsilon}^{-i\infty+\mu-\epsilon}+\int_{-i\infty+\mu+\epsilon}^{i\infty+\mu+\epsilon}\right)dq^0 f(q^0)\frac{-1}{e^{\beta(q^0-\mu)}+1}. \tag{8.30}$$

We now let $\epsilon \to 0$ on the contours on the positive side of the x axis. This procedure will deform the two linear contours at $\mu \pm \epsilon$ back to the small circles around the points $i(2n+1)\pi T$, this part will become similar to the initial contour C_1. The rest of the contour can be closed by including the infinite arc in the $q^0 = +\infty$ direction in the clockwise sense. This multiply connected contour is indicated as $C_4^a - C_1$ and displayed on the right of the fourth plot in Fig. (8.4). The linear contour on the negative side may be closed off as always by the infinite arc extending to $q^0 = -\infty$. This is indicated as C_4^b and shown as the left contour in the fourth plot of the figure. The contour integration over either contour may be replaced by the sum over all the residues at all the poles enclosed by the contour. We note that the poles at $i(2n+1)\pi T + \mu$, excluded by the multiply connected contour, are not to be included in the sum over residues. Thus our final, formal result is,

$$\begin{aligned}\frac{T}{2\pi i}\oint_{C_1} dq^0 f(q^0)\frac{1}{2}\beta\tanh\left(\frac{1}{2}\beta(q^0-\mu)\right) &= \frac{1}{2\pi i}\int_{-i\infty}^{i\infty} dq^0 f(q^0) \\ &\quad -\sum_i \theta(-\omega_i)\mathrm{Res.}[f(q^0)]\frac{1}{e^{\beta(-q^0+\mu)}+1}\bigg|_{q^0=\omega_i} \\ &\quad +\sum_i \theta(\omega_i)\mathrm{Res.}[f(q^0)]\frac{1}{e^{\beta(q^0-\mu)}+1}\bigg|_{q^0=\omega_i}.\end{aligned} \tag{8.31}$$

We may substitute the full integrand in Eq. (8.24) to obtain the result of contour integration as

$$\begin{aligned}\mathcal{T}^{\mu\nu\rho} = &\left\{\frac{1}{2\pi i}\int_{-i\infty}^{i\infty} dq^0 + \sum_i\left[\ \frac{\theta(\omega_i)}{e^{\beta(q^0-\mu)}+1} - \frac{\theta(-\omega_i)}{e^{\beta(-q^0+\mu)}+1}\ \right]\right\} \\ &\times\frac{eg^2\delta^{bc}}{2\beta}\int\frac{d^3q}{(2\pi)^3}\mathrm{Res.Tr}\left[\ \frac{\mathfrak{B}^{\mu\nu\rho}_{\alpha\beta\gamma}q^\alpha(q-k)^\beta(q-p)^\gamma}{(\mathbf{q}^2-m^2)((\mathbf{q}-\mathbf{k})^2-m^2)((\mathbf{q}-\mathbf{p})^2-m^2)}\right. \\ &\left.+\,4\frac{g^{\mu\nu}(q-p-k)^\rho+g^{\mu\rho}(q-k+p)^\nu+g^{\nu\rho}(q+k-p)^\mu}{(\mathbf{q}^2-m^2)((\mathbf{q}-\mathbf{k})^2-m^2)((\mathbf{q}-\mathbf{p})^2-m^2)}\ \right]\bigg|_{q^0=\omega_i}.\end{aligned} \tag{8.32}$$

A similar contour analysis as above may be performed for Eq. (8.25), with the added extra step of setting $q^0 \to -q^0, \vec{q} \to -\vec{q}$. This procedure will produce a

final contour of integration which is a mirror image of C_4. There will, once again, be an infinite semicircle extending to $+\infty$ connected with the line running from $-i\infty+\epsilon \to i\infty+\epsilon$. There will also be an infinite semicirle extending to $-\infty$ connected to the vertical line running on the negative side of the x axis. This contour will however be multiply connected with the poles at $-i(2n+1)\pi T - \mu$ excluded from the region bounded by the infinite semicircle. As before these poles shall be excluded from the sum over residues. Following this procedure, we obtain the result of the contour integration for Eq. (8.25) as,

$$\begin{aligned}\mathcal{T}^{\mu\rho\nu} = &\left\{ \frac{-1}{2\pi i}\int_{-i\infty}^{i\infty} dq^0 - \sum_i \left[\frac{\theta(\omega_i)}{e^{\beta(q^0+\mu)}+1} + \frac{\theta(-\omega_i)}{e^{\beta(-q^0-\mu)}+1} \right] \right\} \\ &\times \frac{eg^2\delta^{bc}}{2\beta}\int \frac{d^3q}{(2\pi)^3}\mathrm{Res.Tr}\left[\frac{\mathfrak{B}^{\mu\nu\rho}_{\alpha\beta\gamma}q^\alpha(q-k)^\beta(q-p)^\gamma}{(\mathbf{q}^2-m^2)((\mathbf{q}-\mathbf{k})^2-m^2)((\mathbf{q}-\mathbf{p})^2-m^2)} \right. \\ &\left. + 4\frac{g^{\mu\nu}(q-p-k)^\rho + g^{\mu\rho}(q-k+p)^\nu + g^{\nu\rho}(q+k-p)^\mu}{(\mathbf{q}^2-m^2)((\mathbf{q}-\mathbf{k})^2-m^2)((\mathbf{q}-\mathbf{p})^2-m^2)} \right]\Bigg|_{q^0=\omega_i}. \end{aligned} \tag{8.33}$$

Note, that the vacuum term is at least naively linearly divergent and thus the shift in momentum integrations may not be performed as above. However, from Furry's theorem we know that the sum of the vacuum terms from Eqs. (8.32) and (8.33) must be identically zero. Also note that the presence of the thermal distribution functions over quark momenta renders these integrals ultra-violet finite. Quark momentum shifts are thus definitely allowed for the thermal parts of Eqs. (8.32,8.33). Hence, We ignore the vacuum pieces and combine the matter pieces of both terms to obtain $T^{\mu\nu\rho} = \mathcal{T}^{\mu\nu\rho} + \mathcal{T}^{\mu\rho\nu}$ as,

$$\begin{aligned}T^{\mu\nu\rho} = &\sum_i \left[\theta(\omega_i)\left(\frac{1}{e^{\beta(q^0-\mu)}+1} - \frac{1}{e^{\beta(q^0+\mu)}+1}\right) + \theta(-\omega_i)\left(\frac{1}{e^{\beta(-q^0-\mu)}+1} - \frac{1}{e^{\beta(-q^0+\mu)}+1}\right) \right] \\ &\times \frac{eg^2\delta^{bc}}{2\beta}\int \frac{d^3q}{(2\pi)^3}\mathrm{Res.Tr}\left[\frac{\mathfrak{B}^{\mu\nu\rho}_{\alpha\beta\gamma}q^\alpha(q-k)^\beta(q-p)^\gamma}{(\mathbf{q}^2-m^2)((\mathbf{q}-\mathbf{k})^2-m^2)((\mathbf{q}-\mathbf{p})^2-m^2)} \right. \\ &\left. + 4\frac{g^{\mu\nu}(q-p-k)^\rho + g^{\mu\rho}(q-k+p)^\nu + g^{\nu\rho}(q+k-p)^\mu}{(\mathbf{q}^2-m^2)((\mathbf{q}-\mathbf{k})^2-m^2)((\mathbf{q}-\mathbf{p})^2-m^2)} \right]\Bigg|_{q^0=\omega_i} \end{aligned} \tag{8.34}$$

We find, as would have been expected, that the entire contribution is proportional to the difference of the quark and anti-quark distribution functions. We denote these as $\Delta\tilde{n}(q^0,\mu)(=\frac{1}{e^{\beta(q^0-\mu)}+1}-\frac{1}{e^{\beta(q^0+\mu)}+1})$. The residues will be evaluated at the various poles of the integrand. A close inspection of Eq. (8.34) indicates that there are three poles on the positive x axis at,

$$q^0=\sqrt{q^2+m^2}=E_q \tag{8.35}$$

$$q^0=\sqrt{|\vec{q}-\vec{k}|^2+m^2}+k^0=E_{q-k}+k^0 \tag{8.36}$$

$$q^0=\sqrt{|\vec{q}-\vec{p}|^2+m^2}+p^0=E_{q-p}+p^0. \tag{8.37}$$

and three on the negative x axis,

$$q^0=-\sqrt{q^2+m^2}=-E_q \tag{8.38}$$

$$q^0=-\sqrt{|\vec{q}-\vec{k}|^2+m^2}+k^0=-E_{q-k}+k^0 \tag{8.39}$$

$$q^0=-\sqrt{|\vec{q}-\vec{p}|^2+m^2}+p^0=-E_{q-p}+p^0. \tag{8.40}$$

We denote the residue at each of these poles as Residues (1-6). Before evaluating the function at each of these residues, we consider the fate of the remaining imaginary frequencies in the expressions k^0, p^0. The even frequency k^0 also has to be summed in similar fashion as q^0. The external photon frequency p^0 will have to be analytically continued to a general complex value and finally the discontinuity of the full self-energy across the real axis of p^0 will be considered. We perform this procedure in the next section.

8.6 *The photon self-energy and its imaginary part*

We are now in a position to calculate the contribution made by the diagram of Fig. 8.2 to the dilepton spectrum emanating from a quark gluon plasma. To achieve this aim we choose to calculate the discontinuity of the photon self-energy as represented

by the diagram of Fig. 8.5 across the real axis of p^0. In the previous section we wrote down expressions for $T^{\mu\nu\rho}(p,k,p-k)$ *i.e.*, the vertex with the the two gluon energies entering and the photon energy leaving. To write down the expression for the full self-energy we also need expressions for $T'^{\mu\nu\rho}(-p,-k,k-p)$ *i.e.*, the vertex with the photon energy entering and the gluon energies leaving. This vertex also admits a decomposition into two pieces for quark number running in opposite directions,

$$T'^{\mu\nu\rho}(-p,-k,k-p) = \mathcal{T}'^{\mu\nu\rho} + \mathcal{T}'^{\mu\rho\nu} \tag{8.41}$$

The Feynman rule for $\mathcal{T}'^{\mu\nu\rho}$ is given as

$$\begin{aligned}\mathcal{T}'^{\mu\nu\rho} = \mathfrak{B}^{\mu\gamma\nu\beta\rho\alpha}\mathfrak{T}'_{1\gamma\beta\alpha} + \mathcal{A}'^{\mu\nu\rho}_1 = \frac{eg^2\delta^{bc}}{2\beta}\int\frac{d^3q}{(2\pi)^3}\sum_n \mathrm{Tr}\\ \left[\frac{\mathfrak{B}^{\mu\gamma\nu\beta\rho\alpha}q_\gamma(q+k)_\beta(q+p)_\alpha}{(\mathbf{q}^2-m^2)((\mathbf{q}+\mathbf{k})^2-m^2)((\mathbf{q}+\mathbf{p})^2-m^2)}\right.\\ \left.+\frac{\mathfrak{A}^{\mu\gamma\nu\rho}q_\gamma + \mathfrak{A}^{\mu\nu\beta\rho}(q+k)_\beta + \mathfrak{A}^{\mu\nu\rho\alpha}(q+p)_\alpha}{(\mathbf{q}^2-m^2)((\mathbf{q}+\mathbf{k})^2-m^2)((\mathbf{q}+\mathbf{p})^2-m^2)}\right]\end{aligned} \tag{8.42}$$

A close inspection of the traces of four and six γ matrices allows us to derive the following identities:

$$\mathfrak{A}^{\mu\gamma\nu\rho} = \mathfrak{A}^{\rho\nu\gamma\mu} = \mathfrak{A}^{\mu\rho\nu\gamma} \tag{8.43}$$

$$\mathfrak{A}^{\mu\nu\beta\rho} = \mathfrak{A}^{\rho\beta\nu\mu} = \mathfrak{A}^{\mu\rho\beta\nu} \tag{8.44}$$

$$\mathfrak{A}^{\mu\nu\rho\alpha} = \mathfrak{A}^{\alpha\rho\nu\mu} = \mathfrak{A}^{\mu\alpha\rho\nu} \tag{8.45}$$

$$\mathfrak{B}^{\mu\gamma\nu\beta\rho\alpha} = \mathfrak{B}^{\alpha\rho\beta\nu\gamma\mu} = \mathfrak{B}^{\mu\alpha\rho\beta\nu\gamma} \tag{8.46}$$

In each equation above the first equality uses the fact that the trace of n γ matrices in a particular order is the same if the order is fully reversed (or alternatively if mirror image of the order is used). The second equality uses the cyclic properties of the trace to put γ^μ at the start in each case. Substituting the above identities in Eq. (8.42), we may easily demonstrate that $\mathcal{T}'^{\mu\nu\rho} = \mathcal{T}^{\mu\rho\nu}$. We may also easily demonstrate that

$\mathcal{T}'^{\mu\rho\nu} = \mathcal{T}^{\mu\nu\rho}$. Thus we obtain the simple relation that the expression for either vertex is the same,

$$T'^{\mu\nu\rho}(-p,-k,k-p) = T^{\mu\nu\rho}(p,k,p-k) \tag{8.47}$$

Implementing the above simplifications we may, formally, write down the full expression for the photon self-energy as,

$$\begin{aligned} i\Pi^{\mu\nu}(p) &= \frac{i}{\beta}\sum_{k^0}\int\frac{d^3k}{(2\pi)^3} iT'^{\mu\rho\gamma}(-p,-k,k-p)\mathcal{D}_{\rho\zeta}(k) iT^{\nu\zeta\delta}(p,k,p-k)\mathcal{D}_{\delta\gamma}(p-k) \\ &= \frac{i}{\beta}\sum_{k^0}\int\frac{d^3k}{(2\pi)^3} iT^{\mu\rho\gamma}(p,k,p-k)\mathcal{D}_{\rho\zeta}(k) iT^{\nu\zeta\delta}(p,k,p-k)\mathcal{D}_{\delta\gamma}(p-k). \end{aligned} \tag{8.48}$$

The diagram that we are considering is that of the upper figure in Fig. (8.5). We

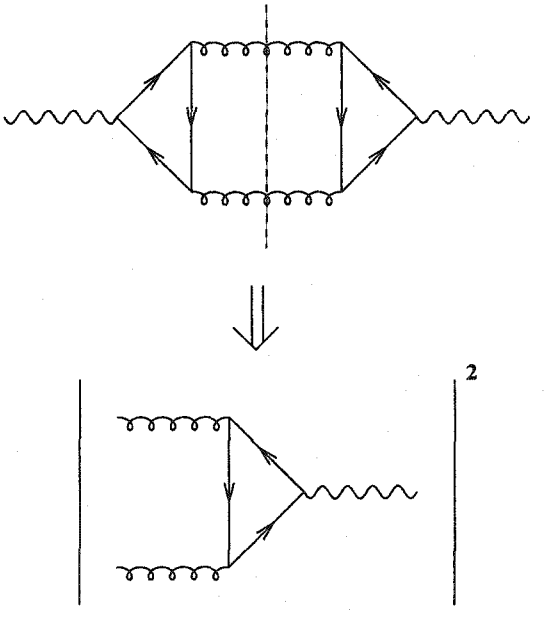

Figure 8.5: The Full photon self-energy at three loop and the cut that is evaluated.

perform this calculation in the Feynman gauge for the gluons, thus

$$\mathcal{D}_{\rho\zeta}(k) = \frac{-ig_{\rho\zeta}}{k^2}. \tag{8.49}$$

In order to calculate the differential rate of back to back dileptons we need to evaluate the discontinuity of the photon self-energy, as was elucidated in the preceding chapter. This involves, first, converting the sum over discrete k^0 frequencies into a contour integral over a complex continuous k^0, as was done for q^0. This would be followed by the evaluation of the contour integral by summing over the residues of the integrand at each of the poles of k^0. Finally we look for poles and branch cuts in this expression in terms of p^0 by analytically continuing p^0 onto the real axis. There are many poles in k^0 for which we have to evaluate residues. Some of these poles are in the denominators of the gluon propagators, while some are in the vertices $T^{\mu\nu\rho}, T'^{\mu\nu\rho}$. As the residues at each of these poles is analytically continued in p^0 from a discrete imaginary frequency to a complex number and finally to a real continuous energy, various branch cuts in will appear. These are branch cuts of the self-energy as a function of p^0 on the real line of p^0. Evaluating the residue of a function at a particular k^0, essentially means removing the pole and substituting that value of k^0 in the remaining expression. This changes the analytic structure of the entire function in terms of k^0. When we are looking for discontinuities in p^0, we will essentially return to the residues that we evaluated, recall that we have not performed the d^3k or d^3q integrations, at this stage the branch cuts on the real p^0 axis are manifested in the expressions which will encounter poles in the d^3k or d^3q integrations as $p^0 \to E + i\epsilon$. The presence of the $i\epsilon$ will allow each integrand to be unambiguously broken up into a set of principle values and imaginary parts. Twice the integral over the imaginary parts will give us the required discontinuity.

This procedure is throughly expanded upon in the next chapter for two-loop self-energies. For our present purposes, we note that to obtain the discontinuity we have essentially chosen a pair of poles in the expression, and evaluated the residue at the pole in the dk^0 integration and twice the imaginary part at the pole in the d^3k, d^3q integration as $p^0 \to E + i\epsilon$. Each such combination constitutes a 'cut' of the self energy or a part of a cut of a self-energy. A cut is represented as a line drawn across the self-energy, through the objects (propagators, vertices) whose poles were

chosen to constitute the cuts. Which exact propagators inside a vertex, the cut line passes through will be set by the energy momentum delta functions obtained from the residue and discontinuity procedure. Suffice to say that a cut line necessarily cuts a self energy diagram into two disjoint pieces. If we denote the feynman rule for one of the pieces as $\mathcal{M}_1$ and the other by $\mathcal{M}_2$ then this particular discontinuity of the self-energy gives the Feynman rule for $\mathcal{M}_2^*\mathcal{M}_1$ or $\mathcal{M}_1^*\mathcal{M}_2$. If the cut is symmetric *i.e.*, $\mathcal{M}_1 = \mathcal{M}_2$, then we obtain the square of the amplitude for the process $|\mathcal{M}_1|^2$. For this calculation we are solely interested in the square of the amplitude of the process shown in the lower diagram in Fig. (8.5). Our preceding discussion indicates that this will be given by the cut line indicated in the upper diagram. This is a new process of gluon gluon fusion to produce a heavy photon resulting in a dilepton. This is an entirely new process which has never been discussed before. The other cuts represent extra finite density contributions to processes already non-vanishing at zero density.

The above discussion indicates that we merely have to look for poles in the denominators of the gluon propagators. The denominators are

$$\frac{1}{\mathbf{k}^2}\frac{1}{\mathbf{p}^2} = \frac{1}{(k^0-k)(k^0+k)}\frac{1}{(k^0-p^0-E_{p-k})(k^0-p^0+E_{p-k})} \tag{8.50}$$

Where $E_{p-k} = |\vec{p}-\vec{k}|$. The k^0 integration will encounter four possible poles at $k^0 = \pm k$, and $k^0 = p^0 \pm E_{p-k}$ Where the discontinuity in p^0 will result will depend on which pole of k^0 is chosen. All choices will not lead to the desired process.

We begin evaluating the residue of the remaining integrand at the pole $k^0 = k$. At this pole the remaining denominators are

$$\frac{1}{2k}\frac{1}{p^0-k+E_{p-k}}\frac{1}{p^0-k-E_{p-k}}.$$

On analytically continuing p^0 we will obtain two possibilities: $p^0 = E = k + E_{p-k}$ or $p^0 = k - E_{p-k}$. The second pole will lead to the photon invariant mass $E^2 - p^2 < 0$ *i.e.*a space like photon, we ignore this cut. Substituting the first value for p^0, we obtain the discontinuity of the self energy at $E = k + E_{p-k}$. This turns the gluon denominators into

$$-i\pi\delta(E-k-E_{p-k})\frac{1}{2k}\frac{1}{E_{p-k}}.$$

Evaluating the residue at $k^0=-k$, we obtain the remaining denominators as

$$\frac{1}{-2k}\frac{1}{-p^0-k-E_{p-k}}\frac{1}{-p^0-k+E_{p-k}}.$$

This leads to possible values for $p^0=-k-E_{p-k}$ or $E_{p-k}-k$, one leads to a negative energy and the other to a spacelike invariant mass, thus we ignore this k^0 pole altogether.

Evaluating the residue at $k^0=p^0+E_{p-k}$, we once again obtain a negative energy or space like photon and thus this residue is ignored as well. The final residue is at $k^0=p^0-E_{p-k}$. This leads to possible discontinuities at $p^0=E=k+E_{p-k}$ and $E_{p-k}-k$. The second possibility leads to a spacelike photon and is ignored. The first gives a time like photon with positive energy and thus is included in the cuts considered. This set of choices turns the gluon denominators into

$$-i\pi\delta(E-k-E_{p-k})\frac{1}{2k}\frac{1}{-2E_{p-k}}$$

Thus, in performing the sum over the Matsubara frequencies k^0 we will only confine our selves to two poles: one on the positive side of the real axis at $k^0=k$, this will be a residue of the semicircular contour on the right hand side; one on the negative side at $k^0=p^0-E_{p-k}$, this will be a residue of the semicircular contour on the left hand side. As would have been noted, we are now precisely following the method prescribed in chapter 3 of Ref. [74]. In the first pole we will analytically continue p^0 to $E=k+E_{p-k}$; in the second pole we will analytically continue p^0 to $E=k+E_{p-k}$ leading to a

$$k^0=p^0-E_{p-k}=E-E_{p-k}=k+E_{p-k}-E_{p-k}=k.$$

Thus in the rest of the expression we will simply replace $k^0\rightarrow k$ and use the appropriate distribution functions in each case depending on whether the initial k^0 pole

was on the positive or negative side. Then we will use the delta function to set the value of k. The results of this procedure as well as the final expressions and their properties will be discussed in the next section.

8.7 The calculation

In this section we evaluate the particular cut of Fig. (8.5) of the three loop photon self-energy. Focusing on the two poles of k^0 highlighted in the preceding section and performing the associated analytic continuation of p^0 we obtain the discontinuity in the photon self-energy as

$$\begin{aligned}
\mathrm{Disc}\Pi^{\mu\nu} = & \int \frac{d^3k}{(2\pi)^3} T^{\mu\rho\gamma}(E,k,E_{p-k}) \frac{g_{\rho\zeta}}{2k} T^{\nu\zeta\delta}(E,k,E_{p-k}) \frac{g_{\delta\gamma}}{2E_{p-k}} \\
& \times \left[\frac{1}{2} + \frac{1}{e^{\beta k}-1}\right](-1)\Big(-2\pi i\delta(E-k-E_{p-k})\Big) \\
& - \int \frac{d^3k}{(2\pi)^3} T^{\mu\rho\gamma}(E,k,E_{p-k}) \frac{g_{\rho\zeta}}{2k} T^{\nu\zeta\delta}(E,k,E_{p-k}) \frac{g_{\delta\gamma}}{2E_{p-k}} \\
& \times \left[\frac{1}{2} + \frac{1}{e^{\beta(-E_{p-k})}-1}\right](-1)\Big(-2\pi i\delta(E-k-E_{p-k})\Big)
\end{aligned} \tag{8.51}$$

Combining the gluon distribution functions and using the relation $E_{p-k}+k=E$, we obtain

$$\begin{aligned}
\mathrm{Disc}\Pi^{\mu\nu} = & \int \frac{d^3k}{(2\pi)^3} T^{\mu\rho\gamma}(E,k,E_{p-k}) \frac{g_{\rho\zeta}}{2k} T^{\nu\zeta\delta}(E,k,E_{p-k}) \frac{g_{\delta\gamma}}{2E_{p-k}} \\
& \times \Big(e^{\beta E}-1\Big) n(k) n(E_{p-k}) \Big(2\pi i\delta(E-k-E_{p-k})\Big)
\end{aligned} \tag{8.52}$$

To obtain the differential rate for dilepton production we need the quantity $r = \left[\frac{p_\mu p_\nu}{\mathbf{p}^2} - g_{\mu\nu}\right] \mathrm{Disc}[-i\Pi^{\mu\nu}]$. We substitute the expression for $\mathrm{Disc}[\Pi^{\mu\nu}]$ and note that the intervening factors of the metric as well the factor $\frac{p_\mu p_\nu}{\mathbf{p}^2} - g_{\mu\nu}$ may be obtained from the sum over the polarizations of the gluons and the photon *i.e.*,

$$\sum_i \varepsilon^*_{i\,\rho}(\mathbf{k})\varepsilon_{i\zeta}(\mathbf{k}) \to -g_{\rho\zeta} \tag{8.53}$$

$$\sum_l \varepsilon_{l\mu}(\mathbf{p})\varepsilon^*_{l\,\nu}(\mathbf{p}) = \frac{p_\mu p_\nu}{\mathbf{p}^2} - g_{\mu\nu} \tag{8.54}$$

Substituting the above relations into r, we obtain

$$\begin{aligned} r = \sum_i \sum_j \sum_l \int \frac{d^3k}{(2\pi)^3 2k 2E_{p-k}} \Big[\varepsilon_{l\mu} T^{\mu\rho\gamma} \varepsilon^*_{i\,\rho} \varepsilon^*_{j\,\gamma}\Big] \Big[\varepsilon^*_{l\,\nu} T^{\nu\zeta\delta} \varepsilon_{j\,\delta} \varepsilon_{i\zeta}\Big] \\ \times \Big(e^{\beta E} - 1\Big) n(k) n(E_{p-k}) \Big(2\pi\delta(E - k - E_{p-k})\Big) \end{aligned} \tag{8.55}$$

Introducing factors of 2π and extra delta functions we may formally write the above as a straightforward kinetic theory equation,

$$\begin{aligned} r = \sum_i \sum_j \sum_l \int \frac{d^3k}{(2\pi)^3 2k} \int \frac{d^3\omega}{(2\pi)^3 2\omega} \Big[\mathcal{M}_{i,j,l}\Big]^* \Big[\mathcal{M}_{i,j,l}\Big] \\ \times \Big(e^{\beta E} - 1\Big) n(k) n(E_{p-k}) \Big((2\pi)^4 \delta^4(\mathbf{p} - \mathbf{k} - \mathbf{w})\Big) \end{aligned} \tag{8.56}$$

Where $\mathcal{M}_{i,j,l}$ is the matrix element for two gluons in polarization states i, j to make a transition into a photon in a polarization state l. The entire process is weighted by the appropriate thermal gluon distribution functions and has the usual energy momentum conserving delta function.

In this calculation both gluons are massless; thus they have only two physical polarizations. For a gluon travelling in the positive z direction, these are,

$$\varepsilon^\mu_+ = \frac{1}{\sqrt{2}} \begin{pmatrix} 0 \\ 1 \\ i \\ 0 \end{pmatrix} \qquad \varepsilon^\mu_- = \frac{1}{\sqrt{2}} \begin{pmatrix} 0 \\ 1 \\ -i \\ 0 \end{pmatrix}$$

The photon being massive has an extra polarization ε^μ_3. For a massive photon with energy E and three momentum p travelling in the positive z direction this is ,

$$\varepsilon_3^\mu = \frac{1}{|\mathbf{p}|}\begin{pmatrix} p \\ 0 \\ 0 \\ E \end{pmatrix}$$

Using these polarization vectors, the matrix elements may be easily expressed. Recall that in the evaluation of $T^{\mu\nu\rho}$ we had performed a contour integration over q^0 an obtained six residues. We did not elucidate the residues at the time, as we still had two complex frequencies, k^0 and p^0, in the expressions. Before we provide the expressions for these quantities we note the following relations between them, noted during the calculation and subsequent contraction with the polarization vectors,

$$\mathcal{M}_{i,j,+} = \mathcal{M}_{i,j,-} = 0 \tag{8.57}$$

i.e., there is no contribution to the transverse modes of the photon.

$$\mathcal{M}_{+,-,j} = \mathcal{M}_{-,+,j} = 0 \tag{8.58}$$

as expected (and pointed out before), both gluons have to arrive with the same polarization, *i.e.*, either both must be right handed or both left handed.

We are now in a position to write down the various matrix elements $\mathcal{M}$. Recall that in the initial q^0 contour integration, there were six poles at which residues were calculated. As a result we have six matrix elements one from each residue. We did not present the results of the contour integration at that point as many angular integrations, and imaginary frequencies remained. Thus, performing all the angular integrations, frequency sums and contractions with polarization vectors, the results are:

$$\mathcal{M}_{+,+,3} = \mathcal{M}_{-,-,3} = \mathcal{M}_1 + \mathcal{M}_2 + \mathcal{M}_3 + \mathcal{M}_4 + \mathcal{M}_5 + \mathcal{M}_6$$

$$
\begin{aligned}
&= \int \frac{dqq^2\Delta\tilde{n}(E_q,\mu)}{(2\pi)^3 E_q|\mathbf{p}|}\left[32\,\frac{\pi\,m^2 p\,(4\,q^2-p^2+E^2+4\,m^2)\ln(\left|-\sqrt{q^2+m^2}+q\right|)}{[(E-p)^2-4(q^2+m^2)]\,[(E+p)^2-4(q^2+m^2)]\,q}\right.\\
&-32\,\frac{\pi\,m^2 p\,(4\,q^2-p^2+E^2+4\,m^2)\ln(\sqrt{q^2+m^2}+q)}{[(E-p)^2-4(q^2+m^2)]\,[(E+p)^2-4(q^2+m^2)]\,q}\\
&-16\,\frac{\pi\,m^2\left(E-2\sqrt{q^2+m^2}\right)\ln(\left|-1/2\,E^2+1/2\,p^2+E\sqrt{q^2+m^2}-qp\right|)}{q\left(E+p-2\sqrt{q^2+m^2}\right)\left(2\sqrt{q^2+m^2}-E+p\right)}\\
&+16\,\frac{\pi\,m^2\left(2\sqrt{q^2+m^2}+E\right)\ln(\left|-1/2\,E^2+1/2\,p^2-E\sqrt{q^2+m^2}-qp\right|)}{q\left(-2\sqrt{q^2+m^2}-E+p\right)\left(2\sqrt{q^2+m^2}+E+p\right)}\\
&+16\,\frac{\pi\,m^2\left(E-2\sqrt{q^2+m^2}\right)\ln(\left|-1/2\,E^2+1/2\,p^2+E\sqrt{q^2+m^2}+qp\right|)}{q\left(E+p-2\sqrt{q^2+m^2}\right)\left(2\sqrt{q^2+m^2}-E+p\right)}\\
&\left.-16\,\frac{\pi\,m^2\left(2\sqrt{q^2+m^2}+E\right)\ln(\left|-1/2\,E^2+1/2\,p^2-E\sqrt{q^2+m^2}+qp\right|)}{q\left(-2\sqrt{q^2+m^2}-E+p\right)\left(2\sqrt{q^2+m^2}+E+p\right)}\right]
\end{aligned}
\tag{8.59}
$$

Where, for obvious reasons we have chosen $\vec{p}$ in the z direction. In the interest of simplicity, we have limited the $\vec{k}$ to also be only along the z direction. Thus we will not be performing the angular integration on d^3k. Thus we will be concentrating on the virtual photon produced only by back to back gluons of unequal momenta, and will eventually compare with the rate of production from only back-to-back quarks of unequal momenta. We are thus breaking Yang's symmetry by the introduction of a net three momentum p. The above expression gives the appearance of being plagued with singularities, however, on expanding around each of the singularities, we note that all of them cancel between the six terms. There is still the dq integration to be performed, this is done numerically.

The differential production rate for pairs of massless leptons with total energy E and and total momentum $\vec{p} = (0, 0, p)$ is given in terms of the discontinuity in the photon self-energy as (see chapter 6)

$$
\frac{dR}{d^4p} = \frac{e^2}{3(2\pi)^5}\frac{r}{(\mathbf{p}^2)}\frac{1}{e^{\beta E}-1} \tag{8.60}
$$

As we have limited the gluons to be back-to-back with one of them parallel to the

direction of the virtual photon, we are not performing the incoming angular integration. Thus we calculate the derivative of the above mentioned rate with respect to the incoming gluon angle, *i.e.*,

$$\frac{dR}{d^4p d\Omega_k} = \frac{e^2}{3(2\pi)^5(\mathbf{p}^2)\left[e^{\beta E}-1\right]}\frac{dr}{d\Omega_k} \tag{8.61}$$

Where $r = \left[\frac{p_\mu p_\nu u}{\mathbf{p}^2} - g_{\mu\nu}\right] \mathrm{Disc}\left[-i\Pi^{\mu\nu}\right]$. The three momentum p, chosen in the z direction.

As mentioned before, temperatures in the plasma formed at RHIC and LHC have been predicted to lie in the range from 300-800 MeV [64, 77]. For this calculation, we use a $T = 400$ MeV and 800 MeV. To evaluate the effect of a finite chemical potential we perform the calculation with two extreme values of chemical potential $\mu = 0.1T$ (left plot in Fig. 8.6) and $\mu = 0.5T$ (Right plot in Fig. 8.6) [66]. This calculation, is performed for two flavours of quarks, with current masses.

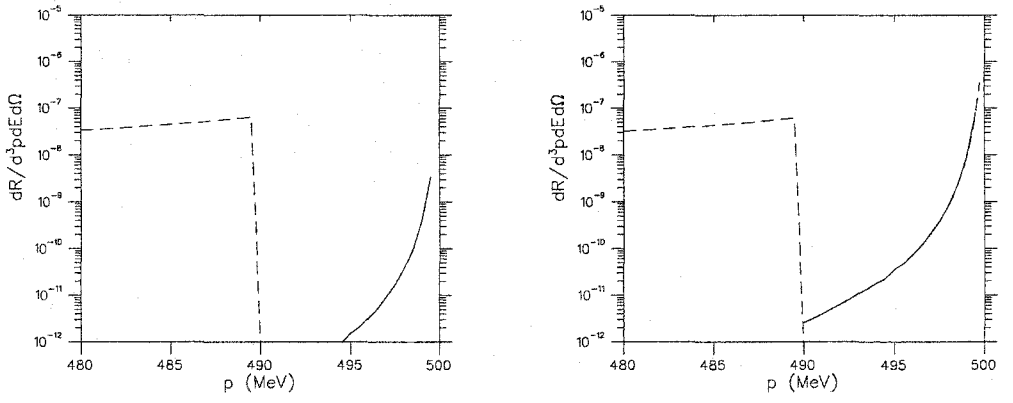

Figure 8.6: The differential production rate of low mass dileptons from two back-to-back processes. Invariant mass runs from 30 MeV to 0 MeV. The energy of the dilepton is $E = 500$MeV, and the abscissa is the three momentum p. The dashed line represents the contribution from the process $q\bar{q} \to e^+e^-$. The solid line corresponds to the process $gg \to e^+e^-$. Temperature is 400 MeV. Quark chemical potential is 0.1T. The second figure is the same as the first but with $\mu = 0.5T$

In Fig. (8.6), the differential rate (Eq. (8.61)) for the production of dileptons with an invariant mass from 0 to 140 MeV is presented. The energy is held fixed at 500 MeV and the three momentum p of the dilepton is varied. In the figures, the

dashed line is the rate from tree level $q\bar{q}$ (Eq. (8.10)); the solid line is that from the process $gg \rightarrow e^+e^-$. We note that in both cases the gluon-gluon process dominates at very low mass and dies out at higher mass leaving the $q\bar{q}$ process dominant at higher mass or lower momentum. The Born term displays a sharp cutoff at photon invariant mass$M = \sqrt{2mE}$. The back-to-back annihilation of two massive quarks (of mass m.) to form the virtual photon of energy E and invariant mass M is no longer kinematically allowed. Also, the annihilation of a quark anti-quark pair to form a dilepton is not allowed for any incoming angle for dileptons with an invariant mass $M < 2m$. The gluons being massless, continue to contribute in this region: this contribution is shown in the right panel of Fig. (8.7). They are thus the main signal at very low invariant mass and intermediate dilepton energy. In Fig. (8.7), we indicate the influence of a higher plasma temperature on the rates. Here, a plasma temperature of 800 MeV and $\mu = 0.5T$ is used; the left panel displays the rates below the Born term threshold and the right panel displays the rates above threshold. We note in the left panel of Fig. (8.7), as expected, that the gluon fusion term rises further due to thermal loop enhancement. In the right panel we note that the rates for $gg \rightarrow e^+e^-$ continue to rise due to the growing distribution functions for soft gluons.

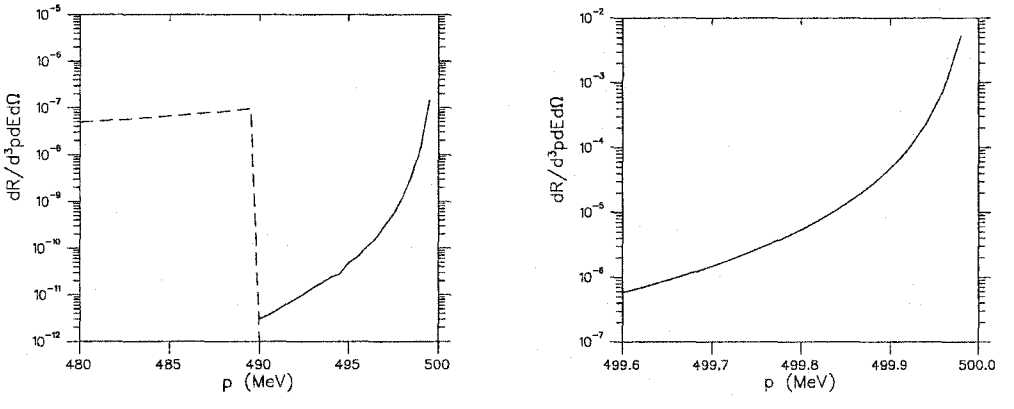

Figure 8.7: Left panel is same as Fig. (8.6) but with a temperature of 800 MeV. Quark chemical potential is 0.5T. Right panel is the rate of $gg \rightarrow e^+e^-$ beyond the Born term threshold.

However, the overall magnitude of the gluon gluon fusion term is rather small compared to the Born term at comparable invariant masses. Thus, this process may be completely masked at large invariant mass by the Born term in equilibrium plasmas, but it is certainly worth additional scrutiny.

8.8 Summary and discussions

In this chapter we have performed a calculation to estimate the effects of a non-zero quark chemical potential on the intermediate mass dilepton spectra. We have found that a new set of diagrams may become important at finite temperature and finite density. These diagrams lead to a new contribution to the photon self-energy at the 3-loop order. There are various cuts to this diagram. Most of these result in finite density contributions, and/or higher order excess contributions to well known processes. One of the cuts however represents an entirely new process. The contribution of this diagram to the differential production rate of back-to-back ($|\vec{p}| = 0$ to $|\vec{p}| \to E$) dileptons is estimated. This is then compared with the contribution emanating from the tree level process of $q\bar{q}$ annihilation. The rate from this new process is found to be comparable and even larger than the simple tree level rate at low invariant mass. One possible reason for this large magnitude could be that the gluon-gluon diagram is enhanced by the Bose-Einstein distribution function of the gluons. Also, due to the Born term threshold at twice the quark mass, there is no contribution from the Born term for invariant masses below this limit. The finite density contribution from two gluon fusion may become the most dominant contribution in this regime.

These results demonstrate the importance of these finite μ processes on the dilepton spectra emanating from a quark gluon plasma with a quark-antiquark asymmetry. It is simple to note that this diagram is most sensitive to gluon number. The early stages of the plasma have been predicted to be gluon dominated [103]. The contribution from this diagram should clearly shine in such an environment.

The treatment in this thesis is rather exploratory, and will be improved upon. Our

goal here was simply to establish the existence of a signal. One may have desired, for example, that the calculation be extended to arbitrary $\vec{p}$. However, similar extensions, even in the HTL approximation, are known to be rather involved [104]. There are also the other cuts which have yet to be computed. Most of these diagrams also suffer from the defect of having an internal line which may go on shell. The bare propagators will have to replaced by resumed HTL propagators, in the event that the momentum flowing through it becomes very small, or close to on shell. These aspects, along with others, will be addressed in upcoming work.

9

High Mass Dileptons and Mass Divergences

9.1 Introduction

In the final chapter of this thesis, we move our attention to high energy dilepton production *i.e.*, the energy of the virtual photon $E >> T$. Far enough in this regime, the hard thermal loop effects of chapter 7 and the finite density effects of chapter 8 have become negligible. By now, one might expect, that the Born term has achieved the stature as the most dominant, thermal contribution from the plasma by far. This picture may be upset by yet another possibility. The energy of the dilepton and as a result the scale of the processes under consideration is much higher than the temperature, which in turn, is much higher than the mass of the quarks m involved. If, in the expressions for higher order contributions, m were to appear in a denominator or as the argument of a log, higher order contributions would be greatly enhanced. If m were set to zero in such an expression, one would, no doubt, obtain an infinite expression. This is referred to as a mass divergence.

Physically, such a condition is realised in a collinear emission or absorption process involving only massless particles. This is to be distinguished from the infrared divergence, encountered in the emission or absorption of massless gauge particles (photons, gluons) from massive or massless fermions. Such divergences are present in most individual diagrams that together constitute the contribution to a process at a given order. In vacuum processes in QED, with or without electron mass, such divergences are present in individual diagrams. They however cancel order by order, when

all the different diagrams at a given order in the coupling constant are summed. This may be demonstrated by explicit proof [106, 107, 108]. A general theorem has also been deduced, that indicates the cancellation of such divergences in the evaluation of physically measurable quantities (the Kinoshita, Lee, Nauenberg (KLN) theorem [109, 110]).

The question of whether these results may be generalized from QED to QCD, from vacuum to thermal calculations; and if so how such a generalization may be realised, has led to a lot of theoretical activity. It may even be true that thermal field theories introduce an entirely new brand of divergences not present in the vacuum theory [111] (see also Ref. [74]). The explicit diagramatic cancellation fails for a class of NNLO[1] processes in QCD [112]. However, the NLO[2] (and obviously LO) e^+e^- annihilation to hadrons has been shown to be both collinear and infrared safe (see Ref. [113]). Note that this vacuum process is very similar to just the reverse of dilepton production from a QGP. The difference lies in the mere absence of thermal factors. The infrared and collinear singularity, behaviour of dilepton production at NLO or two loops will involve our attention in this chapter.

There is also another reason for exploring this problem. The reader may have sensed a rather sudden transition to three loops or NNLO dilepton production in the previous chapter. This became necessary to allow one to traverse the, dilepton, energy spectrum, in ascending order. There we chose to concentrate on only one cut of the entire self-energy and stifled discussion regarding the variety of other cuts. Such will not be the case here: the massive vector self-energies at two loops will be throughly examined. Each cut will be ascribed a physical interpretation. The imaginary parts of these retarded self-energies represent extremely important quantities in thermal field theory. They provide information about various quantities of physical interest in the medium. Primary among these are the decay and formation rates of particles [114]. Boson self-energies provide information about quantities like Z decay rates

[1]Next to Next to Leading Order

[2]Next to Leading Order

[101], and as is the case in this thesis, the production rates of dileptons and real photons [115] from a quark-gluon-plasma (QGP). Thus a physical understanding of the various cuts may aid in our understanding of these processes.

The possibility that a divergence may arise in NLO dilepton production was explored previously using various methods. First, among these was the calculation by Baier *et al.* [116]. This included reactions like three particle fusion ($q\bar{q}g \to \gamma^*$), Compton scattering ($qg \to q\gamma^*$ or $\bar{q}g \to \bar{q}\gamma^*$), pair annihilation ($q\bar{q} \to g\gamma^*$), Born term with vertex correction, and Born term with quark or antiquark self-energy correction. This calculation was performed in the real time formalism, both in a Feynman diagram approach in thermo-field dynamics, and by taking the imaginary part of the two loop photon self-energy. In the case of massless QCD, each of the contributions mentioned above contain infrared or collinear singularities. These were regulated at intermediate stages of the calculation by giving masses to the quarks and gluons. The combined rate from all these processes was then found to be free of all divergences in the limit of vanishing masses. This calculation was also performed simultaneously by another group [117], who dimensionally regularized the singularities at intermediate stages of the calculation. The end result remained the same: when all the different processes were summed, the divergences cancelled and dilepton rate at next-to-leading order remained finite.

However, recently, the calculation was repeated yet again [99, 101]. This time employing a multiple scattering expansion obtained by reorganizing cuts with loops in terms of incoming and outgoing particles with the same quantum numbers [118]. In the following, we will show how such an expansion may result in some cuts of the two-loop photon self-energy. These authors found the surprising new result that the divergences do not cancel when the various physical contributions to the NLO rate are summed. A remnant collinear divergence remained. The regulator, in this case, was a minimum virtuality of internal propagators, which tended to become singular. The virtuality may be time-like or space-like depending on the process in question. A number of observations are in order here. The processes are limited to the region

where the dilepton mass is much larger than the temperature i.e., $E >> T$. The decay or formation of such a virtual photon always requires at least two real hard partons (where hard indicates energy or momentum far greater than the temperature). In the interest of simplicity, these authors focus attention on a small part of the phase space of the processes, where they claim the most dominant contribution may reside. These are processes containing two real hard and at least one soft parton (where soft indicates energy or momentum of the order of the temperature). All other kinematic regions, designated as sub-dominant, are neglected. In this limit one may obtain simple analytical relations for the various processes; the expressions for each of the processes were truncated at order T^2/E^2. As their final answer remains divergent, the remaining parts of phase space and parts of the expressions truncated do not make any further appearance. This observation of a remnant collinear divergence is a result of extreme importance: on a theoretical level it signals a failure of the KLN theorem [109, 110] for dilepton production even in the presence of a large mass scale; on an phenomenological level it indicates that higher order processes may not be negligible compared to the Born term even for large mass dilepton production.

This result has been commented upon [119], and the issue of divergences remained unresolved [120]. In the wake of this strife, we revisit this problem in a systematic calculation. Also, to the best of our knowledge, a complete calculation of the imaginary part of a heavy vector boson retarded self-energy in the imaginary time formalism has yet to be performed. This is the subject of this chapter. The scalar boson self-energy was examined recently [121]. There are various advantages to such a calculation: the basic Feynman rules are easily generalized from zero-temperature; there is no doubling of degrees of freedom and no matrix structure of propagators; multiple poles which lead to ill-defined products of delta functions in the real-time formalism are easily and naturally handled both in the Matsubara sums and in the analytic continuation. The purpose of this calculation is thus many-fold. A first goal is to enumerate and interpret the various physical contributions contained in the imaginary part of the two-loop self-energies. In doing this, it shall then be shown that cuts containing

loops may be re-expressed as interference between tree diagrams and Born term with a thermal medium spectator. Importantly, we also demonstrate how double poles may be simply and elegantly dealt with, in the Matsubara sum and in the analytic continuation to real energies. We finally concentrate on eventual collinear and infrared divergences in the ensuing rates. In this study, we focus on the singularity structure in the region of phase space investigated by the authors of Refs. [99, 101]. Even though we explicitly calculate the self-energies of static virtual photons, the results may be easily applied to other vector bosons in-medium, with the exception of the gluon which admits other self-energies in a QGP.

The various sections are organized as follows: in Sect. 9.2 we begin by evaluating one of the self-energy diagrams of a static photon with an imaginary energy at two loops (the impatient reader may skip ahead to Sect. 9.6 where the various cuts of the self-energy are recombined to provide physical interpretations of the various terms obtained; following which the infra-red behaviour of heavy photon production will be discussed); in Sect. 9.3 we analytically continue the photon energy to real values and obtain the imaginary part of the corresponding retarded self-energy; in Sect. 9.4 we evaluate the other self-energy topology; in Sect. 9.5 we analytically continue this self-energy to real values of photon energy and find the retarded imaginary self-energy; in Sect. 9.6 we combine the tree-like cuts and reinterpret them as physical processes with thermal distributions on the phase space factors; in Sect. 9.7 we attempt to interpret cuts containing loops in terms of the recently proposed spectator interpretation [118]; in Sect. 9.8 we take the limit of heavy-photon production ($E >> T$), and evaluate the various contributions; in Sect. 9.9 we combine all cuts, demonstrate the cancellation of the collinear and infrared divergences, and present our results; we present our conclusions and brief discussions in Sect. 9.10. A few short appendices follow. In the interest of quantitative accuracy and repeatability, we have presented many calculational details: the issue being addressed here is technical, and thus demands a rigorous treatment.

9.2 The self-energy: Topology I

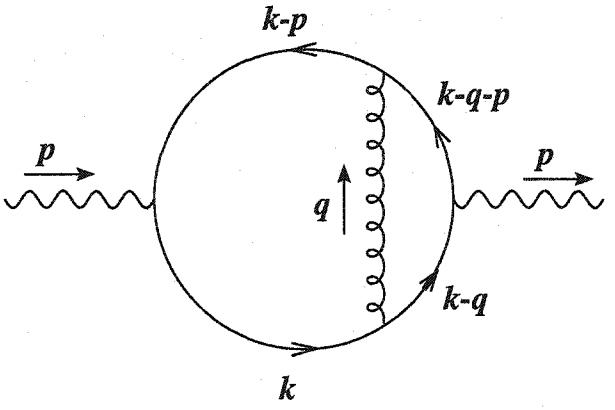

Figure 9.1: The first topology for the self-energy.

We evaluate the photon self-energy with a gluon running across as shown in Fig. 9.1. To begin with, we derive the expression for the effective quark photon vertex corrected by a gluon running across, *i.e.*,

$$ie\Gamma^{\mu} = ie\gamma^{\mu} + ie\delta\Gamma^{\mu}.$$

Where e may be taken to be the electric charge of the quark. In standard notation, the expression for the effective vertex in Feynman gauge may be written down as

$$ie\Gamma^{\mu} = \frac{i}{\beta}\sum_{q^0}\int\frac{d^3q}{(2\pi)^3}\frac{-ig_{\rho\sigma}\delta^{ab}}{q^2}(it^a_{i,j}g\gamma^{\rho})\frac{i(\not{k}-\not{q}-\not{p})}{(k-q-p)^2}(ie\gamma^{\mu})\frac{i(\not{k}-\not{q})}{(k-q)^2}(it^b_{j,k}g\gamma^{\sigma}). \quad (9.1)$$

The Matsubara sum in the effective vertex may be simply evaluated using the method of Pisarski [76]. In our notation (see chapter VI, see also [97]), this is given in the static limit ($\vec{p}=0$) as,

$$\delta\Gamma^{\mu} = \frac{g^2C_{ik}}{4}\int\frac{d^3q}{(2\pi)^3}\sum_{s_1,s_2,s_3}\frac{(\not{k}-\not{q})_{s_2}\gamma^{\mu}(\not{k}-\not{q})_{s_3}}{qE_{q-k}E_{q-k}(p^0-(s_2-s_3)E_{q-k})}$$
$$\times\left\{-s_3\frac{(s_1+s_2)/2-s_1\tilde{n}(E_{q-k})+s_2n(q)}{k^0-s_1q-s_2E_{q-k}}+s_2\frac{(s_1+s_3)/2-s_1\tilde{n}(E_{q-k})+s_3n(q)}{k^0-p^0-s_1q-s_3E_{q-k}}\right\}. \quad (9.2)$$

Where s_1, s_2, s_3 are sign factors which are summed over the values of ± 1. We may now use the above result to write the full self-energy of the photon in the static limit as

$$i\Pi^{\mu}_{\mu} = \frac{i}{\beta}\sum_{k^0}\int\frac{d^3k}{(2\pi)^3}(-1)Tr\sum_{ss_4}\left[e\gamma_\mu\delta_{ki}\frac{\gamma^\beta s_4\hat{k}_{\beta,s_4}}{2(k^0-p^0-s_4k)}e\delta\Gamma^{\mu}_{i,k}\frac{\gamma^\alpha s\hat{k}_{\alpha,s}}{2(k^0-sk)}\right]. \quad (9.3)$$

Where, $\hat{k}_s$ stands for the four component quantity:

$$\left\{s,\frac{k_x}{k},\frac{k_y}{k},\frac{k_z}{k}\right\} = \left\{s,0,0,1\right\}.$$

We note that the effective vertex may be written as

$$\delta\Gamma^{\mu} = \gamma^\rho\gamma^\mu\gamma^\sigma\delta\Gamma_{\rho\sigma},$$

to highlight the structure of γ matrices contained within it. The trace of the γ matrices is given simply as,

$$Tr[\gamma_\mu\gamma^\beta\gamma^\rho\gamma^\mu\gamma^\sigma\gamma^\alpha] = 16g^{\beta\rho}g^{\sigma\alpha}.$$

This gives the full self-energy as

$$\Pi^{\mu}_{\mu} = \frac{-4}{\beta}\sum_{k^0}\int\frac{d^3k}{(2\pi)^3}\sum_{ss_4}e^2\left[\frac{s\hat{k}_{\alpha,s}}{k^0-sk}\delta\Gamma^{\beta\alpha}\frac{s_4\hat{k}_{\beta,s_4}}{k^0-p^0-s_4k}\right]. \quad (9.4)$$

For convenience we change $s_2 \to -s_3$ and $s_3 \to -s_2$. To evaluate the Matsubara sum we follow the method of reference [74]. This method converts the Matsubara sum into a contour integration in the complex plane of k^0, *i.e.*,

$$\begin{aligned}\Pi^{\mu}_{\mu} = \frac{-4e^2g^2}{2\pi i}\int_{-i\infty+\epsilon}^{i\infty+\epsilon}dk^0\int\frac{d^3kd^3q}{(2\pi)^6}[1/2-\tilde{n}(k^0)]\frac{s\hat{k}_{\alpha,s}}{s_5k^0-sk}\\ \times\left[\frac{\widehat{(q-k)}^{\alpha}_{s_2}\widehat{(q-k)}^{\beta}_{s_3}}{q(p^0-(s_2-s_3)E_{q-k})}\left\{s_2\frac{(s_1-s_3)/2-s_1\tilde{n}(E_{q-k})-s_3n(q)}{s_5k^0-s_1q+s_3E_{q-k}}\right.\right.\\ \left.\left.+\,s_3\frac{(s_1-s_2)/2-s_1\tilde{n}(E_{q-k})-s_2n(q)}{p^0-s_5k^0+s_1q-s_2E_{q-k}}\right\}\right]\frac{s_4\hat{k}_{\beta,s_4}}{s_5k^0-p^0-s_4k}. \quad (9.5)\end{aligned}$$

Where, $(\widehat{q-k})_s$ stands for the four component quantity:

$$\left\{s, \frac{q_x-k_x}{|q-k|}, \frac{q_y-k_y}{|q-k|}, \frac{q_z-k_z}{|q-k|}\right\}$$
$$= \left\{s, \frac{q\sin\theta\cos\phi}{\sqrt{k^2+q^2-2kq\cos\theta}}, \frac{q\sin\theta\sin\phi}{\sqrt{k^2+q^2-2kq\cos\theta}}, \frac{q\cos\theta-k}{\sqrt{k^2+q^2-2kq\cos\theta}}\right\}.$$

The k^0 integration is from $-\infty \to \infty$ on the positive side of the real axis. We may thus close the contour on the positive side. Note that the function is vanishing as $k^0 \to \infty$. The result of this integration will simply be the sum of the residues at the corresponding poles. Looking at the above expression we note that the pole structure is different depending on whether the term being considered is the first or the second one in the curly brackets. We note the following poles:

i) 1st order pole: at $k^0 = k$, requires $s_5 = s$ (in both terms).

ii) 1st order pole: at $k^0 = k + s_5 p^0$, requires $s_5 = s_4$ (in both terms).

iii) 1st order pole: at $k^0 = s_5 s_1 q - s_5 s_3 E_{q-k}$, requires $s_5 s_1 q - s_5 s_3 E_{q-k} > 0$ (only in the first term).

iv) 1st order pole: at $k^0 = s_5 p^0 - s_5 s_2 E_{q-k} + s_5 s_1 q$ (only in the second term).

In the following, each of the poles are evaluated in a separate subsection and then summed up. The conditions and phrases in brackets will be expanded upon.

1st order pole at $k^0 = k$

This is the pole of the first outer propagator (*i.e.*, not a propagator in the effective vertex), it is a pole for the entire self-energy expression. It has the obvious residue of

$$\Pi^\mu_\mu(A) = 4e^2g^2 \int \frac{d^3k d^3q}{(2\pi)^6}[1/2 - \tilde{n}(k)]\frac{s\hat{k}_{\alpha,s}}{s}$$
$$\times \left[\frac{(\widehat{q-k})^\alpha_{s_2}(\widehat{q-k})^\beta_{s_3}}{q(p^0-(s_2-s_3)E_{q-k})}\left\{s_2\frac{(s_1-s_3)/2 - s_1\tilde{n}(E_{q-k}) - s_3 n(q)}{sk - s_1 q + s_3 E_{q-k}}\right.\right.$$

$$+ s_3 \frac{(s_1 - s_2)/2 - s_1 \tilde{n}(E_{q-k}) - s_2 n(q)}{p^0 - sk + s_1 q - s_2 E_{q-k}} \Bigg\} \Bigg] \frac{s_4 \hat{k}_{\beta, s_4}}{sk - p^0 - s_4 k}. \tag{9.6}$$

Note that there is an extra negative sign in the residue as the contour is being taken in the clockwise sense.

1st order pole at $k^0 = k + s_5 p^0$

This is the pole of the second outer propagator, it is a pole for the entire self-energy expression. It gives the residue,

$$\begin{aligned}\Pi^{\mu}_{\mu}(B) = 4e^2 g^2 \int \frac{d^3k d^3q}{(2\pi)^6} [1/2 - \tilde{n}(k)] \frac{s \hat{k}_{\alpha, s}}{p^0 + s_4 k - sk} \\ \times \Bigg[\frac{(\widehat{q-k})^{\alpha}_{s_2} (\widehat{q-k})^{\beta}_{s_3}}{q(p^0 - (s_2 - s_3) E_{q-k})} \Bigg\{ s_2 \frac{(s_1 - s_3)/2 - s_1 \tilde{n}(E_{q-k}) - s_3 n(q)}{p^0 + s_4 k - s_1 q + s_3 E_{q-k}} \\ + s_3 \frac{(s_1 - s_2)/2 - s_1 \tilde{n}(E_{q-k}) - s_2 n(q)}{-s_4 k + s_1 q - s_2 E_{q-k}} \Bigg\} \Bigg] \frac{s_4 \hat{k}_{\beta, s_4}}{s_4}. \end{aligned} \tag{9.7}$$

Note that the p^0 in the distribution function has been dropped. This may be done as $e^{p^0 \beta} = 1$ (p^0 is a discrete even frequency), and, secondly, as we are eventually going to analytically continue the self-energy to complex values of p^0. The correct analytic continuation is given by that function which has no non-analytic behaviour off the real axis [122]. One may easily check that the above function with a p^0 in the distribution function will have poles at $p^0 = -k + i2(n+1)\pi T$. Note that in this pole we may switch

$$s \to -s_4, \; s_4 \to -s, \; s_2 \to -s_3, \; s_3 \to -s_2, \; s_1 \to -s_1,$$

and noting that $\hat{k}_{-s} (\widehat{q-k})_{-s_2} = \hat{k}_s (\widehat{q-k})_{s_2}$, we find

$$\Pi^{\mu}_{\mu}(B) = \Pi^{\mu}_{\mu}(A).$$

1st order pole at $k^0 = s_5 s_1 q - s_5 s_3 E_{q-k}$

In the expression for the effective vertex (Eq. (9.2) or Eq. (9.5)), we note the presence of two terms inside the curly brackets with different pole structures. This is a pole of the first term, and is realized only if $s_5 s_1 q - s_5 s_3 E_{q-k} > 0$. Thus the residue is

$$\Pi^{\mu}_{\mu}(C) = 4e^2g^2 \int \frac{d^3kd^3q}{(2\pi)^6}[1/2 - \tilde{n}(s_5s_1q - s_5s_3E_{q-k})]\frac{s\hat{k}_{\alpha,s}}{s_1q - s_3E_{q-k} - sk}$$
$$\times \left[\frac{(\widehat{q-k})^{\alpha}_{s_2}(\widehat{q-k})^{\beta}_{s_3}}{q(p^0 - (s_2 - s_3)E_{q-k})}\left\{s_2\frac{(s_1 - s_3)/2 - s_1\tilde{n}(E_{q-k}) - s_3n(q)}{s_5}\right\}\right]$$
$$\times \frac{s_4\hat{k}_{\beta,s_4}\Theta(s_5s_1q - s_5s_3E_{q-k})}{s_1q - s_3E_{q-k} - p^0 - s_4k}. \tag{9.8}$$

1st order pole at $k^0 = s_5p^0 + s_5s_1q - s_5s_2E_{q-k}$

This is the pole of the second term in the curly bracket mentioned in the previous section. It is realized only if $s_5s_1q - s_5s_2E_{q-k} > 0$. The residue is

$$\Pi^{\mu}_{\mu}(D) = 4e^2g^2 \int \frac{d^3kd^3q}{(2\pi)^6}[1/2 - \tilde{n}(s_5s_1q - s_5s_2E_{q-k})]\frac{s\hat{k}_{\alpha,s}}{p^0 + s_1q - s_2E_{q-k} - sk}$$
$$\times \left[\frac{(\widehat{q-k})^{\alpha}_{s_2}(\widehat{q-k})^{\beta}_{s_3}}{q(p^0 - (s_2 - s_3)E_{q-k})}\left\{s_3\frac{(s_1 - s_2)/2 - s_1\tilde{n}(E_{q-k}) - s_2n(q)}{-s_5}\right\}\right]$$
$$\times \frac{s_4\hat{k}_{\beta,s_4}\Theta(s_5s_1q - s_5s_2E_{q-k})}{s_1q - s_2E_{q-k} - s_4k}. \tag{9.9}$$

Note that in this pole we may switch

$$s_2 \to -s_3,\ s_3 \to -s_2,\ s_1 \to -s_1,\ s_5 \to -s_5,\ s \to -s_4,\ s_4 \to -s.$$

With this operation, we find

$$\Pi^{\mu}_{\mu}(D) = \Pi^{\mu}_{\mu}(C).$$

Thus the full photon self-energy to second order in the coupling constant for the diagram of Fig. 9.1 is given by summing up the results of the preceding four subsections, *i.e.*,

$$\Pi^{\mu}_{\mu} = 2\Pi^{\mu}_{\mu}(A) + 2\Pi^{\mu}_{\mu}(C).$$

9.3 *Imaginary part of the first self-energy topology*

We now proceed with evaluating the discontinuity in the first self-energy as p^0 is analytically continued towards the positive real axis from above *i.e.*, $p^0 \to E + i\epsilon$. Analytically continuing p^0 will give us the retarded self-energy of the photon in real time in terms of a real continuous energy $p^0 = E$. The expressions to be continued are $\Pi^\mu_\mu(A)$ and $\Pi^\mu_\mu(D)$, *i.e.*,

$$\begin{aligned}\Pi^\mu_\mu(A) = -4e^2g^2 \int \frac{d^3kd^3q}{(2\pi)^6} \frac{s_4[\hat{k}_s \cdot \widehat{(q-k)}_{s_2}][\hat{k}_{s_4} \cdot \widehat{(q-k)}_{s_3}]}{q(p^0 - (s_2 - s_3)E_{q-k})} \\ \times \left\{ s_2 \frac{(s_1 - s_3)/2 - s_1\tilde{n}(E_{q-k}) - s_3 n(q)}{sk - s_1 q + s_3 E_{q-k}} \right. \\ \left. + s_3 \frac{(s_1 - s_2)/2 - s_1\tilde{n}(E_{q-k}) - s_2 n(q)}{p^0 - sk + s_1 q - s_2 E_{q-k}} \right\} \frac{[1/2 - \tilde{n}(k)]}{p^0 - (s - s_4)k}. \end{aligned} \tag{9.10}$$

and

$$\begin{aligned}\Pi^\mu_\mu(D) = -4e^2g^2 \int \frac{d^3kd^3q}{(2\pi)^6} \frac{ss_4[\hat{k}_s \cdot \widehat{(q-k)}_{s_2}][\hat{k}_{s_4} \cdot \widehat{(q-k)}_{s_3}]}{q(p^0 - (s_2 - s_3)E_{q-k})(p^0 + s_1 q - s_2 E_{q-k} - sk)} \\ \times \left\{ s_3 \frac{(s_1 - s_2)/2 - s_1\tilde{n}(E_{q-k}) - s_2 n(q)}{s_5} \right\} \\ \times \frac{[1/2 - \tilde{n}(s_5 s_1 q - s_5 s_2 E_{q-k})]\Theta(s_5 s_1 q - s_5 s_2 E_{q-k})}{s_1 q - s_2 E_{q-k} - s_4 k}. \end{aligned} \tag{9.11}$$

The presence of the theta function in $\Pi^\mu_\mu(D)$ complicates the pole structure that one would obtain during analytic continuation of this expression. The theta function may be realized with the following set of delta and theta functions:

$$\delta_{s_5,s_1}\delta_{s_5,-s_2} + \delta_{s_5,s_1}\delta_{s_5,s_2}\Theta(q - E_{k-q}) + \delta_{s_5,-s_1}\delta_{s_5,-s_2}\Theta(E_{k-q} - q). \tag{9.12}$$

Incorporating the above equation into Eq. (9.11), we obtain

$$\Pi^\mu_\mu(D) = -4e^2g^2 \int \frac{d^3kd^3q}{(2\pi)^6} \frac{ss_4s_3}{q}$$

$$\times\Bigg\{\frac{[\hat{k}_s\cdot(\widehat{q-k})_{-s_5}][\hat{k}_{s_4}\cdot(\widehat{q-k})_{s_3}][1-\tilde{n}(E_{q-k})+n(q)][1/2-\tilde{n}(E_{q-k}+q)]}{[p^0-(sk-s_5E_{q-k}-s_5q)][p^0-(-s_5-s_3)E_{q-k}][s_5(E_{q-k}+q)-s_4k]}$$
$$-\frac{[\hat{k}_s\cdot(\widehat{q-k})_{s_5}][\hat{k}_{s_4}\cdot(\widehat{q-k})_{s_3}][\tilde{n}(E_{q-k})+n(q)][1/2-\tilde{n}(q-E_{q-k})]}{[p^0-(sk+s_5E_{q-k}-s_5q)][p^0-(s_5-s_3)E_{q-k}][s_5(q-E_{q-k})-s_4k]}\Bigg\}. \qquad (9.13)$$

Analysing the expressions for $\Pi^\mu_\mu(A)$ and $\Pi^\mu_\mu(D)$, we note the following discontinuities:

Poles of type $p^0 = 2k$:

i) 1st order pole in $\Pi^\mu_\mu(A)$: at $p^0 = 2k$, requires $s = -s_4 = 1$ (in both terms that make up $\Pi^\mu_\mu(A)$).

Poles of type $p^0 = 2E_{q-k}$:

ii) 1st order pole in $\Pi^\mu_\mu(A)$: at $p^0 = 2E_{q-k}$, requires $s_2 = -s_3 = 1$ (in both terms that make up $\Pi^\mu_\mu(A)$).

iii) 1st order pole in $\Pi^\mu_\mu(D)$: at $p^0 = 2E_{q-k}$, requires $s_5 = s_3 = -1$ (only in first term of $\Pi^\mu_\mu(D)$).

iv) 1st order pole in $\Pi^\mu_\mu(D)$: at $p^0 = 2E_{q-k}$, requires $s_5 = -s_3 = 1$ (only in second term of $\Pi^\mu_\mu(D)$).

Poles of type $p^0 = sk + s_1q + s_2E_{k-q}$:

v) 1st order pole in $\Pi^\mu_\mu(A)$: at $p^0 = sk-s_1q+s_2E_{q-k}$, requires $sk-s_1q+s_2E_{q-k} > 0$ (only in the second term of $\Pi^\mu_\mu(A)$).

vi) 1st order pole in $\Pi^\mu_\mu(B)$: at $p^0 = sk-s_5q-s_5E_{q-k}$, requires $sk-s_5q-s_5E_{q-k} > 0$ (only in the first term of $\Pi^\mu_\mu(B)$).

vii) 1st order pole in $\Pi^\mu_\mu(B)$: at $p^0 = sk-s_5q+s_5E_{q-k}$, requires $sk-s_5q+s_5E_{q-k} > 0$ (only in the second term of $\Pi^\mu_\mu(B)$).

We may write down the expression for $2\Pi^{\mu}_{\mu}(A)$ highlighting its real and imaginary parts as $p^0 \to E + i\epsilon$ as

$$\begin{aligned}
2\Pi^{\mu}_{\mu}(A)] = -8e^2g^2 \int \frac{d^3kd^3q}{(2\pi)^6} \frac{s_4[\hat{k}_s \cdot \widehat{(q-k)}_{s_2}][\hat{k}_{s_4} \cdot \widehat{(q-k)}_{s_3}]}{E_{q+k}} \\
\times \left[\mathrm{P}\left(\frac{1}{E - (s_2 - s_3)E_{q-k}} \right) - i\pi\delta(E - (s_2 - s_3)E_{q-k}) \right] \\
\times \left\{ s_2 \frac{(s_1 - s_3)/2 - s_1\tilde{n}(E_{q-k}) - s_3 n(q)}{sk - s_1 q + s_3 E_{q-k}} + s_3((s_1 - s_2)/2 - s_1\tilde{n}(E_{q-k}) - s_2 n(q)) \right. \\
\left. \times \left[\mathrm{P}\left(\frac{1}{E - sk + s_1 q - s_2 E_{q-k}} \right) - i\pi\delta(E - sk + s_1 q - s_2 E_{q-k}) \right] \right\} [1/2 - \tilde{n}(k)] \\
\times \left[\mathrm{P}\left(\frac{1}{E - (s - s_4)k} \right) - i\pi\delta(E - (s - s_4)k) \right]. \qquad (9.14)
\end{aligned}$$

We now write down the various discontinuities as enumerated above (Note: we are now looking at $2\Pi^{\mu}_{\mu}(A)$ and $2\Pi^{\mu}_{\mu}(D)$, so the overall factors have doubled):

$$\begin{aligned}
Disc[2\Pi^{\mu}_{\mu}(A)]_a = (+2\pi i)8e^2g^2 \int \frac{d^3kd^3q}{(2\pi)^6} \frac{-2[\hat{k}_+ \cdot \widehat{(q-k)}_{s_2}][\hat{k}_- \cdot \widehat{(q-k)}_{s_3}]}{q(E - (s_2 - s_3)E_{q-k})} \\
\times s_2 \frac{(s_1 - s_3)/2 - s_1\tilde{n}(E_{q-k}) - s_3 n(q)}{k - s_1 q + s_3 E_{q-k}} [1/2 - \tilde{n}(k)]\delta(E - 2k). \qquad (9.15)
\end{aligned}$$

$$\begin{aligned}
Disc[2\Pi^{\mu}_{\mu}(A)]_b = (+2\pi i)8e^2g^2 \int \frac{d^3kd^3q}{(2\pi)^6} \frac{s_4[\hat{k}_s \cdot \widehat{(q-k)}_+][\hat{k}_{s_4} \cdot \widehat{(q-k)}_-]}{q} \\
\times \left\{ \frac{[1 - 2\tilde{n}(E_{q-k})]2q}{(sk - E_{q-k})^2 - q^2} \right\} \frac{[1/2 - \tilde{n}(k)]}{E - (s - s_4)k} \delta(E - 2E_{k-q}). \qquad (9.16)
\end{aligned}$$

$$\begin{aligned}
Disc[2\Pi^{\mu}_{\mu}(D)]_b = (+2\pi i)8e^2g^2 \int \frac{d^3kd^3q}{(2\pi)^6} \frac{1}{q} \left\{ \frac{[\hat{k}_s \cdot \widehat{(q-k)}_+][\hat{k}_s \cdot \widehat{(q-k)}_-]}{E_{q-k}^2 - (sk + q)^2} \right. \\
\left. + \frac{[\hat{k}_s \cdot \widehat{(q-k)}_+][\hat{k}_s \cdot \widehat{(q-k)}_+]}{q^2 - (E_{q-k} - sk)^2} \right\} \Big\{ [1 - \tilde{n}(E_{q-k}) + n(q)][1/2 - \tilde{n}(E_{q-k} + q)] \\
- [\tilde{n}(E_{q-k}) + n(q)][1/2 - \tilde{n}(q - E_{q-k})] \Big\} \delta(E - 2E_{q-k}). \qquad (9.17)
\end{aligned}$$

We now proceed to the evaluations of the discontinuities of the type $p^0 = sk + s_2E_{q-k} + s_1q$. We first change $s_1 \to -s_1$ in $2\Pi^\mu_\mu(A)$, and $s_5 \to -s_5$ in the first part of $2\Pi^\mu_\mu(D)$. Hence the discontinuity occurs in $2\Pi^\mu_\mu(A)$ at $p^0 = sk + s_2E_{q-k} + s_1q$ only when $sk + s_2E_{q-k} + s_1q > 0$. This may happen in only one of four instances: $s = +, s_2 = +, s_1 = +$; $s = -, s_2 = +, s_1 = +$, $s = +, s_2 = -, s_1 = +$; $s = +, s_2 = +, s_1 = -$. In $2\Pi^\mu_\mu(D)$ the discontinuity occurs in the first term when $s = +, s_5 = +$ or when $s = -, s_5 = +$; in the second term when $s = +, s_5 = +$ or when $s = +, s_5 = -$.

Thus the discontinuity in $2\Pi^\mu_\mu(A)$ occurs in four parts:

$$
\begin{aligned}
Disc[2\Pi^\mu_\mu(A)]_c = (+2\pi i)8e^2g^2 \int \frac{d^3kd^3q}{(2\pi)^6 q}[1/2 - \tilde{n}(k)] \\
\times \Bigg\{ & \frac{s_3s_4[\hat{k}_+ \cdot \widehat{(q-k)}_+][\hat{k}_{s_4} \cdot \widehat{(q-k)}_{s_3}][-1 + \tilde{n}(E_{q-k}) - n(q)]}{[k + q + s_3E_{q-k}][q + E_{q-k} + s_4k]}\delta(E - k - E_{q-k} - q) \\
& + \frac{s_3s_4[\hat{k}_- \cdot \widehat{(q-k)}_+][\hat{k}_{s_4} \cdot \widehat{(q-k)}_{s_3}][-1 + \tilde{n}(E_{q-k}) - n(q)]}{[-k + q + s_3E_{q-k}][q + E_{q-k} + s_4k]}\delta(E + k - E_{q-k} - q) \\
& + \frac{s_3s_4[\hat{k}_+ \cdot \widehat{(q-k)}_-][\hat{k}_{s_4} \cdot \widehat{(q-k)}_{s_3}][\tilde{n}(E_{q-k}) + n(q)]}{[k + q + s_3E_{q-k}][-E_{q-k} + q + s_4k]}\delta(E - k + E_{q-k} - q) \\
& + \frac{s_3s_4[\hat{k}_+ \cdot \widehat{(q-k)}_+][\hat{k}_{s_4} \cdot \widehat{(q-k)}_{s_3}][-\tilde{n}(E_{q-k}) - n(q)]}{[k - q + s_3E_{q-k}][E_{q-k} - q + s_4k]}\delta(E - k - E_{q-k} + q)\Bigg\}.
\end{aligned}
\tag{9.18}
$$

The discontinuity in $2\Pi^\mu_\mu(D)$ also occurs in four parts:

$$
\begin{aligned}
Disc[2\Pi^\mu_\mu(D)]_c = (-2\pi i)8e^2g^2 \int \frac{d^3kd^3q}{(2\pi)^6 q}\Bigg[& [1/2 - \tilde{n}(E_{q-k} + q)] \\
\times \Bigg\{ & \frac{s_3s_4[\hat{k}_+ \cdot \widehat{(q-k)}_+][\hat{k}_{s_4} \cdot \widehat{(q-k)}_{s_3}][1 - \tilde{n}(E_{q-k}) + n(q)]}{[k + q + s_3E_{q-k}][q + E_{q-k} + s_4k]}\delta(E - k - E_{q-k} - q) \\
& - \frac{s_3s_4[\hat{k}_- \cdot \widehat{(q-k)}_+][\hat{k}_{s_4} \cdot \widehat{(q-k)}_{s_3}][1 - \tilde{n}(E_{q-k}) + n(q)]}{[-k + q + s_3E_{q-k}][q + E_{q-k} + s_4k]}\delta(E + k - E_{q-k} - q)\Bigg\} \\
& + [1/2 - \tilde{n}(q - E_{q-k})] \\
\times \Bigg\{ & - \frac{s_3s_4[\hat{k}_+ \cdot \widehat{(q-k)}_-][\hat{k}_{s_4} \cdot \widehat{(q-k)}_{s_3}][\tilde{n}(E_{q-k}) + n(q)]}{[k + q + s_3E_{q-k}][-E_{q-k} + q + s_4k]}\delta(E - k + E_{q-k} - q)
\end{aligned}
\tag{9.19}
$$

$$- \frac{s_3 s_4 [\hat{k}_+ \cdot \widehat{(q-k)}_+][\hat{k}_{s_4} \cdot \widehat{(q-k)}_{s_3}][\tilde{n}(E_{q-k}) + n(q)]}{[k - q + s_3 E_{q-k}][E_{q-k} - q + s_4 k]} \delta(E - k - E_{q-k} + q) \Bigg\} \Bigg].$$

9.4 The self-energy: Topology II

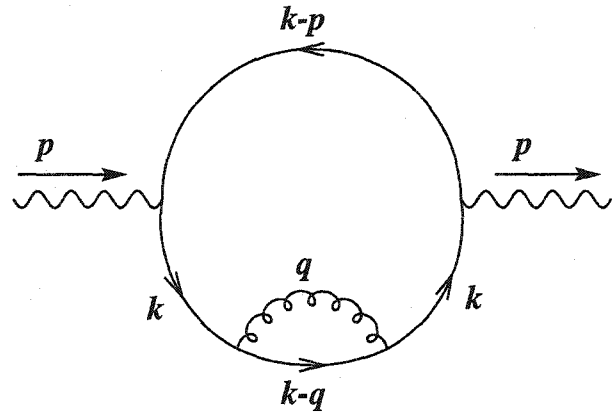

Figure 9.2: The second topology for the self-energy.

We begin by evaluating the photon self-energy with one quark line containing a gluon loop. The quark self-energy may be written as:

$$-i\Sigma(k)_{i,k} = (ie)^2 \frac{i}{\beta} \sum_{q^0} \int \frac{d^3q}{(2\pi)^3} t^a_{i,j} \gamma^\mu \frac{\not{q}}{q^2} t^b_{j,i} \gamma_\mu \frac{-i\delta^{a,b}}{(k-q)^2}. \tag{9.20}$$

Using the identity $\gamma^\mu \not{q} \gamma_\mu = -2 \not{q}$, q being the momentum of the gluon, the Matsubara sum in the quark self-energy is evaluated using the method of Pisarski [76]. It is given in our notation as

$$\Sigma(k)_{i,k} = \frac{g^2 t^a_{i,j} t^b_{j,k} \delta^{a,b}}{2} \int \frac{d^3q}{(2\pi)^3} \sum_{s_1 s_2} \frac{\widehat{(\not{k} - \not{q})}_{s_2}}{q} \frac{(s_1 + s_2)/2 - s_1 \tilde{n}_1(E_{k-q}) + s_2 n(q)}{k^0 - s_2 E_{k-q} - s_1 q} = \gamma^\beta \Sigma_{i,k\beta}. \tag{9.21}$$

Where, the self-energy has been written in the final form to highlight its matrix structure. We may use this to write the full self-energy of the photon in the static limit as

$$\Pi^{\mu}_{\mu} = \frac{1}{\beta}\sum_{k^0}\int\frac{d^3k}{(2\pi)^3}(-1)\mathbf{Tr}\sum_{s_1s_2s_3s_4s_5}\left[e\gamma_\mu\frac{\gamma^\alpha s_3\hat{k}_{\alpha,s_3}\delta_{j,i}}{2(k^0-s_3k)}\gamma^\beta\right.$$
$$\left.\Sigma_{i,k_\beta}(k)\frac{\gamma^\gamma s_4\hat{k}_{\gamma,s_4}\delta_{k,l}}{2(k^0-s_4k)}e\gamma^\mu\frac{\gamma^\delta s_5\hat{k}_{\delta,s_5}\delta_{l,j}}{2(k^0-p^0-s_5k)}\right]. \tag{9.22}$$

Now, looking at the trace of the gamma matrices,

$$Tr[\gamma_\mu\gamma^\alpha\gamma^\beta\gamma^\gamma\gamma^\mu\gamma^\delta] = -2Tr[\gamma^\gamma\gamma^\beta\gamma^\alpha\gamma^\delta] = -8(g^{\gamma\beta}g^{\alpha\delta} - g^{\gamma\alpha}g^{\beta\delta} + g^{\gamma\delta}g^{\beta\alpha}),$$

this gives the numerator as,

$$-8s_3s_4s_5e^2[(\hat{k}_{s_4}\cdot\Sigma)(\hat{k}_{s_3}\cdot\hat{k}_{s_5}) - (\hat{k}_{s_4}\cdot\hat{k}_{s_3})(\Sigma\cdot\hat{k}_{s_5}) + (\hat{k}_{s_4}\cdot\hat{k}_{s_5})(\Sigma\cdot\hat{k}_{s_3})].$$

We choose the z direction to be defined by the direction of k. Note that $\hat{k}_{s_4}\cdot\hat{k}_{s_5} = -2\delta_{s_4,-s_5}$. Note also that the s_4 and s_3 dependence of the photon self-energy is identical. This allows us to write down the self-energy as,

$$\Pi^{\mu}_{\mu} = \frac{-1}{\beta}\sum_{k^0}\int\frac{d^3k}{(2\pi)^3}2e^2\left[\frac{2(-s_3)\Sigma_{jj}\cdot\hat{k}_{s_3}}{(k^0-s_3k)(k^0-s_4k)(k^0-p^0+s_4k)} - \frac{2(-s_5)\Sigma_{jj}\cdot\hat{k}_{s_5}}{(k^0-p^0-s_5k)((k^0)^2-k^2)}\right]. \tag{9.23}$$

Where summation is implied over all the sign variables present *i.e.*, s_1, s_2, s_3, s_4, s_5. Note that the double pole is only present in the first term.

We now need to evaluate the Matsubara sum over k^0. For this we follow the method of reference [74]. This method converts the Matsubara sum into a contour integration in the complex plane of k^0. An example of this method applied to fermions at finite density was presented in the preceding chapter. The colour factor from the quark self-energy combined with that from the rest of the diagram becomes $\mathrm{tr}[t^a, t^b]\delta^{ab} = 4$. Using this we obtain the self-energy of the photon as:

$$\Pi^{\mu}_{\mu} = \frac{8e^2g^2}{2\pi i}\int_{-i\infty+\epsilon}^{i\infty+\epsilon}dk^0\int\frac{d^3kd^3q}{(2\pi)^6}\frac{[1/2-\tilde{n}(k^0)][(s_1+s_2)/2 - s_1\tilde{n}(E_{k-q}) + s_2n(q)]}{q[sk^0 - s_2E_{k-q} - s_1q]}$$
$$\times\left\{\frac{s_3\widehat{(k-q)}_{s_2}\cdot\hat{k}_{s_3}}{[sk^0-s_3k][sk^0-s_4k][sk^0-p^0+s_4k]} - \frac{s_5\widehat{(k-q)}_{s_2}\cdot\hat{k}_{s_5}}{[sk^0-p^0-s_5k][(k^0)^2-k^2]}\right\}. \tag{9.24}$$

The k^0 integration is from $-\infty \to \infty$ on the positive side of the real axis. We may thus close the contour on the positive side. Note that the function is vanishing as $k^0 \to \infty$. The result of this integration will simply be the sum of the residues at the corresponding poles. Looking at the above expression we note the following poles:

i) 2nd order pole: at $k^0 = k$, requires $s_3 = s_4 = s$ (only in the first term).

ii) 1st order pole: at $k^0 = k$, no requirement (only in the second term); requires $s_3 = -s_4 = s$ or $-s_3 = s_4 = s$ (only in the first term).

iii) 1st order pole: at $k^0 = k + sp^0$, requires $s_4 = -s$ (only in first term); requires $s_5 = s$ (only in second term).

iv) 1st order pole: at $k^0 = ss_2E_{k-q} + ss_1q$, requires $ss_2E_{k-q} + ss_1q > 0$.

In the following each of these poles will be evaluated in a separate subsection and then summed up.

2nd order pole at $k^0 = k$

We begin by evaluating the 2nd order pole. The origin of this pole can be traced back to the two propagators which may go on-shell simultaneously. In the real time formalism this leads to the ill-defined square of the Dirac delta function. In imaginary time, however, this pole is easily dealt with: the residue of a function $f(k^0)$ at a second order pole at $k^0 = k$ is simply given as $\frac{d}{dk^0}(k^0 - k)^2 f(k^0)|_{k^0=k}$. Using this we get the residue of Π at this pole as

$$\Pi^{\mu}_{\mu}(A) = 8e^2g^2 \int \frac{d^3k d^3q}{(2\pi)^6} \frac{[(s_1+s_2)/2 - s_1\tilde{n}(E_{k-q}) + s_2 n(q)]}{q} \widehat{(k-q)}_{s_2} \cdot \hat{k}_s$$
$$\times \left\{ \frac{s(1/2 - \tilde{n}(k))'}{[sk - s_2E_{k-q} - s_1q][p^0 - 2sk]} - \frac{1/2 - \tilde{n}(k)}{[sk - s_2E_{k-q} - s_1q]^2[p^0 - 2sk]} \right.$$

$$+\frac{1/2-\tilde{n}(k)}{[sk-s_2E_{k-q}-s_1q][p^0-2sk]^2}\Bigg\}. \tag{9.25}$$

Note that as in the case of the first self-energy topology there is an extra negative sign in the residue as the contour is closed in the clockwise sense.

1st order pole at $k^0 = k$

This obvious residue may be easily evaluated using the methods outlined in the previous section,

$$\Pi^\mu_\mu(B) = -8e^2g^2\int\frac{d^3kd^3q}{(2\pi)^6}\frac{[(s_1+s_2)/2-s_1\tilde{n}(E_{k-q})+s_2n(q)][1/2-\tilde{n}(k)]}{q[sk-s_2E_{k-q}-s_1q]}$$
$$\times\left\{\frac{-s(\widehat{k-q})_{s_2}\cdot\hat{k}_s}{2kp^0}+\frac{s(\widehat{k-q})_{s_2}\cdot\hat{k}_{-s}}{2k[p^0-2sk]}+\frac{s_5(\widehat{k-q})_{s_2}\cdot\hat{k}_{s_5}}{2k[p^0-(s-s_5)k]}\right\}. \tag{9.26}$$

In the above, we sum over the two possibilities of $s_5 = \pm s$ to get the factor in the bracket as

$$\left\{\frac{-s(\widehat{k-q})_{s_2}\cdot\hat{k}_s}{2kp^0}+\frac{s(\widehat{k-q})_{s_2}\cdot\hat{k}_{-s}}{2k[p^0-2sk]}+\frac{s(\widehat{k-q})_{s_2}\cdot\hat{k}_s}{2kp^0}\right.$$
$$\left.+\frac{-s(\widehat{k-q})_{s_2}\cdot\hat{k}_{-s}}{2k[p^0-2sk]}\right\}=0$$

Hence, $\Pi^\mu_\mu(B) = 0$.

1st order pole at $k^0 = k + sp^0$

This gives the residue

$$\Pi^\mu_\mu(C) = -8e^2g^2\int\frac{d^3kd^3q}{(2\pi)^6}\frac{[(s_1+s_2)/2-s_1\tilde{n}(E_{k-q})+s_2n(q)][1/2-\tilde{n}(k)]}{q[p^0-(s_2E_{k-q}+s_1q-sk)][p^0+2sk]}$$
$$\times\left\{\frac{s_3(\widehat{k-q})_{s_2}\cdot\hat{k}_{s_3}}{s(p^0-(s_3-s)k)}-\frac{(\widehat{k-q})_{s_2}\cdot\hat{k}_s}{p^0}\right\}. \tag{9.27}$$

Switching $s \to -s$, and summing over $s_3 = \pm s$ we get,

$$\Pi^{\mu}_{\mu}(C) = 8e^2g^2 \int \frac{d^3kd^3q}{(2\pi)^6} \frac{[(s_1+s_2)/2 - s_1\tilde{n}(E_{k-q}) + s_2 n(q)][1/2 - \tilde{n}(k)]}{q[p^0 - (s_2E_{k-q} + s_1 q + sk)][p^0 - 2sk]} \times \left\{ \frac{(\widehat{k-q})_{s_2} \cdot \hat{k}_s}{(p^0 - 2sk)} \right\}. \tag{9.28}$$

1st order pole at $k^0 = ss_2E_{k-q} + ss_1q$

This pole is realized only if $ss_2E_{k-q} + ss_1q > 0$. This condition may be enforced with the following set of delta and theta functions:

$$\delta_{s,s_2}\delta_{s,s_1} + \delta_{s,s_2}\delta_{s,-s_1}\Theta(E_{k-q} - q) + \delta_{s,-s_2}\delta_{s,s_1}\Theta(q - E_{k-q}). \tag{9.29}$$

We start with the second and third terms:

$$\Pi^{\mu}_{\mu}(D,2) = 8e^2g^2 \int \frac{d^3kd^3q}{(2\pi)^6} \frac{[1/2 - \tilde{n}(E_{k-q} - q)][\tilde{n}(E_{k-q}) + n(q)]}{q} \times \left\{ \frac{s_3(\widehat{k-q})_s \cdot \hat{k}_{s_3}}{[sE_{k-q} - sq - s_3k][sE_{k-q} - sq - s_4k][p^0 - (s_4k + sE_{k-q} - sq)]} - \frac{s_5(\widehat{k-q})_s \cdot \hat{k}_{s_5}}{[p^0 - (sE_{k-q} - sq - s_5k)][(E_{k-q}-q)^2 - k^2]} \right\} \Theta(E_{k-q} - q). \tag{9.30}$$

Similarly we find for the third term

$$\Pi^{\mu}_{\mu}(D,3) = 8e^2g^2 \int \frac{d^3kd^3q}{(2\pi)^6} \frac{[1/2 - \tilde{n}(q - E_{k-q})][-\tilde{n}(E_{k-q}) - n(q)]}{q} \times \left\{ \frac{s_3(\widehat{k-q})_{-s} \cdot \hat{k}_{s_3}}{[-sE_{k-q} + sq - s_3k][-sE_{k-q} + sq - s_4k][p^0 - (s_4k - sE_{k-q} + sq)]} - \frac{s_5(\widehat{k-q})_{-s} \cdot \hat{k}_{s_5}}{[p^0 - (-sE_{k-q} + sq - s_5k)][(E_{k-q}-q)^2 - k^2]} \right\} \Theta(q - E_{k-q}). \tag{9.31}$$

Now, switch $s \to -s$ in the 3rd term, and noting that $1/2 - \tilde{n}(q - E_{k-q}) = -1/2 + \tilde{n}(E_{k-q} - q)$, we note that the second and third terms can be combined to give

$$\Pi^{\mu}_{\mu}(D,2+3) = 8e^2g^2 \int \frac{d^3kd^3q}{(2\pi)^6} \frac{[1/2 - \tilde{n}(E_{k-q} - q)][\tilde{n}(E_{k-q}) + n(q)]}{q}$$

$$\times \left\{ \frac{s_3(\widehat{k-q})_s \cdot \hat{k}_{s_3}}{[sE_{k-q} - sq - s_3 k][sE_{k-q} - sq - s_4 k][p^0 - (s_4 k + sE_{k-q} - sq)]} - \frac{s_5(\widehat{k-q})_s \cdot \hat{k}_{s_5}}{[p^0 - (sE_{k-q} - sq - s_5 k)][(E_{k-q} - q)^2 - k^2]} \right\}. \tag{9.32}$$

Note the absence of the theta functions in the above equation. Now we may also write down the residue from the first set of delta functions in Eq. (9.29) as,

$$\Pi^\mu_\mu(D,1) = 8e^2 g^2 \int \frac{d^3k d^3q}{(2\pi)^6} \frac{[1/2 - \tilde{n}(E_{k-q} + q)][1 - \tilde{n}(E_{k-q}) + n(q)]}{q} \times \left\{ \frac{s_3(\widehat{k-q})_s \cdot \hat{k}_{s_3}}{[sE_{k-q} + sq - s_3 k][sE_{k-q} + sq - s_4 k][p^0 - (s_4 k + sE_{k-q} + sq)]} - \frac{s_5(\widehat{k-q})_s \cdot \hat{k}_{s_5}}{[p^0 - (sE_{k-q} + sq - s_5 k)][(E_{k-q} + q)^2 - k^2]} \right\}. \tag{9.33}$$

The total expression obtained by summing up the results from the preceding 4 subsections will give us the full self-energy of the photon to second order in the coupling constant for the diagram of Fig. 9.2, *i.e.*,

$$\Pi^\mu_\mu = \Pi^\mu_\mu(A) + \Pi^\mu_\mu(B) + \Pi^\mu_\mu(C) + \Pi^\mu_\mu(D,1) + \Pi^\mu_\mu(D,2+3).$$

9.5 *Imaginary part of the second self-energy topology*

We now proceed with evaluating the discontinuity in the second self-energy as p^0 is analytically continued to a positive real value *i.e.*, $p^0 \to E + i\epsilon$. Analysing the expressions derived in the above sections we note the following discontinuities:

a) Poles of type $p^0 = 2k$:

i) 1st order pole in $\Pi^\mu_\mu(A)$: at $p^0 = 2k$, requires $s = 1$ (only in first and second terms).

ii) 2st order pole in $\Pi^\mu_\mu(A)$: at $p^0 = 2k$. This occurs in the third term in the bracket and requires $s = 1$.

iii) 2nd order pole in $\Pi^{\mu}_{\mu}(C)$: at $p^0 = 2k$, requires $s = 1$ and $s_3 = 1$ (only in first term).

b) Poles of type $p^0 = sk + s_1 q + s_2 E_{k-q}$:

iv) 1st order pole in $\Pi^{\mu}_{\mu}(C)$: at $p^0 = sk + s_1 q + s_2 E_{k-q}$, requires $s = s_1 = s_2 = 1$, or $-s = s_1 = s_2 = 1$, or $s = -s_1 = s_2 = 1$, or $s = s_1 = -s_2 = 1$ (in both terms).

v) 1st order pole in $\Pi^{\mu}_{\mu}(D, 2+3)$: at $p^0 = s_4 k + s E_{k-q} - sq$, requires $s_4 = s = 1$ or $s_4 = -s = 1$ (only in first term); at $p^0 = -s_5 k + s E_{k-q} - sq$, requires $-s_5 = s = 1$ or $s_5 = s = -1$ (only in second term).

vi) 1st order pole in $\Pi^{\mu}_{\mu}(D, 1)$: at $p^0 = s_4 k + s E_{k-q} + sq$, requires $s_4 = s = 1$ or $-s_4 = s = 1$ (only in first term), at $p^0 = -s_5 k + s E_{k-q} + sq$, requires $-s_5 = s = 1$ or $s_5 = s = 1$ (only in second term).

The discontinuity across a second order pole is derived in Appendix B. We now write down the various discontinuities as enumerated above:

$$
\begin{aligned}
Disc[\Pi^{\mu}_{\mu}(A)]_a = (-2\pi i) 8 e^2 g^2 \int \frac{dk d\theta d\phi \sin\theta d^3 q}{(2\pi)^6 q} \delta(E - 2k) \\
\times \Bigg\{ & \frac{k^2 \mathcal{NS}[1/2 - \tilde{n}(k)]'}{[k - s_2 E_{k-q} - s_1 q]} - \frac{k^2 \mathcal{NS}[1/2 - \tilde{n}(k)]}{[k - s_2 E_{k-q} - s_1 q]^2} \\
& - \frac{1}{2} \frac{2k \mathcal{NS}[1/2 - \tilde{n}(k)]}{[k - s_2 E_{k-q} - s_1 q]} - \frac{1}{2} \frac{k^2 (\mathcal{NS})'[1/2 - \tilde{n}(k)]}{[k - s_2 E_{k-q} - s_1 q]} \\
& - \frac{1}{2} \frac{k^2 \mathcal{NS}[1/2 - \tilde{n}(k)]'}{[k - s_2 E_{k-q} - s_1 q]} - \frac{1}{2} \frac{k^2 \mathcal{NS}[1/2 - \tilde{n}(k)][-1 + s_2 E'_{k-q}]}{[k - s_2 E_{k-q} - s_1 q]^2} \Bigg\}.
\end{aligned}
\tag{9.34}
$$

Where, the prime "A'" denotes derivation only with respect to k. The symbol $\mathcal{N}$ stands for the factor $[(s_1 + s_2)/2 - s_1 \tilde{n}(E_{k-q}) + s_2 n(q)]$, while the factor $(\widehat{k - q})_{s_2} \cdot \hat{k}_+$ is represented by the symbol $\mathcal{S}$.

$$Disc[\Pi^{\mu}_{\mu}(C)]_a = (2\pi i)8e^2g^2\int\frac{dkd\theta d\phi\sin\theta d^3q}{(2\pi)^6}\delta(E-2k)$$
$$\times\left\{\frac{1}{2}\frac{2k\mathcal{NS}[1/2-\tilde{n}(k)]}{[E-s_2E_{k-q}-s_1q-k]}+\frac{1}{2}\frac{k^2(\mathcal{NS})'[1/2-\tilde{n}(k)]}{[E-s_2E_{k-q}-s_1q-k]}\right.$$
$$\left.+\frac{1}{2}\frac{k^2\mathcal{NS}[1/2-\tilde{n}(k)]'}{[E-s_2E_{k-q}-s_1q-k]}+\frac{1}{2}\frac{k^2\mathcal{NS}[1/2-\tilde{n}(k)][1+s_2E'_{k-q}]}{[E-s_2E_{k-q}-s_1q-k]^2}\right\}. \tag{9.35}$$

The two terms above are the result of the discontinuities at $p^0\to E=2k$. In the following we shall enumerate those terms that result as we take the discontinuities at $p^0\to E=sk+s_1q+s_2E_{k-q}$.

$$Disc[\Pi^{\mu}_{\mu}(C)]_c = (-2\pi i)8e^2g^2\int\frac{d^3kd^3q}{(2\pi)^6}\frac{[(s_1+s_2)/2-s_1\tilde{n}(E_{k-q})+s_2n(q)][1/2-\tilde{n}(k)]}{q[s_2E_{k-q}+s_1q-sk]}$$
$$\times\left\{\frac{s_3\widehat{(k-q)}_{s_2}\cdot\hat{k}_{s_3}}{s[s_2E_{k-q}+s_1q-s_3k]}-\frac{\widehat{(k-q)}_{s_2}\cdot\hat{k}_{-s}}{s_2E_{k-q}+s_1q+sk}\right\}\delta(E-sk-s_1q-s_2E_{k-q})$$
$$\times\left[\delta_{s,+}\delta_{s_1,+}\delta_{s_2,+}+\delta_{s,-}\delta_{s_1,+}\delta_{s_2,+}+\delta_{s,+}\delta_{s_1,-}\delta_{s_2,+}+\delta_{s,+}\delta_{s_1,+}\delta_{s_2,-}\right]. \tag{9.36}$$

Recall that even though not explicitly mentioned there is an implied summation over all sign factors. We may now perform the sum over $s_3=\pm s$ to get

$$Disc[\Pi^{\mu}_{\mu}(C)]_c = (-2\pi i)8e^2g^2\int\frac{d^3kd^3q}{(2\pi)^6}\frac{[(s_1+s_2)/2-s_1\tilde{n}(E_{k-q})+s_2n(q)][1/2-\tilde{n}(k)]}{q[s_2E_{k-q}+s_1q-sk]^2}$$
$$\times\widehat{(k-q)}_{s_2}\cdot\hat{k}_s\delta(E-sk-s_1q-s_2E_{k-q})$$
$$\times\left[\delta_{s,+}\delta_{s_1,+}\delta_{s_2,+}+\delta_{s,-}\delta_{s_1,+}\delta_{s_2,+}+\delta_{s,+}\delta_{s_1,-}\delta_{s_2,+}+\delta_{s,+}\delta_{s_1,+}\delta_{s_2,-}\right]. \tag{9.37}$$

Finally, the discontinuity in parts D of the second self-energy is given as

$$Disc[\Pi^{\mu}_{\mu}(D,2+3)]_c = (-2\pi i)8e^2g^2\int\frac{d^3kd^3q}{(2\pi)^6}\frac{[1/2-\tilde{n}(E_{k-q}-q)][\tilde{n}(E_{k-q})+n(q)]}{q}$$
$$\left\{\frac{s_3\widehat{(k-q)}_s\cdot\hat{k}_{s_3}}{[sE_{k-q}-sq-s_3k][sE_{k-q}-sq-s_4k]}\left[\delta_{s_4,+}\delta_{s,+}\delta(E-k-E_{k-q}+q)+\delta_{s_4,+}\delta_{s,-}\delta(E-k+E_{k-q}-q)\right]\right.$$
$$\left.-\frac{s_5\widehat{(k-q)}_s\cdot\hat{k}_{s_5}}{[(E_{k-q}-q)^2-k^2]}\left[\delta_{s_5,-}\delta_{s,+}\delta(E-k-E_{k-q}+q)+\delta_{s_5,-}\delta_{s,-}\delta(E-k+E_{k-q}-q)\right]\right\}. \tag{9.38}$$

We may now sum over $s_3 = \pm 1$ to get

$$Disc[\Pi^{\mu}_{\mu}(D, 2+3)]_c = (-2\pi i)8e^2g^2 \int \frac{d^3kd^3q}{(2\pi)^6} \frac{[1/2 - \tilde{n}(E_{k-q} - q)][\tilde{n}(E_{k-q}) + n(q)]}{q}$$
$$\times \left\{ \frac{(\widehat{k-q})_- \cdot \hat{k}_+}{[k + E_{k-q} - q]^2} \delta(E - k + E_{k-q} - q) + \frac{(\widehat{k-q})_+ \cdot \hat{k}_+}{[k + q - E_{k-q}]^2} \delta(E - k - E_{k-q} + q) \right\}. \quad (9.39)$$

$$Disc[\Pi^{\mu}_{\mu}(D, 1)]_c = (-2\pi i)8e^2g^2 \int \frac{d^3kd^3q}{(2\pi)^6} \frac{[1/2 - \tilde{n}(E_{k-q} + q)][1 - \tilde{n}(E_{k-q}) + n(q)]}{q}$$
$$\times \left\{ \frac{s_3(\widehat{k-q})_s \cdot \hat{k}_{s_3}}{[sE_{k-q} + sq - s_3k][sE_{k-q} + sq - s_4k]} \left[\delta_{s_4,+}\delta_{s,+}\delta(E - k - E_{k-q} - q) + \delta_{s_4,-}\delta_{s,+}\delta(E + k - E_{k-q} - q \right.\right.$$
$$\left.\left. - \frac{s_5(\widehat{k-q})_s \cdot \hat{k}_{s_5}}{[(E_{k-q} + q)^2 - k^2]} \left[\delta_{s_5,-}\delta_{s,+}\delta(E - k - E_{k-q} - q) + \delta_{s_5,+}\delta_{s,+}\delta(E + k - E_{k-q} - q) \right] \right\}. \quad (9.4$$

We may sum over $s_3 = \pm 1$ to obtain

$$Disc[\Pi^{\mu}_{\mu}(D, 1)]_c = (-2\pi i)8e^2g^2 \int \frac{d^3kd^3q}{(2\pi)^6} \frac{[1/2 - \tilde{n}(E_{k-q} + q)][1 - \tilde{n}(E_{k-q}) + n(q)]}{q}$$
$$\times \left\{ \frac{(\widehat{k-q})_+ \cdot \hat{k}_+}{[E_{k-q} + q - k]^2} \delta(E - k - E_{k-q} - q) - \frac{(\widehat{k-q})_+ \cdot \hat{k}_-}{[E_{k-q} + q + k]^2} \delta(E + k - E_{k-q} - q) \right\}. \quad (9.41)$$

9.6 *Physical interpretation: tree-like cuts*

We now begin the process of combining terms from the discontinuities of the two self energies to obtain the square of amplitudes of physical processes. Essentially we shall follow the method outlined by H. A. Weldon [114]. Our method is a three step process:

i) collect together terms that have the same energy conserving delta functions.

ii) reorganize the thermal distribution functions to express them as a difference of the thermal weights for particle emission and absorption.

iii) reorganize the remaining momentum dependent part as the square of the amplitude of the process hinted at by the previous two steps.

For easy identification we indicate the contribution from the first self-energy topology by Π^1 and from the second topology by Π^2. We begin with the discontinuities where no loops are left in the final result. These are the discontinuities given by Eqs. (9.18,9.19) for the first self-energy topology, and Eqs. (9.37,9.39,9.41) for the second self-energy topology. These discontinuities will result in physical amplitudes for three kinds of processes: photon decay, Compton scattering and pair creation.

9.6.1 *Photon Decay and Formation.*

We begin by analysing the terms which containing the delta function $\delta(E-k-q-E_{k-q})$. The contributions to this from Π^1 are

$$Disc[\Pi^1(A)](E-k-E_{q-k}-q) = (+2\pi i)8e^2g^2\int\frac{d^3kd^3q}{(2\pi)^6q}[1/2-\tilde{n}(k)]\delta(E-k-E_{q-k}-q) \times \frac{s_3s_4[\hat{k}_+\cdot\widehat{(q-k)}_+][\hat{k}_{s_4}\cdot\widehat{(q-k)}_{s_3}][-1+\tilde{n}(E_{q-k})-n(q)]}{[k+q+s_3E_{q-k}][q+E_{q-k}+s_4k]}. \tag{9.42}$$

and

$$Disc[\Pi^1(D)](E-k-E_{q-k}-q) = (-2\pi i)8e^2g^2\int\frac{d^3kd^3q}{(2\pi)^6q}[1/2-\tilde{n}(E_{q-k}+q)] \times\delta(E-k-E_{q-k}-q)\,\frac{s_3s_4[\hat{k}_+\cdot\widehat{(q-k)}_+][\hat{k}_{s_4}\cdot\widehat{(q-k)}_{s_3}][1-\tilde{n}(E_{q-k})+n(q)]}{[k+q+s_3E_{q-k}][q+E_{q-k}+s_4k]}. \tag{9.43}$$

Note that

$$\tilde{n}(E_{q-k}+q)\Big[1-\tilde{n}(E_{q-k})+n(q)\Big] = \tilde{n}(E_{q-k})n(q)$$

using the above identity we may combine the two terms and rewrite the distribution functions to give,

$$Disc[\Pi^1](E-k-E_{q-k}-q) = (-2\pi i)8e^2g^2\int\frac{d^3kd^3q}{(2\pi)^6q} \times\Big\{[1-\tilde{n}(k)][1+n(q)][1-\tilde{n}(E_{q-k})]-\tilde{n}(k)n(q)\tilde{n}(E_{q-k})\Big\} \times\frac{s_3s_4[\hat{k}_+\cdot\widehat{(q-k)}_+][\hat{k}_{s_4}\cdot\widehat{(q-k)}_{s_3}]}{[k+q+s_3E_{q-k}][q+E_{q-k}+s_4k]}\delta(E-k-E_{q-k}-q). \tag{9.44}$$

We may combine the coefficients of the same delta function from the second self-energy to get

$$Disc[\Pi^2](E-k-q-E_{k-q}) = 2\times(-2\pi i)8e^2g^2\int\frac{d^3kd^3q}{(2\pi)^6q} \times\Big\{[1-\tilde{n}(k)][1+n(q)][1-\tilde{n}(E_{q-k})]-\tilde{n}(k)n(q)\tilde{n}(E_{q-k})\Big\} \times\frac{\widehat{(k-q)}_+\cdot\hat{k}_+}{[E_{k-q}+q-k]^2}\delta(E-k-E_{k-q}-q). \tag{9.45}$$

The overall factor of 2 is the ratio of the symmetry factor of this diagram to the denominator obtained from perturbation theory. Note that we obtain the same form of the distribution functions, this indicates the generic structure of heavy photon decay and reformation. In the distribution function factor, terms like $1+n(q)$ indicate Bose-Einstein enhancement in the emission of a gluon. The 1 is from spontaneous emission, and the $n(q)$ represents stimulated emission of a boson into a thermal bath. Terms like $1-\tilde{n}(k)$ represents the "Pauli blocked" emission of a quark of momentum k into the thermal bath. The product of the three factors $[1-\tilde{n}(k)][1+n(q)][1-\tilde{n}(E_{q-k})]$ (along with the phase space integral and delta function) can thus be interpreted as the statistical factor associated with a heavy photon outside a thermal bath decaying by emitting a quark, antiquark, and a gluon into a thermal bath. Subtracted from this is the factor $\tilde{n}(k)n(q)\tilde{n}(E_{q-k})$; this represents the formation of a heavy photon from a quark, antiquark and a gluon, all three emitted from the thermal bath (Fig. 9.3). The photon subsequently escapes from the bath without further interaction.

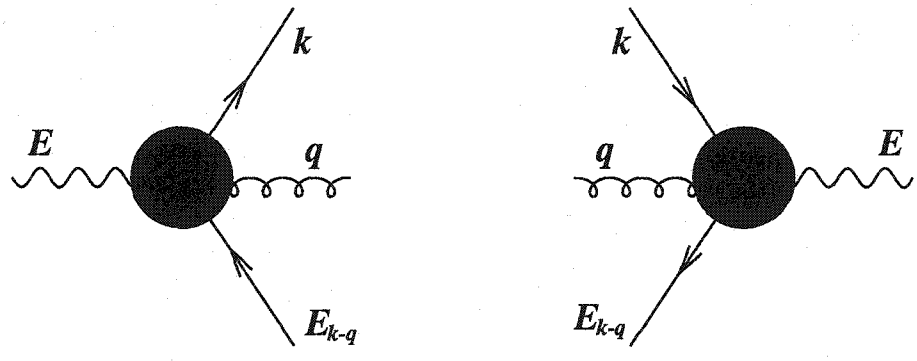

Figure 9.3: Heavy photon decay and formation.

To convert the above expressions into cross sections for heavy photon decay and reformation, we start by first defining a new four-vector $\mathbf{w} = (w, \vec{w})$, such that $w = E - k - q$(in order to avoid confusion we introduce the notation of four-vectors as bold face characters). This relation is indicated by the one dimensional delta function. To obtain the probability of photon decay, we need to generalize the delta function to a four-delta function. We thus need to generalize the definition of $\mathbf{w}$:

$$\mathbf{w} = \mathbf{p} - \mathbf{k} - \mathbf{q}.$$

Where, $\mathbf{p} = (E, 0, 0, 0)$ is the mass of the off-shell photon. As denoted by Fig. 9.3. $\mathbf{k}$, $\mathbf{q}$ and $\mathbf{w}$ are all on shell. The above relation also implies $\vec{w} = -\vec{k} - \vec{q}$. We may set $\mathbf{k}^0 = k = |\vec{k}|$ and $\mathbf{q}^0 = q = |\vec{q}|$. Now, requiring that $\mathbf{w}$ be on shell imposes the condition that

$$(E - k - q)^2 = k^2 + q^2 + 2kq\cos\theta$$

$$\Rightarrow E(E - 2k - 2q) = -\mathbf{k} \cdot \mathbf{q}.$$

Where θ is the angle between the three vectors $\vec{q}$ and $\vec{k}$. Using the above relations we many now rewrite the discontinuity obtained from Π^2. In the numerator of the integrand we notice the factor $\widehat{(k-q)}_+ \cdot \hat{k}_+$, this may be changed appropriately by setting $\vec{k} \leftrightarrow -\vec{k}$ in the integrand. Noting that $\widehat{(-k)}_s = -\hat{k}_{-s}$ we get the above factor

as $-\hat{w}_+ \cdot \hat{k}_-$. Introducing the standard denominators $2k, 2w$ and factors of 2π we obtain Eq.(9.45) as

$$Disc[\Pi^2](E-k-q-E_{k-q}) = -2i \times 8e^2g^2 \int \frac{d^3kd^3qd^3w}{(2\pi)^9 2q2k2w} 8(2\pi)^4\delta^4(\mathbf{p}-\mathbf{k}-\mathbf{q}-\mathbf{w}) \times \Big\{[1-\tilde{n}(k)][1+n(q)][1-\tilde{n}(w)] - \tilde{n}(k)n(q)\tilde{n}(w)\Big\} \times \left[-\frac{\mathbf{w}_+ \cdot \mathbf{k}_-}{[w+q-k]^2}\right] \tag{9.46}$$

We now split the above integrand into two parts and in one of them switch $w \leftrightarrow k$. Note that $-\mathbf{w}_+ \cdot \mathbf{k}_- = wk + \vec{w} \cdot \vec{k} = (E-2k)(E-2w)/2$, finally gives the above discontinuity as

$$Disc[\Pi^2](E-k-q-E_{k-q}) = -i \int \frac{d^3kd^3qd^3w}{(2\pi)^9 2q2k2w} (2\pi)^4\delta^4(\mathbf{p}-\mathbf{k}-\mathbf{q}-\mathbf{w}) \times \Big\{[1-\tilde{n}(k)][1+n(q)][1-\tilde{n}(w)] - \tilde{n}(k)n(q)\tilde{n}(w)\Big\} \times 32e^2g^2\left[\frac{E-2k}{E-2w} + \frac{E-2w}{E-2k}\right]. \tag{9.47}$$

We now perform the same procedure on the corresponding discontinuity from Π^1, to get

$$Disc[\Pi^1](E-k-q-E_{k-q}) = -i \times 8e^2g^2 \int \frac{d^3kd^3qd^3w}{(2\pi)^9 2q2k2w} 8(2\pi)^4\delta^4(\mathbf{p}-\mathbf{k}-\mathbf{q}-\mathbf{w}) \times \Big\{[1-\tilde{n}(k)][1+n(q)][1-\tilde{n}(w)] - \tilde{n}(k)n(q)\tilde{n}(w)\Big\} \times \frac{s_3s_4[\mathbf{k}_+ \cdot \mathbf{w}_+][\hat{k}_{s_4} \cdot \hat{w}_{s_3}]}{[k+q+s_3w][q+w+s_4k]}. \tag{9.48}$$

The part of the integrand besides the distribution function part(depends on the angle between $\vec{k}$ and $\vec{q}$, will be denoted as the matrix part) may be expanded by summing over s_3, s_4 as

$$\frac{\mathbf{k}\cdot\mathbf{w}}{kw}\left[\frac{\mathbf{k}_+ \cdot \mathbf{w}_+}{(k+q+w)^2} + \frac{\mathbf{k}_+ \cdot \mathbf{w}_-}{(k+q)^2-w^2} + \frac{\mathbf{k}_- \cdot \mathbf{w}_+}{(q+w)^2-k^2} + \frac{\mathbf{k}_- \cdot \mathbf{w}_-}{(q^2-(k-w)^2}\right].$$

Using the relations

$$\mathbf{k}_+ \cdot \mathbf{w}_- = \mathbf{k}_- \cdot \mathbf{w}_+ = -(1/2)[E-2k][E-2w],$$

$$\mathbf{k}_+ \cdot \mathbf{w}_+ = \mathbf{k}_- \cdot \mathbf{w}_- = (E/2)[E-2q],$$

and the relation imposed by the delta function (*i.e.*,$E = k+q+w$) we can simplify the matrix part to give

$$\frac{E(E-2q)}{[E-2w][E-2k]},$$

substituting the above into the expression for Π^1 and then combining the results from Π^1 and Π^2 we get

$$\begin{aligned} Disc[\Pi](E-k-q-E_{k-q}) = -i\int \frac{d^3k d^3q d^3w}{(2\pi)^9 2q2k2w}(2\pi)^4\delta^4(\mathbf{p}-\mathbf{k}-\mathbf{q}-\mathbf{w}) \\ \times\Big\{[1-\tilde{n}(k)][1+n(q)][1-\tilde{n}(w)] - \tilde{n}(k)n(q)\tilde{n}(w)\Big\} \\ \times 32e^2g^2\left[\frac{E-2k}{E-2w}+\frac{E-2w}{E-2k}+2\frac{E(E-2q)}{[E-2w][E-2k]}\right]. \end{aligned} \tag{9.49}$$

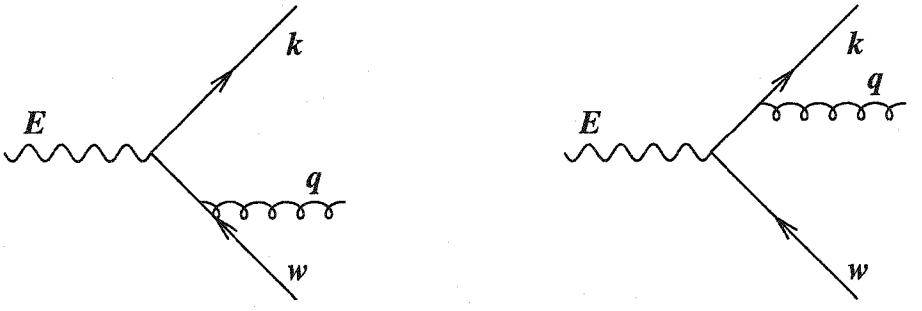

Figure 9.4: Heavy photon decay at first order in α and α_s.

Photon decay into a quark, antiquark and a gluon at first order in the electromagnetic and strong coupling constant can occur by two types of Feynman diagrams

[113] as shown in Fig. 9.4. The matrix element for the first diagram may be written as $\mathcal{M}_1 = \mathcal{M}_1^\mu \epsilon_\mu(\mathbf{p})$, where

$$\mathcal{M}_1^\mu = \bar{u}(k) ie\gamma^\mu \frac{i(\not{k} - \not{p})}{(k-p)^2} ig\gamma^\rho \epsilon_\rho^*(q) v(w)$$

for the second diagram

$$\mathcal{M}_2^\mu = \bar{u}(k) ig\gamma^\rho \epsilon_\rho^*(q) \frac{i(\not{p} - \not{w})}{(p-w)^2} ie\gamma^\mu v(w)$$

Taking the product $\mathcal{M}_1^{*\mu}\mathcal{M}_{1\mu}$ and summing over the spins and colours of the quark, antiquark and the gluon gives

$$\mathcal{M}_1^{*\mu}\mathcal{M}_{1\mu} = -32e^2g^2\frac{E-2w}{E-2k}. \tag{9.50}$$

Similarly

$$\mathcal{M}_2^{*\mu}\mathcal{M}_{2\mu} = -32e^2g^2\frac{E-2k}{E-2w}. \tag{9.51}$$

Notice that as the three 3-vectors $\vec{k}, \vec{q}, \vec{w}$ form a triangle, $E - 2k = w + q - k$ is always positive. By the same argument $E-2w$ and $E-2q$ are also positive. We thus note that $\mathcal{M}_1^{*\mu}\mathcal{M}_{1\mu}, \mathcal{M}_2^{*\mu}\mathcal{M}_{2\mu}$ are negative. This is to be expected as the square of the full matrix element $|\mathcal{M}|^2$ is positive, where from the sum over the photon's spin we get

$$|\mathcal{M}|^2 = -g_{\mu,\nu}\mathcal{M}^{*\mu}\mathcal{M}^\nu = -\mathcal{M}^{*\mu}\mathcal{M}_\mu.$$

The cross term is

$$\mathcal{M}_2^{*\mu}\mathcal{M}_{1\mu} = -32e^2g^2\frac{2E(E-2q)}{[E-2w][E-2k]}. \tag{9.52}$$

Comparing the above three equations with the result from the loop calculation (Eq.9.49, 9.47) gives us the relations:

$$Disc[\Pi^{2\mu}_{\mu}](E-k-q-E_{k-q}) = i\int \frac{d^3kd^3qd^3w}{(2\pi)^9 2q2k2w}(2\pi)^4\delta^4(\mathbf{p}-\mathbf{k}-\mathbf{q}-\mathbf{w}) \times \Big\{[1-\tilde{n}(k)][1+n(q)][1-\tilde{n}(w)] - \tilde{n}(k)n(q)\tilde{n}(w)\Big\} \times \Big[\mathcal{M}_1^{*\mu}\mathcal{M}_{1\mu} + \mathcal{M}_2^{*\mu}\mathcal{M}_{2\mu}\Big], \tag{9.53}$$

$$Disc[\Pi^{1\mu}_{\mu}](E-k-q-E_{k-q}) = i\int \frac{d^3kd^3qd^3w}{(2\pi)^9 2q2k2w}(2\pi)^4\delta^4(\mathbf{p}-\mathbf{k}-\mathbf{q}-\mathbf{w}) \times \Big\{[1-\tilde{n}(k)][1+n(q)][1-\tilde{n}(w)] - \tilde{n}(k)n(q)\tilde{n}(w)\Big\} \times \Big[\mathcal{M}_2^{*\mu}\mathcal{M}_{1\mu} + \mathcal{M}_1^{*\mu}\mathcal{M}_{2\mu}\Big], \tag{9.54}$$

and hence we get the relation written down by Weldon [114]

$$Disc[\Pi^{\mu}_{\mu}](E-k-q-E_{k-q}) = i\int \frac{d^3kd^3qd^3w}{(2\pi)^9 2q2k2w}(2\pi)^4\delta^4(\mathbf{p}-\mathbf{k}-\mathbf{q}-\mathbf{w}) \times \Big\{[1-\tilde{n}(k)][1+n(q)][1-\tilde{n}(w)] - \tilde{n}(k)n(q)\tilde{n}(w)\Big\} \times \Big[\mathcal{M}^{*\mu}\mathcal{M}_{\mu}\Big], \tag{9.55}$$

where $\mathcal{M} = \mathcal{M}^{\mu}\epsilon_{\mu}(p) = \mathcal{M}_1 + \mathcal{M}_2$ is the full matrix element of heavy photon decay.

9.6.2 *Compton Scattering.*

The analysis for Compton scattering is slightly more tricky. Note that there are two sets of terms from Eqs. (9.18,9.19) and Eqs. (9.37,9.39,9.41) that may lead to Compton scattering. One appears with the delta function $\delta(E+k-q-E_{k-q})$ and the other with the delta function $\delta(E+E_{k-q}-k-q)$. The delta functions can be turned into one another simply by replacing $\vec{k} \to \vec{k}+\vec{q}$, followed by $\vec{q} \to -\vec{q}$. One notes on performing this operation that the rest of the integrand looks rather different. This happens as there are 4 topologically distinct diagrams that may fall under the category of Compton scattering (it is well known that that for a given in state there are two diagrams that lead to Compton scattering; there are four here as we sum

over the possibilities of the incoming fermion being a quark or antiquark). Let us consider the contribution from Π^1 :

$$Disc[\Pi^1](E+k-E_{q-k}-q) = (2\pi i)8e^2g^2\int\frac{d^3kd^3q}{(2\pi)^6q} \times\left\{\tilde{n}(k)[1-\tilde{n}(E_{q-k})][1+n(q)]-[1-\tilde{n}(k)]\tilde{n}(E_{q-k})n(q)\right\} \times\frac{s_3s_4[\hat{k}_-\cdot\widehat{(q-k)}_+][\hat{k}_{s_4}\cdot\widehat{(q-k)}_{s_3}]}{[-k+q+s_3E_{q-k}][q+E_{q-k}+s_4k]}\delta(E+k-E_{q-k}-q). \tag{9.56}$$

For the contribution from Π^2 , recall that we have an overall factor of two on each of the results of Eqs. (9.37,9.39,9.41) coming from the overall symmetry factor of Π^2 being double that of Π^1 . We take half of the contribution from the $\delta(E+k-E_{k-q}-q)$ term, and half from the $\delta(E+E_{k-q}-k-q)$ term, and in the second contribution change $\vec{k}\to\vec{k}+\vec{q}$, followed by $\vec{q}\to-\vec{q}$. This gives the total contribution from Π^2 as

$$Disc[\Pi^2](E+k-E_{q-k}-q) = (2\pi i)8e^2g^2\int\frac{d^3kd^3q}{(2\pi)^6q} \times\left\{\tilde{n}(k)[1-\tilde{n}(E_{q-k})][1+n(q)]-[1-\tilde{n}(k)]\tilde{n}(E_{q-k})n(q)\right\} \times\left[\frac{\hat{k}_-\cdot\widehat{(q-k)}_+}{[k+q+E_{q-k}]^2}+\frac{\hat{k}_-\cdot\widehat{(q-k)}_+}{[k-q+E_{q-k}]^2}\right]\delta(E+k-E_{q-k}-q). \tag{9.57}$$

Notice that the combination of distribution functions appearing in the curly brackets are identical. The product of the three factors $\tilde{n}(k)[1-\tilde{n}(E_{q-k})][1+n(q)]$ has the interpretation of an incoming quark(or an antiquark) from the medium fusing with the photon coming in from outside the bath, resulting in an gluon and a quark(or antiquark) going into the medium. Subtracted from this is the product $[1-\tilde{n}(k)]\tilde{n}(E_{q-k})n(q)$, which has the interpretation of an incoming quark(antiquark) from the medium fusing with an incoming gluon from the medium, resulting in a

quark(antiquark) going back into the medium, and a virtual photon which leaves the medium (Fig. 9.5).

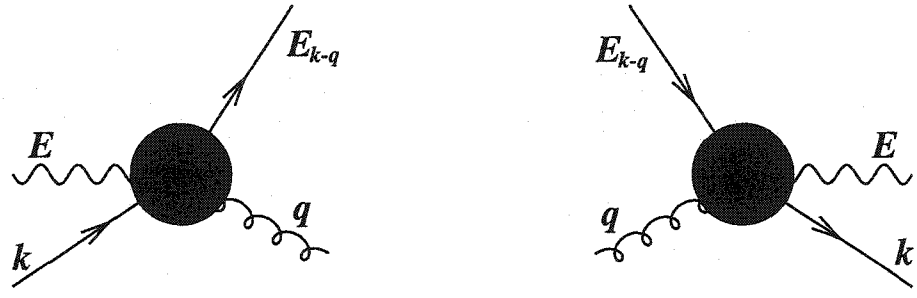

Figure 9.5: Quark Compton scattering.

To convert the above expressions into cross sections for Compton scattering, we again define the new four-vector $\mathbf{w} = (w, \vec{w})$, such that $w = E + k - q$. This is generalized to

$$\mathbf{w} = \mathbf{p} + \mathbf{k} - \mathbf{q}.$$

as a result $\vec{w} = \vec{k} - \vec{q}$. Now, requiring that $\mathbf{w}$ be on shell imposes the condition that

$$(E + k - q)^2 = k^2 + q^2 - 2kq\cos\theta$$

$$\Rightarrow E(E + 2k - 2q) = \mathbf{k} \cdot \mathbf{q}.$$

Using the above relations we many now rewrite the discontinuity obtained from Π^2. In the numerators of the integrand we notice the factor $(\widehat{k - q})_+ \cdot \hat{k}_-$, which may be written as $\hat{\mathbf{w}}_+ \cdot \hat{\mathbf{k}}_- = (E+2k)(E-2w)/2$. We introduce the standard denominators $2k, 2w$ and factors of 2π and perform a similar set of operations as for photon decay to obtain the full result for Compton scattering as

$$\begin{aligned} Disc[\Pi](E + k - q - E_{k-q}) = i \int \frac{d^3k d^3q d^3w}{(2\pi)^9 2q 2k 2w} (2\pi)^4 \delta^4(\mathbf{p} + \mathbf{k} - \mathbf{q} - \mathbf{w}) \\ \times \left\{ \tilde{n}(k)[1 + n(q)][1 - \tilde{n}(w)] - [1 - \tilde{n}(k)]n(q)\tilde{n}(w) \right\} \\ \times 32e^2g^2 \left[\frac{E + 2k}{E - 2w} + \frac{E - 2w}{E + 2k} + 2\frac{E(E - 2q)}{[E - 2w][E + 2k]} \right]. \end{aligned} \tag{9.58}$$

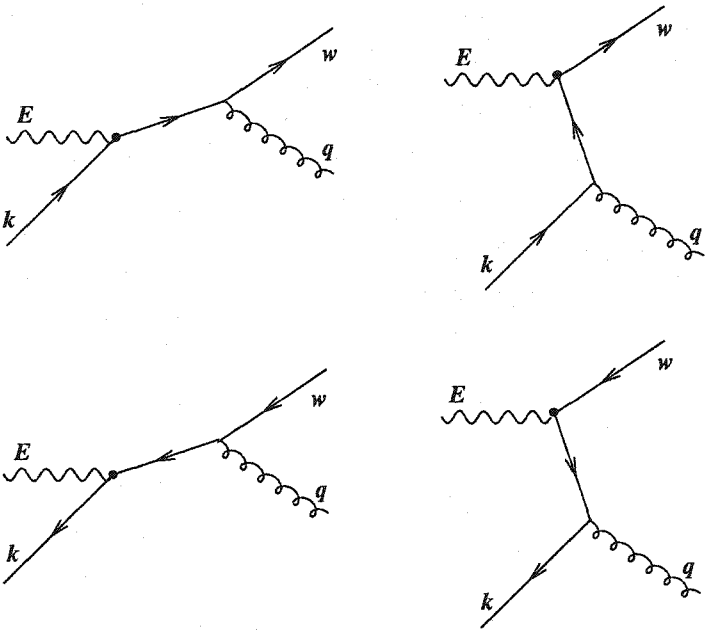

Figure 9.6: Compton scattering at first order in α and α_s.

Recall that in Π^1 there is another term, the coefficient of the delta function $\delta(E + E_{q-k} - k - q)$, that leads to Compton scattering. Also, in the Compton scattering contributions from Π^2, we only used a half of both the terms. Following almost the same method as above, one can demonstrate that the form of the contribution from these terms is almost the same as above with k and w interchanged. In it, one may interchange $\vec{w} \to \vec{k}$ to get the same contribution as Eq. (9.58); hence doubling the total contribution from Compton scattering.

Compton scattering by an incoming photon of a thermal medium of quarks and antiquarks, at first order in the electromagnetic and strong coupling constant can occur as a result of four processes as shown in Fig. 9.6. The matrix element for the diagrams may be written as $\mathcal{M}_n = \mathcal{M}_n^\mu \epsilon_\mu(\mathbf{p})$, where

$$\mathcal{M}_1^\mu = \bar{u}(\mathbf{w}) i g \gamma^\rho \epsilon_\rho^*(\mathbf{q}) i \frac{\not{p} + \not{k}}{(\mathbf{p}+\mathbf{k})^2} i e \gamma^\mu \epsilon_\mu(\mathbf{p}) u(\mathbf{k})$$

$$\mathcal{M}_2^\mu = \bar{u}(\mathbf{w}) i e \gamma^\mu \epsilon_\mu(\mathbf{p}) \frac{\not{w} - \not{p}}{(\mathbf{w}-\mathbf{p})^2} i g \gamma^\rho \epsilon_\rho^*(\mathbf{q}) u(\mathbf{k}).$$

The amplitude for the third and fourth diagram can be obtained from the two amplitudes above simply changing $u \to v$. Taking the products and summing over spins and colours (remember diagrams 1 and 2 interfere with each other, and so do 3 and 4), we get

$$\mathcal{M}_1^{*\mu}\mathcal{M}_{1\mu} = 32e^2g^2\frac{E-2w}{E+2k}, \tag{9.59}$$

$$\mathcal{M}_2^{*\mu}\mathcal{M}_{2\mu} = 32e^2g^2\frac{E+2k}{E-2w}. \tag{9.60}$$

Once again, note that $\mathcal{M}_1^{*\mu}\mathcal{M}_{1\mu}, \mathcal{M}_2^{*\mu}\mathcal{M}_{2\mu}$ are negative. This is because $E-2w = q-k-w$ is always negative due to the triangle condition mentioned in the previous subsection. The cross term is

$$\mathcal{M}_2^{*\mu}\mathcal{M}_{1\mu} = 32e^2g^2\frac{2E(E-2q)}{[E-2w][E+2k]}. \tag{9.61}$$

Comparing the above three equations with the result from the loop calculation (Eq. (9.58)) gives us the relation:

$$\begin{aligned} Disc[\Pi_\mu^\mu](E+k-q-E_{k-q}) = i\int \frac{d^3kd^3qd^3w}{(2\pi)^9 2q2k2w}(2\pi)^4\delta^4(\mathbf{p}+\mathbf{k}-\mathbf{q}-\mathbf{w}) \\ \times\left\{\tilde{n}(k)[1+n(q)][1-\tilde{n}(w)] - [1-\tilde{n}(k)]n(q)\tilde{n}(w)\right\} \\ \times\left[\mathcal{M}_1^{*\mu}\mathcal{M}_{1\mu} + \mathcal{M}_2^{*\mu}\mathcal{M}_{2\mu} + 2\mathcal{M}_2^{*\mu}\mathcal{M}_{1\mu}\right]. \end{aligned} \tag{9.62}$$

Once again we note the interesting fact that in this gauge the mixed terms $\mathcal{M}_2^{*\mu}\mathcal{M}_{1\mu} + \mathcal{M}_1^{*\mu}\mathcal{M}_{2\mu}$ are always given by Π^1 and the square terms $\mathcal{M}_1^{*\mu}\mathcal{M}_{1\mu} + \mathcal{M}_2^{*\mu}\mathcal{M}_{2\mu}$ are furnished by Π^2.

9.6.3 *Pair Creation*

The analysis for pair creation(often referred to as photon-gluon fusion) is almost identical to the two previous sections. Its contribution is furnished by the only remaining delta functions in Eqs. (9.18,9.19) in the first self-energy, and Eqs. (9.37,9.39,9.41) in

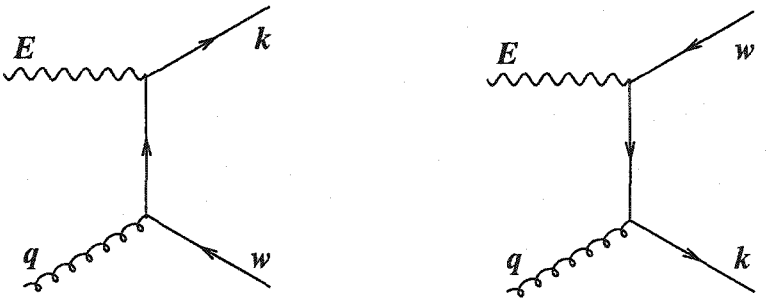

Figure 9.7: Pair creation at first order in α and α_s.

the second self-energy, *i.e.*, $\delta(E+q-k-E_{k-q})$. We simply state the results here: pair creation can occur through two types of processes, and has the discontinuity in the total self-energy as

$$\begin{aligned} Disc[\Pi^2](E+q-k-E_{k-q}) = -i\int \frac{d^3kd^3qd^3w}{(2\pi)^9 2q2k2w}(2\pi)^4\delta^4(\mathbf{p}-\mathbf{k}+\mathbf{q}-\mathbf{w}) \\ \times\left\{[1-\tilde{n}(k)]n(q)[1-\tilde{n}(w)]-[1+n(q)]\tilde{n}(k)\tilde{n}(w)\right\} \\ \times 32e^2g^2\left[\frac{E-2k}{E-2w}+\frac{E-2w}{E-2k}+2\frac{E(E+2q)}{[E-2w][E-2k]}\right]. \end{aligned} \tag{9.63}$$

9.7 *Physical interpretation: loop-containing cuts*

We now analyse the various discontinuities of Π^1 and Π^2 which contain loops. We start with the discontinuities of Π^1. These are given by Eqs. (9.15,9.16,9.17). We note that there are two terms with the delta function $\delta(E-2E_{k-q})$ these correspond to the cut of Fig. 9.8. There is, also, one term with the cut $\delta(E-2k)$, this corresponds to the cut of Fig. 9.9.

One may be satisfied with this interpretation of the cut diagrams and not proceed further. A recent paper [118], however, has drawn attention to the fact that one can obtain a somewhat different interpretation of these diagrams, in terms of interference between simple tree like diagrams and diagrams containing particles called "spectators". Spectators are essentially on-shell particles from the heat bath that enter with

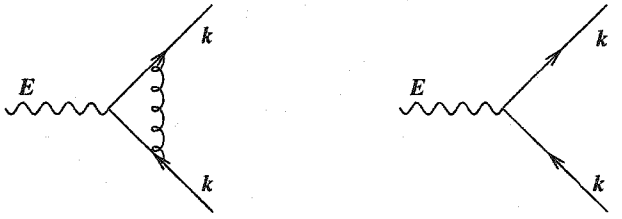

Figure 9.8: Photon decay at one loop corresponding to the cut $\delta(E-2E_{k-q})$.

the in-state and leave with the out-state without having interacted with the the rest of the "participants".

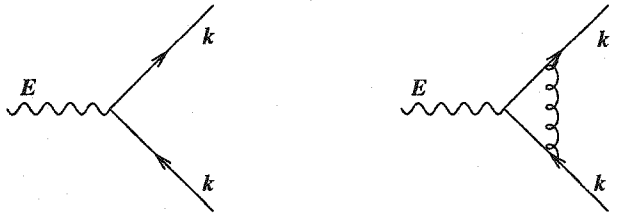

Figure 9.9: Photon decay at one loop corresponding to the cut $\delta(E-k)$.

We start by summing over the variable s_1 in Eq. 9.15. This immediately gives two terms, distinguished by the combination of distribution functions they carry:

$$Disc[2\Pi^{\mu}_{\mu}(A)]_{a1} = (-2\pi i)8e^2g^2\int\frac{d^3kd^3q}{(2\pi)^6}\frac{[\hat{k}_+\cdot\widehat{(q-k)}_{s_2}][\hat{k}_-\cdot\widehat{(q-k)}_{s_3}]}{q(E-(s_2-s_3)E_{q-k})} \times s_2\frac{[1-2\tilde{n}(k)][1-2\tilde{n}(E_{q-k})]q}{(k+s_3E_{k-q})^2-q^2}\delta(E-2k). \tag{9.64}$$

and

$$Disc[2\Pi^{\mu}_{\mu}(A)]_{a2} = (-2\pi i)8e^2g^2\int\frac{d^3kd^3q}{(2\pi)^6}\frac{[\hat{k}_+\cdot\widehat{(q-k)}_{s_2}][\hat{k}_-\cdot\widehat{(q-k)}_{s_3}]}{q(E-(s_2-s_3)E_{q-k})}\delta(E-2k) \times(-s_2)[1-2\tilde{n}(k)][1+2n(q)]\frac{s_3k+E_{q-k}}{(k+s_3E_{k-q})^2-q^2}. \tag{9.65}$$

In Eq.9.64, if we replace $s_2\rightarrow -s_4$,$s_3\rightarrow -s$, followed by $\vec{k}\rightarrow\vec{q}-\vec{k}$ we get

$$Disc[2\Pi^{\mu}_{\mu}(A)]_{a1} = (+2\pi i)8e^2g^2\int\frac{d^3kd^3q}{(2\pi)^6}\frac{[(\widehat{q-k})_-\cdot\hat{k}_{s_4}][(\widehat{q-k})_+\cdot\hat{k}_s]}{q(E-(s-s_4)E_{q-k})}$$
$$\times\, s_4\frac{[1-2\tilde{n}(k)][1-2\tilde{n}(E_{q-k})]q}{(E_{q-k}-sk)^2-q^2}\delta(E-2E_{q-k}). \tag{9.66}$$

The above is exactly the same as Eq.(9.16). This is to be expected as the two cuts should in principle represent the same diagram up to a shift in momenta. We thus double this contribution and focus on it. It represents photon decay into two quarks with quark emission and absorption from the final state quarks. The other part from Eq. (9.65) along with Eq. (9.17) will represent photon decay with gluon emission and absorption off the external quarks.

9.7.1 *Photon decay with quark emission-absorption off vertex and final state.*

We begin by summing over the remaining sign variables s_2, s_3 in $Disc[2\Pi^{\mu}_{\mu}(A)]_{a1}$ to get

$$Disc[2\Pi^{\mu}_{\mu}]_4 = 2\times(-2\pi i)8e^2g^2\int\frac{d^3kd^3q}{(2\pi)^6}[1-2\tilde{n}(k)][1-2\tilde{n}(E_{q-k})]\delta(E-2k)$$
$$\times\left[\frac{[\hat{k}_+\cdot(\widehat{q-k})_+][\hat{k}_-\cdot(\widehat{q-k})_+]}{E[(k+E_{k-q})^2-q^2]}-\frac{[\hat{k}_+\cdot(\widehat{q-k})_-][\hat{k}_-\cdot(\widehat{q-k})_+]}{(E+2E_{q-k})[(k+E_{k-q})^2-q^2]}\right.$$
$$\left.+\frac{[\hat{k}_+\cdot(\widehat{q-k})_+][\hat{k}_-\cdot(\widehat{q-k})_-]}{(E-2E_{q-k})[(k-E_{k-q})^2-q^2]}-\frac{[\hat{k}_+\cdot(\widehat{q-k})_-][\hat{k}_-\cdot(\widehat{q-k})_-]}{E[(k-E_{k-q})^2-q^2]}\right]. \tag{9.67}$$

As in the previous section, the distribution functions will be reorganized to allow for an interpretation in terms of thermal weights for particle emission and absorption. In the first two terms we define the new lightlike four-vector **w** such that $\vec{w}=\vec{q}-\vec{k}$. In the last two terms we define **w** such that $\vec{w}=-\vec{q}+\vec{k}$. This allows us to change the variable of integration as $d^3q\rightarrow d^3w$, as k is a constant as far as the q integration is concerned. We may also redefine the distribution functions as

$$[1-2\tilde{n}(k)][1-2\tilde{n}(w)] = \Big[[1-\tilde{n}(k)][1-\tilde{n}(k)] - \tilde{n}(k)\tilde{n}(k)\Big]\Big[[1-\tilde{n}(w)] - [\tilde{n}(w)]\Big].$$

The first set of factors in the larger square brackets has the usual interpretation [114] of the thermal factors that are associated with the probability of particle emission into a heat bath or particle absorption from a heat bath. In this case they carry the obvious meaning of: [emit fermion of energy k][emit fermion of energy k] − [absorb fermion of energy k][absorb fermion of energy k]. The reader will note that unlike the self-energy cuts considered in [114] or those of the previous section, the two cut diagrams that will result from this imaginary part of the self-energy will not be symmetric, in the sense that it will be the interference between a diagram with a loop and a simple tree diagram. The thermal factors discussed above will be the same for either diagram as they pertain to the quark and anti-quark that emanate from the decay of the photon (or those that combine to form the photon). Both amplitudes that result from this imaginary part contain this process and thus have identical thermal factors.

The second set of thermal factors has a new interpretation. These thermal factors pertain to the particles in the remaining loop and thus are germane to only one of the two interfering amplitudes. We will demonstrate that these signal the difference of two amplitudes: that for the emission of a quark or anti-quark into the bath and its subsequent absorption from the bath, and vice-versa. Thus the second set of distribution functions is to be understood as: [emit fermion of four-momentum w][absorb the same fermion of four-momentum w] − [absorb fermion of four-momentum w][emit the same fermion of four-momentum w].

The process of emission of a fermion of four-momentum $\mathbf{w}$ into a bath followed by its reabsorption is formally achieved by the action of creation and annihilation operators on the bath state $|\tilde{n}_{\mathbf{w}}\rangle$ i.e,

$$aa^{\dagger}|\tilde{n}_{\mathbf{w}}\rangle = \big(1-\tilde{n}_{\mathbf{w}}\big)|\tilde{n}_{\mathbf{w}}\rangle. \tag{9.68}$$

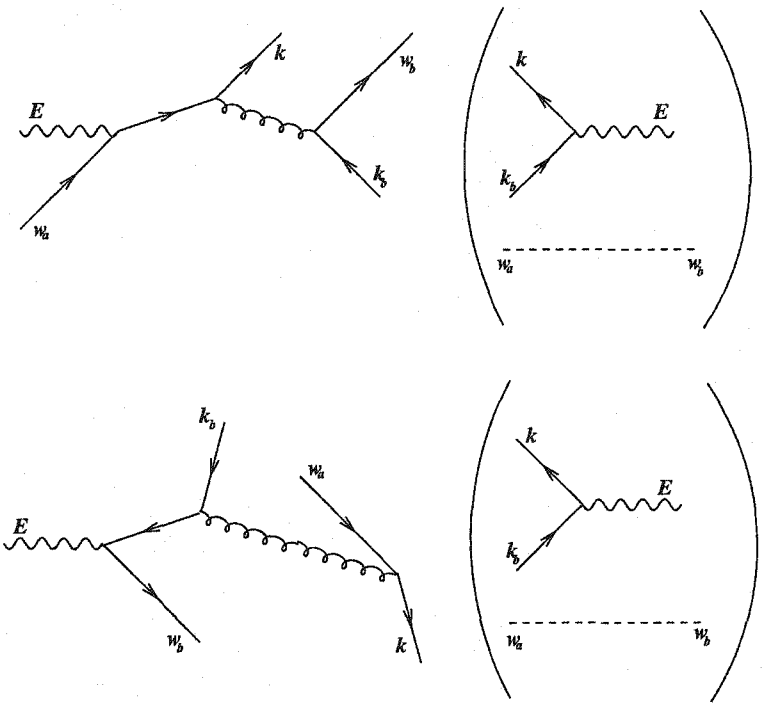

Figure 9.10: Interference between diagrams of different order in α_s. The diagrams on the left indicate $2 \to 3$ reactions like $\gamma Q \to q\bar{q}Q$ (where the Q indicates that the incoming and outgoing quarks are identical). The diagrams on the right indicate the complex conjugate of Born term photon decay with a comoving quark spectator *i.e.*, $(\gamma \to q\bar{q}) \otimes (Q \to Q)$.

The reverse process, i.e., the absorption of a fermion from the bath and it subsequent re-emission into the bath is formally achieved by the action of annihilation and creation operators on the bath state i.e.,

$$a^\dagger a|\tilde{n}_{\mathbf{w}}\rangle = \left(\tilde{n}_{\mathbf{w}}\right)|\tilde{n}_{\mathbf{w}}\rangle. \tag{9.69}$$

The discontinuity of the self-energy will represent the amplitude of a particular process multiplied with the complex conjugate of another. In one of these processes the above mentioned fermion will perform the emission and absorption procedure referred to above. In the other amplitude, as we will show shortly, it will simply enter and leave without having interacted with the rest of the particles. Due to this reason, it has been referred to previously (see [118, 99]) as a spectator.

We introduce the usual denominators of $2w, 2k$ to get

$$
\begin{aligned}
Disc[\Pi^{\mu}_{\mu}]_4 = 2 \times (-2\pi i) 8e^2 g^2 \int \frac{d^3k d^3\omega}{(2\pi)^6 kwkw} \delta(E-2k) \\
\times \Big[[1-\tilde{n}(k)][1-\tilde{n}(k)] - \tilde{n}(k)\tilde{n}(k)\Big] \\
\times \Big[[1-\tilde{n}(w)] - [\tilde{n}(w)]\Big] \\
\times \Bigg[\frac{[\mathbf{k}_+ \cdot \mathbf{w}_+][\mathbf{k}_- \cdot \mathbf{w}_+]}{E[(k+w)^2-q^2]} - \frac{[\mathbf{k}_+ \cdot \mathbf{w}_-][\mathbf{k}_- \cdot \mathbf{w}_+]}{(E+2w)[(k+w)^2-q^2]} \\
+ \frac{[\mathbf{k}_+ \cdot \mathbf{w}_-][\mathbf{k}_- \cdot \mathbf{w}_+]}{(E-2w)[(k-w)^2-q^2]} - \frac{[\mathbf{k}_+ \cdot \mathbf{w}_+][\mathbf{k}_- \cdot \mathbf{w}_+]}{E[(k-w)^2-q^2]}\Bigg].
\end{aligned} \tag{9.70}
$$

We now introduce the new four-vector $\mathbf{k}_b = (k, -\vec{k})$, and generalize the delta function to a four delta function. We then combine the first two terms and the last two terms to write

$$
\begin{aligned}
Disc[\Pi^{\mu}_{\mu}]_4 = i8e^2 g^2 \int \frac{d^3k d^3w d^3k_b}{(2\pi)^9 8kwk_b} 16(2\pi)^4 \delta^4(\mathbf{p}+\mathbf{w}-\mathbf{k}-\mathbf{k}_b-\mathbf{w}) \\
\times \Big[[1-\tilde{n}(k)][1-\tilde{n}(k_b)] - \tilde{n}(k)\tilde{n}(k_b)\Big] \\
\times \Big[[1-\tilde{n}(w)] - [\tilde{n}(w)]\Big] \\
\times \Bigg[\frac{[\mathbf{k}_b \cdot \mathbf{w}][\mathbf{k}_a \cdot (\mathbf{p}+\mathbf{w})]}{[(E+w)^2-w^2][(k+w)^2-q^2]} \\
+ \frac{[\mathbf{k}_a \cdot \mathbf{w}][\mathbf{k}_b \cdot (\mathbf{w}-\mathbf{p})]}{[(w-E)^2-w^2][(k-w)^2-q^2]}\Bigg].
\end{aligned} \tag{9.71}
$$

The above, has the interpretation of Fig. 9.10. This indicates the interference between two diagrams of different order in coupling constants. Let the matrix elements of the two tree-level diagrams with two propagators be denoted as $\mathcal{M}_1 = \mathcal{M}_1^{\mu}\epsilon_{\mu}(\mathbf{p})$ and $\mathcal{M}_2 = \mathcal{M}_2^{\mu}\epsilon_{\mu}(\mathbf{p})$. The matrix element of the term in brackets is simply denoted as $m^{\mu}\epsilon_{\mu}(\mathbf{p})$. Where the dotted line called the spectator is simply a product of Dirac delta functions over four momenta and Kronecker delta functions over the spins and colours of the incoming and outgoing fermions denoted by w_a and w_b (here, for brevity we indicate all the different quantum numbers, both continuous and discreet, of the incoming and outgoing particles by a single label).

It is now simple to verify that the result obtained in Eq. (9.71) can be written as

$$\begin{aligned} Disc[\Pi^{\mu}_{\mu}]_4 = i \int \frac{d^3k d^3w d^3k_b}{(2\pi)^9 8kwk_b}(2\pi)^4\delta^4(\mathbf{p}+\mathbf{w}-\mathbf{k}-\mathbf{k}_b-\mathbf{w}) \\ \times \Big[[1-\tilde{n}(k)][1-\tilde{n}(k_b)]-\tilde{n}(k)\tilde{n}(k_b)\Big] \\ \times \Big[\{1-\tilde{n}(w)\}-\tilde{n}(w)\Big] \\ \times \Big[2m^{\mu *}\mathcal{M}_1^{\mu}+2m^{\mu *}\mathcal{M}_2^{\mu}\Big]. \end{aligned} \tag{9.72}$$

Where the Kronecker and Dirac delta functions over the fermions w_a and w_b have been used to set $w_a = w_b = w$. The factor of 2 preceding the interference matrix elements is due to the fact that a similar process may be obtained by replacing an incoming quark spectator with an anti-quark spectator.

9.7.2 *Photon decay with gluon emission-absorption from final state quarks.*

This term receives contributions from $Disc[2\Pi^{\mu}_{\mu}(A)]_{a2}$ and $Disc[2\Pi^{\mu}_{\mu}(D)]_b$. The fate of this discontinuity is essentially similar to the previous section and results once again in the interference of tree level diagrams of different order. There are two sets of diagrams with two propagators here as well, the difference being that the incoming, outgoing particle with the same set of quantum numbers or in other words the spectator is a gluon. We once again introduce the on-shell four-vector $\mathbf{w}$, such that $\vec{w} = \vec{k} - \vec{q}$. We use this to change the variable of integration in $Disc[2\Pi^{\mu}_{\mu}(D)]_b$. $Disc[2\Pi^{\mu}_{\mu}(A)]_{a2}$ we relabel the dummy variable $\vec{k} \to \vec{w}$. Both discontinuities give essentially the same contribution thus the total discontinuity from such processes (Fig. 9.11) is given as

$$\begin{aligned} Disc[\Pi^{\mu}_{\mu}]_5 = i8e^2g^2 \int \frac{d^3w d^3q d^3w_b}{(2\pi)^9 8kwk_b} 32(2\pi)^4\delta^4(\mathbf{p}+\mathbf{q}-\mathbf{w}-\mathbf{w}_b-\mathbf{q}) \\ \times \Big[[1-\tilde{n}(w)][1-\tilde{n}(w_b)]-\tilde{n}(w)\tilde{n}(w_b)\Big] \end{aligned}$$

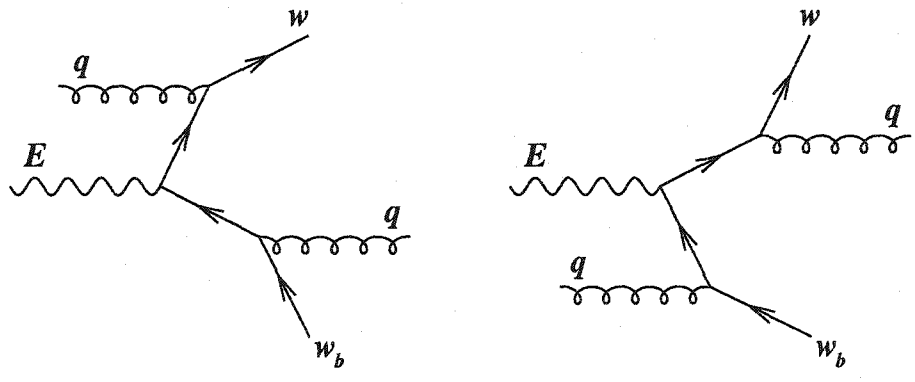

Figure 9.11: Photon decay with spectator gluon (the Born term with spectator gluon is implied, see Fig. 9.10).

$$\times \Big[[1+n(q)]+[n(q)]\Big]$$
$$\times \left[\frac{[\mathbf{w}_b\cdot(\mathbf{q}-\mathbf{w})][\mathbf{w}_a\cdot(\mathbf{q}-\mathbf{w}_b)]}{[(q-w)^2-k^2][(q+w)^2-k^2]}\right]. \tag{9.73}$$

Which is once again equal to

$$\begin{aligned} Disc[\Pi^\mu_\mu]_5 = i\int \frac{d^3w d^3q d^3w_b}{(2\pi)^9 8kwk_b}(2\pi)^4\delta^4(\mathbf{p}+\mathbf{q}-\mathbf{w}-\mathbf{w}_b-\mathbf{q}) \\ \times \Big[[1-\tilde{n}(w)][1-\tilde{n}(w_b)]-\tilde{n}(w)\tilde{n}(w_b)\Big] \\ \times \Big[[1+n(q)]+[n(q)]\Big] \\ \times \Big[m^{\mu*}\mathcal{M}_1^\mu + m^{\mu*}\mathcal{M}_2^\mu\Big]. \end{aligned} \tag{9.74}$$

Where m represents the same process as in the previous subsection. The amplitudes $\mathcal{M}_1$ and $\mathcal{M}_2$ represent the processes of Fig. 9.11. The interpretation of the first set of distribution functions is the same as before *i.e.*, emission and absorption of two particles of energy k. The second term has the interpretation of a gluon spectator exactly identical to that of the quark spectator in the earlier subsection, but with Pauli factors replaced with Bose factors. Note that, unlike in the previous section, there is no factor of 2 preceding the matrix elements as the spectators are gluons.

9.7.3 *Photon decay with quark and gluon emission-absorption off the same quark line*

We, now, begin the analysis of the last loop-containing cut. This is essentially given by the discontinuities of Eqs. (9.34,9.35). Combining these two discontinuities, and writing $k = E - k$ in the denominators of the terms from $Disc[\Pi^{\mu}_{\mu}(A)]_a$ (note that we have to double this contribution as it emanates from the second self-energy diagram which has a symmetry factor of 2 more than the first self-energy diagram), we get

$$\begin{aligned} Disc[\Pi^{\mu}_{\mu}]_6 &= (2\pi i)8e^2g^2\int\frac{dkd\theta d\phi\sin\theta d^3q}{(2\pi)^6 q}\delta(E-2k)[1-2\tilde{n}(k)] \\ &\times\left\{\frac{2k\mathcal{NS}}{[E-s_2E_{k-q}-s_1q-k]}+\frac{k^2(\mathcal{NS})'}{[E-s_2E_{k-q}-s_1q-k]}\right. \\ &\left.+\frac{k^2\mathcal{NS}[1+s_2E'_{k-q}]}{[E-s_2E_{k-q}-s_1q-k]^2}\right\}. \\ &= (2\pi i)8e^2g^2\int\frac{dkd\theta d\phi\sin\theta d^3q}{(2\pi)^6 q}\delta(E-2k)[1-2\tilde{n}(k)] \\ &\times\frac{d}{dk}\left\{\frac{k^2\mathcal{NS}}{[E-s_2E_{k-q}-s_1q-k]}\right\}. \end{aligned} \tag{9.75}$$

The above term does not readily admit a physical interpretation, however, the infrared limit will be evaluated with the above expression as the starting point as it is formally correct. To try and obtain a physical interpretation from the expression given above, an integration by parts is performed to obtain the discontinuity as

$$\begin{aligned} Disc[\Pi^{\mu}_{\mu}]_6 &= (2\pi i)8e^2g^2\int\frac{dkd\theta d\phi\sin\theta d^3q}{(2\pi)^6 q}\Big\{-\frac{d\delta(E-2k)}{dk}\Big\}[1-2\tilde{n}(E/2)] \\ &\times\frac{k^2\mathcal{NS}}{[E-s_2E_{k-q}-s_1q-k]} \\ &= (2\pi i)8e^2g^2\int\frac{d^3kd^3q}{(2\pi)^6 q}\frac{\mathcal{NS}}{[k-s_2E_{k-q}-s_1q]} \\ &\times\Big\{2\delta'(E-2k)[1-2\tilde{n}(E/2)]\Big\}. \end{aligned} \tag{9.76}$$

Where, we have used the property that

$$\frac{d\delta(E-2k)}{dk} = 2\frac{d\delta(E-2k)}{d(2k)} = -2\frac{d\delta(E-2k)}{d(E)} = -2\delta'(E-2k).$$

Interestingly, as an aside, we note that one may still obtain a physical interpretation of the above term in terms of spectators with retarded propagators. To obtain this, we expand the factor $\frac{\mathcal{NS}}{[k-s_2E_{k-q}-s_1q]}$ by summing over s_1 and s_2. Here, as expected, we will obtain a part dependent on Bose distribution functions and a part dependent on Fermi distribution functions. We will illustrate the physical interpretation using the part containing the Bose distribution functions. We begin by writing the delta function in Eq. (9.76) using the following representation:

$$\delta(x) = \lim_{\epsilon\to 0}\frac{1}{\pi}\frac{\epsilon}{x^2+\epsilon^2}. \tag{9.77}$$

In this representation scheme, we obtain

$$\delta'(x) = -2\left[\frac{\delta(x)}{x+i\epsilon} + i\pi\delta^2(x)\right]. \tag{9.78}$$

Substituting the above relation in Eq. (9.76) we get

$$\begin{aligned} Disc[\Pi^{\mu}_{\mu}]_6 = (2\pi i)16e^2g^2\int\frac{d^3kd^3q}{(2\pi)^6q}(-2)\delta(E-2k)[1-2\tilde{n}(E/2)] \\ \times\frac{\mathcal{NS}}{[E-s_2E_{k-q}-s_1q-k]}\left\{\frac{1}{(E-2k)+i\epsilon}+i\pi\delta(E-2k)\right\}. \end{aligned} \tag{9.79}$$

We now write unity in the form of an integral as

$$\begin{aligned} 1 &= \int_{\infty}^{\infty}d\omega^0\frac{1}{2}\Big\{\delta(\omega^0+k)+\delta(\omega^0+k)\Big\} \\ &= \int_{\infty}^{\infty}d\omega^0 k\delta(\omega^{0^2}-k^2). \end{aligned} \tag{9.80}$$

Substituting Eq. (9.80) in Eq. (9.79), we obtain

$$
\begin{aligned}
Disc[\Pi^{\mu}_{\mu}]_6 &= (2\pi i)16e^2g^2\int d\omega^0(E/2)\delta(\omega^{0\,2}-(E/2)^2)\int\frac{d^3kd^3q}{(2\pi)^6q}(-2)\delta(E-2k)\\
&\times\frac{[1-2\tilde{n}(E/2)]\mathcal{NS}}{[E-s_2E_{k-q}-s_1q-k]}\Big\{\frac{1}{(E-2k)+i\epsilon}+2\pi i\tilde{n}(\omega^0)\delta(E-2k)\\
&\quad-2\pi i(\tilde{n}(\omega^0)-1/2)\delta(E-2k)\Big\}\\
&=(2\pi i)(-16e^2g^2)\int d\omega^0\int\frac{d^3kd^3q}{(2\pi)^6q}\delta(\omega^{0\,2}-(E/2)^2)\delta(E-2k)[1-2\tilde{n}(E/2)]\\
&\times\frac{E\mathcal{NS}}{[E-s_2E_{k-q}-s_1q-k]}\Big\{\frac{1}{(E-2k)+i\epsilon}+2\pi i\tilde{n}(\omega^0)\delta(E-2k)\\
&\quad-2\pi i(\tilde{n}(\omega^0)-\theta(-\omega^0))\delta(E-2k)\Big\}. \qquad (9.81)
\end{aligned}
$$

In the above we have simply added and subtracted the factor $2\pi i\tilde{n}(\omega^0)\delta(E-2k)$ inside the curly brackets and rewritten $1/2$ as $\theta(-\omega^0)$, as the rest of the integrand is an even function of ω^0.

We now introduce the three vector part of ω as

$$
\begin{aligned}
\delta(\omega^{0\,2}-(E/2)^2)\delta(E-k-k) &= \int d^3\omega\delta(\omega^{0\,2}-(E/2)^2)\delta(E-k-k)\delta^3(-\vec{k}-\vec{\omega})\\
&= \int d^3\omega\delta(\omega^{0\,2}-|\vec{\omega}|^2)\delta(E-k-|\vec{\omega}|)\delta^3(-\vec{k}-\vec{\omega}).
\end{aligned}
\qquad (9.82)
$$

As stated previously we now concentrate on the part of $\mathcal{NS}/[k-s_2E_{k-q}-s_1q]$ which depends on the Bose distribution function. This gives

$$
\begin{aligned}
Disc[\Pi^{\mu}_{\mu}]_6 &= i\int\frac{d^4\omega}{(2\pi)^4}\int\frac{d^3kd^3q}{(2\pi)^6 2q2k}2\pi\delta(\omega^{0\,2}-|\vec{\omega}|^2)(2\pi)^4\delta^4(\mathbf{p}-\mathbf{k}-\mathbf{w})\\
&\times\Big[\{1-\tilde{n}(k^0)\}\{1-\tilde{n}(\omega^0)\}-\tilde{n}(k^0)\tilde{n}(\omega^0)\Big]\Big[\{1+n(q)\}+n(q)\Big]\\
&\times(-64e^2g^2)E^2\Big[\frac{k(E-k-q)-\vec{k}\cdot(\vec{k}-\vec{q})}{(E-k-q)^2-|\vec{k}-\vec{q}|^2}+\frac{k(E-k+q)-\vec{k}\cdot(\vec{k}-\vec{q})}{(E-k+q)^2-|\vec{k}-\vec{q}|^2}\Big]\\
&\times\Big\{\tilde{\Delta}_R(\omega)\Big\}
\end{aligned}
$$

$$= i \int \frac{d^4\omega}{(2\pi)^4} \int \frac{d^3k d^3q}{(2\pi)^6 2q 2k} 2\pi\delta(\omega^{0^2} - |\vec{\omega}|^2)(2\pi)^4\delta^4(\mathbf{p} - \mathbf{k} - \mathbf{w})$$
$$\times \Big[\{1 - \tilde{n}(k^0)\}\{1 - \tilde{n}(\omega^0)\} - \tilde{n}(k^0)\tilde{n}(\omega^0)\Big]\Big[\{1 + n(q)\} + n(q)\Big]$$
$$\times \Big[m^{\mu *}\mathcal{M}_{1,\mu} + m^{\mu *}\mathcal{M}_{2,\mu}\Big]. \tag{9.83}$$

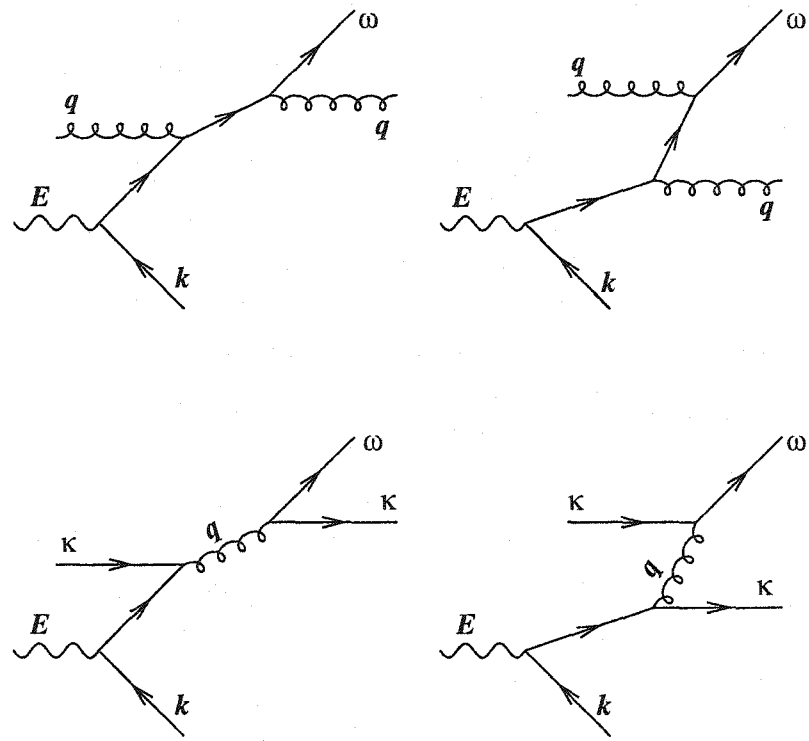

Figure 9.12: Photon decay into a $q\bar{q}$ pair. The quark then emits or absorbs a quark or a gluon.

Where $i \not{\omega}\tilde{\Delta}_R(\omega)$ is the retarded propagator. One may note that the integrand in the above equation is simply the interference matrix elements of the first ($\mathcal{M}_1 = \epsilon^\mu(p)\mathcal{M}_{1,\mu}$) and second diagram ($\mathcal{M}_2 = \epsilon^\mu(p)\mathcal{M}_{2,\mu}$)of Fig. 9.12 and the Born term ($m = \epsilon_\mu(p)m^\mu$) with a gluon spectator. A similar interpretation may be obtained for the the third and fourth diagrams of Fig. 9.12 in terms quark spectators. However, as the above equation is not mathematically well defined; it will not be used in evaluating the infrared limit. Eq. (9.75) will be used instead.

9.8 Infrared behaviour

We now examine closely the infra-red and collinear singularity structure of the terms enumerated in the two sections above. We will examine the infra-red behaviour in the limit of heavy dilepton production from a plasma of massless quarks *i.e.*, $E >> T$. There are essentially five terms:

F: Photon Gluon production denotes the reaction $q + \bar{q} \to g + \gamma$

C: Compton like reaction between a gluon and quark/anti-quark $g + q \to \bar{q} + \gamma$

D: denotes the three body fusion to form the photon $g + q + \bar{q} \to \gamma$

V: denotes photon formation from vertex corrected quark, antiquark.

S: denotes photon formation from self-energy corrected quark, anti-quark.

The full imaginary part of the two loop self-energy may be schematically written as

$$2\mathrm{Im}\Pi^{\mu}_{\mu} = -\frac{8e^2g^2}{(2\pi)^3}\int dw\Big\{n(w)[F(w) + D_g(w) + V_g(w) + S_g(w)] + \tilde{n}(w)[C(w) + D_q(w) + V_q(w) + S_q(w)]\Big\}. \tag{9.84}$$

The first four terms represent the part of the terms mentioned above which are proportional to the gluon distribution function. The last four terms are those proportional to the quark/antiquark distribution function. This is essentially the same notation as used by the authors of [101]. We now compute these contributions in turn.

9.8.1 Self-Energy correction S_g & S_q

The self-energy correction is essentially given by Eq. (9.75), *i.e.*,

$$Disc[\Pi^{\mu}_{\mu}]_6 = (2\pi i)8e^2g^2\int\frac{dkd\theta d\phi\sin\theta d^3q}{(2\pi)^6 q}\delta(E-2k)[1-2\tilde{n}(k)] \frac{d}{dk}\sum_{s_1,s_2}\frac{k^2\mathcal{NS}}{[E - s_2E_{k-q} - s_1q - k]}. \tag{9.85}$$

We concentrate, first, on the sum $\mathcal{S} = \sum_{s_1,s_2} \frac{k^2 \mathcal{N} \mathcal{S}}{[E - s_2 E_{k-q} - s_1 q - k]}$. This may be expanded as

$$\mathcal{S} = \frac{k}{w}\left[\frac{[1/2 - \tilde{n}(w) + 1/2 + n(q)]\mathbf{w}_+ \cdot \mathbf{k}_+}{E - k - w - q} + \frac{[1/2 - \tilde{n}(w) - (1/2 + n(q))]\mathbf{w}_+ \cdot \mathbf{k}_-}{E - k + w - q} + \frac{[-(1/2 - \tilde{n}(w)) + 1/2 + n(q)]\mathbf{w}_+ \cdot \mathbf{k}_+}{E - k - w + q} + \frac{[-(1/2 - \tilde{n}(w)) - (1/2 + n(q))]\mathbf{w}_+ \cdot \mathbf{k}_-}{E - k + w + q}\right]. \tag{9.86}$$

We now concentrate on the terms proportional to $1/2 + n(q)$, *i.e.*,

$$\mathcal{S}_g = k\left[\frac{1}{2} + n(q)\right]\left[\frac{2k(E - k - q) - 2\vec{w} \cdot \vec{k}}{(E - k - q)^2 - w^2} + \frac{2k(E - k + q) - 2\vec{w} \cdot \vec{k}}{(E - k + q)^2 - w^2}\right]. \tag{9.87}$$

Introducing the variables $\alpha = E - 2k - 2q$, $\beta = E - 2k + 2q$ and $y = \cos\theta$(where θ is the angle between $\vec{k}$ and $\vec{q}$), we obtain

$$\mathcal{S}_g = k\left[\frac{1}{2} + n(q)\right]\left[2 + \frac{(2k - E)\alpha}{E\alpha + 2kq(1 + y)} + \frac{(2k - E)\beta}{E\beta - 2kq(1 - y)}\right]. \tag{9.88}$$

Dropping the $\frac{1}{2}$ ahead of the gluon distribution function we obtain the matter part of $\mathcal{S}_g$. Using only this part we obtain (performing the unimportant angle integrations)

$$-\frac{8e^2g^2}{(2\pi)^3}\int dq n(q) S_g(q) = \frac{8e^2g^2}{(2\pi)^3}\int dk[1 - 2\tilde{n}(k)]\delta(k - E/2)\int dqq\int dy \frac{d}{dk}\mathcal{S}_{g,mat}. \tag{9.89}$$

The limits of the y integration are the locations for the onset of collinear singularities, these are shielded by removing a small part of phase space ϵ *i.e.*, the y integration is performed within the limits $-1 + \epsilon \to 1 - \epsilon$. The results will now depend on ϵ. This gives the result as

$$-\frac{8e^2g^2}{(2\pi)^3}\int dq n(q) S_g(q) = \frac{-8e^2g^2}{(2\pi)^3}\int dq n(q)\left[-4q - 4q\log\left(\frac{2}{\epsilon}\right)\right]. \tag{9.90}$$

In the above, the term $2\tilde{n}(E/2)$ has been dropped, as we are interested in the heavy dilepton limit where $E >> T$ and as a result $\tilde{n}(E/2) \to 0$. Thus, we get

$$S_g(w) = -4w - 4w \log\left(\frac{2}{\epsilon}\right). \tag{9.91}$$

We now concentrate on the terms, in Eq. (9.86), which are proportional to the factor $1/2 - \tilde{n}(w)$. Following a similar procedure as above we obtain

$$-\frac{8e^2g^2}{(2\pi)^3}\int dw\tilde{n}(w)S_q(w) = \frac{-8e^2g^2}{(2\pi)^3}\int dw\tilde{n}(w)\left[-4w - 4w\log\left(\frac{2}{\epsilon}\right)\right] \tag{9.92}$$

Thus, giving us the relation

$$S_q(w) = -4w - 4w \log\left(\frac{2}{\epsilon}\right). \tag{9.93}$$

Note that in both the expressions for S_q and S_g there is a $\log\left(\frac{2}{\epsilon}\right)$ term which blows up as $\epsilon \to 0$. This is a collinear singularity. We shall allow ϵ to vanish only when all the different contributions to the dilepton rate have been added together.

9.8.2 *Vertex correction V_g & V_q*

We concentrate first on the term proportional to the fermionic frequency *i.e.*, V_q. This vertex correction is essentially given by Eqs. (9.64, 9.66, 9.67). The first two need to be doubled, as mentioned before in Sect. 9.6. Extracting only the part proportional to the fermionic distribution function $\tilde{n}(w)$, we obtain the V_q integral as

$$-\frac{8e^2g^2}{(2\pi)^3}\int dw\tilde{n}(w)V_q(w) = 2\times(-2\pi i)8e^2g^2\int\frac{d^3kd^3w}{(2\pi)^6k^2w^2}\Big\{[1-2\tilde{n}(k)][-2\tilde{n}(w)]\Big\}$$
$$\times\left[\frac{(\mathbf{k}_+\cdot\mathbf{w}_{s_2})(\mathbf{k}_-\cdot\mathbf{w}_{s_3})s_2}{[E-(s_2-s_3)w][(k+s_3w)^2-q^2]}\right]\delta(E-2k). \tag{9.94}$$

Performing the sum on s_2, s_3 and setting $y = \cos\theta$(where θ is the angle between $\vec{k}$ and $\vec{w}$), we can perform one of the integrations with the help of one of delta function to get

$$-\frac{8e^2g^2}{(2\pi)^3}\int dw\tilde{n}(w)V_q(w) = \frac{32e^2g^2}{(2\pi)^3}\int dww(-\tilde{n}(w))\int_{-1+\epsilon}^{1-\epsilon}dy\frac{1}{2}\left[\left\{\frac{E}{E+2w}+\frac{E}{E-2w}\right\}\frac{1+y}{1-y}\right.$$
$$\left.+\left\{\frac{w}{E+2w}-\frac{w}{E-2w}\right\}(1+y)\right]. \quad (9.95)$$

Note, once again, that the limits of the final angular integration y signal the onset of collinear singularities. These are, once again, regulated by removing the small part of phase space ϵ. At this point we introduce the condition that the limit of interest is for dilepton mass much larger than the temperature *i.e.*, $E >> T$. The presence of the distribution function $\tilde{n}(w)$ on the energy w severely restricts the contribution from regions where $w >> T$ to the integral. Thus, the dominant contribution to the integral is from the regions where $w << T$ or $w \sim T$. Hence, in the integral we may make the approximation that $w << E$ and expand the factors in the square brackets to linear power in w/E. This finally gives

$$-\frac{8e^2g^2}{(2\pi)^3}\int dw\tilde{n}(w)V_q(w) = -\frac{8e^2g^2}{(2\pi)^3}\int dw\tilde{n}(w)\left[-8w+8w\log\left(\frac{2}{\epsilon}\right)\right]. \quad (9.96)$$

Thus we obtain that

$$V_q(w) = -8w+8w\log\left(\frac{2}{\epsilon}\right). \quad (9.97)$$

Following almost a similar method as above we may obtain V_g from Eq. (9.65) (with an overall factor of 2 as there is another cut which gives an identical contribution) as,

$$V_g(w) = 4w-\frac{2E^2}{w}\log\left(\frac{2}{\epsilon}\right). \quad (9.98)$$

Once again, note that both expressions demonstrate a collinear divergence as $\epsilon \to 0$. The term V_g also displays an infrared divergence as $w \to 0$.

9.8.3 Photon formation from quark, antiquark and gluon D_g & D_q

The reverse reaction to this process represents heavy photon "decay" into a $q\bar{q}\gamma$. Due to this reason, the process is denoted by the letter D [101]. The full decay contribution is given by Eq. (9.49) as,

$$\begin{aligned} Disc[\Pi^2](E-k-q-E_{k-q}) = -i\int \frac{d^3kd^3qd^3w}{(2\pi)^9 2q2k2w}(2\pi)^4\delta^4(\mathbf{p}-\mathbf{k}-\mathbf{q}-\mathbf{w}) \\ \times\Big\{[1-\tilde{n}(k)][1+n(q)][1-\tilde{n}(w)]-\tilde{n}(k)n(q)\tilde{n}(w)\Big\} \\ \times 32e^2g^2\left[\frac{E-2k}{E-2w}+\frac{E-2w}{E-2k}+2\frac{E(E-2q)}{[E-2w][E-2k]}\right]. \end{aligned} \tag{9.99}$$

In the above equation, note that if three of the delta functions are used to set $\vec{w}=-\vec{k}-\vec{q}$, then the remaining delta function imposes the condition that

$$E = k+q+\sqrt{k^2+q^2+2kq\cos\theta}$$

As mentioned before, we work in the limit $E >> T$, in this case the delta function can be satisfied by the following regions of phase space:

a) $k \sim E$, $q \sim E$ and hence $w \sim E$; in this case all the distribution functions $n(q), \tilde{n}(k), \tilde{n}(w) \to 0$, and, thus, so do products of distribution functions.

b) $k \sim T << E$, $q \sim E$ and hence $w \sim E$; in this case $\tilde{n}(k) \sim 1$. However $n(q), \tilde{n}(w) \to 0$, and so do products of distribution functions.

c) $w \sim T << E$, $q \sim E$ and hence $k \sim E$; in this case $\tilde{n}(w) \sim 1$. However $n(q), \tilde{n}(k) \to 0$, and so do products of distribution functions.

d) $q \sim T << E$, $k \sim E$ and hence $w \sim E$; in this case $n(q) \sim 1$. However $\tilde{n}(w), \tilde{n}(k) \to 0$, and so do products of distribution functions.

Contributions from b) and c) will give us D_q, d) will give us D_g, while the contribution from a) is negligible in comparison. We begin by calculating D_q from the regions b) and c) of phase space. Here we can ignore all combinations of distribution functions containing $n(q)$. As before, we also ignore the vacuum term, concentrating

only on the matter contribution. Noting the symmetry in the matrix element under interchange of k and w, we may change variables $w \to k$ in the part of the integrand proportional to the distribution function $\tilde{n}(w)$ to get

$$-\frac{8e^2g^2}{(2\pi)^3}\int dk\tilde{n}(k)D_q(k) = \int \frac{d^3kd^3q}{(2\pi)^5 2q2k2w}\delta(E-k-q-w)\Big\{2\tilde{n}(k)\Big\}$$
$$32e^2g^2\left[\frac{E-2k}{E-2w}+\frac{E-2w}{E-2k}+2\frac{E(E-2q)}{[E-2w][E-2k]}\right]. \tag{9.100}$$

The argument of the delta function is the equation $g(q) = k + q + w(q) - E = 0$. The solution of this equation is at $q = q_s(k, E)$:

$$q_s = \frac{1}{2}\frac{E(E-2k)}{E-k(1-y)}. \tag{9.101}$$

The delta function can be written as

$$\delta(g(q)) = \frac{\delta(q-q_s)}{|g'(q_s)|}.$$

Substituting this back into the equation for D_q, we can do the dq integration with the above mentioned delta function. We can then perform the remaining angular integration by removing the small part of phase space ϵ to shield the collinear singularities. Now expanding up to linear order in k as $k << E$, we get

$$-\frac{8e^2g^2}{(2\pi)^3}\int dk\tilde{n}(k)D_q(k) = -\frac{8e^2g^2}{(2\pi)^3}\int dk\tilde{n}(k)\left[2k+\Big(-2k-E\Big)\log\left(\frac{2}{\epsilon}\right)\right]. \tag{9.102}$$

Thus we get

$$D_q(w) = 2w + \Big(-2w-E\Big)\log\left(\frac{2}{\epsilon}\right). \tag{9.103}$$

We can now obtain D_g by concentrating on region d) of phase space and ignoring all combinations of distribution functions containing $\tilde{n}(k)$ or $\tilde{n}(w)$, this gives us,

$$D_g(w) = -2w + \left(2w - 2E + \frac{E^2}{w}\right)\log\left(\frac{2}{\epsilon}\right). \tag{9.104}$$

9.8.4 *Pair annihilation F & Compton scattering C*

The procedure to obtain these is almost exactly identical to the two terms of the previous section. The total Compton scattering contribution can be obtained from Eq. (9.58) by doubling it as mentioned in the paragraph immediately following Eq. (9.58). We may, once again, from phase space considerations show that the dominant contribution to Compton scattering occurs from a region where $k \sim T << E$(k is the incoming quark or antiquark energy). The leading term of Compton scattering is, thus, proportional to the quark or antiquark distribution function. From similar considerations the leading term of pair annihilation can be demonstrated to be proportional to the outgoing gluon distribution function. Expanding them up to linear order in the quark or gluon energy w, we get:

$$C(w) = 2w + \Big(-2w + E \Big) \log\left(\frac{2}{\epsilon}\right). \tag{9.105}$$

and

$$F(w) = -2w + \left(2w + 2E + \frac{E^2}{w}\right) \log\left(\frac{2}{\epsilon}\right). \tag{9.106}$$

9.9 *Results*

In the previous seven sections we evaluated the two different self-energies of the photon at two loops; then evaluated the various cuts of the self-energies which constituted its imaginary part; we then recombined the various cuts and reinterpreted them as physical processes; finally we evaluated these terms in the limit of heavy photon emission. In the last section we have concentrated solely on the thermal or matter part of these expressions. The vacuum part is well known. All the expressions contain collinear singularities(as $\epsilon \to 0$), which for the moment have been shielded by removing the small part of phase space(ϵ) where these singularities occur. Some of the expressions also display infrared singularities as $w \to 0$. Hence, the final integrations over w are yet to be performed. In the following we will combine all these terms and

perform this integration.

We now re-substitute the terms F, C, D, V, and S back in Eq. (9.84) to get the coefficients of the bosonic and fermionic distribution functions as

$$n(w)\Big(F + D_g + V_g + S_g\Big) = n(w)(-4w). \tag{9.107}$$

$$\tilde{n}(w)\Big(C + D_q + V_q + S_q\Big) = \tilde{n}(w)(-8w). \tag{9.108}$$

Thus, we find that when all the cuts are summed, the collinear and infrared singularities cancel. This is in contradistinction with the results of Refs. [99, 101], where the infrared singularities cancel but the collinear singularities persist. With these, we get the full imaginary part of the self-energy as

$$\begin{aligned} \mathrm{Im}\Pi^{\mu}_{\mu\,2\mathrm{loop,thermal}} &= -\frac{4e^2g^2}{(2\pi)^3}\left[-\frac{4\pi^2T^2}{3}\right] \\ &= \frac{8e^2\alpha_s T^2}{3}. \end{aligned} \tag{9.109}$$

We may also derive the Born term and quote the two-loop vacuum contribution(from [113]) as

$$\mathrm{Im}\Pi^{\mu}_{\mu\,1\mathrm{loop}} + \mathrm{Im}\Pi^{\mu}_{\mu\,2\mathrm{loop,vacuum}} = \frac{-3e^2}{4\pi}E^2\left(1+\frac{\alpha_s}{\pi}\right). \tag{9.110}$$

9.10 Summary and discussions

In this chapter, we have calculated the imaginary part of the two-loop heavy boson retarded self-energy in the imaginary time formalism. We also elucidated the analytic structure of the self-energy by recombining and reinterpreting various cuts of the self-energy as physical processes which occur in the the medium. Cuts with loops have been interpreted as interference terms between $O(\alpha)$ tree scattering amplitudes and the Born term with spectators. At each stage the results from the self-energy cuts was

matched by re-deriving the amplitudes of the tree level diagrams. This constitutes an important check of each of the contributions from the self-energy.

Each of the contributions contain infrared and collinear singularities. In accord with our stated goals, we analysed this singular behaviour in the region where the dilepton mass is far greater than the temperature. This allowed us to neglect a series of terms which appear sub-dominant. In each case we retained terms only up to order T^2/E^2. One might argue that this represents a considerable approximation of the result. However the resulting simplification allows us to analyse far simpler and analytically integrable expressions. We would point out that this was precisely the approximation used in [101, 99] where a remnant collinear divergence was deduced at $O(T^2/E^2)$. When all the contributions were summed, all infrared and collinear divergences cancelled; leaving a finite result of $O(T^2/E^2)$. This is consistent with the KLN theorem [109, 110], even though a formal proof of the theorem at finite temperature is still elusive.

In light of the above, one may conclude that for very high invariant mass M dileptons, the Born term or LO contribution is the most dominant, thermal contribution from the plasma. As the energy of the incoming particles scales with the dilepton energy $E >> T$, there are no high temperature enhancements to speak of here. The finite density effects are mostly driven by the difference of the quark and antiquark distribution functions. These differences are negligible for quark energies much greater than the temperature. Thus, the finite density enhancements from two gluon fusion are miniscule here. The solitary higher order effect that may outshine the LO contribution, would have been one born of divergences in the NLO rates. This has turned out to be not the case.

9.11 Appendix

Discontinuity across a second order pole.

Imagine we have a function of a complex variable $F(z)$, and it is given to be in the form

$$F(z) = \int dx \frac{f(z,x)}{z-x} + \frac{g(z,x)}{(z-x)^2}, \tag{9.111}$$

where x is a real variable, integrated on the real axis. Most of the discontinuities that we evaluate can be cast in this general form. This can be rewritten as

$$-F(z) = \int dx \frac{f(z,x)}{x-z} - \frac{g(z,x)}{(x-z)^2}, \tag{9.112}$$

The functions $f(z,x)$ and $g(z,x)$ are analytic in x and hence admit a Taylor expansion.

$$f(z,x) = f(z,x=z) + \frac{df}{dx}(z,x=z)[x-z] + \frac{1}{2}\frac{d^2f}{dx^2}(z,x=z)[x-z]^2 + ... \tag{9.113}$$

Substituting Eq.(9.113) in Eq.(9.112) we get

$$\begin{aligned} -F(z) = \int dx \frac{f(z,x=z)}{x-z} + \frac{df}{dx}(z,x=z) + \frac{d^2f}{dx^2}(z,x=z)[x-z] + ... \\ - \frac{g(z,x=z)}{(x-z)^2} - \frac{dg}{dx}(z,x=z)\frac{1}{x-z} - \frac{1}{2}\frac{d^2g}{dx^2}(z,x=z)\frac{1}{(x-z)^2} - ... \end{aligned} \tag{9.114}$$

Recalling that only the pure first order poles develop a discontinuity or imaginary part at the pole we get the imaginary part of Eq.(9.114) as

$$Disc[-F(z)] = \int dx 2\pi i \delta(x-z)\left[f(z,x) - \frac{dg}{dx}(z,x)\right]. \tag{9.115}$$

10

CONCLUSION

In this thesis, we initiated a two pronged study of highly excited, strongly interacting matter, produced in heavy-ion collisions. One endeavour was at intermediate energies characterized by energy densities of $\sim 1 - 10$ MeV/nucleon, in the central region. Another was at ultra-relativistic energies, with energy densities of about $\sim 1 - 10$ GeV/nucleon. In each region we focused on the spectra of various particles and nuclear clusters emanating from such collisions. No doubt the degrees of freedom and their interplay, in other words the physics involved in each scenario is quite different. As a result, we employed different theoretical formalisms in the study of each phenomena.

10.1 Intermediate energy and multifragmentation

At intermediate energies, we focused on the pervasive phenomena of multi-fragmentation. This constitutes the explosive decomposition of the highly excited systems produced in heavy ion collisions into a large variety of nuclear clusters. As the energy densities involved are below the particle production threshold, no new particles are produced. We studied these phenomena in a thermal model approach *i.e.*, we assumed full thermal and chemical equilibrium being reached in the system. We then modelled the system in terms of the relevant degrees of freedom.

The degrees of freedom were nucleons and nuclei, treated as non-relativistic hard spheres with a quantum mechanical excitation spectrum. These were considered as non-interacting (except for a Coulomb force) and enclosed in a box of volume V.

The volume V is the volume of the system at at the time when interactions between various clusters cease and we achieve freezeout. We applied the methods of standard statistical mechanics in the canonical ensemble, to this system. The various partitions of the partition function consisted of the different ways of distributing A nucleons in monomeric and/or polymeric clusters.

As a 'base' or starting point we adopted the recently developed RSM model. After a cursory introduction to the model (see chapter 2), we invoked a variety of refinements to this simple model. We began with a detailed analysis of the excluded volume correction (see Chapter 3). Here we introduced a novel Monte-Carlo technique to estimate the excluded volume in such systems. We demonstrated how this may vary with multiplicity and be quite different at higher densities from previous naïve estimates. In a subset of situations we managed to parametrize this effect with an analytical expression (though a complete general expression evaded us). We also demonstrated the effect of the excluded volume correction on the equation of state.

In Chapter 4, we demonstrated how this model may be used to perform realistic calculations. We introduced isospin dependence in the calculation of the partition function. For isotopes up to ^{20}F, exact energy levels obtained from experiment were used. For isotopes above ^{20}F, an empirical mass formula was used. We devised a new secondary decay mechanism based on the Weisskopf formalism. Instead of calculating decay level to level, we have blurred out such details by using a smooth level density. Though approximate, this method enjoys the advantage of being a natural extension of the canonical ensemble calculations performed previously. As demonstrated in the plots, we obtain very good agreement with the data (see Sect. 4.6-4.7). We may, thus, claim that our two step model provides a realistic interpretation of the physics involved in such multifragmentation processes.

With this confidence, we begin the study of the critical phenomena observed in such experiments. A first order liquid-gas-phase transition has been seen in experiments [4]. There have also been recent claims of the excited system disintegrating in the vicinity of a second order point [16]. The latter are based on the observation

of a scaling behaviour in a certain subset of the yields. Using the Fisher scaling formula a critical temperature was also deduced. We demonstrate that the same subset of yields obtained from the above mentioned model also demonstrate a similar scaling behaviour. This is observed even when the calculations are performed near a clear first order phase transition. The scaling behaviour is observed not only in our explicit model, but also in a general thermodynamic model with explicit first order phase transition. This scaling behaviour is only apparent in that small subset of yields and is no longer observed if the range of yields is increased. The so called critical temperature that is deduced is nothing other than the boiling temperature of a first order phase transition. We thus refute the claim of Ref. [16] of the observation of critical phenomena.

10.2 High energy and dilepton production

At high energies, we focused on the phenomena of dilepton production. Due to their small rescattering cross section electromagnetic probes provide a window into the hot and dense matter created early in the history of a heavy-ion collision. They are thus privileged probes for detecting the possible formation of a quark-gluon-plasma in these collisions.

In the majority of calculations of the dilepton spectrum from such systems, the LO or Born term (see Fig. (6.2)) has been used as the sole channel of dilepton production. The argument provided for neglecting higher order contributions has been that the formation of a large region of deconfined quarks and gluons testifies to the fact that the strong coupling constant must be small enough to subdue these contributions. This statement has been subjected to close scrutiny in the second part of the thesis. We explore a variety of higher order effects which may lead to the NLO contributions becoming dominant over the Born term. We divide up the parameter space of dileptons (based on the energy of the virtual photon E and the temperature T) into soft ($E << T$), hard ($E \sim T$) and very hard ($E >> T$); and look at higher

order effects characteristic to each region.

In the soft sector, much work preceded the author's own efforts. The main results are listed in chapter 7 . Most of these calculations are performed in the limit of asymptotically high temperature $T \to \infty$. In this limit, the strong coupling constant is, in fact, very small $g \to 0$. However, one notes that, even in such a situation, the one loop resummed rates which contain higher order contributions, completely over shadow the Born term in the very soft sector. As the energy increases, the Born term eventually achieves dominance (see Fig. (7.5)). It is believed that the spectrum at realistic temperatures may look qualitatively similar to that at high temperatures. If this is so, then the soft spectrum is completely dominated by higher order effects. As a result, the LO or Born term is, most possibly, not the dominant contribution in this sector.

In the hard sector (chapter 8), the high temperature effects mentioned in the preceding paragraph have waned away leaving the Born term dominant. This is true for plasmas with zero charge densities. It has been noticed in recent experiments at RHIC, that there is a remnant baryon density and hence a charge density in the central region [90]. In such a medium, Furry's theorem is explicitly broken and a new set of diagrams arise. After highlighting the general class of diagrams, we focus on the lowest order process in this class. This turned out to contribute to the photon self energy at three loops. Different cuts of the self energy lead to different channels of dilepton production. Most of the cuts lead to finite density contributions on preexisting processes. There also arose an entirely new channel of dilepton production from two gluon fusion. Such a channel has never been explored previously. We focused our efforts solely on the contributions from this process. Besides charge conjugation invariance, this diagram is also protected by rotational invariance. On breaking each of these symmetries in turn, we obtain a non-zero contribution from this process (see chapter 8 for details). We focused on the subset of configurations where the gluons were confined to be back-to-back and compared it to the Born term where the quarks are also confined to be back to back. Within reasonable values of baryon density,

this contribution turns out to be much smaller than the Born term at large invariant mass. However, it becomes comparable to the Born term at low invariant mass (see Fig. (8.6)). In our calculation the quarks are endowed with current masses m and the gluons are massless. In this situation the back to back Born term suffers from having a threshold at dilepton mass $\sqrt{2mE}$. The overall Born term has a threshold at $2m$. The back-to-back Born term and the overall Born term are zero below the respective thresholds. As the gluons are massless, the $gg \to e^+e^-$ continues to contribute beyond both thresholds. It thus may become the dominant source of dileptons at very low invariant mass. Though much work remains to be done in this scenario, we have clearly demonstrated the existence of an important new channel. Its full effect may only be realised on a full three momentum integration of the signal, summing the contribution of all the cuts, and folding this rate with a realistic model of plasma evolution which explicitly includes a high gluon density phase. As the mandate of this thesis has been to stipulate the set of higher order processes that may become comparable to the Born term, we leave such extensions for a future effort.

Having enumerated important higher order effects in the soft and hard sector, we finally turned to the very hard sector ($E >> T$) in chapter 9. In this regime, both high temperature effects and finite density effects have become negligible. At such high energies the current quark masses are negligible compared to the energy scale of the problem. Such a situation may lead to the NLO contributions displaying mass divergences. The presence of this small mass would lead to large logarithms and we would have the NLO contributions larger than the Born term. Such a situation was suggested in Refs. [99, 101] for dilepton production at NLO. We calculate the imaginary part of the retarded self-energy of a heavy vector boson in the imaginary time formalism. The vector boson was taken to be static with a very large invariant mass. We then elucidated the analytic structure of the self-energy by recombining and reinterpreting various cuts as physical processes which occur in the medium. This calculation was performed for the massless theory. Each of the contributions was, as expected, in possession of a collinear and/or an infrared divergence. However, when

all the different contributions were summed, all collinear and infrared divergences cancelled and we obtained a finite contribution. This is consistent with the KLN theorem. This result implies that at very large invariant mass, the Born term is dominant over the NLO contribution. This however may not be the situation for the NNLO contribution. This contribution, yet to be estimated, is left for future analysis.

BIBLIOGRAPHY

[1] A. S. Hirsch *et al.*, Phys. Rev. C. **29**, 508 (1984).

[2] T. K. Nayak *et al.*, Phys. Rev. C. **45**, 132 (1992).

[3] K. Adcox *et al.*, Phys. Rev. Lett. **87**, 052301 (2001).

[4] J. Pochodzalla *et al.*, Phys. Rev. Lett. **75**, 1040 (1995).

[5] H. M. Xu *et al.*, Phys. Rev. C **40**, 186(1989).

[6] K. Hagel *et al.*, Phys. Rev. C. **50**, 2017 (1994).

[7] L. Bealieu *et al.*, Phys. Rev. C. **64**, 064604 (2001).

[8] V. F. Weisskopf, Phys. Rev., **52**, 295 (1937).

[9] W. A. Friedman, W. G. Lynch, Phys. Rev. C **28**, 16 (1983).

[10] S. Das Gupta, A. Z. Mekjian, and M. B. Tsang, Adv. Nuc. Phys. **26**, 91 (2001).

[11] A. Z. Mekjian, Phys. Rev. Lett. **38**, 640 (1977); S. Das Gupta and A. Z. Mekjian, Phys. Rep. **72** ,131 (1981).

[12] H. Jaquaman, A. Z. Mekjian, and L. Zamick, Phys. Rev. C. **27**, 2782 (1983).

[13] A. L. Goodman, J. I. Kapusta and A. Z. Mekjian, Phys. Rev **C30**, 851 (1984).

[14] H. R. Jaqaman, A. Z. Mekjian, and L. Zamick, Phys. Rev. C **29**, 2067 (1984).

[15] J. E. Finn *et. al.*, Phys. Rev. Lett. **49**, 1321 (1982).

[16] J. B. Elliot *et. al.*, Phys. Rev. Lett. **88**, 042701 (2002).

[17] J. B. Natowitz *et al.*, **nucl-ex/0106016**.

[18] W.A. Friedman, Phys. Rev. C. **42**, 667 (1990).

[19] W. Bauer, Phys. Rev. C. **38**,1297(1988).

[20] X. Campi, Phys. Lett. **B208**,351(1988).

[21] J.Pan and S. Das Gupta, Phys. Rev. C. **51**, 1384 (1995).

[22] G. F. Bertsch and S. Das Gupta, Phys. Rep. **160**,189 (1988).

[23] J. Randrup and S. Koonin, Nucl. Phys. **A356**, 321 (1981).

[24] G. Fai and J. Randrup, Nucl. Physics. **A404**, 551 (1983).

[25] D.H.E. Gross, Rep. Prog. Phys. **53**, 605 (1990).

[26] J.P. Bondorf, A.S. Botvina, A.S. Ijilnov, I.N. Mishustin and K. Sneppen, Phys. Rep. **257**, 133 (1995).

[27] K.C. Chase and A.Z. Mekjian, Phys. Rev. C. **52**, R2339(1995)

[28] S. Das Gupta and A.Z. Mekjian, Phys. Rev. C **57**, 1361 (1998).

[29] F. Reif, *Fundamentals of Statistical and Thermal Physics*, McGraw Hill, Singapore, (1985).

[30] D. Hahn, and H. Stocker, Nucl. Phys. **A452**, 723 (1986); G. Fai, and J. Randrup, Nucl. Phys. **A381**, 557 (1982).

[31] A. Majumder, and S. Das Gupta, Phys. rev. C. **59**, 2135 (1999).

[32] Bao-An Li, S. Pratt and P.J. Siemens, Phys. Rev. C. **37**, 1473 (1988).

[33] A. Majumder and S. Das Gupta, Phys. Rev. C. **61**, 34603 (2000).

[34] D. H. E. Gross, Phys. Rep. **279**, 119 (1997).

[35] S. E. Koonin, and J. Randrup, Nucl. Phys. **A474**, 173 (1987).

[36] R. K. Pathria, *Statistical Mechanics* , (Pergamon, New York, 1972), Chap. 9.

[37] H. Xi *et al.* , Phys. Rev. C. **58**, R2636 (1998)

[38] A. Bohr, B. R. Mottelson, *Nuclear Structure* , Vol. 1 (W. A. Benjamin, Inc., New York,1969), pp281-293

[39] W. Hauser, H. Feshbach, Phys. Rev., **87**, 366 (1952).

[40] H. Xi, W.G. Lynch, M. B. Tsang, W. A. Friedman, D. Durand, Phys. Rev. C **59**, 1567 (1999).

[41] M. E. Fisher, Physics (Long Island City, N.Y.) **3**, 255 (1967).

[42] M. B. Tsang et al., to be published in Phys. Rev. C.

[43] P. Bhattacharyya, S. Das Gupta and A. Z. Mekjian, Phys. Rev **C60**, 64625 (1999).

[44] K. A. Bugaev, M.I. Gorenstein, I. N. Mishustin and W. Greiner, Phys. Rev **C62**, 44320 (2000).

[45] K. A. Bugaev, M. I. Gorenstein, I. N. Mishustin and W. Greiner, Phys. Lett **B498**, 144 (2001).

[46] J. B. Elliott and A. S. Hirsch, Phys. Rev **C61**, 54605 (2000).

[47] F. Gulminelli and Ph. Chomaz, Phys. Rev. Lett. **82**, 1402 (1999).

[48] C. A. Ogilvie et al., Phys. Rev. Lett. **67**, 1214 (1991).

[49] J. B. Elliott et al., Phys. Rev. Lett. **85**, 1194 (2000).

[50] M. W. Zemansky, and R. H. Dittman, *Heat and Thermodynamics.*, McGraw Hill, Singapore, (1981).

[51] S. Pratt, C. Montoya, and F. Ronning, Phys. Lett. **B314**, 261 (1995).

[52] J. Pan, S. Das Gupta and M. Grant, Phys. Rev. Lett. **80**, 1182 (1998).

[53] K.C. Chase and A.Z. Mekjian, Phys. Rev. C. **50**, 2078 (1994).

[54] J. C. Collins, and M. J. Perry, Phys. Rev. Lett. **34**, 1353 (1975).

[55] T. Matsui, and H. Satz, Phys. Lett. **B178**, 416, (1986).

[56] J. Rafelski, and B. Müller, Phys. Rev. Lett. **48**, 1066, (1982).

[57] E. Shuryak, Phys. Rep. **80**, 71 (1980).

[58] P. Braun-Munzinger, I. Heppe, and J. Stachel, Phys. Lett. **B465**, 15 (1999).

[59] J. I. Kapusta and S. M. H. Wong, Phys. Rev. Lett. **86**, 4251 (2001).

[60] K. Adcox *et al.*, Phys. Rev. Lett. **88**, 242301 (2002).

[61] F. Karsch, Nucl. Phys. **A698**, 199 (2002).

[62] D. J. Gross, and F. Wilczek, Phys. Rev. Lett. **30**, 1343 (1973).

[63] H. D. Politzer, Phys. Rev. Lett. **30**, 1346 (1973).

[64] R. Rapp, Phys. Rev. C. **63**, 054907 (2001).

[65] J. Alam, B. Sinha and S. Raha, Phys. Rept. **273**, 243 (1996).

[66] K. Geiger, and J. I. Kapusta, Phys. Rev. D. **47**, 4905 (1993).

[67] S. A. Bass *et al.*, Prog. Part. Nucl. Phys. **41**, 225 (1998).

[68] K. Kajantie, J. Kapusta, L. McLerran, and A. Mekjian, Phys. Rev. D. **34**, 2746 (1986).

[69] F. Karsch, E. Laermann, P. Petreczky, S. Stickan, and I. Wetzorke, Phys. Lett. **B530**, 147 (2002).

[70] H. A. Weldon, Phys. Rev. D. **42**, 2384 (1990).

[71] C. Gale, and J. I. Kapusta, Nucl. Phys. **B357**, 65 (1991).

[72] L. P. Kadanoff and G. Baym, *Quantum Statistical Mechanics*, Benjamin/Cummings Publishing, Reading, Massachusetts (1962).

[73] M. Le Bellac, *Thermal Field Theory* , Cambridge University Press, (1996).

[74] J. I. Kapusta, *Finite Temperature Field Theory*, Cambridge University Press, (1989).

[75] M. E. Peskin, and D. E. Schroeder, *An Introduction to Quantum Field Theory*, Addison-Wesley, Reading, Mass. (1995).

[76] R. D. Pisarski, Nucl. Phys. **B309**, 476 (1988).

[77] X. N. Wang, Phys. Rept. **280**, 287 (1997).

[78] D. J. Gross, R. D. Pisarski, and L. G. Yaffe, Rev. Mod. Phys. **53**, 43 (1981).

[79] K. Kajantie and J. I. Kapusta, Ann. Phys. (N.Y.) **160**, 477 (1985).

[80] U. Heinz, K. Kajantie, and T. Toimela, Ann. Phys. (N.Y.) **176**, 218 (1987).

[81] R. Kobes and G. Kunstatter, Phys. Rev. Lett. **61**, 392 (1988).

[82] E. Braaten and R. D. Pisarski, Nucl. Phys. **B337**, 569 (1990); Nucl. Phys. **B339**, 310 (1990).

[83] J. Frenkel and J. C. Taylor, Nucl. Phys. **B334**, 199 (1990).

[84] R. D. Pisarski, Phys. Rev. Lett. **63**, 1129 (1989).

[85] E. Braaten and R. D. Pisarski, Phys. Rev. Lett. **64**, 1338 (1990).

[86] E. Braaten, R. D. Pisarski, and T. C. Yuan, Phys. Rev. Lett. **64**, 2242 (1990).

[87] P.Aurenche, F. Gelis, H. Zaraket and R. Kobes, Phys. Rev. D. **60**, 085003 (1999).

[88] E. Shuryak, Phys. Rev. Lett. **68**, 3270 (1992).

[89] Z. Lin, and C. M. Ko, Nucl. Phys. **A671**, 567 (2000).

[90] B. B. Back *et al.*, Nucl. Phys. **A698**, 655 (2002).

[91] H. Vija, M. H. Thoma, Phys. Lett. **B342**, 212 (1995).

[92] A. Dumitru, D.H. Rischke, T. Schonfeld, L. Winckelmann, H. Stocker, and W. Greiner, Phys. Rev. Lett. **70**, 2860 (1993).

[93] C. Itzykson, J. B. Zuber, *Quantum Field Theory*, McGraw Hill, New York, (1980).

[94] S. Weinberg, *The Quantum Theory of Fields*, Vol. 1, Cambridge University Press, (1995).

[95] See for example, S. A. Chin, Ann. Phys. 108, 301 (1977); H. A. Weldon, Phys. Lett. B **274**, 133 (1992).

[96] The Particle Data Group, Eur. Phys. J. C. **15**, 1 (2000).

[97] A. Majumder, and C. Gale, Phys. Rev. D. **63**, 114008 (2001).

[98] A. Majumder and C. Gale, Proc. MRST01, (2001).

[99] J. I. Kapusta, and S. M. H. Wong, Phys. Rev. C. **62**, 027901 (2000).

[100] J. I. Kapusta, P. Lichard, and D. Seibert, Phys. Rev. D. **44**, 2774 (1991); Erratum-ibid. D. **47**, 4171 (1993).

[101] J. I. Kapusta, and S. M. H. Wong, Phys. Rev. D. **62**, 037301 (2000).

[102] C. N. Yang, Phys. Rev. **77**, 242 (1950).

[103] K. J. Eskola, K. Kajantie, P. V. Ruuskanen and K. Tuominen, Nucl. Phys. **B570**, 379 (2000).

[104] S. M. H. Wong, Z. Phys. C. **53**, 465 (1992).

[105] P.Aurenche, F. Gelis, H. Zaraket and R. Kobes, Phys. Rev. D. **58**, 085003 (1998).

[106] F. Bloch and A. Nordsieck, Phys. Rev. **52**, 54 (1937).

[107] D.R. Yennie, S.C. Frautschi, and H. Suura, Ann. Phys. (N.Y.) **13**, 379 (1961).

[108] S. Weinberg, Phys. Rev. **140**, B516 (1965).

[109] T. Kinoshita, J. Math. Phys. **3**, 650 (1961).

[110] T. D. Lee, and M. Nauenberg, Phys. Rev. **133B**, 1549 (1964).

[111] A. D. Linde, Phys. Lett. **B96**, 289 (1980).

[112] R. Doria, J. Frenkel, and J.C. Taylor, Nucl. Phys. **B168**, 93 (1980).

[113] R. D. Field, *Applications of Perturbative QCD*, Addison-Wesley, New York (1995).

[114] H. A. Weldon, Phys. Rev. D. **28**, 2007 (1983).

[115] L. D. McLerran and T. Toimela, Phys. Rev. D **31**, 545 (1985).

[116] R. Baier, B. Pire, and D. Schiff, Phys. Rev. D. **38**, 2814 (1988).

[117] T. Altherr, P. Aurenche, and T. Becherrawy, Nucl. Phys. **B315**, 436 (1989); T. Altherr, and P. Aurenche, Z. Phys. **C 45**, 99 (1989).

[118] S. M. H. Wong, Phys. Rev. D. **64**, 025007 (2001).

[119] P. Aurenche *et al.*, Phys. Rev. D. **65** 038501 (2002).

[120] J. I. Kapusta, and S. M. H. Wong, Phys. Rev. D. **65** 038502 (2002).

[121] J. I. Kapusta, and S. M. H. Wong, Phys. Rev. D. **64** 045008 (2001).

[122] G. Baym, and N. D. Mermin, J. Math. Phys. **2**, 232 (1961).